THE FLUID-STRUCTURE INTERACTION OF AN AXISYMMETRIC UNDEREXPANDED JET FLOWING ACROSS AN ADJACENT COMPLIANT SURFACE

BY

RUBEN HORTENSIUS

DISSERTATION

Submitted in partial fulfillment of the requirements
for the degree of Doctor of Philosophy in Aerospace Engineering
in the Graduate College of the
University of Illinois at Urbana-Champaign, 2017

Urbana, Illinois

Doctoral Committee:

Professor Gregory S. Elliott, Chair and Co-Director of Research
Professor J. Craig Dutton, Co-Director of Research
Professor Jonathan B. Freund
Associate Professor Daniel J. Bodony

Abstract

The current work characterizes, via detailed experiments, the flowfield and surface states of the relatively little-explored problem of an underexpanded axisymmetric jet flowing across an adjacent parallel surface, in both rigid-surface and compliant-surface configurations. To date, the vast majority of the literature for both the rigid- and compliant-surface cases has been generated by the acoustics community, and so most of the results obtained in those studies are rooted in pointwise measurements. This has resulted in little interest in the many relevant fluid-mechanical phenomena present in this turbulent flow. Meanwhile, there has been a growing interest in the area of fluid-structure interactions (FSIs) as we continue to push technological, engineering, and operational boundaries towards lighter and stronger structures at increasingly high speeds, pressures, and temperatures. The simultaneous acquisition of flowfield and structural conditions in fullfield has recently become a priority for the FSI community, but it presents a significant experimental challenge, and only a few studies to-date have successfully done so, and none (to the author's knowledge) have done so for high-speed flows.

It is the purpose of this work to document and experimentally characterize the rigid- and compliant-surface flowfields, and their corresponding surface states, towards the goals of improving the measurement quality and better understanding of the fluid-structure interactions involved. The study takes a multi-step approach. First, the fundamental flow - that of an isolated jet emanating from a 12.7-mm exit-diameter converging nozzle - is characterized in both a flowfield-velocimetry and unsteady manner at a nozzle pressure ratio, *NPR*, of 5.0. Next, the rigid-surface case is considered at three jet/surface separation distances, h/D_j (0.50, 0.55, and 0.60), and the flowfield and accompanying surface conditions are documented in detail, so as to provide a baseline for comparison. Then, the simultaneous acquisition of fullfield instantaneous velocity fields and surface deflection data are demonstrated and rigorously validated using particle image velocimetry (PIV) and stereo/3D digital image correlation (sDIC), respectively, for the compliant-surface case. These data provide insights into the relevant fluid-structure interaction involved via a comparison to the rigid-surface case.

The results obtained for the isolated jet case were consistent with the theoretical expectations and previous findings. Compressible waves visualized using high-speed schlieren

photography aligned well with the PIV velocity-vector fields. A shock-position oscillation time-history analysis conducted using the high-speed schlieren imagery identified distinct narrowband spectral peaks. These peaks were found to agree well with those observed in the acoustic spectra, as well as semi-empirical screech tone prediction models. Good agreement was observed for all tested operating conditions, leading to the conclusion that high-speed schlieren can be used to identify jet screech in the absence of acoustic spectra. Tomographic PIV data revealed the three-dimensional nature of the jet.

High-speed schlieren, planar PIV, steady pressure-sensitive paint (PSP), and surface oil flow visualization (SOFV) data obtained for the rigid-surface case were mutually consistent with each other, providing insight into the structure of the flowfield. For small h/D_j, a "plate-induced shock", formed in response to the restricted near-wall flow expansion, was observed in the schlieren imagery. This shock wave interacts with the barrel shock to cause the formation of a prominent shock/boundary-layer interaction (SBLI) near the wall, replacing the traditional first-cell Mach disk structure. Surface pressure was found to decrease within the initial jet expansion region, and to be approximately constant within the separation region, and to increase near the reattachment point. The pressure ratio across the plate surface was observed to be less than unity everywhere within the first shock cell and SBLI, imposing a loading that would lead to a jetward deflection in the compliant-surface case. PIV data reveal the presence of a small normal shock above the SBLI separation region, inducing large losses. Farther downstream, the schlieren, PIV, PSP, and SOFV data show the shock-cell structure of the jet, typified by a crossing-type shock structure. Increasing h/D_j resulted in a reduction in SBLI size and strength, eventually restoring the isolated jet structure. Detailed PIV measurement uncertainties were calculated in a thorough manner using an in-house developed code, and surface temperature and unsteady PSP measurements (limited success) were obtained.

The compliant-surface model was constructed using a frame and steel sheet shim stock (0.003" thick) approach. The compliant surface was 125-mm square, and all four edges were clamped. Surface deflection data were obtained on the backside of the surface using sDIC, while PIV data were obtained simultaneously on the other side. sDIC out-of-plane measurement resolution and accuracies were quantified and both experiments were rigorously validated individually, and a cross-validation was performed by plotting the sDIC results on the raw PIV images. Support frame out-of-plane deflections were accounted for via sDIC. The compliant

surface was found to take a quasi-static/steady response characterized by a standing wave pattern with a large jetward deflection in the first shock cell (~0.7 mm), and smaller oscillations farther downstream primarily oriented away from the jet. The mean deflected shape was reminiscent of the anticipated (3,1) vibrational mode shape. Surface strains were below the material's elastic strain limit. The large first-cell jetward deflection was found to impose a supersonic compression-expansion effect on the flow, transitioning near the deflected-surface inflection point. This altered the SBLI in-flow conditions, leading to a weaker SBLI shock system, and slightly elevated velocities and Mach number upon exiting the SBLI region. The compliant-surface case separation region was found to be longer and relatively thinner, and the boundary layer thickness throughout the measurement domain was increased, as compared to the rigid-surface case. In addition, the downstream shock-cell structure was different, where one of the shock-trains was attenuated, resulting in a zig-zag pattern. The jet primary shear layer position and size were found to be equivalent, and velocity and turbulence statistics profiles near the end of the measurement domain were found to be similar.

To my wife.

Acknowledgements

During the course of this journey, I often found myself doubting whether or not I could accomplish this monumental task. Were it not for the complete and unwavering support of the good people the Lord has placed in my life, I could not have done so. Thank you all.

Thank you Rebecca, my wife, for standing by, supporting me, and for your patience, as we waded through graduate school. I truly could not have done this without you in my life; I love you with all I have. My own parents, as well as my parents' in-law, encouraged me throughout and reminded me that I am capable of doing this. Chester, our Barbet and dog-child, has taught me to find joy in everything, and especially the simple things, like walks, and new toys.

The support and encouragement Rebecca and I have received from University Baptist Church, particularly from Pastor Brett Smith, will be remembered throughout my life. I can't say how much I have enjoyed talking to you about grad school, family, sports, and competition. Those conversations were casual and simple, but very meaningful to me. UBC has been our family while in Champaign-Urbana.

My Friday morning meetings at I Love Jesus Group with Greg, Phil, and Brent will be a lasting memory of my time in graduate school. I am honored to know these men who love the Lord, and to have had their support and friendship. ILJG is truly special.

My advisors, Professors Elliott and Dutton, have shown me how to become a thorough researcher, think critically, and learn for myself. Professor Dutton joined up at a time when his guidance was needed and gratefully received. Professor Elliott stuck with me through these years, vouched for me on a number of occasions, secured my financial support, and exposed me to two of my primary interests: diagnostics for fluid mechanics and teaching. His support and loyalty were undeserved, yet gratefully received. Professor Lambros kindly provided access to VIC-3D (sDIC software), and post-doc Michael Rossol gave me much valuable advice regarding sDIC.

My fellow graduate students and lab mates have been a constant, albeit rotating, source of support. The older classes showed me the way, the middle classes were my truest friends, and I helped lift up the younger classes. Special mention is owed to Todd Reedy, Tommy Herges, Ryan Fontaine, Andrew Knisely, Joe Bottalla, Brent Pomeroy, Jeff Diebold, Marianne Monastero, Jon Retter, Rohit Gupta, and James Favale. The list is longer, but I've filled the page - sorry guys.

Table of Contents

List of Abbreviations

°C	degree Celsius
ALA	Aeronautical Laboratory A
AOI	Area of interest
BL	boundary layer
CCD	charge-coupled device
CFD	computational fluid dynamics
CLAHE	contrast-limited adaptive histogram equalization
DAQ	data acquisition
DIC	digital image correlation
DEHS	Bis(2-ethylhexyl) sebacate
DNS	direct numerical simulation
FFT	fast-Fourier transform
FSI	fluid-structure interaction
fps	frames per second
GB	gigabyte
Hz, kHz	Hertz, kilohertz
ISSI	Innovative Scientific Solutions Inc.
K	Kelvin
kg	kilogram
LCO	limit cycle oscillations
LED	light emitting diode
m, cm, mm, μm	meter, centimeter, millimeter, micrometer (micron)
mJ	millijoules
in	inch
NI	National Instruments
NPR	nozzle pressure ratio
Pa, kPa	Pascal, kilopascal
PFV	Photon FASTCAM Viewer software
PID	proportional-integral-derivative

PIV	particle image velocimetry
pix	pixel
psi	pounds per square inch
psia	pounds per square inch (absolute)
psid	pounds per square inch (differential)
PSD	power spectral density
PSP	pressure-sensitive paint
RANS	Reynolds-averaged Navier Stokes
RMS	root-mean-square
SBLI	shock/boundary-layer interaction
sCMOS	scientific complementary metal-oxide semiconductor
sDIC	stereo/3D digital image correlation
SLS	selective laser sintering
SOFV	surface oil flow visualization
TIFF	tagged image file format
UIUC	University of Illinois at Urbana-Champaign
VI	virtual instrument, software interface for LabVIEW

List of Symbols

a	speed of sound
a_p	particle acceleration
$C_{D,p}$	particle drag coefficient
d_w	distance from the wall
d_p	mean particle diameter
D_j	jet exit diameter
D	flexural rigidity
E	material elastic modulus, also called Young's modulus
e_{xx}	normal strain in the X direction
e_{yy}	normal strain in the Y direction
e_{xy}	shear strain
e_1	major principal strain
e_2	minor principal strain
f	frequency
f	focal length
h	surface to jet axis distance
I	intensity counts
M	Mach number
m	mode number, transverse direction
n	mode number, axial direction
n	number of instantaneous measurements
P	static pressure
r	radial coordinate
R	universal gas constant
Re	Reynolds number
Re_p	particle Reynolds number
t	time
t	thickness
T	Temperature

u	jet axial velocity
u_f	fluid velocity
u_p	particle velocity
u_{slip}	particle slip velocity
$\overline{u'u'}$	Reynolds normal stress (streamwise direction)
$\overline{u'w'}$	Reynolds shear stress
$\mathscr{u}$	pixel displacement along X axis
$\bar{U}$	mean streamwise velocity
$\mathcal{U}$	metric displacement along X axis
v	transverse velocity
$\mathscr{v}$	pixel displacement along Y axis
$\|V\|$	velocity magnitude (speed)
$\bar{V}$	mean transverse velocity
$\mathcal{V}$	metric displacement along Y axis
$\mathscr{w}$	measurement uncertainty
w	wall-normal velocity
$\overline{w'w'}$	Reynolds normal stress (wall-normal direction)
$\bar{W}$	mean wall-normal velocity
$\mathcal{W}$	metric displacement along Z axis
ω_{mn}	vibrational natural frequency
$\mathcal{X}$	metric position along X axis
X	axial direction, sDIC coordinate frame
x	streamwise (axial) coordinate, measured from nozzle exit plane
$\mathcal{Y}$	metric position along Y axis
Y	transverse direction, sDIC coordinate frame
y	transverse coordinate, measured from the nozzle centerline
$\mathcal{Z}$	metric position along Z axis
Z	wall-normal direction, sDIC coordinate frame
z	wall-normal coordinate, measured from the nozzle centerline
α	coefficient of thermal expansion
δ	boundary-layer thickness

δ	oblique-shock turning angle
ε_y	material elastic strain limit
ε_{xx}	in-plane normal strain in the *x* direction
ε_{yy}	in-plane normal strain in the *y* direction
μ	dynamic viscosity
μ_f	fluid dynamic viscosity
γ	specific heat ratio
σ	correlation confidence interval
σ_{Cal}	PSP calibration uncertainty
σ_{Prec}	PSP precision error
σ_y	yield strain
$\sigma_{\mathcal{Z}}$	standard deviation about mean $\mathcal{Z}$
ρ	density
τ_p	particle time response
ν	kinematic viscosity
ν	Poisson ratio

Symbols

$\overline{(\,)}$	average quantity

Subscripts

amb	ambient conditions
d	design conditions
f	fluid property
frame	property of the model support frame
i, ideal	ideally-expanded conditions
p	particle property
ref	reference conditions, typically ambient
0	total or stagnation condition
∞	freestream condition
u, v, w	instantaneous velocity components

U, V, W	mean velocity components

Superscripts

equip	uncertainty due to equipment
lag	uncertainty due to particle lag
proc	uncertainty due to PIV processing
sampling	uncertainty due to sampling effects
total	combined instantaneous uncertainty
Total	combined mean uncertainty
‘	velocity fluctuation from the mean
°	degree

Chapter 1 Introduction

1.1 Background and Motivation

The flow of an isolated supersonic jet, as one of the fundamental compressible fluid flows, has been thoroughly investigated and is generally well understood. Jet/surface interactions, particularly in the form of impinging jets in both normal and oblique inclinations, have also been commonly studied due to relevant real-world applications (engine exhaust/airframe surfaces, rocket launches, carrier decks), and the wide array of fluid mechanic phenomena present (shock waves, expansion fans, boundary layers, shock-boundary layer interactions, flow separation, etc.). Aside from some attention from the acoustics community, relatively little literature exists concerning jets flowing across a nearby, parallel, rigid surface. The literature regarding the flow of a supersonic jet across such a compliant surface is even more limited, all studies having been conducted, to the knowledge of the current author, by a single investigator and his colleagues.

The jet and nearby parallel surface arrangement, in both the rigid- and compliant-surface configurations, has importance in terms of real-world applications, fundamental fluid mechanics phenomena, and fluid-structure interaction. This scenario has been little explored, leaving many aspects of the problem, as of yet, un-investigated. In particular, the acoustics-driven work, although necessarily unsteady, has largely neglected a steady or instantaneous fullfield characterization of either the fluid flowfield (velocity and turbulence) or the surface response. It is the purpose of this work to document and characterize the rigid-surface and compliant-surface case flowfields and the corresponding surface state in terms of deflection and pressure. The isolated jet is explored first, followed by the rigid-surface case, and ending with the compliant-surface case. This experimental arrangement allows for comparison of cases that facilitates a better understanding of the effect of the rigid versus compliant surface. The current study employs simultaneous acquisition of instantaneous jet operating conditions, fullfield velocities (planar particle image velocimetry), and fullfield out-of-plane surface deflections (stereo/3D digital image correlation). To this author's knowledge, this is the first time that these data have been simultaneously obtained for a high-speed flow; this work sets an experimental precedent and offers a significant opportunity to increase the understanding of fluid-structure interactions.

The remainder of this chapter is divided into several sections. First, the state of research concerning the underexpanded axisymmetric isolated jet is discussed, as it is the fundamental flow

under consideration. Next, an overview of the relevant jet and rigid-surface case literature is presented, which serves as a baseline for comparison for future experiments. The rigid-surface case discussion is followed by an overview of the extremely limited literature concerning the jet and compliant-surface case. This is followed by an introduction to the field of fluid-structure interactions (FSIs), a summary to the current state of research and understanding therein, and descriptions of the many experimental challenges encountered in the study of FSIs. The chapter concludes with a statement of the contributions of the present investigation, and the goals and achievements that were met during the course of this study.

1.2 Isolated Axisymmetric Underexpanded Jets

As a canonical flow, the wave structure of an isolated underexpanded jet is well understood (Figure 1) and many mean flowfield descriptions of the familiar shock-cell structure can be found.[1-4] The flow exiting the nozzle accelerates outward through an expansion fan emanating from the nozzle lip, due to the pressure difference between the exit and ambient conditions. A free-surface shear layer forms at the edge of the jet, and the expansion fan reflects from it as compression waves which, for a high enough degree of underexpansion, coalesce into a barrel shock. The barrel shock extends downstream until it intersects with an oblique shock, a Mach disk, and a slip-line at the triple point. The Mach disk (which is a normal shock) slows the inner flow stream (inside of the barrel shock), which had been continually accelerating up until that point. A reflected oblique shock propagates radially outward and downstream from the triple point. A constant-pressure slip line separates the post-Mach disk (subsonic) flow from the supersonic flow that passed through the oblique shock. As the oblique shock encounters the shear layer, it reflects as an expansion fan, and the shock-cell structure begins anew. This shock-cell structure repeats with decreasing strength as viscous effects increase.

Jets have been commonly used to study a myriad of compressible fluid phenomena. Following the extension of fundamental acoustical theories to high-speed flows by Ffowcs Williams,[5] jet acoustics became an area that garnered significant research attention, specifically in the areas such as turbulent mixing noise,[6,7] broadband shock noise,[8] and screech.[9-11] Tam[12] provides an older review on the field, while Jordan and Colonius[13] and Morris[14] both provide more modern overviews including the contributions of coherent structures and wave packets to the acoustic fields. There are also many closely related studies focusing on the stability[15-18] of supersonic jets,

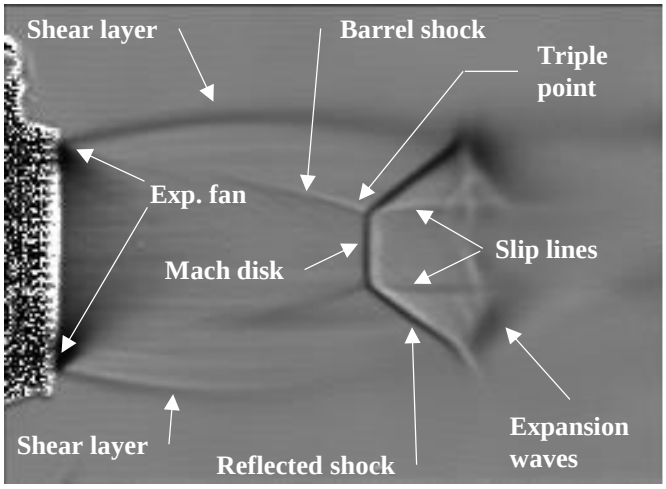

Figure 1. A mean schlieren image depicting the axisymmetric flowfield generated by an isolated underexpanded jet.

the growth[19,20] and control[21,22] of the shear layer, and jet turbulence.[23] The role of vortices, including their formation at the nozzle lip as Taylor-Goertler instabilities,[24,25] and their tendency to pair and merge,[26] have also been studied. There have also been numerous studies regarding the position and motion of the Mach disk.[27-29] Diagnostic techniques including schlieren,[30] LDV/LDA,[31,32] PIV,[33] and CARS[34,35] (to name only a few) have further contributed to the understanding of underexpanded jet flows.

1.3 Jet and Rigid-Surface Case

In addition to the flowfield asymmetry imposed by the adjacent surface, this jet and nearby parallel surface configuration exhibits unusual compressible-wave interactions, shear layers, boundary layers, and shock-boundary layer interactions (SBLIs), any of which may be influenced by instabilities, acoustic feedback loops, and other unsteady phenomena. At typical Reynolds numbers, the flow is generally turbulent, and hence a large degree of mixing can be expected. Figure 2 presents an instantaneous schlieren image of the flow under consideration; many of the features previously mentioned are evident in the image. The compliant surface case is of particular interest given the current state of research in the area of fluid-structure interactions.

The jet/rigid surface literature can largely be grouped into papers pertaining to either aerodynamics, rocketry, or acoustics. The majority of the published work relevant to the current investigation utilize axisymmetric jets. However, there have been a number of jet and rigid-surface studies that have used non-axisymmetric jets. Some studies of note include the Seiner et al.[36] study on screech effects for 7:1 and 7.7:1 rectangular jets, and a recent effort by Kwak and Lee[37] studying

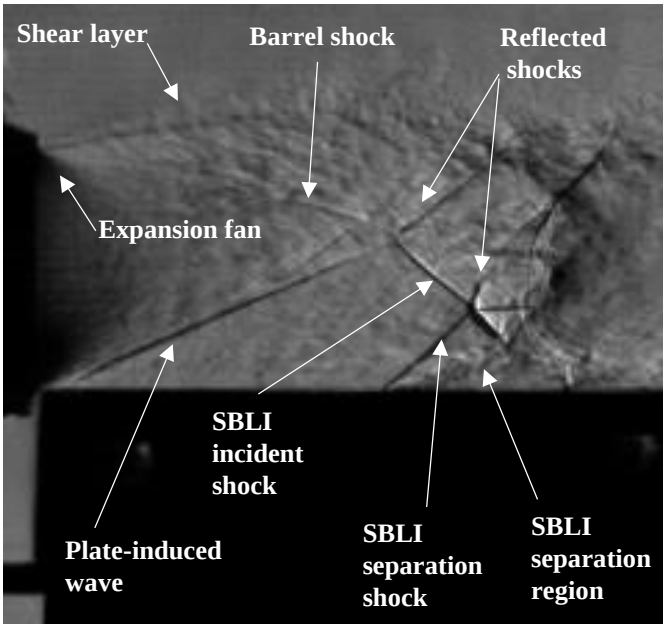

Figure 2. An instantaneous schlieren image depicting the flowfield generated by an underexpanded jet and a nearby rigid parallel surface.

flowfield structure, surface pressure, and jet thrust-force vectoring effects induced by variation in the plate's axial extent and the jet nozzle pressure ratio for 3:1 rectangular jets.

With the advent of the jet age, a series of NACA studies was conducted to investigate in-flight interactions and the effect on aerodynamic performance caused by jet-engine exhausts and nearby airframe surfaces.[38–45] These studies were generally limited to steady pointwise measurements and the determination of mean aerodynamic coefficients. Later, aerodynamic aspects such as engine-exhaust upper surface blowing for STOL aircraft, [46] the Coanda effect,[47] and circulation-controlled airfoils[48] were considered, but these studies, although compressible, were often not supersonic. There is some literature considering jet/parallel surface interactions in rocketry,[49–52] but these studies' relevance toward the current work is complicated by extreme operational conditions (temperature, pressure, and chemical composition) brought upon by combustion and space environments. There are some dated papers published in Russian sources that consider this particular flowfield. They explore topics such as the development of numerical methods suitable for mixed subsonic/supersonic flows[53–56] (which the currently investigated flow is a good example of), combined analytical, numerical, and experimental methods to study surface pressure[57] and heat transfer,[58] and even an attempt at a similarity solution.[59]

As with free and impinging jets, underexpanded jets flowing across a rigid surface have received a significant amount of attention by the acoustics community. Acoustics studies can be largely separated into two groups: those focusing exclusively on jet screech, and those concerned with jet noise in a more general manner (that is, also considering broadband shock noise and/or turbulent mixing in addition to screech). Both groups have considered the shielding/reflection implications induced by the surface.

Screech is a self-sustaining feedback loop driven by the interaction of shear layer instabilities and shock waves that results in a directional characteristic frequency-tone primarily found in the upstream-oriented acoustic spectra.[60] Ahuja et al.[61] found that for axisymmetric jets, instability wave suppression due to plate-induced asymmetry destroys the screech feedback cycle, especially for the two relevant helical instability modes for underexpanded jets. Wlezien's axisymmetric jet study found that screech and surface loading were maximized at intermediate wall separation distances ($h/D_j \sim 1$).[62] He suggested that the intermediate separation distance allowed for surface reflections to bolster the screech normal-direction flapping mode, leading to amplified screech and coherent surface pressure loading. More recent experimental studies also observed screech suppression for small separation distances.[63,64]

More recently, researchers at NASA Glenn have been building a general jet noise prediction code that also includes the effects of surface shielding and reflections due to jet/surface interactions. To this end, they have conducted a series of experiments to support the development of jet/surface interaction noise spectra prediction models by investigating the jet nozzle pressure ratio, jet/surface separation distance, and surface trailing edge effects.[65–69] The NASA Glenn studies primarily focused on the jet/surface interactions caused by propulsion systems and the airframe. In Ref. 69, the authors documented PIV flowfields of a subsonic axisymmetric jet near an adjacent parallel rigid surface. Another important jet/surface interaction case that has received attention is that of propulsion systems and the ground.[70] This case is most relevant for takeoff and landing.

1.4 Jet and Compliant-Surface Case

To the knowledge of the current author, all studies concerning the flow of a supersonic jet across a compliant surface have been conducted by a single investigator and his colleagues, resulting in limited available literature. Maestrello's experiments investigated the interaction of an

underexpanded air jet (propulsion system exhaust plume) and a nearby panel-stringer structure (fuselage wall) with the goal of reducing wall-panel acoustic fatigue and in-fuselage noise for passengers via the application of active feedback control.[71-73] He explored the application of control using an electromagnetic shaker by two means: either directly to the surface[71] or by using a ring at the nozzle lip.[72,73] Strain gauges were mounted on the panel-stringer structure to measure vibrational response while pressure transducers were positioned in the anechoic chamber to obtain data at various distances and angles from the jet. The flexible panel-stringer surface structure was oriented at a 12° angle relative to the jet axis and located approximately five nozzle diameters away. Figure 3 a) contains a schematic of Maestrello's experimental arrangement.

The uncontrolled data indicated that the jet generated broadband, nonlinear, nonstationary pressure and acoustic fields that were modulated by shock waves. Strong coherence was observed between the jet acoustic pressure modulation and surface strain, including the modulation attributed to shock impingement. Further coherence was observed between the surface strain and the radiated pressure measured on the shielded side of the panel. The surface was observed to respond to acoustic pressure, which then led to a corresponding acoustic radiation event, despite the nonlinear nature of the initial forcing.

In the first active-control case, control was applied directly to the panel-stringer structure via an electromagnetic shaker.[71] A strain gauge mounted at the center of the panel-stringer structure

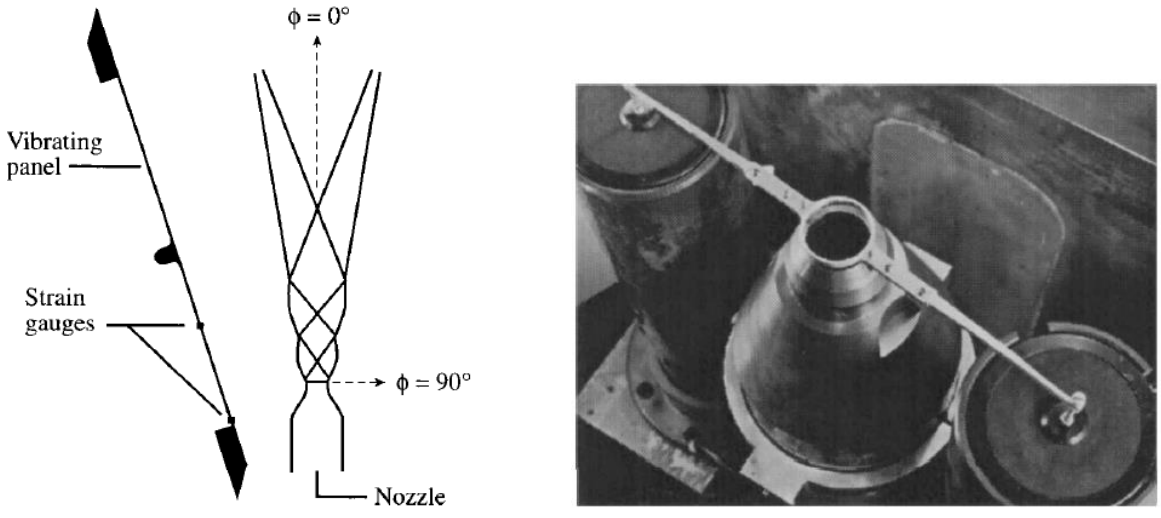

Figure 3. Maestrello used a) a flexible panel-stringer structure located five jet diameters away and oriented 12° relative to the jet axis and, and b) an electromagnetic shaker to oscillate a ring positioned at the nozzle lip as an active control mechanism. Images courtesy of Maestrello.[73]

was used to provide feedback control. In this case, the surface oscillation was attenuated by phase-amplitude mismatch that corresponded with the shock impingement events. This was observed to lead to a redistribution of the structural-response energy into the harmonics, but at reduced power. A reduction factor of 63 was observed in the spectrum peak, which was equivalent to an 18 dB change in strain response. The acoustic radiation was also reduced.

In the alternative case, active control was applied to the jet by means of an oscillating ring at the nozzle lip, as shown in Figure 3 b).[72,73] The ring oscillated at the shock oscillation frequency and was controlled via feedback from a pressure transducer located near the jet, but not on the panel surface. Upon initiation of the control loop, the shock fundamental frequency and its harmonics decreased by several orders of magnitude to the broadband level. The jet's flapping and helical instability modes were strongly damped and the shocks disappeared. As the surface forcing mechanism had been attenuated by jet active control, the surface oscillation frequencies were also attenuated. Maestrello ultimately showed that the shock oscillation cycle of an underexpanded supersonic jet could be attenuated through a single active feedback mechanism, leading to a subsequent reduction in noise from the jet and the oscillatory response of a nearby panel-stringer structure.[72,73]

Maestrello (with colleagues) also conducted a number of numerical studies exploring the coupling between panel responses and acoustics,[74-79] although never for underexpanded jets. These studies were conducted for cases without a jet,[74] for two-dimensional subsonic[75,76] and ideally-expanded supersonic jets,[77,78] and for subsonic circular jets.[79] These coupled studies used the unsteady nonlinear Euler equations to represent the fluid, and the nonlinear plate equation for the structure. An impulse excitation was applied to the fluid, and the long-time response of the panels was monitored. Due to the simplified models employed, these studies neglected small-scale turbulence-induced noise and shock-associated noise sources, focusing instead on noise generated from the convection of shear layer instabilities. Still, fluid-structure coupling was observed in each of these studies in the panel vibrations, as well as in the reflected and radiated fluid domains.

When Maestrello exercised control on the structure,[71] the shock-cycle of the jet was attenuated, and, alternatively, application of control on the fluid[72,73] resulted in attenuations in the structural response. These feedback-control experiments definitively showed that the fluid and structural problems were connected. Related numerical studies,[75-79] although simplified, further demonstrate the interconnectivity between the fluid and structure for the jet and compliant-surface

case under consideration here. This type of coupling is generally known as a fluid-structure interaction, which will be reviewed in more detail in the following section.

1.5 Fluid-Structure Interaction

The term "fluid-structure interaction" (FSI) refers to the dynamic behavior of flexible structures in the presence of a fluid and how the structure and fluid affect and influence each other. FSIs exhibit a broad spectrum of fluid/structure couplings, ranging from weakly coupled to strongly coupled. In weak coupling, the interaction occurs with low amplitudes or at slow rates, leading to small interfacial forcing terms, subsequently small effects on the other domain, and even smaller return responses. Strongly coupled FSIs, on the other hand, involve large amplitudes and/or high repetition rates, leading to forcing terms sufficiently large to induce non-negligible reactions, altering both the fluid and structural states. Weakly coupled FSIs typically fall within a linear regime and are called stable, while strongly coupled FSIs are typically nonlinear and oscillatory or chaotic in nature.

The physical modes through which FSIs act are many and diverse, allowing FSIs to occur across a myriad of different fluids, solids of varying degrees of strength and rigidity (elastic properties), flow regimes, and time scales. In order to highlight the variety of FSIs, several examples are presented here with short descriptions of the scenarios and their respective modes of action. Dynamic stall is an example of an FSI in which the lift of a pitching airfoil increases because the motion reduces the severity of the suction-side adverse pressure gradient, causing a delay in boundary layer separation.[80] In this case, the interaction is unidirectional, as the airfoil aerodynamics are greatly influenced by the motion of the pitching airfoil. Researchers at the University of Bath[81,82] have identified bidirectional interactions between wing-membrane fluctuations and separated-wake vortex shedding in micro air vehicles (MAVs). Similar MAV studies conducted at the University of Florida[83] have shown that significant wing twisting coincides with the presence of high flow velocities and strong vortices. Aerothermoelasticity can be especially important for hypersonic applications. The X-15, for instance, exhibited numerous FSIs related to reduced structural strength and stiffness due to vehicle heating. In one case, a wing leading edge expansion slot induced turbulent transition, causing increased heat loads and uneven thermal expansion, and resulted in several permanently bowed wing panels.[84] Another common FSI is flutter,[85] which occurs when aerodynamic loads on a structure (typically a panel) exceed the

structure's damping threshold, leading to panel motion. The motion may cause panel buckling or even become self-sustaining if the aerodynamic forcing frequencies coincide with the structure's natural vibration frequencies. These so-called limit cycle oscillations (LCOs) can cause structural failure, and therefore represent hazardous, and even fatal, flight regimes. The previously described experiments conducted by Maestrello are another example of an FSI.[71-73] In this case, aeroacoustic interactions led to structural fatigue and increased in-fuselage noise. It was these effects that Maestrello's efforts were aimed at controlling. Other examples for which FSIs are important include the flow of blood through the body[86] and reeded woodwind instruments.[87]

Fluid-structure interaction research is extremely challenging due to the complex linear and nonlinear interactions that may occur between an expansive variety of relevant physical phenomena that are themselves nonlinear (Navier-Stokes equations for fluids, and beam/plate/shell equations for structures). In both numerical and experimental cases, the conditions for the scenario of interest must be identified, accurately quantified, and truly implemented. This can be especially difficult to accomplish for things like boundary conditions, which are extremely sensitive parameters influencing the overall interaction. Numerically, the models representing the fluid and structure must not only contain the appropriate physical and dynamic terms, but also must allow for the coupling between the two in a realistic and efficient manner. They must do so accurately, within all computational domains and across the interfacial boundaries, with sufficient resolution in both space and time to capture the dynamics of the problem, and under manageable computational cost and time constraints.

The difficulty in computationally studying FSIs is illustrated by the evolution of the methods used to study panel flutter in a supersonic freestream flow, which have been traditionally predicated on simplifying assumptions. These simplifications have been employed for the fluid, structure, and their coupling. For instance, the fluid domain has been modeled, to varying degrees of accuracy, using potential flow theories,[85] (inviscid) Euler's equations,[88,89] Reynolds-Averaged Navier-Stokes (RANS) solvers with various turbulence models,[90] and higher-order Navier-Stokes solvers.[91,92] Analogous progressions exist for the structural-motion and FSI-coupling theories and models, respectively. The evolution towards more complete and exact models in all three areas has resulted in some of the more physically-complete FSI panel flutter studies completed to date. Ostoich et al.[93,94] studied the interaction of a Mach 2.25 turbulent boundary layer and a fluttering panel using Direct Numerical Simulation (DNS) in order to capture all of the turbulence scales and

minimize the number of simplifying assumptions. They found that the turbulent boundary layer induced a standing-wave panel motion with sufficiently large amplitude to cause the formation of weak unsteady shock waves. They further observed a change in the boundary-layer Reynolds shear stresses and other turbulence quantities downstream of the panel, but the change did not persist downstream.

Experimentally, fluid-structure interaction research is also challenging. This is due to the difficulty in replicating specific scenarios seen in the real world, and in obtaining appropriate and accurate measurements. Historically, FSI experiments have relied on pointwise unsteady measurements. These include high-speed pressure and acoustic measurements using devices like KuLite transducers[95] and microphones,[72-74] as well as structural-dynamic measurements including both contacting (strain gauges[72-74] and accelerometers[96]) and non-contacting (laser vibrometers[95,96] and capacitive displacement sensors[95]) types. As these measurements yield pointwise data, there remains a need to obtain fullfield data. With the advancements of technology, particularly high frame-rate cameras, experimentalists have been able to visualize the unsteady nature of an FSI flowfield through diagnostics like shadowgraph or schlieren imagery.[95] However, these diagnostics provide a qualitative understanding of the flow and, as line-integrating techniques, do not provide single-plane data. Fullfield velocimetry diagnostics, especially those in the particle image velocimetry (PIV) family, do provide fullfield, location-specific, quantitative data in the form of velocity fields. However, these techniques are traditionally difficult to implement in near-surface flows due to difficulties in obtaining sufficient near-wall particle seeding, in obtaining sufficient near-wall illumination while simultaneously avoiding excessive reflections from the wall, or both. These challenges are further exacerbated when attempting to obtain these measurements in situations for which the structure undergoes dynamic motion during data acquisition. Thus, obtaining fullfield flow data for an FSI-relevant flow remains a challenge to overcome.

The experimental capability to monitor the structure in a fullfield nature has improved with the development of diagnostics like digital image correlation (DIC). Originally developed by the structural-mechanics community as a tool to measure in-plane material deflections and strains, the diagnostic has evolved to also include a stereo/3D variant that allows for the measurement of both in- and out-of-plane deflections and strains. In recent years, stereo/3D DIC (sDIC) has been adopted by the larger FSI community and applied in FSI experiments. For instance, Beberniss et

al.[96] have obtained high-speed sDIC measurements on a flexible panel mounted in a wind tunnel wall to assess the panel response to shock loading in a supersonic turbulent flow. In accompanying efforts, fullfield unsteady pressure-sensitive paint pressure data were obtained on the same wall-panel,[97] and comparisons were made to an analogous computational FSI simulation of the same flow.[98,99] In addition to the validation conducted in Ref. 96, others studies[100,101] have also proven sDIC to be a useful technique by which to investigate FSI due to its use in vibration modal analysis.

In the ideal case, simultaneous measurement of both the fluid- and structural-states, each on a fullfield basis, would allow for the best opportunity to capture and better understand the mechanisms behind the fluid-structure interaction coupling. To date, simultaneous acquisition of fullfield velocimetry and structural-deflection data have been accomplished in only a few instances, and then only for low-Reynolds number flows.[81,82,102-104] Rojratsirikul et al. set the precedent in 2008 while studying unsteady membrane airfoils.[81,82] They obtained time-resolved PIV that was synchronized with images of a laser-illumination line on the model surface. Using a spatial calibration, the instantaneous surface deflections were calculated. Timpe et al. (2012) were the first to combine PIV and sDIC measurements; they did so for a wing with flexible panels and a scalloped trailing edge.[102] In 2015, Giovannetti et al. also obtained simultaneous PIV and sDIC data while assessing the bending and twisting of C-shaped daggerboards used in high-performance catamarans.[103] Special mention should be given to the work of Zhang et al., who recently obtained time-resolved simultaneous three-component volumetric flowfield data (using tomographic PIV) and fullfield surface deflection data using an alternative fullfield method (Mach-Zehnder interferometry) for a turbulent boundary layer in a low-speed channel flow.[104]

To the current author's knowledge, there are no documented studies describing simultaneous fullfield flow and structural data for high-speed FSI flows. The experimental investigation of FSI phenomena is a unique opportunity to learn about the mechanisms involved in fluid-structure interactions, particularly when simultaneous fullfield diagnostics are employed for both the fluid and structure, and it remains a challenge to be overcome.

1.6 Present Investigation

The objectives and contributions of this work are to experimentally investigate the underexpanded axisymmetric jet and nearby parallel surface scenario, for both the rigid- and compliant-surface cases, via characterization of the flowfield and surface states with the goal of

exploring the fluid-structure interaction governing the compliant-surface case. To that end, the following specific goals were defined and achieved.

1) Characterize the native isolated jet flow through detailed measurement of the velocity fields (both in-plane and three-component volumetric), and unsteady nature (far-field acoustics and shock wave position) of the flow. These data are a point of reference for the rigid- and compliant-surface cases. The results and discussion of these data are presented in Chapter 3.
2) An investigation of the rigid-surface case in terms of the flowfield and surface conditions is presented in Chapter 4. This is accomplished via velocimetry experiments within the flowfield and pressure-sensitive paint and surface oil flow visualization on the surface. A prominent shock-boundary layer interaction region was observed and its overall three-dimensional structure was investigated using both planar and three-dimensional tools. The effect of varying the nozzle pressure ratio (NPR) and the plate-jet separation distance (h/D_j) is considered in order to isolate a specific NPR, h/D_j combination for further study. The rigid-surface case data serve as a baseline for comparison for the compliant-surface case.
3) Successful investigation of the compliant-surface case is dependent on the ability to simultaneously capture instantaneous flowfield and surface-deflection states. This is a significant experimental challenge as both experiments must be independently validated, must not interfere with each other, must be synchronized to a high precision, and must be ultimately consistent with each other. This study demonstrates, for the first time in a high-speed flow, the simultaneous acquisition of instantaneous planar velocimetry data and out-of-plane surface deflection data using planar particle image velocimetry (PIV) and stereo/3D digital image correlation (sDIC), respectively. The experimental setup and validation are described in Chapter 2.
4) The velocimetry and surface-deflection data obtained for the compliant-surface case are presented in Chapter 5. As the surface can be seen in the PIV data, the two datasets can be shown to be consistent with each other along the common intersection line. The mean and instantaneous flowfield and surface-deflection states are described using both fullfield methods and line profiles. The interaction and correlation between the flowfield and structural state are considered and discussed. The compliant-surface case results are compared to the corresponding rigid-surface case results.

Through the comparison of the compliant- and rigid-surface case data, this study intends to provide insight into the relevant fluid-structure interactions involved in this jet and nearby surface scenario. It is assumed that the FSI does result in significant and measureable surface response. Questions of interest which are hoped to be address in the current study include:

- Does the compliant surface motion induce local flow compression or expansion-like effects in the near-wall flowfield? Can the strength of these effects be assessed in either a qualitative (such as the observation of compression Mach waves) or quantitative manner? How far do these effects extend into the flowfield?
- Does the compliant nature of the surface have an effect on the turbulence characteristics of the flowfield? If so, are these effects lasting?
- How is the overall shock cell structure of the flowfield altered by the compliant nature of the surface?
- Does a nonlinear structural response, induced by the pressure loading imposed on the structure by the flow, induce an effect on the flowfield? Is the effect observed on the flowfield different in the case of a linear structural response?
- Do the unsteady characteristics of the flowfield change as a result of the compliant nature of the surface? For instance, are there changes in shock wave characteristics, such as the frequency and amplitude of positional oscillation?
- How is the boundary layer affected by the compliant nature of the surface?
- Is the jet primary shear layer altered in the compliant-surface case?

Chapter 2 Facility and Experimental Methods

2.1 Anechoic Chamber

The experiments are conducted in an anechoic jet noise facility designed and built in Aeronautical Laboratory A (ALA) at the University of Illinois. The anechoic chamber, shown in Figure 4, has a working volume of 2.1 m x 2.3 m x 2.5 m and was designed for operation with nozzles with diameters on the order of 2.54 cm. Despite a smaller working volume than most jet noise facilities, the chamber was shown to exhibit anechoic characteristics down to a cut-off frequency of 400 Hz.[105]

Figure 4. The anechoic chamber.

In order to allow for the natural entrainment of air into the jet flow, the anechoic chamber has a 2.1 m x 0.28 m screened opening on either side of the jet on the upstream wall of the chamber. These entrainment openings are positioned in a non-line-of-sight manner so as to preserve the chamber's anechoic characteristics. A 2.1 m diameter conical bellmouth captures the flow on the downstream wall of the chamber. Flow is exhausted out of the facility through a 0.6 m x 0.6 m exhaust duct and is then directed outside through turning vanes.

Air, stored in a 140 m^3 tank farm, is dried and pressurized to approximately 862 kPa by two Ingersoll-Rand compressors. The mass flow rate for nozzles smaller than 2.54 cm in diameter is low enough that the jet can be operated continuously. Test air is directed through both a manual globe valve and a 2.54 cm pneumatic Fisher 667-ET-DVC6010 globe valve and then enters a pipe cross that serves as the stagnation chamber. From the stagnation chamber, the air is directed to the nozzle in the anechoic chamber via polyurethane foam-lined piping that also contains noise-

reducing foam baffles and flow conditioning honeycomb and aluminum screens to reduce turbulence levels. The piping extends into the anechoic chamber so that the nozzle is positioned approximately 93 cm from the upstream interior wall. The piping and nozzle are cantilevered into the chamber.

For the majority of the current study, the acoustics wedges were removed from the floor of the anechoic chamber so that an optical table could be positioned on the chamber subfloor beneath the jet. This provided an ideal platform from which to position the test surfaces used in this study as well as associated diagnostic equipment. However, the presence of these large objects/surfaces in the chamber compromised its anechoic qualities, prohibiting the acquisition of quality acoustic data for any cases other than the isolated jet. Isolated jet acoustic data were obtained prior to removal of the floor wedges.

2.2 Jet Data Acquisition and Control

Jet total pressure and total temperature are measured near the start of the nozzle with a Setra Model 206 pressure transducer (0 - 1720 kPa range) and K-type thermocouple, respectively. Ambient pressure is recorded using a Setra Digital Pressure Gage while temperature is recorded using a Control Company 4195 Traceable® digital weather station.

A National Instruments (NI) LabVIEW Virtual Instrument (VI) program was used to obtain data and control the operating condition of the jet. Screenshots of the VI front panel and block diagram are shown in Figures 5 and 6, respectively. Ambient conditions were assumed constant during the course of a run, and so these measurements were recorded only once at the beginning of each run. All other data were acquired during tunnel operation. Jet total temperature data were digitally recorded using a NI USB-TC01. A NI PXI-6133 data acquisition module interfaced with a BNC-2110 connector block to allow for acquisition of jet total pressure and acoustic data. The afore-described instrumentation was used throughout the course of this study. To account for daily variations in atmospheric conditions, the LabVIEW VI incorporated a zero-offset calibration for the jet total pressure transducer.

Pressure-sensitive paint (PSP) experiments required additional pressure data acquisition instrumentation to allow for paint calibration (see Section 2.7.1). For these experiments, a Pressure Systems Inc. NetScanner Model 98RK rack system and accompanying Model 9816 modules were

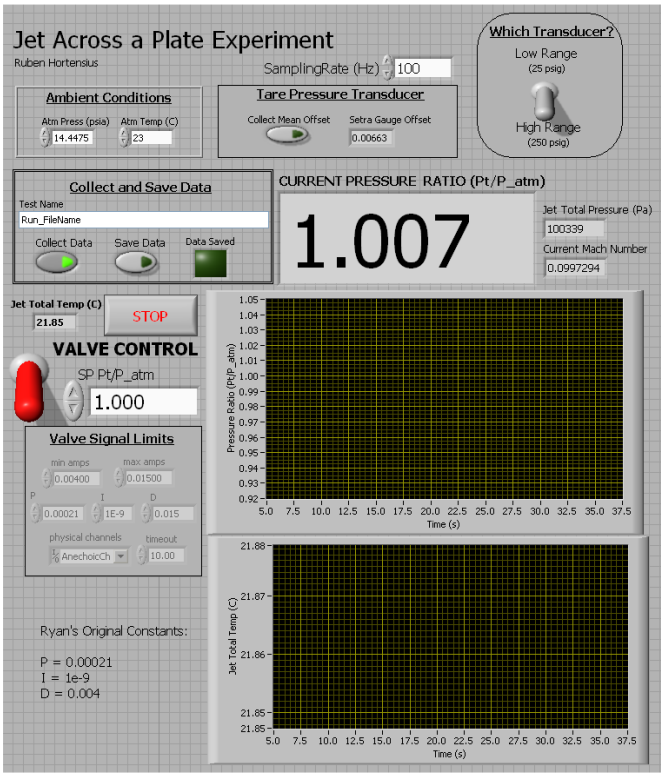

Figure 5. The jet facility operating VI front panel.

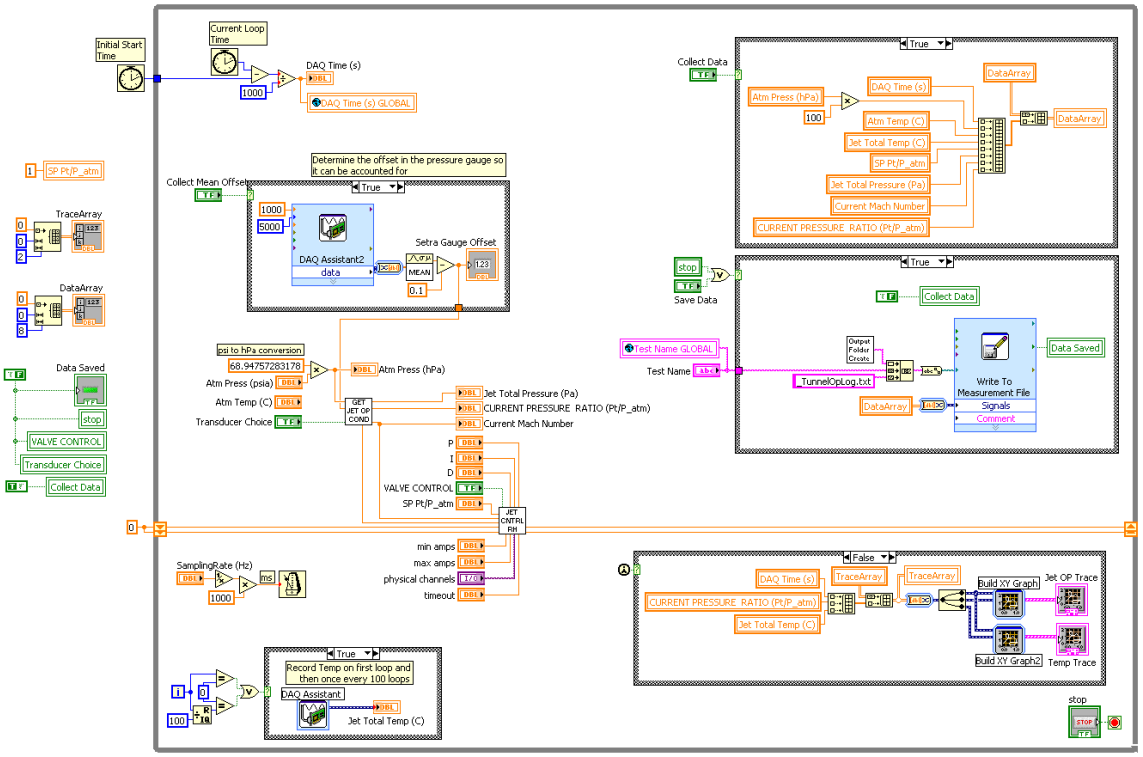

Figure 6. The jet facility operating VI block diagram.

utilized. Pressure measurements were acquired using ±30-psid transducers with ±0.05% full-scale accuracy. A one-point zero calibration was performed prior to data acquisition to reduce the effects of thermal drift and variation in atmospheric conditions. Whenever the NetScanner system was in place, a Model 9034 pressure calibrator was used to measure atmospheric pressure instead of the afore-mentioned Setra Digital Pressure Gage. The Model 9034 calibrator had a 0-310 kPa (45 psia) range with 0.01% full-scale accuracy. All pressure data that were obtained using the NetScanner system used atmospheric pressure as the reference. These pressure data were recorded by the facility control LabVIEW VI.

A LabVIEW-based PID controller is used to set nozzle pressure ratio by varying the setting of a 2.54-cm diameter pneumatic Fisher 667-ET-DVC6010 globe valve. As the controller was originally designed for optimal operation at nozzle pressure ratios lower than those used in the current study, the PID coefficients were tuned for the new operating range. After tuning, variations in nozzle pressure ratio of less than 0.6% (corresponding to less than 0.25% variation in ideally expanded Mach number) are typically achieved within ten seconds of defining the set point. The typical controller overshoot was approximately 3.5% *NPR* (1.3% M_{id}), and the steady-state error was negligible.

2.3 Experimental Setup

Experiments were conducted using a 12.7-mm exit diameter converging nozzle operating at nozzle pressure ratios ($NPR = P_0/P_{amb}$) of 5.0, 4.0, and 3.0. Experiments were conducted for the isolated jet, the jet/rigid-surface, and jet/compliant-surface configurations. Both surface configurations used the same generic construction. The generic surface was a 25.4 cm by 25.4 cm by 0.952 cm thick precision-ground aluminum plate. The leading edge of the surface was aligned with the exit plane of the nozzle, and the surface was oriented parallel to the jet axis as shown in Figure 7 (a). The surface was mounted on a traversing stage so that the jet-to-surface separation distance, h/D_j, could be varied. Data were obtained at three jet-surface separation distances (h/D_j) corresponding to 0.5 (surface directly adjacent to nozzle lip), 0.55, and 0.6. The traversing stage is very heavy, providing a very rigid support, and has a positioning resolution of 1 μm.

A Cartesian coordinate system (Figure 7 (b)) was used. The origin is placed along the jet axis at the nozzle exit plane. The streamwise coordinate, x, is coincident with the jet axis, and is positive with the primary flow direction. The wall-normal coordinate, z, is positive away from the surface

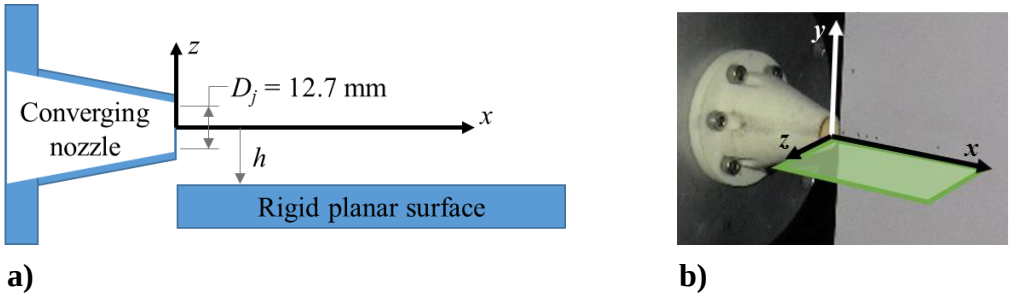

Figure 7. a) A schematic showing the test geometry, and b) an isometric view of the coordinate system. PIV data were obtained on the xz-plane, shown in green.

and negative towards the surface. The spanwise coordinate is *y*, and obeys the right-hand rule in relation to *x* and *z*. Velocity components along each coordinate direction follow the usual conventions: the streamwise component *u* follows the *x*-axis, the spanwise component *v* follows the *y*-axis, and the wall-normal component *w* follows the *z*-axis. This coordinate system is used because it was desired to have the "*z*" nomenclature reserved for the out-of-plane (wall normal) primary surface deflection direction.

2.4 Nozzle

A single nozzle was used in this study. It was an axisymmetric converging nozzle with an exit diameter of 12.7 mm. The lip of the nozzle was approximately 1 mm thick. The nozzle can be seen in Figure 7 (b), while an engineering drawing of the nozzle can be found in Figure 8.

The nozzle was manufactured using the 3D printing technique called Selective Laser Sintering (SLS) at the UIUC Department of Mechanical Science and Engineering Rapid Prototyping Lab

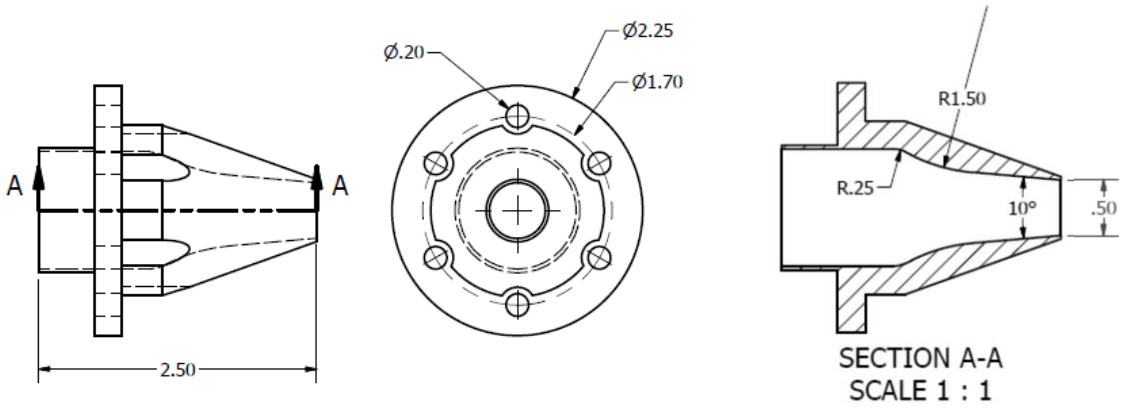

Figure 8. An engineering drawing of the converging nozzle used in this study. Dimensions are in inches.

(formerly the Ford Lab). It was manufactured on a Formiga P100 SLS machine using polyamide white (PA 2200). For the PIV experiments, the nozzle was painted with a matte black spray paint both inside and out.

2.5 Model Construction and Geometry

Two nominal models were considered in this study: a rigid surface and a compliant surface. The compliant surface model utilized a frame-like rigid surface model to support the compliant surface. All models had the same general dimensions; they were 9.525 mm (3/8”) thick and 254 mm (10”) square. Four countersunk clearance holes allowed for model mounting to two angular support brackets.

2.5.1 Rigid-Surface Model

For the PIV experiments, a transparent acrylic model (no surface finish applied) was used, as this material provided the least amount of laser reflections near the surface. For all other experiments, the models were made from precision ground cast aluminum plates obtained from McMaster-Carr. This material selection ensured surface flatness and uniform surface quality. Surface treatments varied depending on the experiment. For instance, black contact paper was applied for the surface oil flow visualization, black matte spray paint for the infrared temperature measurement, and a white primer and pressure-sensitive paint (PSP) were utilized for the surface pressure experiments. The rigid surface model used for the PSP experiments is shown in Figure 9.

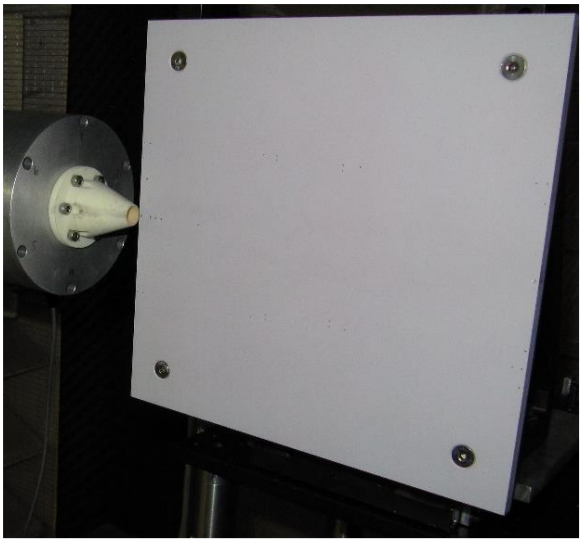

Figure 9. The mounted PSP rigid surface model.

2.5.2 Compliant-Surface Model

The most important factors driving the design of the compliant-surface model were the desired edge boundary conditions and the practical challenges of applying them to the physical model. A free (un-constrained) edge is relatively simple to generate in the lab, but leads to minimal model support. Simultaneously implementing both the zero out-of-plane deflection and the zero-moment

constraint mandated by a pinned boundary condition is difficult in the laboratory. A clamped boundary condition is more easily obtained in the lab, but in this case the model's vibrational natural frequencies and out-of-plane deflection amplitudes increase and decrease, respectively. This effect could compromise the ability to experimentally measure the surface response, and the model design was therefore carefully considered. Another consideration was the difficulty encountered when edges with different boundary conditions meet in a corner. This led to the decision to employ the same boundary condition for all edges.

For practical reasons, a model with four clamped edges was selected for study in this work. The literature suggests a number of different methods by which to obtain/approximate a clamped boundary condition in an experimental model. These solutions include the use of rivets,[106,107] epoxies,[108] single-part models,[109] and various clamping methods.[110] Rivets, due to their discrete-point application, were not considered for this study. Creating a single-part model via machining is attractive, but achieving a uniformly thick surface with consistent material properties is very difficult due to the large surface area, the tendency of the surface to be lifted by the mill bit, and the undetermined degree of local work-hardening applied by the cutting tool. The use of a multiple-component system to clamp the model makes it difficult to achieve a smooth aerodynamic surface transition from the surrounding wall/support to the model surface.

In the current study, it was decided to employ a frame-and-epoxy approach due to its cost effectiveness, simplicity, and relative ease of application. The frame was a rigid-surface model with a simple square cutout. The 125 mm by 125 mm cutout was milled out of the frame using a 3/16" diameter end mill, leaving 3/32" radii fillets in the corners. The cutout was centered in the frame in the transverse direction and was positioned 2.38 mm (3/32") from the upstream edge of the frame so as to provide sufficient surface area over which to apply the clamped boundary condition (epoxy) on the upstream edge.

The compliant surface itself was 1010 cold rolled full hard steel sheet shim stock obtained from W. W. Grainger, Inc. Shim stock was selected due to its uniform thickness and the wide array of thicknesses available. Care was taken to only use sheet shim stock so as to avoid the inherent surface curvature commonly observed in "shim-in-a-can." The 0.003" thick shim stock surface was trimmed to 152 mm by 152 mm (6" square) using a paper cutter. One edge of the model surface was aligned with the leading edge of the frame, and it was centered over the frame cutout in the transverse direction to provide equal-width strips along which to epoxy.

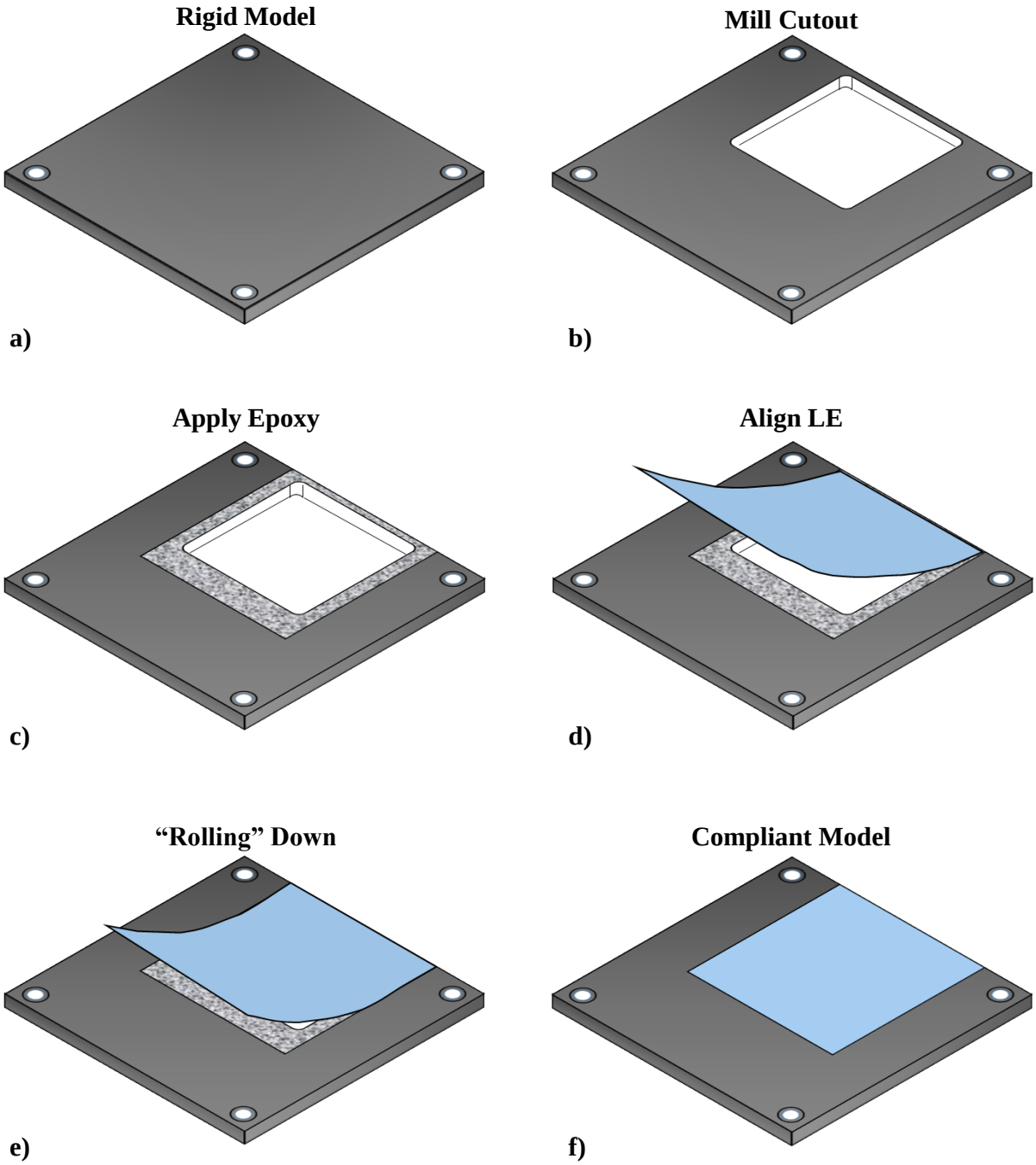

Figure 10. A schematic describing the compliant surface model assembly process. Once assembled, the model was clamped between steel plates and the epoxy was given at least 18 hours to cure.

Prior to model assembly, both the frame and compliant surface were lightly sanded using a high-grit sandpaper to increase surface roughness and improve the epoxy bond. After sanding, all parts were cleaned with separate washes (and subsequent drying) using acetone and isopropyl alcohol. Due to heat-transfer concerns, a thermally conductive epoxy (MG Chemicals Cat. No. 8329TCM-6ML) was used to help ensure that the model was not thermally insulated from the frame. The epoxy was uniformly applied to the frame using a razor blade, in strips with widths corresponding to the overlap region. The surface was then smoothly rolled down onto the epoxy starting from the frame leading edge. 2.5-cm thick steel plates were then placed both above and below the epoxied model and c-clamps were used to firmly hold the assembly together. The epoxy was allowed to dry for at least eighteen hours before the clamps were removed. A razor blade was used to very carefully remove any excess epoxy from the underside of the model surface (in the frame cutout). The compliant-surface model assembly process is shown in Figure 10.

Using a lot number system employed by the shim stock manufacturer (Precision Brand Products, Inc.) for traceability, a chemical and material property report was obtained for the specific material used in these experiments. Table 1 summarizes the geometry of the test surface and the results included in the traceability report. The complete traceability report can be found in Appendix A.

Table 1. Compliant (Test) Surface Geometry and Selected Material Properties

Material:	1010 Cold Rolled Full Hard Steel	
Boundary Conditions:	All edges clamped	
Thickness:	(0.0762 mm)	0.003 in
Length (axial):	125 mm	(4.921 in)
Width (spanwise):	125 mm	(4.921 in)
Corner fillets (radius):	(2.381 mm)	0.09375 in
Tensile Strength:	(652.2 - 660.5 MPa)	94.6 - 95.8 ksi
Yield Strength:	(651.5 - 655.0 MPa)	94.5 - 95.0 ksi
Hardness:	91 R15T	

As shown in the table, the yield and ultimate tensile strengths for this material are nearly identical. Due to the fully-hardened state of the material, failure occurs very soon after yielding, and therefore the linear stress-strain region makes up the majority of the material stress-strain curve. Unfortunately, the values reported in the traceability report cannot be used to estimate elastic material properties, such as Young's Modulus, E, or the coefficient of thermal expansion, α. Material properties for 1010 steel are presented in Table 2, obtained from Ref. 111. One

potential concern with the values reported in the table is that the compliant surface material underwent processing to bring it to the 'cold rolled fully hardened' state. However, elastic material properties are primarily governed by the bond strength at the atomic level.[112,113] It is for this reason that materials with high moduli of elasticity also typically have high melting temperatures. Elastic properties are insensitive to processes that alter the microstructure (i.e., grain size) of the material such as cold-working, irradiation, or other treatments.[112] The table also reports other calculated or estimated material properties, such as the material density, ρ.

Table 2. Compliant Surface Material Properties

Modulus of Elasticity, *E*	190 – 210	GPa
Coefficient of Thermal Expansion, α	12.2	μm/m°K
Poisson's Ratio, ν	0.27 – 0.30	--
Density, ρ	7870	kg/m^3

Following plate theory,[114] the expected natural frequencies for the first several mode pairs were calculated. Recall that these vibrational natural frequencies are calculated using the material geometry, material properties, and edge boundary conditions. However, the values shown in Table 3 assume that the model is in a vacuum and consequently neglect any atmospheric damping effects, and are therefore inexact.

Table 3. Theoretical Vibrational Natural Frequencies

ω_{mn} (Hz)		***m***		
		1	**2**	**3**
n	**1**	28.81	58.83	105.36
	2	58.83	86.92	132.34
	3	105.36	132.34	176.72

2.6 Flowfield Diagnostics

A variety of flowfield diagnostics including schlieren imagery, planar particle image velocimetry (PIV), and tomographic PIV, were employed in this study. The experimental arrangements for each of these diagnostics are described in the following sections.

2.6.1 Schlieren Imagery

Schlieren photography, a technique wherein density gradients can be visualized due to changes in index of refraction, was used to visualize the compressible structures in the flow. The

z-type setup utilizes a custom built Luminus STB-90 LED and heat sink for the illumination source. Identical 8-in diameter parabolic mirrors (64-in focal length) were used. A 12-bit Photron FASTCAM SA5 16 GB camera captured reduced-resolution images (256 pixels x 224 pixels) at up to 100,000 fps with an exposure time of 1 μs. A backwards-oriented Nikon Nikkor 80-200 mm f/2.8 D ED lens was used to focus the images. The LED and first collimating mirrors were positioned inside of the anechoic chamber, while the remaining components were positioned outside of the chamber. The collimated beam exited the chamber through a removable wall panel (window – no pane). A schematic of the high-speed schlieren setup is shown in Figure 11.

Due to the long focal length of the collimating mirrors and the complications of mounting the mirrors vertically, it was not possible to conduct schlieren imaging with the plate oriented in the usual vertical manner. Instead, all schlieren images were acquired with the surface oriented in a horizontal position. However, because the mirror focal length was longer than the distance between the jet and wall of the anechoic chamber, the light source had to be positioned below the jet. In

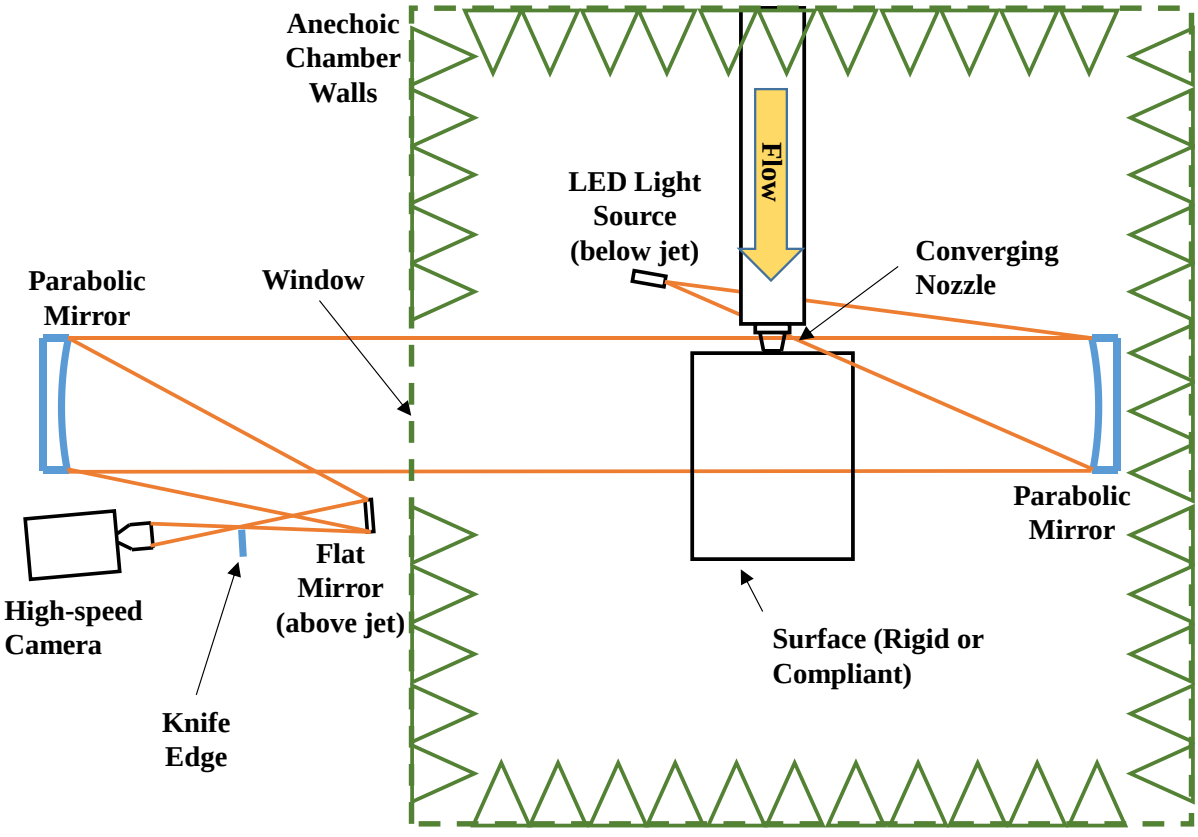

Figure 11. A schematic of the high-speed schlieren setup. Drawing not to scale.

order to maintain a planar setup, the flat mirror, knife edge, and camera were also placed at an angle. Despite careful angular measurements, achieving a perfectly planar z-setup proved difficult, leading to the introduction of optical aberrations. The strongest indication of these aberrations in the experimental setup was that the dark portion of the image rotated as the knife edge position varied. This culminated in a reduced schlieren sensitivity that made the resulting images appear more like shadowgraphs than true schlierens.

At least 10,000 images were collected for each operating condition. Background (light off) and flatfield (light on, no flow) image sets of at least 500 images were also acquired for each run. Image processing was conducted by first subtracting the average background image from both the flow-on images and the average flatfield image, and then dividing the resulting flow-on images by the flatfield. Pixel black-level corrections were conducted before every run using the "Shading" feature in the Photron FASTCAM Viewer (PFV) software. Schlieren image processing was conducted using MatLab.

Mean schlieren images were used to assess the general structure of the flow (shear layer extent and thickness, shock wave position, and shock/boundary-layer interaction region position). Mean results were convenient for comparison to quantitative data– such as the PIV velocity fields. Instantaneous schlieren images were used to assess the turbulent structure of the flow and to allow for shock-position tracking. A MatLab routine was used to record the streamwise position of specific shock waves and to build a time-history of the shock-position fluctuations. Fast-Fourier transforms (FFTs) were then conducted to assess the spectral content of the shock motion and to determine dominant frequencies. See Section 3.2.3 for a complete description of the methodology employed.

2.6.2 Planar Particle Image Velocimetry (PIV)

Two-component planar Particle Image Velocimetry (PIV) was utilized to obtain instantaneous velocity fields along the flowfield symmetry plane. The experimental setup is shown in Figure 12. Two cameras, arranged side-by-side, viewed the particles in side scatter over a wide field of view with high spatial resolution. The plane of interest was illuminated using a surface grazing approach in order to minimize laser surface reflections.

The laser sheet illuminated the test plane in a manner such that the beam grazed the surface from the downstream direction. The grazing approach was employed because of the greatly reduced laser surface reflections, especially when the compliant-panel model was being tested. By

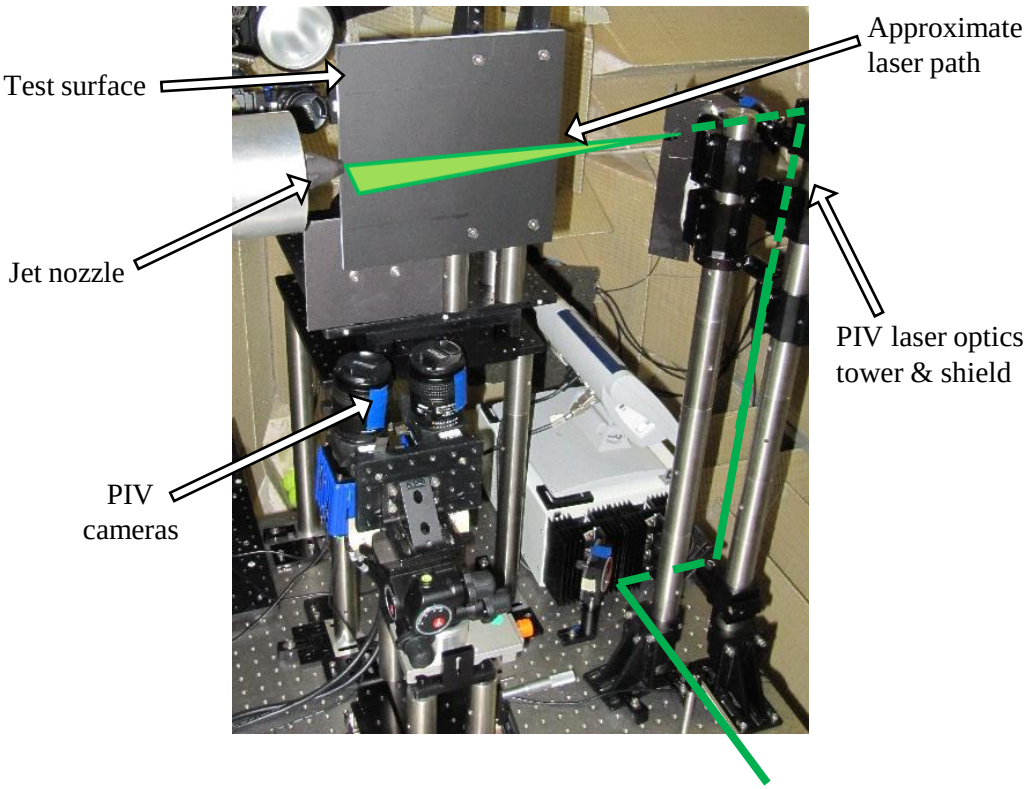

Figure 12. The planar PIV experimental setup.

grazing the surface, only the edge of the laser beam needed to actually contact the surface, allowing for the use of increased laser power. Further, the light that did contact the surface was allowed to scatter in both forward and backward directions, further reducing reflections in the camera imagery. Earlier experimental setups utilized a setup in which the light sheet impinged directly onto the surface; this type of setup results in excessive surface reflections while simultaneously making inefficient use of the laser beam power because of the high degree of beam spreading needed.

To decrease laser reflections even more, a 3/8" thick transparent acrylic plate was used for the rigid-surface model experiments. For the compliant-surface model experiments, the surface was prepared for testing by painting it with several thin coats of a matte black spray paint. Seed particles were invariably deposited on the test surface, leading to a surface wetting effect, which was also found to reduce the surface reflections. Therefore, care was taken to dampen the painted test surface prior to data acquisition.

A dual-head New Wave Gemini Solo 200XT Nd:Yag laser positioned outside of the chamber was aligned with a tubular hole in the side of the anechoic chamber wall. Turning mirrors, a 500

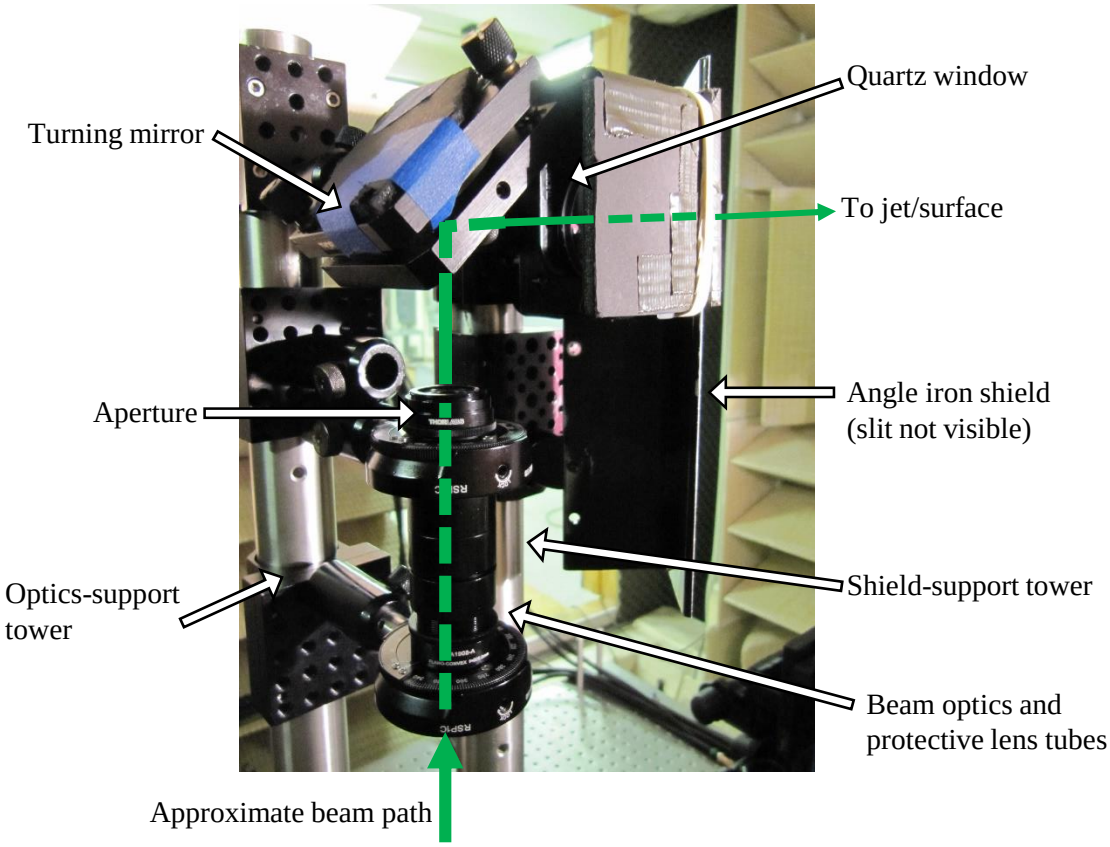

Figure 13. The planar PIV illumination optics were shielded from the jet with a separate free-standing post with an angle-iron fairing and quartz window.

mm spherical lens (ThorLabs LA1908-A), and -100 mm cylindrical lens (ThorLabs LK1743RM-A) were used to generate the approximately 1-mm thick laser sheet. Lenses, a beam-clipping aperture, and a turning mirror were positioned on an optical component tower that was constructed approximately 50 jet diameters downstream of the jet exit plane, as shown in Figure 12. Lens tubes were used to shield the optical lenses from seed particles. A second, non-contacting, tower was constructed directly upstream of the optical-component tower. This tower supported a piece of angle iron with a slit (to allow for laser beam passage) to shield the optical components. This shielding tower also included a removable 2" diameter quartz window to further protect the optical components. This window was removed and cleaned between each data run. Figure 13 shows the beam-optics tower and the separate optical-shielding tower.

Dual flow seeding was employed. A TSI Model 9307 oil droplet Laskin nozzle injected Bis(2-ethylhexyl) sebacate (DEHS) particles of approximately 1-μm diameter in the jet core flow within the facility stagnation chamber. Meanwhile, a Vicount 1300/180/2.2 kW smoke generator was used to seed the entrained air with particles of approximately 0.2 - 0.3 μm diameter.

Seed particles were imaged in side-scatter from below the jet. Two cameras, arranged in a side-by-side manner, were used in order to increase the axial extent of the measurement domain to approximately 128 mm. The nozzle exit was just outside of the camera field-of-view (approximately 1 mm). The overlap region encompassed approximately 10 mm (approximately 15%). Both cameras utilized scheimpflug adapters to allow for optimal off-plane focusing. A two-level calibration plate (LaVision Type 11) was used to calibrate and align the two camera fields of view using the LaVision DaVis Flowmaster software.

The cameras were monochromatic scientific CMOS (sCMOS) Imager cameras obtained from LaVision. These cameras are highly sensitive (16 bit) and have high resolutions (2560 x 2160 pixels). The setup had an average magnification of 36.7 pixels/mm. The cameras were fitted with scheimpflug adapters and Nikon Nikkor 65-mm lenses with variable aperture. No extension tubes were required. For the rigid surface tests, the lenses were set to f8, and the laser was set to 40% power (approximately 50 mJ/pulse). For the compliant-surface tests, the f-number was reduced to 2 because the narrower depth-of-field and reduced laser power required for imaging (20% power, approximately 25 mJ/pulse) were observed to greatly decrease the amount of near-surface laser illumination.

Laser and camera timing were controlled using LaVision DaVis software and accompanying hardware (an external programmable timing unit, PTU X). The laser pulse delay time was 0.5 μs, corresponding to a maximum shift of approximately 10 pixels at NPR = 5. The uncertainty in the timing due to laser jitter was 1 ns, while the uncertainty in the delay time was 1.5 ns. Each laser pulse duration was 5 ns.

All images were processed using LaVision DaVis 8.3.0 software in double-frame mode. Image preprocessing consisted of sliding background removal with an 8-pixel length scale. A representative particle image is shown in Figure 14. Sequential cross-correlation image processing was conducted in a multi-pass approach with decreasing window sizes of 64 x 64 pixel, 32 x 32 pixel, and 16 x 16 pixel windows. The “auto” window weighting function and 50% window overlap were utilized for all passes. Three passes were conducted for each window size. As required for multi-camera processing, “use image correction” was enabled. All passes were conducted using the standard correlation function (FFT, no zero-padding). Multi-pass post-processing consisted of vector removal if the peak Q-ratio was less than 2.

Figure 14. A representative PIV particle image near the nozzle exit.

Final vector post-processing was conducted separately from the PIV calculation step. It consisted of vector removal for Q-ratios less than 2.5, the standard single iteration median filter settings (strongly remove and iteratively replace, 2 and 3 times "stdev of neighbors"), removal of groups with less than five vectors, and the 'optimal' smoothing setting. Interpolation was used to fill small empty spaces. These vector-removal thresholds represent extremely aggressive post-processing filters; Q-ratio thresholds of less than 1.5 are commonly employed.[115,116] Even so, less than 0.5% of the vectors were actually removed in a typical instantaneous velocity field. Refer to Section 3.1.2 for a representative instantaneous snapshot showing the missing vectors.

Following post-processing, the two camera fields were merged using the "merge vectors" DaVis operation. The composite vector fields contained approximately 580 and 125 vectors in the streamwise and wall-normal directions, respectively, for a total of approximately 72,500 total vectors. Approximately 0.22 mm separated individual vectors. At least 1000 image pairs were obtained for each operating condition.

The post-processed and merged vector fields were used to calculate the mean streamwise velocity, mean wall-normal velocity, streamwise and wall-normal RMS velocities, and Reynolds stresses (normal and shear). After calculation of the statistics, linear interpolation was used to fill-up small empty spaces in the instantaneous results (which were then used in uncertainty calculations).

2.6.3 Planar PIV Experimental Uncertainty

Instantaneous and mean uncertainty contributions were calculated due to equipment, particle lag, processing, and sampling effects. The methodology employed is based on a method developed by Lazar et al.[117] The original code estimated only the mean velocity uncertainty, but it has since been extended to allow for the quantification of instantaneous uncertainties as well, including those for fluctuating quantities. The particle lag uncertainty algorithm was also updated so that the valid particle Reynolds number range was no longer limited to the Stokes' regime. Instantaneous uncertainties are calculated for 50 instantaneous PIV snapshots. These 50 instantaneous snapshot uncertainties are then used to estimate the uncertainties in the mean, while making use of an additional corrective term based on statistics obtained from the full data set (1000 images). Uncertainties are calculated in the streamwise and wall-normal directions independently and are calculated on a vector-by-vector basis. All uncertainties are normalized by the maximum mean streamwise velocity, U_{max}.

The reader is referred to Appendix B for a complete explanation of the methodology employed in the latest version of the PIV uncertainty code. An explanation is provided for all contributions to the uncertainty (equipment, particle lag, processing, and sampling), as well as their cumulative effect in both instantaneous results and in the mean.

The equipment error is due to scaling and magnification effects and estimates for optical aberration effects. PIV-processing error accounts for the variations in the results of the complete processing algorithm/steps; it is estimated in a single bulk term, and no attempts were made to separate the processing steps. It also provides some estimation of the effect of particle seeding density as a byproduct. Particle-lag error accounts for how well the seed particles track the flow; it is particularly important in regions with high velocity gradients, such as near shock waves. Sampling error accounts for the variation between snapshots and how well the snapshots represent the mean condition.

PIV uncertainties were calculated for the jet/rigid-surface case with h/D_j = 0.50, NPR = 5.0. Representative instantaneous uncertainties are presented first, followed thereafter by mean uncertainties. Fullfield results are presented in figures, but uncertainties reported in the text and tables are often presented through median and/or maximum values, as these best convey the true uncertainties. Further, so as not to bias the uncertainties by the slow-moving entrainment field, the values reported herein are constrained to $-0.5 \leq z/D_j \leq 0.75$. For the operating condition examined here, the velocity used for nondimensionalization was U_{max} = 576 m/s.

Figures 15 a), b), and c) present the instantaneous uncertainty contributions in the streamwise direction for a single snapshot due to equipment, PIV-processing, and particle lag effects, respectively. Figure 16 contains the same information, but for the wall-normal direction (*w* component) instead. The total streamwise and wall-normal instantaneous uncertainties for a single snapshot are shown in Figures 17 a) and b), respectively. The total instantaneous uncertainty is obtained independently for each direction using the typical root-sum-square method. For the streamwise direction, it is:

$$w_u^{total} = \sqrt{\left(w_u^{equip}\right)^2 + \left(w_u^{proc}\right)^2 + \left(w_u^{lag}\right)^2} \quad (1)$$

Table 4 summarizes the instantaneous uncertainties portrayed in Figures 15 – 17. The maximum uncertainty values are included in the table, but this metric is easily swayed by a single extraneous value and is therefore not an ideal method by which to assess overall uncertainty. For instance, *u*-component particle lag uncertainties as high as $0.607U_{max}$ were observed for the snapshot considered, but 99.0% of the vectors had particle lag uncertainties less than $0.1766U_{max}$ and 99.8% of the vectors were less than $0.2713U_{max}$. Mean values are also easily swayed in the same manner, and so the median values are reported instead; these are considered reliable indicators of the overall uncertainties.

Table 4. Instantaneous PIV Uncertainties

Uncertainty Source	*u* component		*w* component	
	Median	**Maximum**	**Median**	**Maximum**
Equipment	0.012	0.016	0.001	0.007
PIV-processing	0.014	0.140	0.017	0.090
Particle lag	0.031	0.607	0.027	0.299
Total:	**0.038**	**0.609**	**0.033**	**0.299**

Equipment errors, $\mathcal{w}_u^{equip}$ and $\mathcal{w}_w^{equip}$, contribute little to the total uncertainty, at approximately 1% or less of U_{max}. Equipment error is directly dependent on the measured velocities, and therefore the contours have distributions similar to the velocities. Table 4 indicates that PIV-processing uncertainty is the next largest contributor to the total uncertainty. The reported PIV-processing uncertainties, $\mathcal{w}_u^{proc}$ and $\mathcal{w}_w^{proc}$, are actually inflated near the edges of the camera fields of view. Note the vertical banding distribution in $\mathcal{w}_u^{proc}$ within each camera field of view, as shown in Figure 15 b). Similarly, $\mathcal{w}_w^{proc}$ is larger near the bottom of the frame (see Figure 16 b), but near zero at the top (which is actually near the center of the camera field of view). PIV-processing uncertainties are believed to be inflated near the edges of the camera fields of view due to perspective effects caused by the imaging system (i.e., lenses) that could not be replicated within the synthetic images. This leads to overestimation of the PIV-processing uncertainties everywhere except near the frame-centers, where these effects are small. Refer to Appendix B for a full explanation. Extracting values only from regions local to the camera-frame centers yields *u*-component median and maximum PIV-processing uncertainties of 0.5% and 0.9% of U_{max}, respectively. These values are believed to better represent the PIV-processing uncertainties throughout the entire field of view. Note that non-ideal particle seeding density could contribute to increased PIV-processing errors, possibly leading to the increased values near the shock/boundary layer interaction region. Obtaining ideal particle seeding in the associated separation regions is a commonly encountered experimental challenge.[118]

The true dominant source of instantaneous PIV uncertainty is particle lag, $\mathcal{w}_u^{lag}$ and $\mathcal{w}_w^{lag}$, especially within regions of strong velocity gradients such as within the shear layer, near the wall, and, most notably, near shock waves. The median particle lag uncertainties are approximately 3% of U_{max} for both flow directions. Recall that the ability of the particles to track the flow is strongly

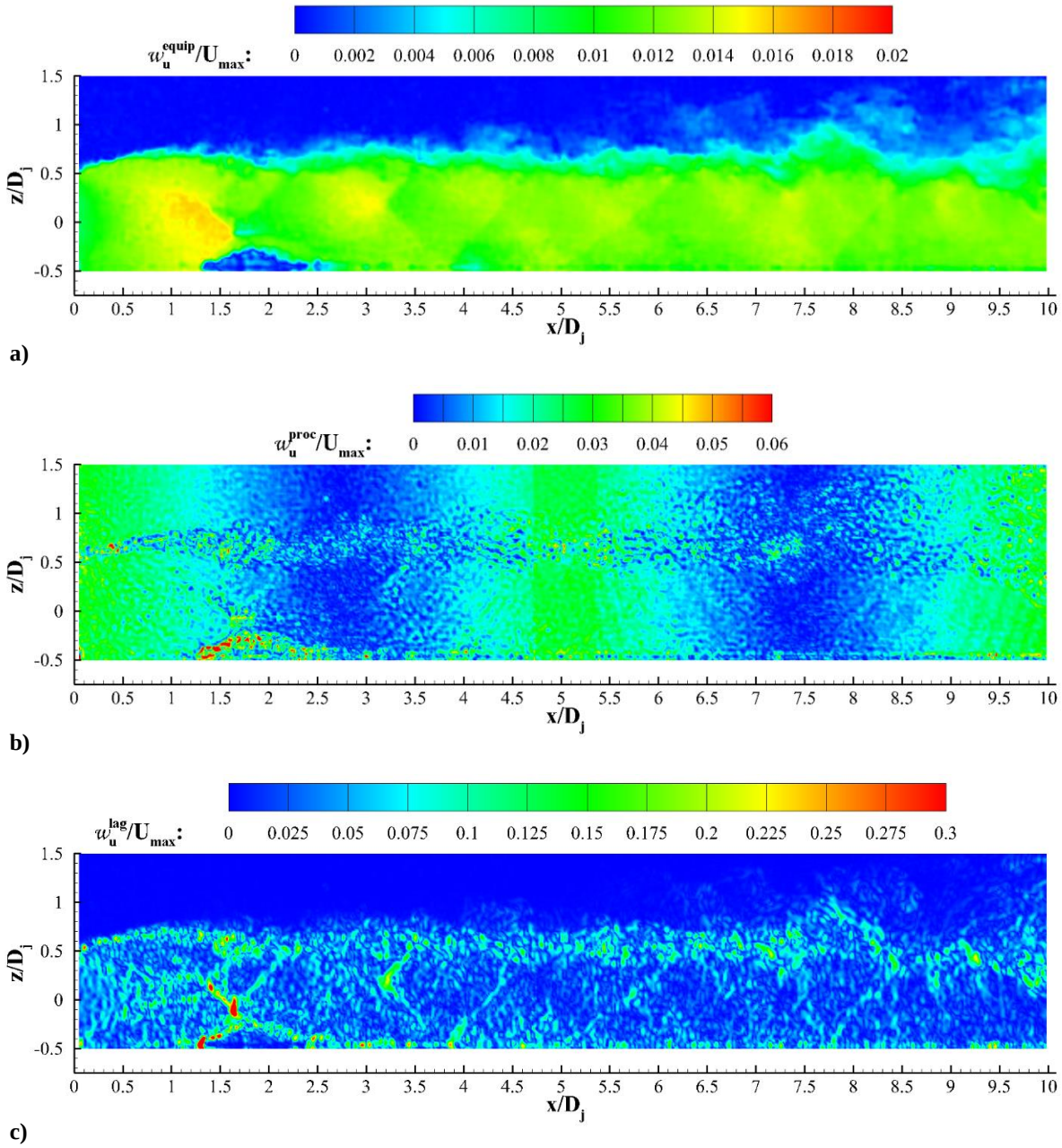

Figure 15. Representative h/D_j = 0.5, NPR = 5.0 (rigid surface) streamwise-direction instantaneous PIV measurement uncertainties due to contributions from a) equipment, b) PIV-processing, and c) particle lag.

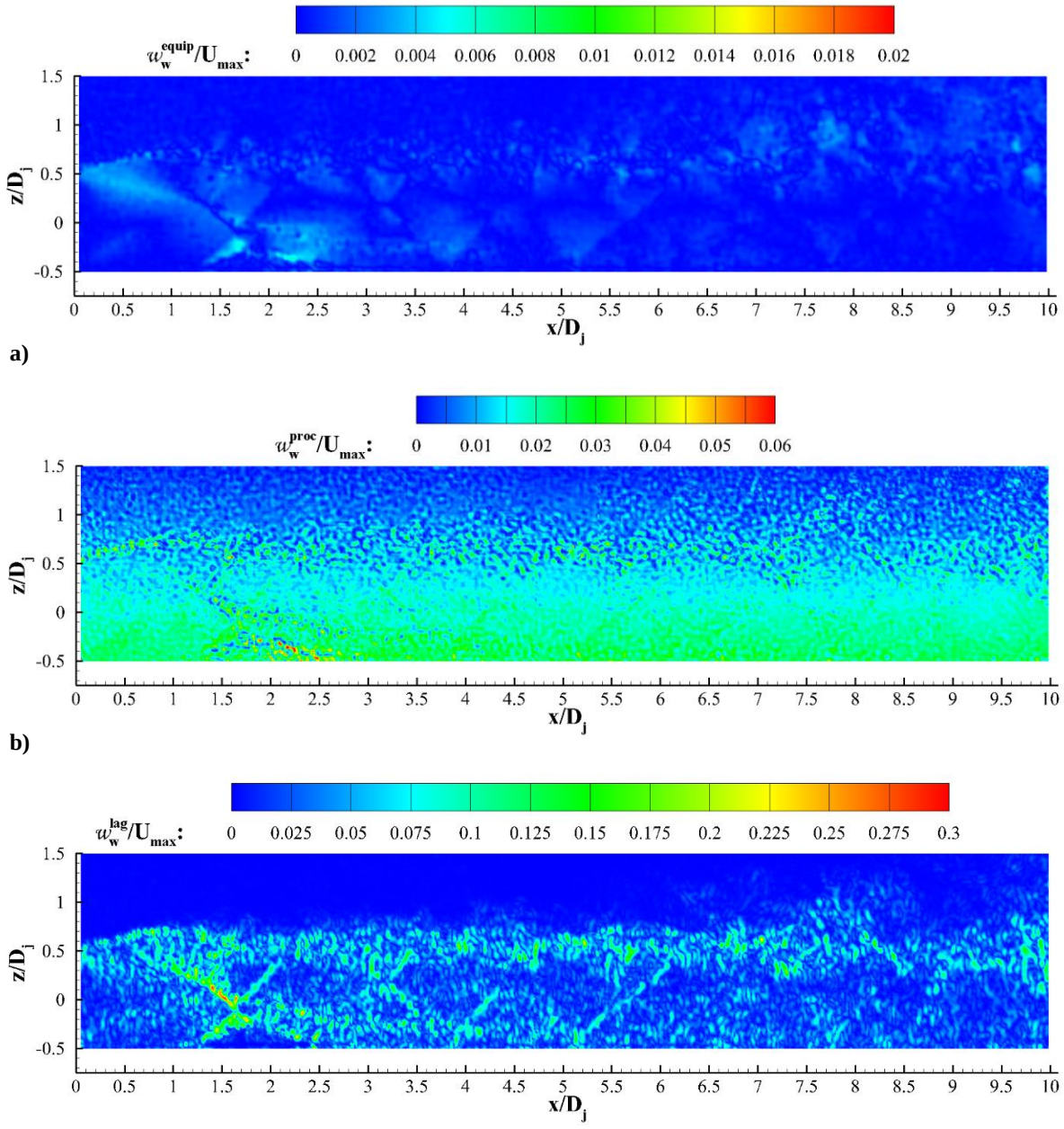

Figure 16. Representative h/D_j = 0.5, NPR = 5.0 (rigid surface) wall-normal direction instantaneous PIV measurement uncertainties due to contributions from a) equipment, b) PIV-processing, and c) particle lag.

affected by seed-particle diameter and that the values reported here are based on the diameter of the larger particles and therefore represent conservative estimates.

Total instantaneous experimental uncertainties, w_u^{total} and w_w^{total}, are calculated by combining the contributions from equipment, particle lag, and processing errors using a root-sum-square approach. The total instantaneous experimental uncertainties are approximately 3-4% of U_{max} for both the *u* and *w* velocity components and are shown in Figure 17. The wall-normal uncertainty is generally lower than that in the streamwise direction, but the overall features of the contours are similar for both directions.

The uncertainty in the mean was also calculated in both the *u* and *w* directions. The fifty instantaneous uncertainties described previously were taken as a subset of the larger data set of 1000 images. The mean experimental uncertainties, w_U^{exp} and w_W^{exp}, were first calculated from the fifty instantaneous uncertainties. Then, the sampling errors, $w_U^{sampling}$ and $w_W^{sampling}$, were calculated using the complete data set (1000 images). These were combined in root-sum-square form to obtain the total PIV uncertainties in the mean, w_U^{Total} and w_W^{Total}. See Appendix B for details regarding these calculations. Figures 18 and 19 contain the mean experimental uncertainty (derived from the fifty instantaneous uncertainties), sampling uncertainty, and the total PIV uncertainty in the mean, for the *u* and *w* components of velocity, respectively. Table 5 presents the median and maximum uncertainties for each. Mean experimental uncertainties are much larger than the sampling uncertainties. The median values for the total uncertainties in the mean are approximately 0.8% and 0.7% of U_{max} for the *u* and *w* directions, respectively. The maximum values are on the order of 6% and 4% of U_{max}, respectively.

Table 5. PIV Velocity Uncertainties in the Mean

Uncertainty Source	*u* direction		*w* direction	
	Median	**Maximum**	**Median**	**Maximum**
Experimental	0.007	0.059	0.007	0.037
Sampling	0.001	0.024	0.001	0.006
Total:	**0.008**	**0.059**	**0.007**	**0.037**

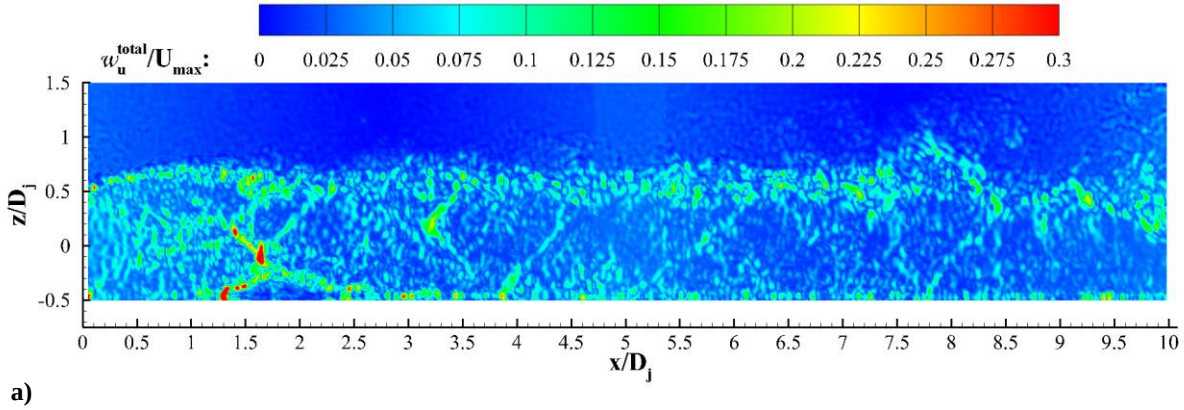

a)

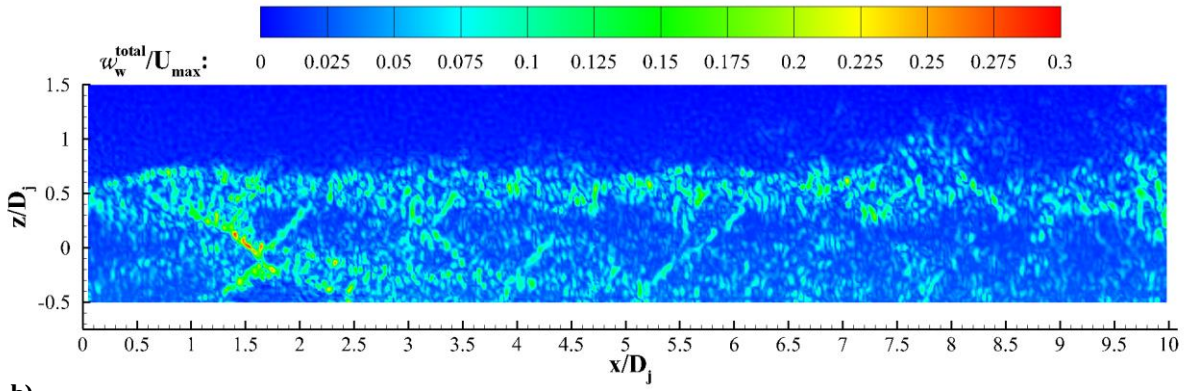

b)

Figure 17. Representative total instantaneous PIV measurement uncertainty in the a) streamwise-direction and b) the wall-normal direction for the $h/D_j = 0.5$, NPR = 5.0 rigid-surface case.

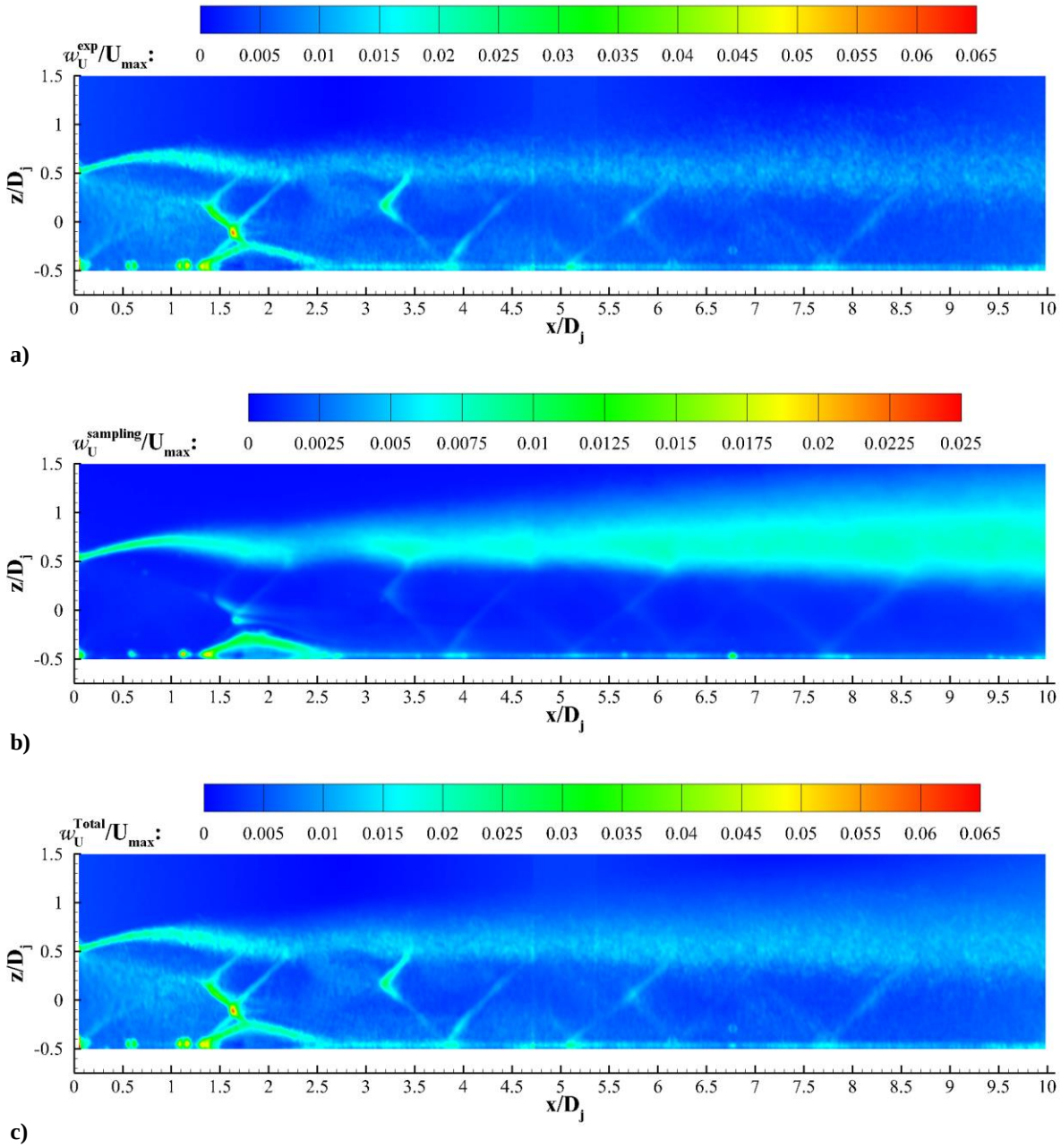

Figure 18. Streamwise-direction PIV measurement uncertainties due to contributions from a) the mean of a subset of 50 instantaneous uncertainties, b) sampling effects, and c) the combined total uncertainty in the mean for the $h/D_j = 0.5$, NPR = 5.0 rigid-surface case.

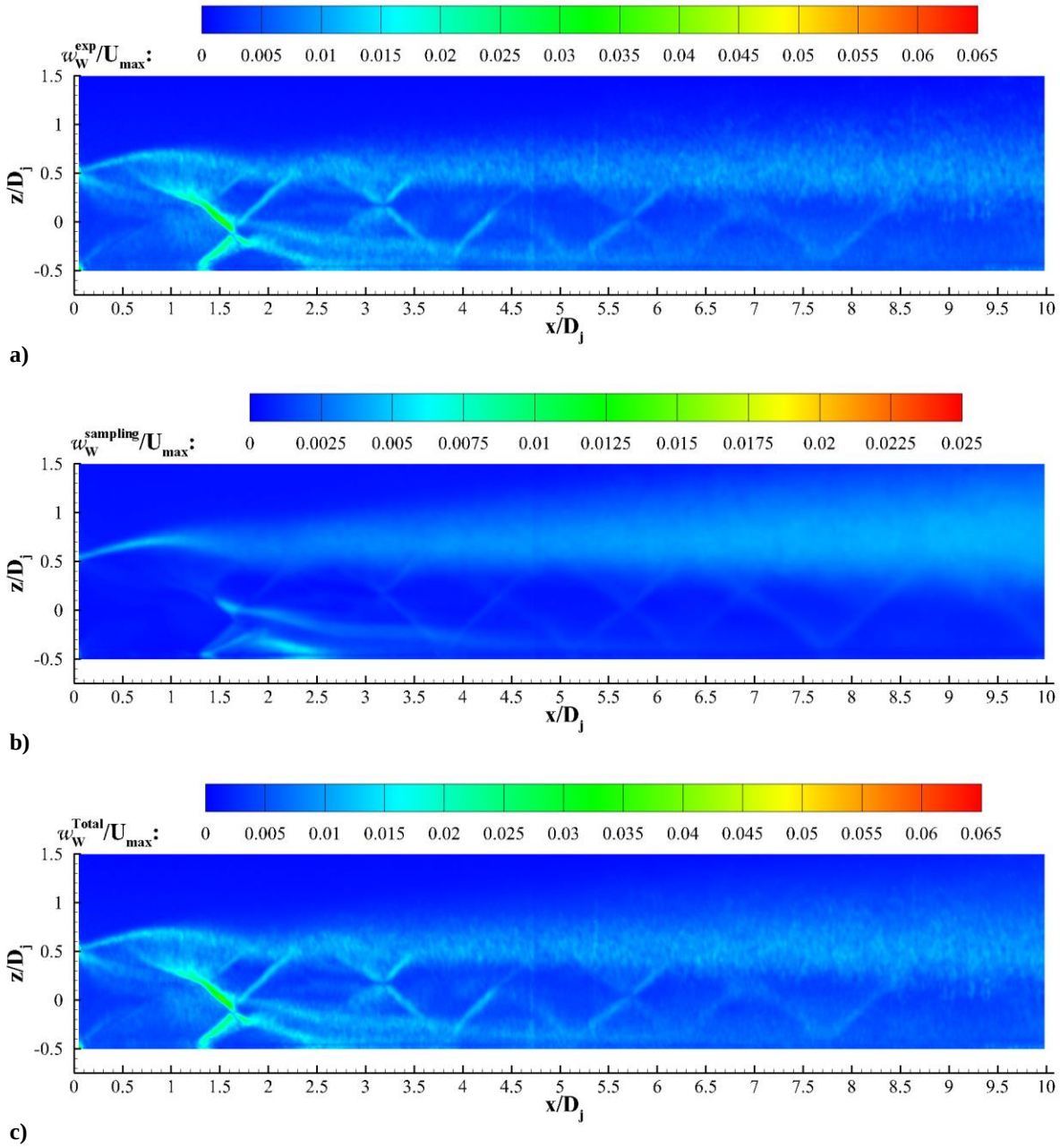

Figure 19. Wall-normal direction PIV measurement uncertainties due to contributions from a) the mean of a subset of 50 instantaneous uncertainties, b) sampling effects, and c) the combined total uncertainty in the mean for the $h/D_j = 0.5$, NPR = 5.0 rigid-surface case.

Uncertainties in the mean can also be calculated for turbulence quantities. These include the uncertainties in the Reynolds normal (one in each primary direction) and shear stresses, $w_{\overline{u'u'}}$, $w_{\overline{w'w'}}$, and $w_{\overline{u'w'}}$, respectively. These uncertainties were determined as recommended by Benedict and Gould,[119] as shown in Equations 2 – 4. The 1.96 factor is associated with a 95% confidence interval from the mean and *n* is the total number of snapshots taken (1000 in this study). The quantities $(\overline{u'u'})$, $(\overline{w'w'})$, and $(\overline{u'w'})$ are obtained directly from DaVis.

$$w_{\overline{u'u'}} = 1.96\sqrt{\frac{2(\overline{u'u'})^2}{n}} \tag{2}$$

$$w_{\overline{w'w'}} = 1.96\sqrt{\frac{2(\overline{w'w'})^2}{n}} \tag{3}$$

$$w_{\overline{u'w'}} = 1.96\sqrt{\frac{(\overline{u'u'})(\overline{w'w'}) + (\overline{u'w'})^2}{n}} \tag{4}$$

The uncertainties in the turbulence quantities are presented in Figure 20. Each is normalized by its corresponding maximum value: $(\overline{u'u'})_{max}$, $(\overline{w'w'})_{max}$, and $(\overline{u'w'})_{max}$, respectively. As the uncertainty in both of the Reynolds normal stresses is directly proportional to the Reynolds normal stresses themselves, they share the same maximum locations. Since the uncertainty in the Reynolds shear stress is weighted by the Reynolds normal and shear stresses, the maximum uncertainty is found near the shock/boundary layer interaction aft recompression region. Table 6 presents the median and maximum normalized uncertainties for each of the Reynolds stresses. The maximum median uncertainty for any Reynolds stress is less than 0.4% of its corresponding maximum value in all cases.

Table 6. Uncertainties in the Mean for Several Turbulence Quantities.

Uncertainty Type	Median	Maximum
$w_{\overline{u'u'}}/(\overline{u'u'})_{max}$	0.0003	0.0877
$w_{\overline{w'w'}}/(\overline{w'w'})_{max}$	0.0036	0.0877
$w_{\overline{u'w'}}/(\overline{u'w'})_{max}$	0.0024	0.1149

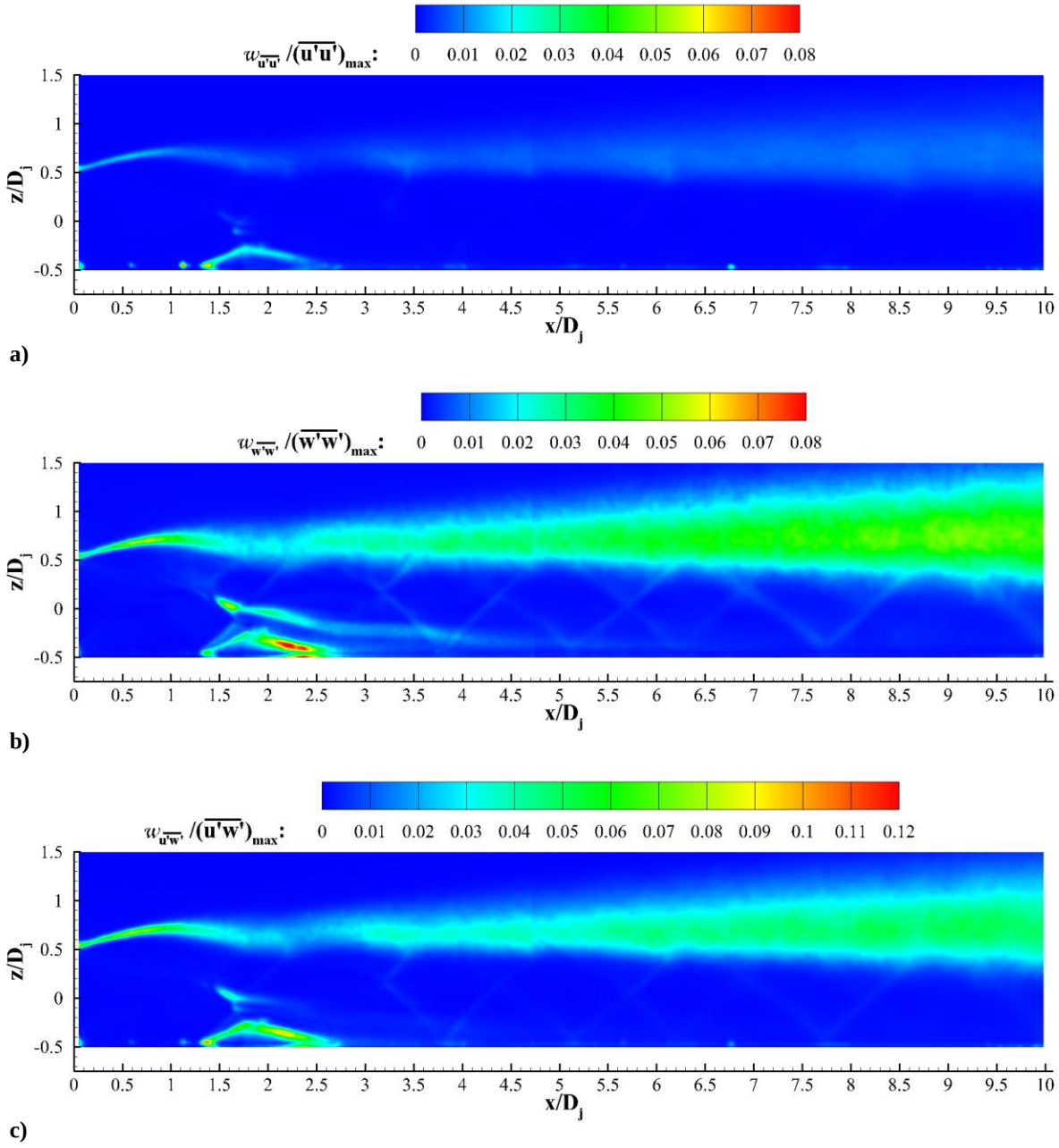

Figure 20. Uncertainties in the mean for a) streamwise Reynolds normal stress, b) wall-normal Reynolds normal stress, and c) Reynolds shear stress. Each is normalized by the maximum corresponding value.

2.6.4 Tomographic PIV

One of the disadvantages of planar PIV is that data can only be obtained for the two velocity components within the illumination plane. By using two cameras, stereo PIV allows for the measurement of all three velocity components on that plane. Tomographic PIV improves upon

these limitations and is a recent advancement in the family of PIV techniques.[120,121] Using a multiple camera system, three-component velocities are obtained within a volume. The method is similar to other PIV techniques, but is carried out using 3D cross correlations within a volume instead of 2D cross correlations on a plane. Particles within a test volume are imaged twice with multiple (typically four) cameras, the particle positions are reconstructed within the volume using a volumetric spatial calibration, and 3D cross correlations calculate three-component velocity vectors within the volume. Tomographic PIV data were obtained for the isolated jet and for the jet/rigid-surface cases.

Tomographic PIV allows for expanded data analysis as compared to traditional PIV, permitting the experimentalist to employ tools that have been traditionally reserved for computationalists. For instance, since all velocity components are obtained simultaneously throughout a volume, the full velocity gradient tensor can be determined, thereby allowing for vortex and coherent structure identification methodologies,[122] such as the Q-criterion or λ_2-criterion, to be used. Elsigna et al. were among the first to successfully use tomographic PIV data in such a manner for high-speed flows.[123] It should be noted that CFD-like methods rooted *only in three-component velocities* can be extended to tomographic PIV data analysis; shock-finding methods utilizing local pressure data or methods based on baroclinic torque, for instance, cannot be directly applied to tomographic PIV data.

While tomographic PIV provides an enormous amount of data and many opportunities for advanced analysis, it also brings additional challenges. As with planar PIV, proper illumination and particle seeding density are required. Additional complications incurred while using tomographic PIV are those arising from increased depth-of-field requirements, camera schiempflug angles and focusing plane, the need for a rectangular aperture, and the need to monitor and control laser reflections for a multiple-camera system. Before data can be obtained, a spatial calibration is needed, followed by a volume self-calibration. Data images undergo preprocessing, volume reconstruction (particle triangulation), volumetric cross-correlation, and vector post-processing.

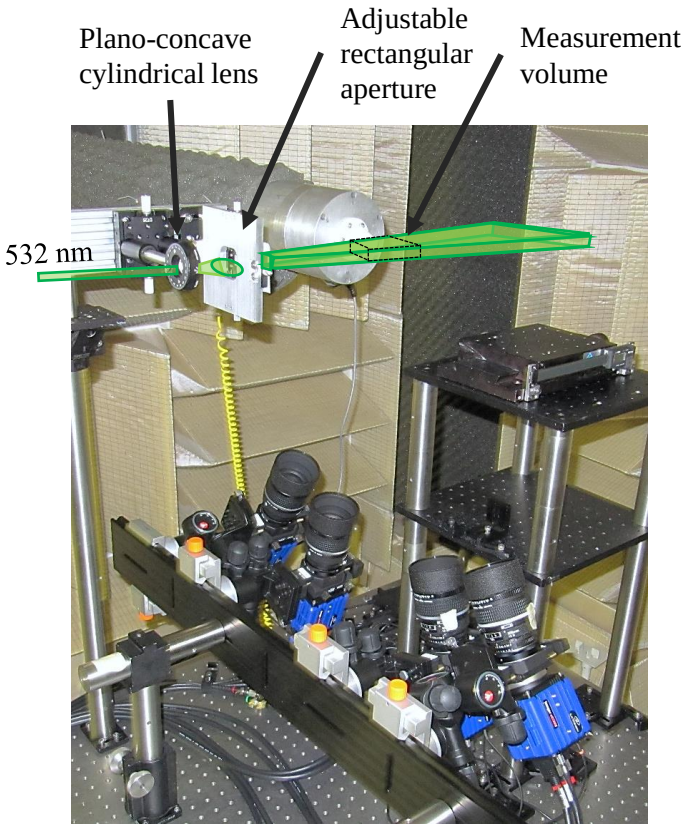

Figure 21. The tomographic PIV experimental arrangement (image shown is for the isolated jet case).

A LaVision tomographic PIV system, with four 16-bit (2560 pixel x 2160 pixel) Imager sCMOS cameras, was used to acquire and process data for this study. Each camera has a schiempflug adapter, which allows the cameras to focus on angled planes, and a tripod head. An external Programmable Timing Unit (PTU X) is used to control laser firing and camera triggering. A personal computer runs LaVision DaVis 8.2.3 software for data acquisition and processing. A variety of cylindrical lenses, extension tubes, and manual-aperture Nikon F-mount lenses was also purchased.

The experimental arrangement for the tomographic PIV system can be seen in Figure 21. The same flow seeding system and laser used in the planar PIV experiments were utilized for tomographic PIV. Illumination was from the side, and the laser beam impinged normally on the vertically-oriented rigid surface (surface not shown in image). Beam optics included a single plano-concave cylindrical lens (f = -75 mm, ThorLabs LK1431RM-A) and an adjustable rectangular aperture to generate a measurement volume with straight edges. Only a single lens was required because the laser beam diameter itself was as wide as the desired test volume thickness.

The lower edge of the volume was approximately located at the jet centerline, allowing for imaging of the upper half of the jet. The cameras were arranged linearly on an optical rail below the jet and imaged the particles in side scatter. Each camera was fitted with a Nikon PK-12 (14 mm) extension tube and a Nikon Nikkor 105 mm 1:2 D lens at f11. Sample particle images for each camera are shown in Figure 22.

An initial pinhole-model spatial calibration was obtained using a LaVision 058-5 two-level calibration plate. The calibration was then refined using an iterative volume self-calibration routine.[124] Particles are triangulated, and their actual positions are compared to their expected positions. The standard deviation of the difference between positions was calculated on a sub-volume basis, and this quantity is referred to as the disparity. The correlation maps for the sub-

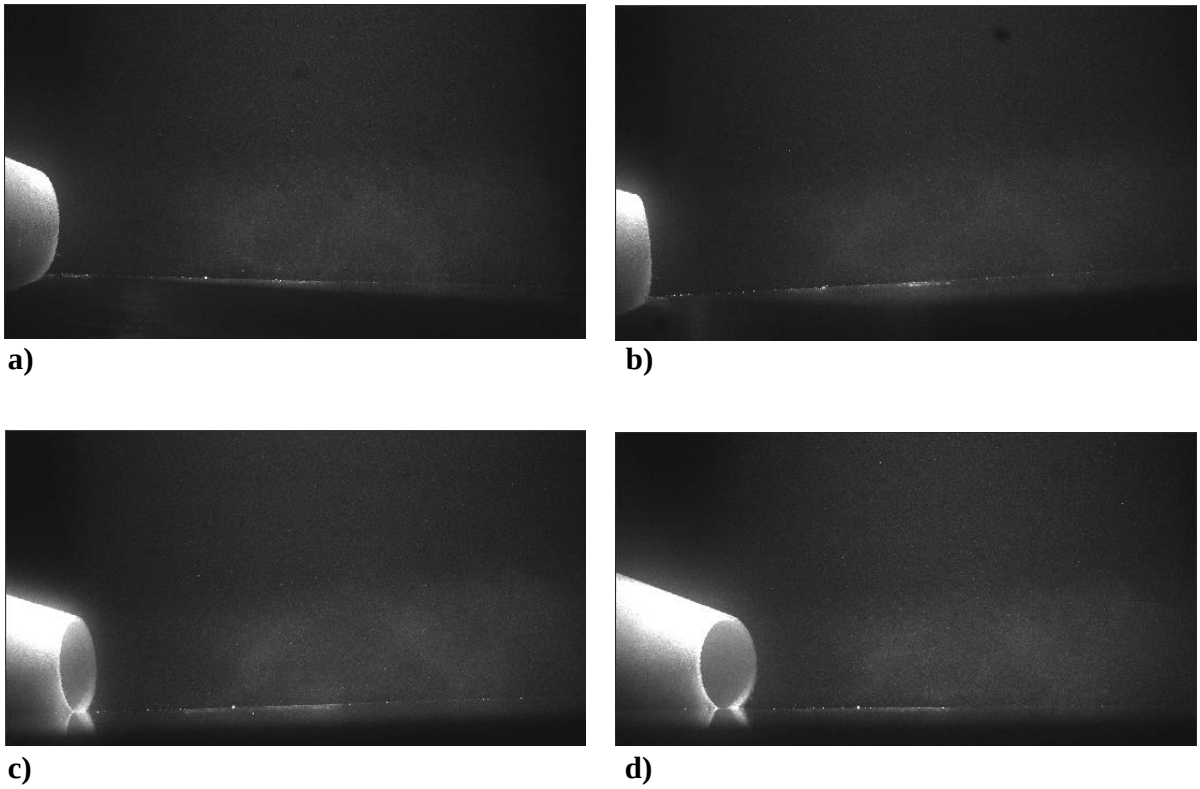

Figure 22. Representative particle images obtained using tomographic PIV for cameras a) 1, b) 2, c) 3, and d) 4. Images have been cropped to remove unused portions of the frame.

volume disparities are generated, as are disparity vectors, drawn from the expected to the true position. If the disparity correlations are strong (distinct peaks), the disparity vectors are used to correct the volume calibration on a sub-volume basis. This procedure is repeated until the disparity vectors are less than 0.3 pixels in length. During the iteration process, the number of sub-volumes (*dx*, *dy*, and *dz*) is increased in order to better refine the calibration.

The final test volume measured approximately 65 mm x 40 mm x 12 mm. Processing was conducted down to voxels (3D interrogation volumes) that were 48 x 48 x 48 pixels with 75% overlap. Each voxel corresponds to a physical space of approximately 1.2 mm^3. Velocity data could not be obtained nearer than 6 mm from the nozzle exit as it was difficult to orient all four cameras without partially shielding the viewing volume with the upstream nozzle apparatus while also keeping all cameras in side scatter.

2.7 Surface Diagnostics

Surface diagnostics, specifically in the form of pressure, temperature, and oil flow visualization, were obtained on the rigid planar surface. Due to the surface rigidity, these measurements were rather easily obtained, as there was little difficulty in conducting image registration (such as for calculating the pressure-sensitive paint intensity ratio) or in mapping the results to physical location. This simplification was not afforded for the compliant-surface case, making the acquisition of quantitative data much more difficult (and for long-time response measurements, impossible). For instance, pressure-sensitive paint requires image registration when using the radiometric method; this is not possible for a moving surface – even if the motion is primarily in an out-of-plane direction. As a result, compliant-surface case surface data were limited to measurement of the three-dimensional surface-deflection state using a technique called stereo/3D Digital Image Correlation (sDIC).

2.7.1 Pressure-Sensitive Paint

Steady surface pressure fields were obtained on the rigid surface using pressure-sensitive paint (PSP). PSPs contain luminescent molecules embedded in an oxygen-permeable binder layer. The luminophores are excited with a narrow-band light source. The excited luminophore can return to the ground state through emission (at a wavelength distinct from the excitation) or via oxygen quenching, a process whereby nearby oxygen molecules absorb the excess energy in vibrational

modes. The degree of fluorescence is inversely proportional to the local oxygen content, and thereby, pressure.

Experiments were conducted using an Innovative Scientific Solutions Inc. (ISSI) UniFIB paint, which is relatively insensitive to temperature. An ISSI LM2XX-DM 2-inch water-cooled LED lamp was used as the excitation light source. The lamp, fitted with an ultraviolet short-pass filter and a parabolic reflector, was positioned approximately 50 cm from the surface, so as to provide uniform illumination intensity. A Cooke Corporation PCO.2000 CCD camera fitted with a Nikon AF Nikkor 50 mm f1.4 lens and optical bandpass filter (to isolate paint response from the excitation and background wavelengths) obtained 500 images with an exposure time of 225 ms. One hundred reference (ambient, no flow) intensity images were acquired prior to data acquisition. The experimental setup is shown in Figure 23 for the fast-response PSP; steady measurements were obtained using a different camera in an otherwise identical setup.

The radiometric method was employed in this study. By ratioing images at known reference (wind-off, I_{ref}) and unknown (wind-on, I) conditions, the spatial variation due to non-uniform lighting, variations in paint thickness, and other effects were eliminated. The image intensity ratio

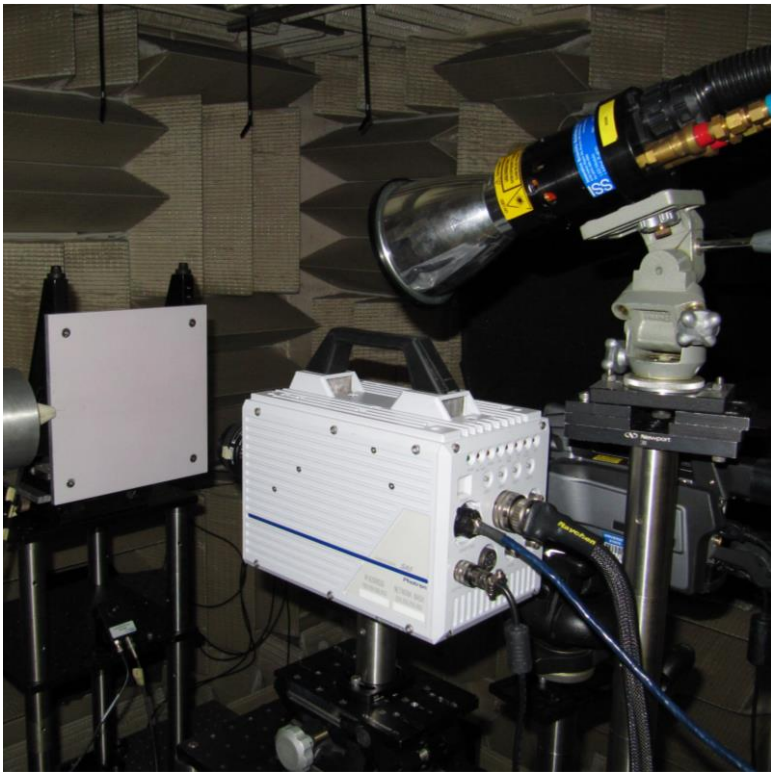

Figure 23. The pressure-sensitive paint experimental set up (high-speed camera shown).

(I_{ref}/I) is inversely related to the pressure ratio (P/P_{ref}) via the Stern-Volmer equation and is the basis for paint calibration.

PSP calibration was conducted via pressure taps. One tap was positioned well outside of the jet interaction region where the pressure was approximately ambient. Five other taps were positioned within the jet interaction region in regions of high and low pressures. Suitable pressure tap locations (to ensure maximal calibration range) were determined using PSP images obtained prior to tap placement for the h/D_j = 0.50 case, as this was the operating condition expected to yield the greatest pressure range. Pressure data were obtained using a Pressure Systems Inc. NetScanner system, described in Section 2.2.

Figure 24 a) displays the PSP calibration curves obtained for the h/D_j = 0.50, 0.55, and 0.60 rigid-surface cases and their corresponding R^2 values. The intensity ratio domain for each curve fit line is defined by the respective maximum and minimum values observed in the data. The extent that each curve-fit line extends beyond the outermost symbols is therefore an indication of the degree of calibration extrapolation. However, the calibration curve alone gives no indication as to how many *pixels* were actually extrapolated. To address this point, an intensity ratio histogram generated from values local to the jet footprint (within ± 0.5D_j from the jet centerline) was generated (Figure 24 b for the h/D_j = 0.50 case); as seen by the limited hashed regions, little extrapolation was actually required.

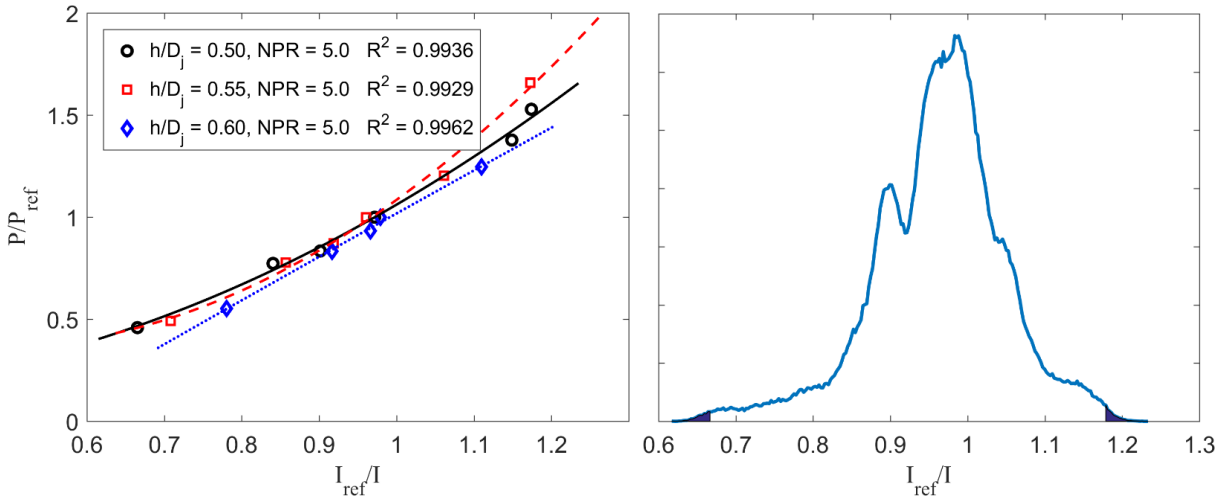

Figure 24. a) PSP pressure tap calibration curves for three h/D$_j$s yielded calibrations with large R-squared values, and b) histogram of intensity ratios obtained within ±0.5D$_j$ of the jet centerline for the h/D$_j$ = 0.50 case highlights how little calibration extrapolation was needed.

A complete PSP measurement uncertainty analysis, such as that conducted by Liu et al.,[125] requires more information than was available in this study, necessitating the use of a simpler method. In this study, the PSP measurement uncertainty was estimated by two mechanisms: a calibration error and a precision/noise error. The calibration error was estimated by calculating the standard deviation of the difference between each pressure tap measurement and the PSP calibration-derived pressure obtained from the intensity ratio local to each pressure tap. This quantity was normalized by the reference pressure (ambient). The PSP calibration uncertainty, σ_{Cal}, was estimated at 0.03 for the h/D_j = 0.5, *NPR* = 5.0 rigid-surface case. Similar (or better) values were obtained for all other tested operating conditions barring one (the h/D_j = 0.6, *NPR* = 4.0 case, which was substantially higher).

The PSP precision error, $\sigma_{Prec,}$ was estimated on a pixel by pixel basis in the following manner. First, the standard deviation of the intensity ratio was calculated. The PSP calibration was then used to calculate the pressure ratio at $(I_{ref}/I)_{mean}$ ± stdev(I_{ref}/I). The difference between these pressure ratios and the mean pressure ratio was then calculated and the larger difference was taken as the precision error. It was normalized by the mean pressure ratio. The average precision error (within ± 2D_j of the centerline) for the h/D_j = 0.5, *NPR* = 5.0 rigid-surface case was 0.023. Figure 25 displays the precision uncertainty estimation for the h/D_j = 0.5, *NPR* = 5.0 case. The PSP uncertainties as calculated by both sources of uncertainty are summarized in Table 7. The median and maximum values are given in addition to the mean values. Due to the small amplitude pressure changes for the *NPR* = 3.0 operation condition (especially for larger h/D_j), PSP data were not obtained for the h/D_j = 0.55 and 0.60 conditions at *NPR* = 3.0.

Table 7. Steady PSP Measurement Uncertainties.

h/D_j	*NPR*	σ_{Cal}	σ_{Prec}		
			Median	**Mean**	**Maximum**
0.50	5.0	0.032	0.023	0.023	0.078
	4.0	0.016	0.021	0.021	0.073
	3.0	--	--	--	--
0.55	5.0	0.034	0.031	0.031	0.124
	4.0	0.036	0.026	0.026	0.069
	3.0	--	--	--	--
0.60	5.0	0.016	0.027	0.027	0.150
	4.0	0.022	0.021	0.021	0.550
	3.0	0.005	0.037	0.038	0.124

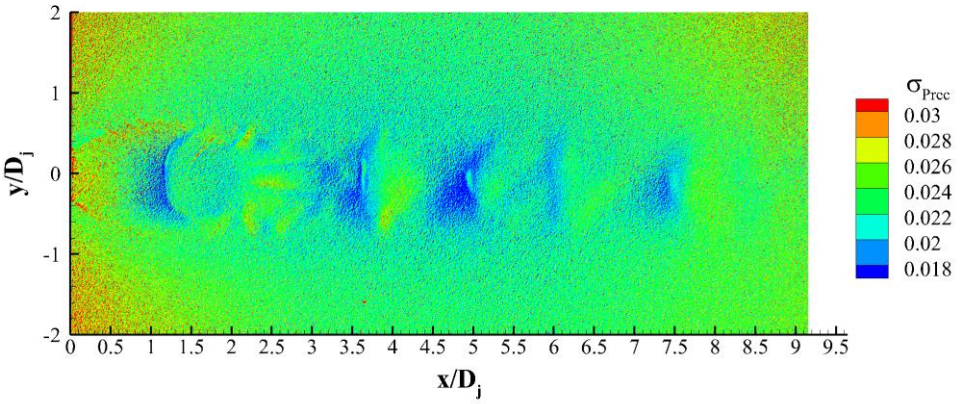

Figure 25. The steady PSP precision error, normalized by the local pressure ratio.

Due to the long time response of the UniFIB PSP, it could only be used to obtain steady pressure data. In order to investigate the unsteady pressure variation on the rigid surface, fast-response PSP measurements were also obtained. However, these data were not judged to be quantitatively accurate and are therefore not included in the primary study. Still, these experiments resulted in a number of useful insights; a summary of these experiments is included in Appendix C.

2.7.2 Surface Oil Flow Visualization

Oil flow visualization is a commonly used technique to assess a flow near a surface, as it provides a visualization of the surface streaklines. These streaklines can reveal flow characteristics such as separation regions, reversed flow, reattachment and saddle points, and vortex locations.

In this study, the surface was prepared for oil flow visualization by applying either black matte contact paper or several thin coats of black-matte spray paint to provide a uniform surface finish and additional contrast with the white oil-based surface-flow mixture. A titanium dioxide and STP oil treatment mixture was uniformly applied to the prepared surface in a very thin layer with a foam brush. The mixture consisted of 2:1 ratio (by mass) of STP oil treatment to titanium dioxide powder. Ten drops of 5W motor oil were added for every gram of titanium dioxide in order to thin the mixture. A Cooke Instruments PCO 2000 camera was used to obtain images during the entire course of a run. Illumination was provided with a white LED or with a 150 W projector bulb.

One challenge with digitally recording surface oil flow visualization images is image contrast. The camera field of view commonly contains both regions of high shear, where the surface is ‘scrubbed’ and the image is very dark, and regions of low shear, where the oil accumulates and

the image is very bright. Inspecting both of these regions simultaneously is difficult, as portions of the image are either overly dark or excessively bright, as shown in Figures 26 a) and b), respectively.

In order to alleviate this problem, a contrast-limited adaptive histogram equalization (CLAHE) scheme was applied using a MatLab routine. The CLAHE method is an image-processing technique in which histogram equalization is performed on subwindows of the larger image. Subwindows are then blended together using a bilinear interpolation to eliminate artificial windowing effects. Application of CLAHE resulted in images with adequate contrast in both high- and low-shear regions, as shown in Figure 26 c). Since oil flow visualization is generally considered a qualitative method, image processing using this technique does not compromise the data. A survey of the literature showed that CLAHE has not been previously utilized within the surface oil flow community to our knowledge.

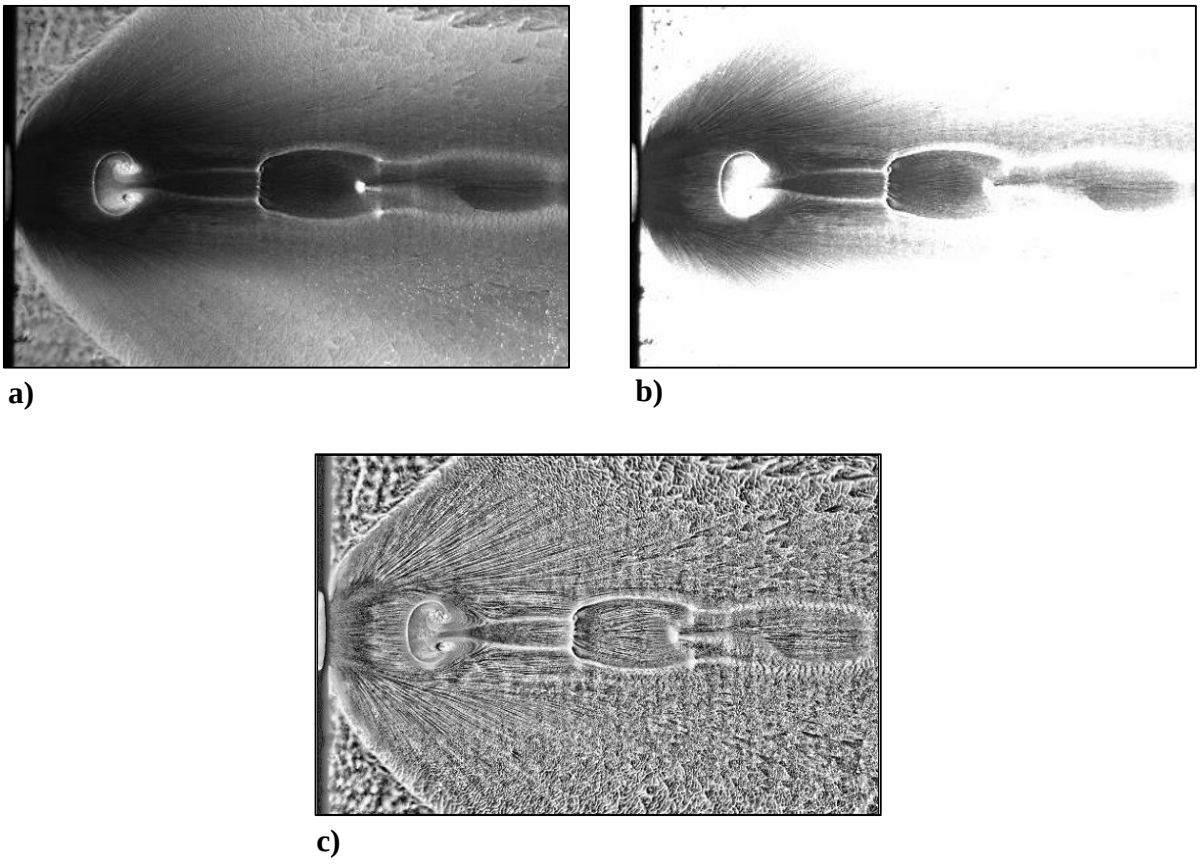

Figure 26. Surface oil flow visualization images with contrast optimized for a) low-shear regions, b) high-shear regions, and c) for all parts of the images (obtained via application of CLAHE).

2.7.3 Stereo Digital Image Correlation

Digital Image Correlation (DIC) is a firmly established technique most commonly employed by the materials and mechanics communities to obtain full-field in-plane strain of a nominally flat surface. The method is based on conducting random speckle pattern image cross-correlations between a reference surface state (typically the initial condition) and an unknown test state to calculate a displacement. The displacements are traditionally used to determine strain. The correlation algorithm is conducted on a subset window basis and is carried out on a speckle pattern applied to the imaging surface.

The discrete image intensities (intensity counts) are obtained from each subset window and are then fitted onto a continuous surface using a B-spline interpolation, as shown in Figure 27. In order to combat decorrelation effects, a subset shape-matching transformation function is used to model the subset translation, shear, and rotation between the reference and test states. A schematic

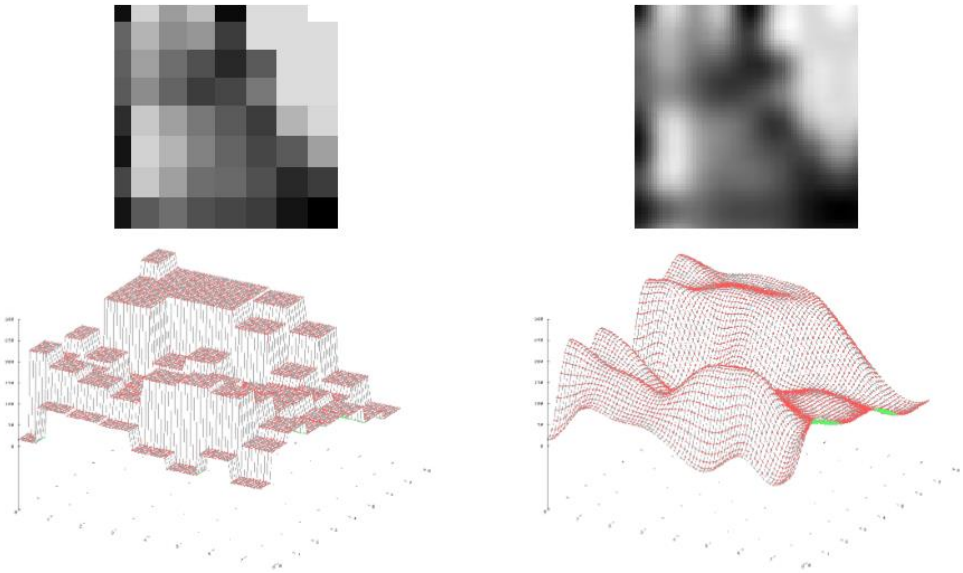

Figure 27. Within each subset, a) the discrete raw image intensities are interpolated onto b) a continuous surface using a bi-cubic B-spline interpolation. Image adapted from Correlated Solutions.[126]

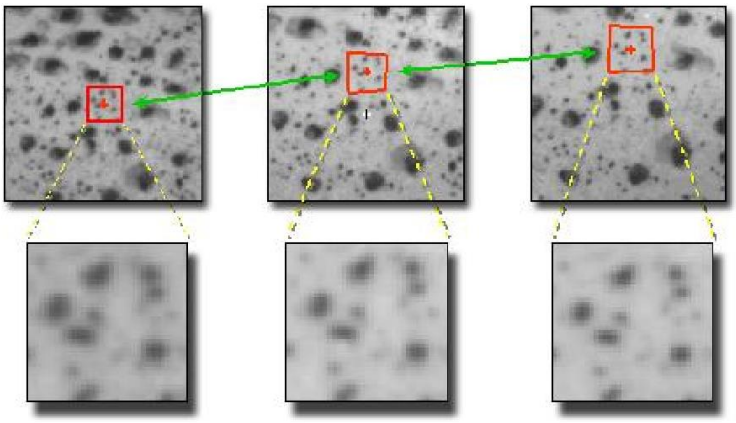

Figure 28. An initially square subset is deformed into a non-square region. Subset shape-matching functions are used to account for this transformation. Image courtesy of Correlated Solutions.[126]

representation of the shape-matching function is shown in Figure 28. The cross-correlation algorithm is then applied to each subset between the reference and test states. Since the correlations are conducted on a continuous surface and the subset is allowed to transform, DIC can resolve shifts of approximately 0.01 pixels.[127] This represents a significant improvement as compared to PIV (typically 0.1 pixels), for which the correlations are instead based on a finite number of particle intensity peaks and the subwindow transformation capabilities are more restrictive.

Stereo DIC (sDIC), also known as 3D-DIC, is a two-camera stereo-vision version of DIC that additionally allows for the reconstruction of the out-of-plane displacement component. In this case, the 3D surface position is reconstructed using a stereo calibration, the subset shape-matching function is applied, the raw image data are interpolated onto a continuous domain, and cross-correlation analysis carried out. For this study, sDIC measurements were obtained on the back side of the compliant surface, while flowfield measurements (PIV) were obtained on the jet-side of the surface.

The sDIC setup is shown in Figure 29. Illumination was provided using an approximately 5-cm diameter 150 W projector bulb powered with a DC power supply. A parabolic reflector was fitted on the bulb to uniformly direct the light onto the surface and to aid in control of surface radiative heating. The bulb illuminated the surface approximately normally so as to minimize any shadows. It was operated continuously at 24V, 6A and was turned on several minutes before data acquisition so as to ensure that it was operating at a steady condition. The end face of the parabolic reflector was positioned approximately 53.5 cm away from the surface, between the two cameras. Although positioning the light nearer to the surface was possible and would have provided

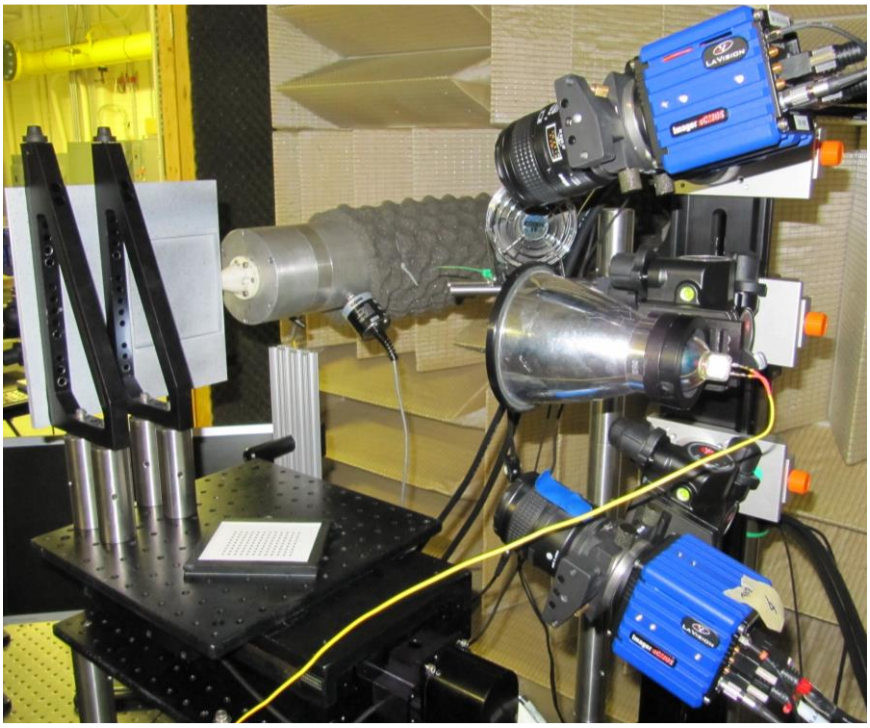

Figure 29. An image of the sDIC experimental arrangement. sDIC measurements were obtained on the underside (back) of the compliant-surface model.

increased illumination, it also caused heat waves rising from the light to affect the upper sDIC camera imagery, completely compromising the images obtained from it. Therefore, the nearest light source position was limited by the cameras. A small desk fan was used to cool the lamp and to ensure that heat waves did not convect into the camera fields of view.

Two cameras, borrowed from the tomographic PIV system, were used to obtain the sDIC measurements. They were positioned vertically, one on either side of the illumination source, to view the compliant surface. The camera stereo angle was approximately 28°. The cameras were fitted with Nikon Nikkor 65 mm lenses and the aperture was set to f5.6, yielding sufficient depth of field to use a single sDIC calibration for all three tested plate offset distances (h/D_j). The scheimpflug angles for both cameras were set to zero, as the sDIC software calibration algorithm does not allow for their use. No extension tubes were required. Ensuring a rigid camera mounting system is critical for sDIC. For this reason, all camera hardware and tripod fasteners were securely tightened, and all camera cables were bundled and tied down so as to avoid any camera motion post stereo calibration.

The camera field of view allowed for imaging of the entire compliant surface. Additional field of view in the axial direction (the sensor aspect ratio is approximately 1.18) was used to image a

portion of the model frame and allowed for quantification of the model rigid motion. This reference region was approximately 15 mm wide and extended the full height of the model surface (125 mm). Representative images from the sDIC cameras are shown in Figure 30. Since sDIC measurements were obtained from the back side of the surface, the jet is positioned on the right side of the images. The portion of the frame used to monitor rigid model motion is shown on the left side of the images.

The surface was prepared for sDIC measurements by applying a speckle pattern after model assembly. The surfaces of interest were cleaned with isopropyl alcohol and allowed to dry before application of the speckle pattern. White primer spray paint (Rust-Oleum Ultra Cover Flat White Primer) was applied to the surface from multiple directions in several thin coats, allowing the paint to dry between coats. The speckle pattern was applied by carefully spray painting over/across the surface, and allowing the paint spatter to speckle the surface of interest. Flat black spray paint (Rust-Oleum Black Flat Protective Enamel) was put in a simple spray paint can holder that allowed fine control of the nozzle pressure using a crossbar and screw. Based on the camera scaling factor and the desired spatial resolution, speckles on the order of 0.5 mm in diameter were desired. The speckle pattern was applied over several coats from multiple directions so as to yield a random, high-contrast, isotropic pattern.

The stereo vision system was calibrated using the bundle-adjustment method and a calibration plate.[127] The calibration plate, shown in Figure 31, was manufactured by Correlated Solutions, Inc., and had a grid of dots spaced 6 mm apart. Three-hundred calibration plate image pairs were obtained at varying angles and positions within the measurement region. These images were then loaded into VID-3D 2010, and a calibration was created and assessed. Residual scores for each image, in the form of grid-point pixel shift standard deviations from the expected locations (an estimate of calibration error), were displayed and used as a metric for manual removal of some image pairs from the calibration. Images yielding poor residual scores were removed and the calibration updated on an iterative basis. The overall calibration score is computed by the square root of the sum of the squares calculation conducted using the average pixel standard deviation for each camera.

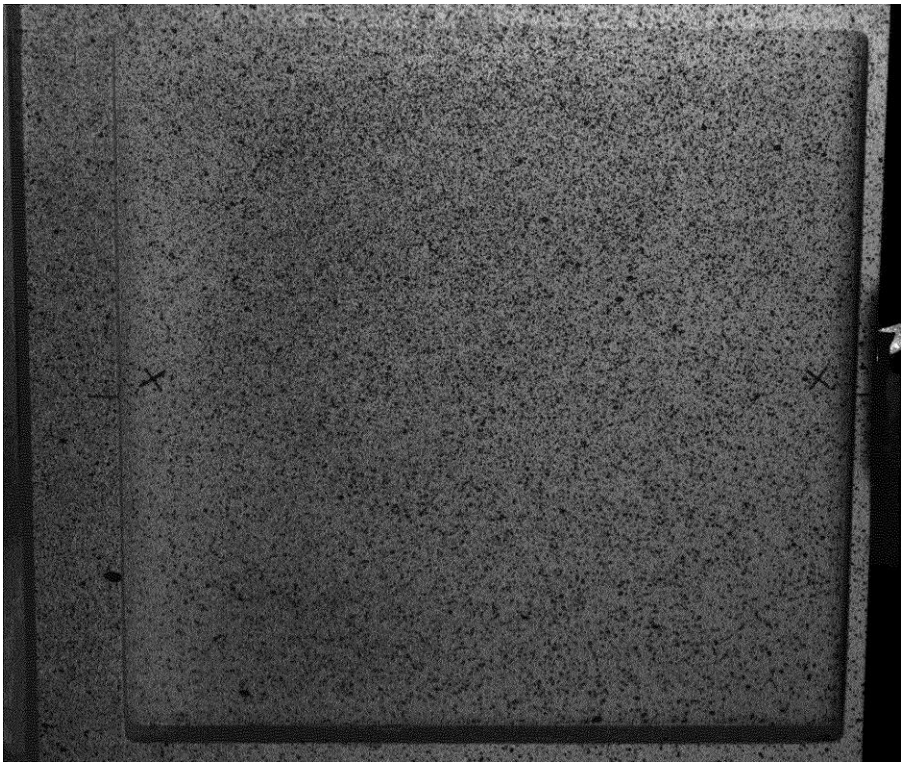

a)

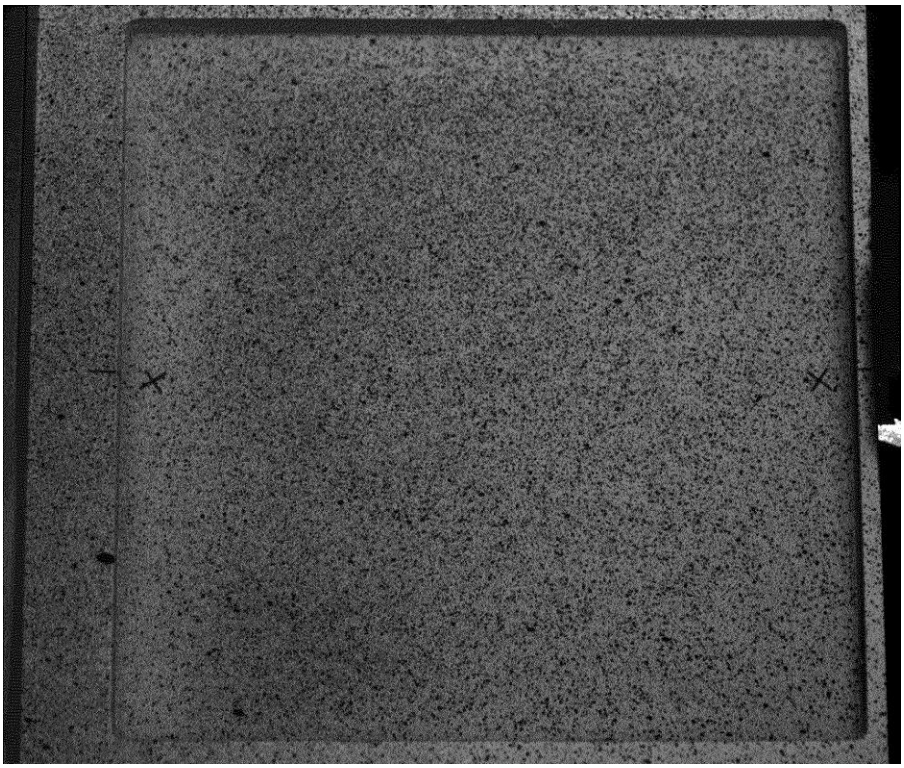

b)

Figure 30. Images of the compliant-surface model obtained from the sDIC cameras. The jet is on the right. A portion of the model frame (left side) was used to assess rigid motion of the model.

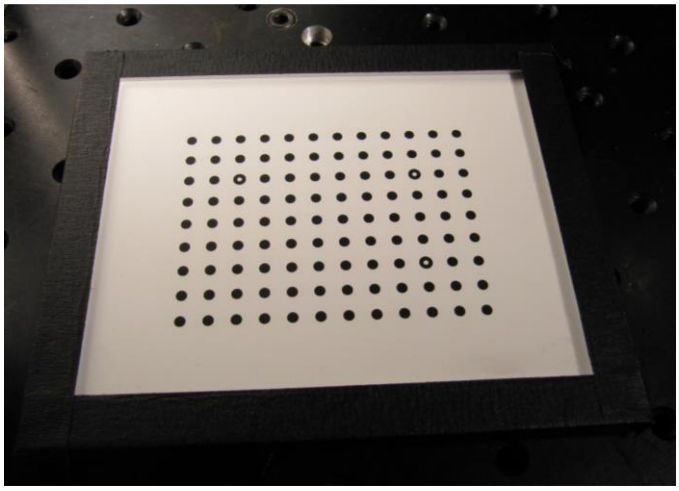

Figure 31. The sDIC calibration plate.

Using this calibration method, an acceptable overall calibration score falls below 0.100 pixels, and an exceptional calibration yields scores below 0.025 pixels. In this study, a single sDIC calibration was obtained for all experiments; the final overall calibration score was 0.046 pixels and was based on approximately half of the original 300 calibration plate images.

The calibration parameters, separated into intrinsic and extrinsic parameters, are shown in Tables 8 and 9, respectively. Intrinsic parameters include the camera sensor center (pixels), camera focal length (pixels), skew, and radial distortion coefficients (K_1) for each camera. Since a first order distortion model was selected, only a single coefficient is given. The quoted confidence margins (one standard deviation) represent small errors for each quantity. Multiplication of the computed focal length (pixels) by the camera pixel size should give an approximation of the dimensional focal length. Carrying out this calculation, results in focal lengths of 65.96 and 65.86 mm; the cameras used 65 mm lenses, showing good agreement.

Table 8. Intrinsic Camera Parameters for the sDIC Calibration.

	Camera 0			**Camera 1**		
X Center (pix)	1284.666	±	0.738	1360.28	±	0.499
Y Center (pix)	1073.587	±	1.779	1014.024	±	0.94
X Focal Length (pix)	10147.711	±	10.073	10131.626	±	9.672
Y Focal Length (pix)	10147.191	±	9.965	10132.196	±	9.654
Skew	0.153	±	0.069	0.518	±	0.069
Kappa 1	0.042	±	0	0.049	±	0

Extrinsic parameters include the physical camera arrangement: orientation angles and the position of the second camera with respect to the first camera. The stereo angle calculated by the calibration agrees well with the measured angle of approximately 28°. The other two angles were small, as was desired. The camera separation distance in the *y*-direction agrees well with the measured value.

Table 9. Extrinsic Camera Parameters for the sDIC Calibration.

	Angle (deg):			**Translation (mm):**		
X axis	-27.841	±	0	-2.513	±	0
Y axis	-0.48	±	0	-280.929	±	0.007
Z axis	-0.527	±	0	68.577	±	0.049

sDIC processing was conducted using the VIC-3D 2010 software. A subset size of 35 pixels was used with a step size of 7 pixels. This yields an effective overlap of approximately 80%, which is not significantly higher than that used within other sources of literature (Sutton et. al,[127] for instance, documents multiple instances where overlaps in the range of 80-90% were used). These subset and steps sizes correspond to a 2.1 mm by 2.1 mm correlation region, with a step distance of approximately 0.42 mm. An optimized 8-tap spline function, which has been previously shown to minimize error and maximize accuracy for minimal extra cost,[127] was used to interpolate discrete intensities to a continuous surface. A Gaussian-weighting distribution was applied to each subset. The default "normalized square differences" correlation criterion was employed. Default thresholding settings were used; the "consistency threshold" was set to 0.02 pixels, the "maximum confidence margin" was set to 0.050 pixels, the "maximum matchability threshold" was set to 0.10 pixels, and the "epipolar threshold" was not used. In addition to conducting the correlation, the confidence margins and strains were also calculated.

The results output by VIC-3D are presented in the reference frame of the first camera. Therefore, a coordinate transformation had to be applied in order to obtain the results in the frame of the jet/surface coordinate system. This was accomplished by using VIC-3D to generate a coordinate system using the "auto plane fit" function based on the compliant-surface model frame (*not* the compliant-surface), which was known to be a planar surface. Registration marks on this frame surface were then used to specify the (*x*,*y*) origin. Since the thickness of the model frame was known, the *z* position was also known, thereby completing the coordinate system definition. The transformation function was saved and then applied to the results obtained for the compliant

surface. A distinct *z*-offset was used for each h/D_j examined. sDIC results are ultimately presented within the same coordinate system as described in Section 2.3. sDIC results were exported to MatLab for further analysis.

VIC-3D outputs a large number of variables for each processed sDIC image. These are given in Table 10, along with a description of each. The VIC-3D outputs can be characterized into coordinate locations, displacements, correlation score, confidence margins, and strains (both coordinate and principal). These results are often given in both pixel and dimensional units. The VIC-3D software reference manual[128] and testing guide[129] provide additional details regarding sDIC image processing and the associated outputs. For clarity, sDIC variables are normally written in script form, while conventional fonts are reserved for PIV results.

Table 10. Summary of the sDIC Output Variables.

Variable	Units	Description
$\mathcal{X}_{\text{ref}}$	mm	metric position along X-axis
$\mathcal{Y}_{\text{ref}}$	mm	metric position along Y-axis
$\mathcal{Z}_{\text{ref}}$	mm	metric position along Z-axis (out-of-plane)
σ	pixel	correlation confidence interval (must be between 0 and 1)
$\mathcal{U}$	mm	metric displacement along X-axis, from the reference state
$\mathcal{V}$	mm	metric displacement along Y-axis, from the reference state
$\mathcal{W}$	mm	metric displacement along Z-axis, from the reference state
u	pixel	displacement along X-axis, from the reference state
v	pixel	displacement along Y-axis, from the reference state
σ_x	mm	metric confidence margin for X-position and displacement
σ_y	mm	metric confidence margin for Y-position and displacement
σ_z	mm	metric confidence margin for Z-position and displacement
e_{xx}	--	normal strain in the X-direction
e_{yy}	--	normal strain in the Y-direction
e_{xy}	--	shear strain
e_1	--	major principal strain
e_2	--	minor principal strain
γ	rad	principal strain angle

The sDIC calibration, setup, and speckle pattern were validated using a few simple tests. Image analysis for all validation tests was based on the frame portion of the model – which was known to be a planar surface.

First, an out-of-plane displacement validation test was conducted by comparing the sDIC-determined displacements to those specified using the linear traverse supporting the model. Approximately 30 images were obtained with displacements ranging from -1.750 mm to 1.750

mm from the h/D_j = 0.5 position. The images were processed in VIC-3D, and the mean and standard deviation of the out-of-plane displacement were exported. The mean displacement was plotted against the known applied displacement, and the standard deviation was used to provide an assessment of the measurement uncertainty. Both the slope and y-intercept of the linear curve fit were inspected to assess the calibration accuracy and any experimental bias. Figure 32 displays data and corresponding linear curve fits for tests conducted both prior-to and after having obtained compliant-panel data. Approximately two weeks passed between the initial and final linear-traverse validation tests. All slopes are near unity, indicating that the sDIC calibration is accurate. Additionally, the y-intercepts are all very small, indicating that there is very little measurement bias. The agreement between the data sets in terms of slope, y-intercept, and R-squared values indicate that the sDIC calibration is of high quality, contains negligible bias, and is stable over time. It was therefore reasonable to conclude that compliant-panel data obtained between the two validation tests were also reliable.

In order to ensure that the PIV seed particles, which are present everywhere within the chamber during a test, did not negatively affect the sDIC results, the out-of-plane displacement

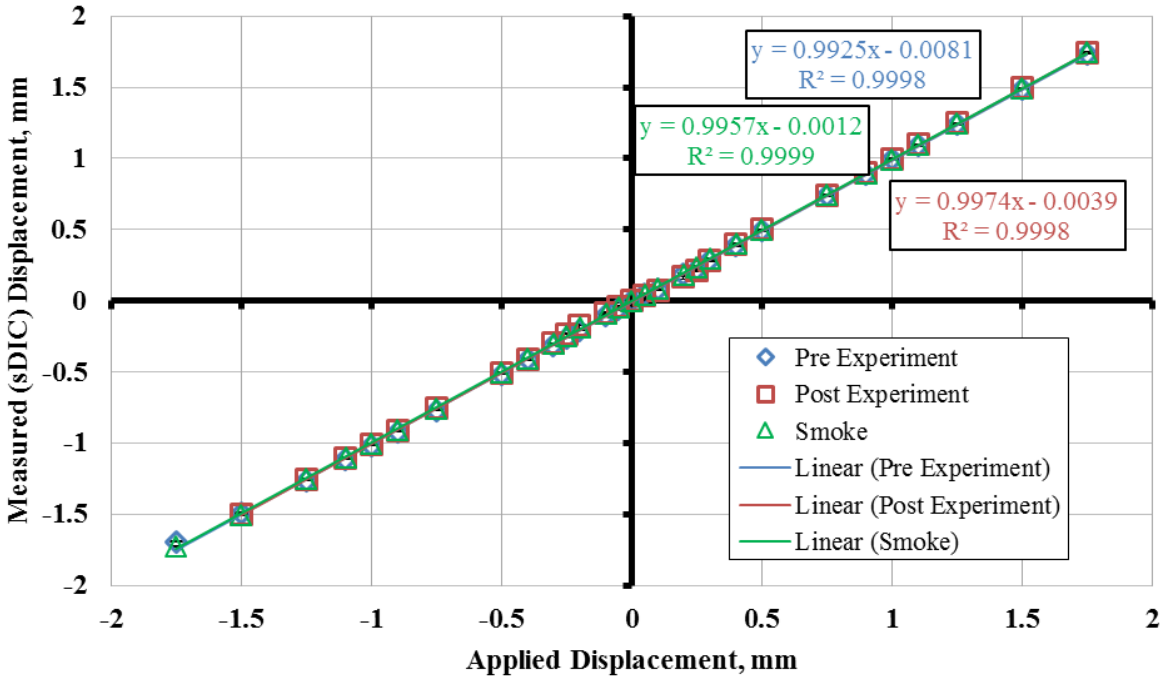

Figure 32. Results of sDIC linear traverse validation tests before obtaining data, after obtaining data, and in the presence of PIV seed particles.

test was also conducted with and without particle seeding. As shown in Figure 32, seed particles were determined to have negligible effect on the sDIC measurements.

A second sDIC validation test was also conducted. In this case, 25 images were obtained without moving the surface. Theoretically, sDIC processing should result in the exact same result for all 25 images. However, in practice, this isn't the case due to random noise errors (precision errors) and possible motion and/or vibration within the system. Statistical quantities extracted from the processed results therefore allow for an estimation of the noise error and overall rigidity of the experimental setup. The mean standard deviation in the out-of-plane displacement, σ_w, from all 25 images was taken as an estimation of the out-of-plane measurement resolution. In this case, σ_w, was determined to be 1.1 μm. This is in good agreement with the stated out-of-plane measurement accuracy of sDIC (1/50,000 multiplied by the camera field of view), which, for a field of view of 130 mm (in the spanwise direction), is approximately 2.6 μm. Conducting this experiment again in the presence of PIV seed particles increased σ_w to 2.3 μm, which is also in very close agreement to the expected out-of-plane measurement accuracy.

The mean standard deviation of the in-plane displacements represent a measure of the in-plane vibrational amplitude and/or in-plane noise. In pixel form, amplitudes of 0.01 pixels or less are regarded as ideal. In the current experimental setup, displacements of 0.007 and 0.009 pixels in the axial and transverse directions, respectively, were observed without PIV seed particles. In the presence of PIV seed particles, these values increased to 0.022 and 0.018 pixels, respectively.

2.7.4 PIV/sDIC Experimental Synchronization

For the compliant-panel tests, PIV and sDIC data were obtained simultaneously. This was accomplished by making use of the tomographic PIV hardware (External Programmable Timing Unit [PTU X], cameras, and DaVis software) described in Section 2.6.2. Two cameras were used to obtain planar PIV measurements (side by side camera arrangement) while the other two cameras were used for sDIC measurements.

The PIV cameras had to be operated in double-frame mode. The sDIC cameras could have been operated in single-frame mode, but it was discovered that the data acquisition system's ability to synchronize cameras operating in single-frame mode was not as precise as for double-frame mode. With the tomographic PIV data acquisition system, cameras operating in double-frame mode can be synchronized with a jitter of approximately 25 ns, but if any of the cameras are operating in single-frame mode the synchronization jitter increases to as much as 5 ms. This

inability to properly synchronize data acquisition necessitated the use of double-frame mode for all cameras. In this study, the sDIC cameras were triggered such that the first frame straddled the PIV laser pulses. Therefore, the second frame obtained from the sDIC cameras was not used.

In double-frame mode, the second frame exposure is open for much longer than the first (long enough to write the first frame to memory). With the sCMOS Imager cameras used in this system, the first frame exposure is fixed at 10 μs, while the second exposure is 19970 μs. In PIV applications, this is usually not a problem, as the majority of the sensor illumination is due to the laser pulse (~5 ns duration). However, this has several implications when using the system for sDIC. First, it means that the illumination source must be bright enough to sufficiently illuminate the first frame. Second, it means that unless a pulsed light source can be used, the second frame will be completely over-saturated, potentially allowing for camera sensor damage.

Tests were conducted to verify that the light source was sufficiently bright to yield accurate sDIC results for the 10 μs exposure time of the first frame. The increased sensitivity of the sCMOS Imager cameras was extremely beneficial in this application, as the resulting maximum image intensity was nearly 4000 counts – sufficient to conduct reliable and accurate sDIC processing. As for the second frame, it was nearly entirely over-saturated. However, since the illumination source in this case was a non-coherent light source, the danger of sensor damage was effectively eliminated.

Synchronized planar PIV and sDIC data images were obtained at random intervals. A LabVIEW program was created to generate 5V trigger signals from an NI USB-6008 DAQ card. The trigger signals were sent to the Programmable Timing Unit (PTU X) while operating in "external random" trigger mode. The minimum time between triggers was governed by the time needed for the data acquisition system to recycle; it was set to 70 ms. The maximum delay time was set to 196 ms so as to minimize the overall run time. Over long records, the mean data acquisition rate was 7.5 Hz. The jet operating condition at the instant of each data acquisition was recorded. A random number generator with a uniform distribution within the LabVIEW VI was used to generate the delay times between trigger signals. The VI block diagram is shown in Figure 33.

Approximately 265 image pairs could be obtained in a single data record when using all four cameras. Four data records were collected for each NPR = 5.0 test condition so as to obtain at least 1000 image pairs. At least one full data record was obtained for each of the lower NPR test

conditions. The PIV-optics shield window, described in Section 2.6.2, was removed and cleaned between each data record.

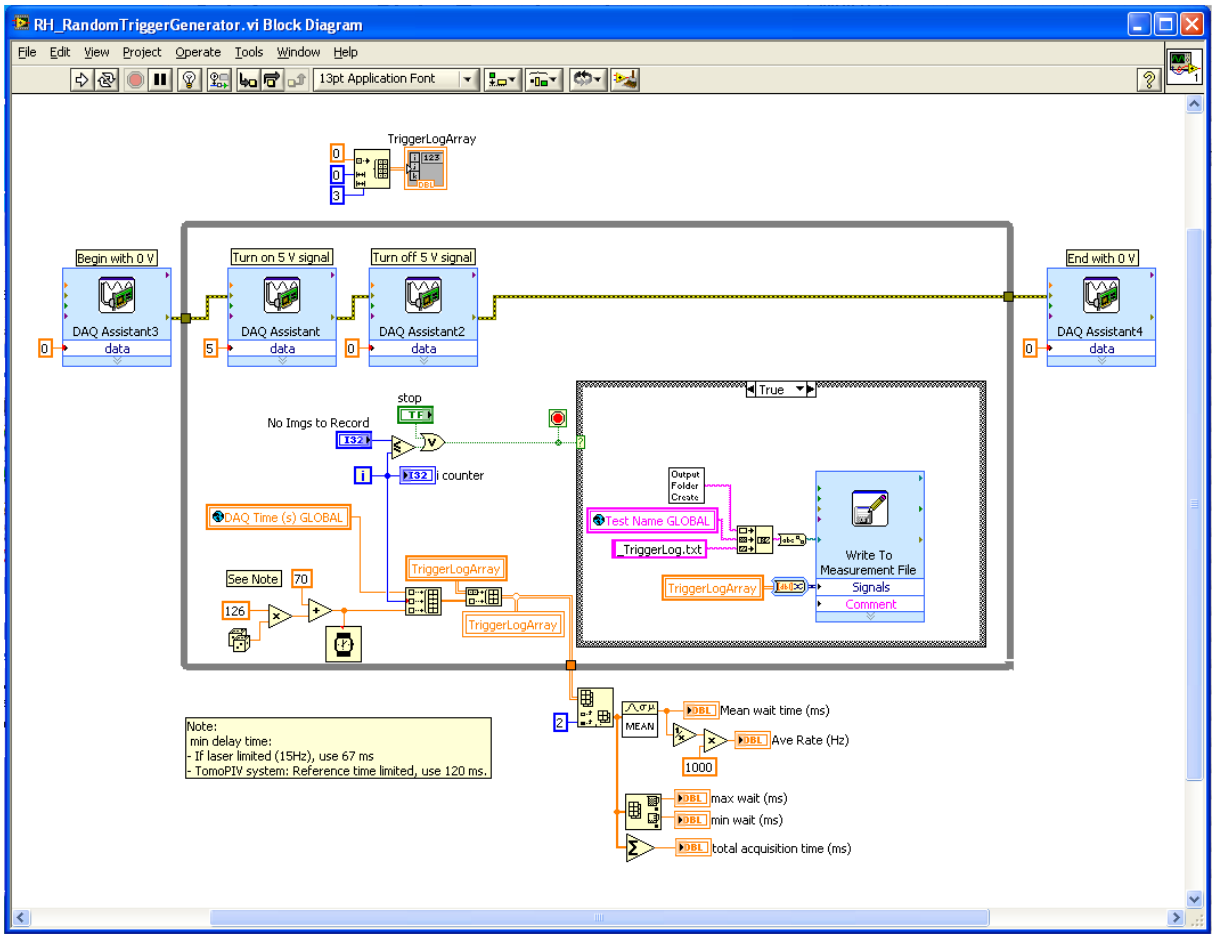

Figure 33. The block diagram of the random data trigger generation VI.

Chapter 3 Isolated Jet

In this chapter, experiments conducted for the isolated jet are discussed. High-speed schlieren data are analyzed for both their time-averaged and instantaneous content. Next, acoustic data are presented, followed thereafter by velocimetry results. These data will be used to establish nominal conditions for this jet flow, and serve as a baseline for comparison for the jet/rigid-surface and jet/compliant-surface cases which are discussed in Chapters 4 and 5.

3.1 High-Speed Schlieren

High-speed schlieren data were obtained at 500 fps, 50k fps, and 100k fps. These frame rates were chosen to provide a long-time (and large field of view) sense of the flow structure (500 fps) and for unsteady analysis (50k and 100k fps). Time-averaged data provide a sense into the overall flow structure, while instantaneous data were used to qualitatively assess the turbulent nature of the jet and for a shock wave position time-history analysis. At least 10,000 images were obtained for each operating condition. The high-speed schlieren experimental setup is described in Section 2.6.1.

3.1.1 Time-Averaged (Mean) Results

The mean schlieren data provide an understanding of the overall flow structure, particularly with regard to compressible-wave structures such as shock waves and expansion fans. The flow structure of isolated jets is well understood;[1-4] therefore, a simple overview of the organization is given here. Data were obtained for the NPR = 5.0 case, which corresponds to a strongly underexpanded operating condition (the nozzle ideally expanded operating condition is NPR_{ideal} = 1.89, M_{ideal} = 1.0).

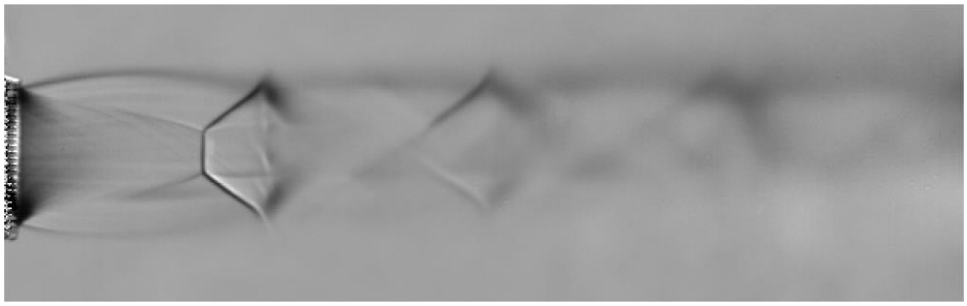

Figure 34. Mean schlieren image for an isolated jet, NPR = 5.0.

A mean schlieren image for the *NPR* = 5.0 case is shown in Figure 34. The main jet flow is bounded by an axisymmetric shear layer. The underexpanded nature of the jet is evidenced by the jet's increased width within the first shock cell, which points to the presence of an expansion fan located at the nozzle lip. At this operating condition, barrel shocks are formed by coalescing compression waves that are generated as the nozzle-lip expansion fans reflect off the shear layer. The barrel shocks extend downstream and terminate upon intersection with the Mach disk. Reflected shocks also form at this intersection (called the triple point), and these reflected shocks propagate radially outward to the shear layer, which are then reflected as expansion waves. These expansion waves are the beginning of the second shock cell, where the expansion/shock process begins anew. The shock-cell pattern repeats with decreasing strength as viscous effects cause shear layer growth and turbulent mixing. Also emanating from the triple point is a constant-pressure slip line (shear layer) separating the post-Mach disk subsonic flow from the supersonic flow that passed outside the Mach disk.

High-speed schlieren data were also obtained for *NPR* = 4.0 and 3.0. Mean images for these operating conditions are shown in Figures 35 (a) and (b), respectively. The shock-cell structure of the jet is clearly visible in these images as well. The decreased degree of underexpansion is evident

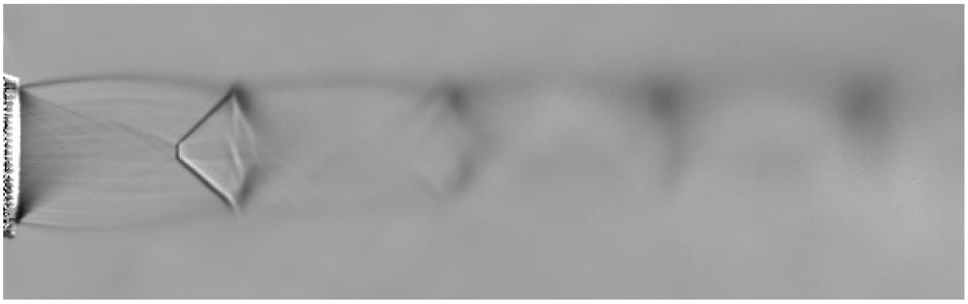

a)

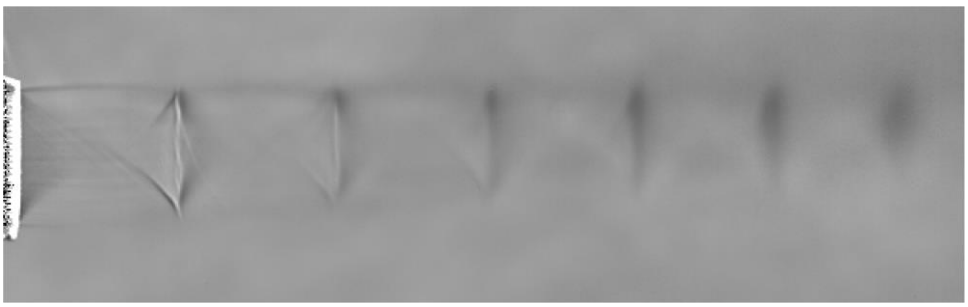

b)

Figure 35. Mean schlieren images for a) NPR = 4.0, and b) NPR = 3.0.

by the decreased Mach-disk diameter (*NPR* = 4.0) and its complete absence in the *NPR* = 3.0 case. Additionally, the first shock-cell plume width is observed to decrease with decreasing *NPR*, as do the shock-cell spacing, and the apparent shock strengths.

3.1.2 Instantaneous Results

Instantaneous schlieren images (Figure 36) clearly show that the flow is turbulent for all operating conditions examined. The jet Reynolds number, based on nozzle exit diameter and the ideally expanded conditions, was found to be in excess of 6 x 10^5 for the *NPR* = 3.0 case, confirming the observations of turbulence (according to Zaman,[130] the transition *Re* for isolated jets is typically on the order of 2.5 x 10^5).

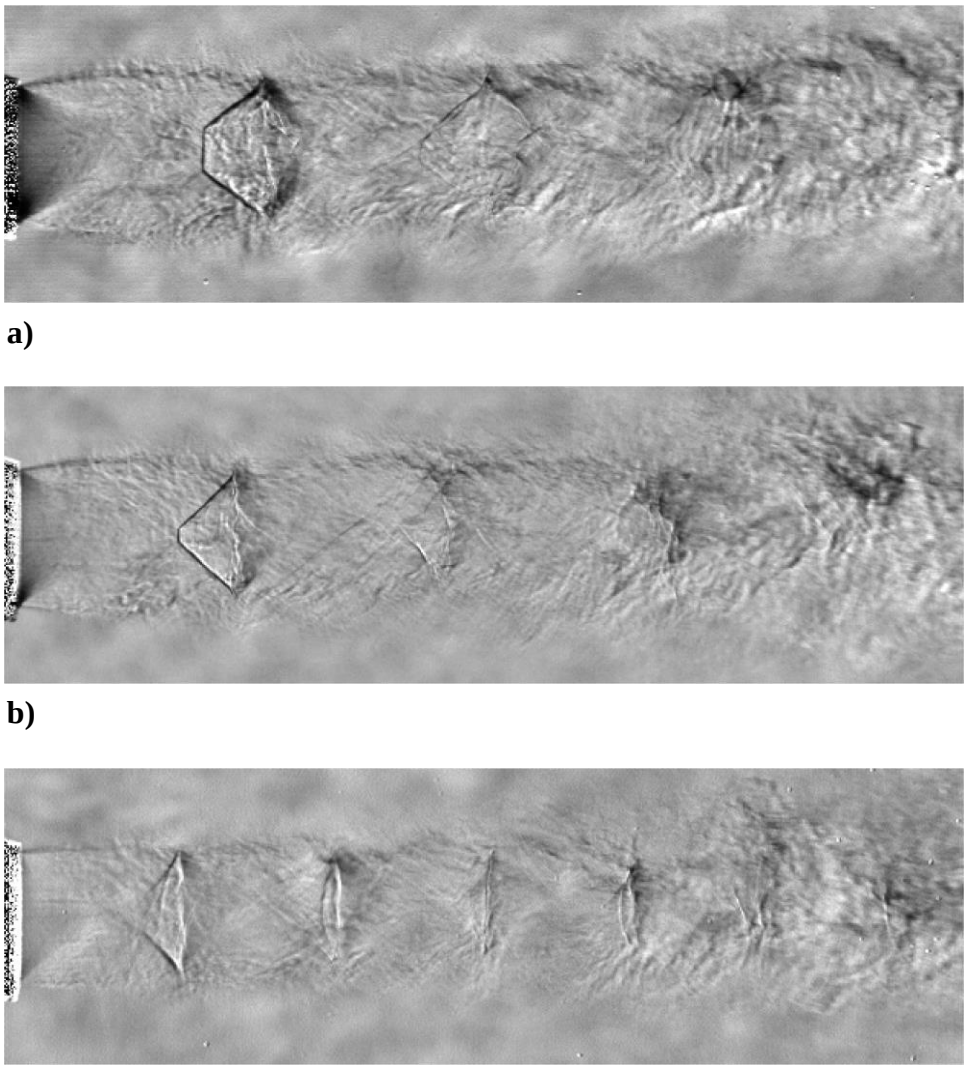

a)

b)

c)

Figure 36. Instantaneous schlieren images for a) NPR = 5.0, b) NPR = 4.0, and c) NPR = 3.0.

High frame-rate data were obtained so as to allow for temporal analysis of the shock wave motion. A data acquisition rate of 50 kHz was found to be sufficient to capture shock motion, but not that of turbulent structures. In an attempt do the latter, images were also obtained at 100 kHz, but these data also failed to capture turbulent structure convection. Instead the 100-kHz data were simply used to confirm the shock-tracking analysis results described below, which were primarily carried out using the 50-kHz data.

The shock-tracking investigation consisted of the application of a Fast-Fourier Transform (FFT) analysis to the fluctuations in shock-wave position, which was estimated to sub-pixel resolution. Three regions of interest, as shown in Figure 37, were selected for analysis for each operating condition; one in the Mach disk and two, approximately symmetrically placed, in the reflected shock waves. Figure 38 describes the procedure used for the shock-tracking investigation. For each image, the pixel intensity was recorded within each region of interest (Figure 38a). The intensity trace was passed through a smoothing filter, and a cubic spline interpolation was applied to obtain resolution down to 0.1 pixels. The position of minimum intensity (dark region) was taken as the shock-wave position (Figure 38b). The interpolated shock position was stored to build a time-history of the axial position of each shock wave for all 10,000+ images (Figure 38c). The shock-position fluctuation was then high-pass filtered using MatLab's *designfilt* function (3^{rd} order IRR filter with 1 kHz passband frequency and 0.2 dB ripple). An FFT was finally applied to each data series in order to identify dominant frequencies using the MatLab *pwelch* function. This function performs FFT analyses on eight equal-length windows from the complete time-history data series. The windows overlap by 50% and a Hanning filter is applied to each window prior to processing. The results from all eight windows are averaged to output a single result as a single-sided power-spectral density (PSD) curve (Figure 38d).

Figure 39 reports the power spectral density curve for each of the three regions of interest for the $NPR = 5.0$ case. A peak can be observed in the plots for the two reflected-shock PSDs, but no peaks are observed in the Mach-disk PSD. This implies that some, currently unidentified, cyclic phenomenon is inducing shock-wave oscillation in the outer portion of the jet plume, but not within the jet core. Both reflected-shock PDSs identified the same frequency peak (7462 Hz), implying that the same phenomenon is active on both sides of the jet. This phenomenon seems to be inducing shock wave oscillation in the outer portion of the jet plume, but was not active in the jet core.

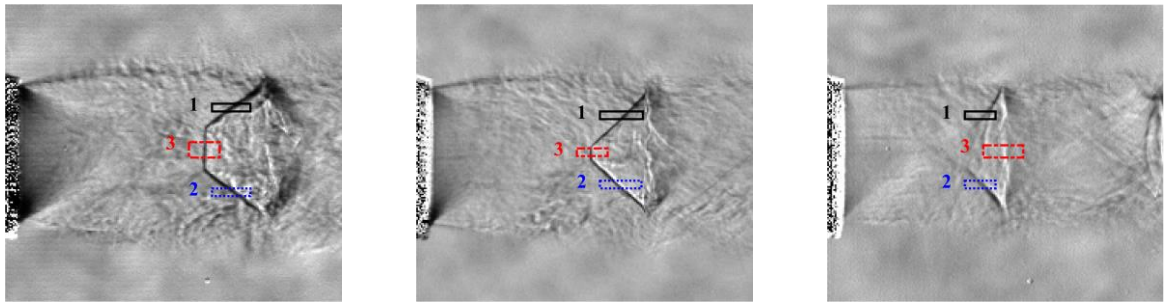

Figure 37. Three regions of interest were used for shock wave position-tracking analysis for a) NPR = 5.0, b) NPR = 4.0, and c) NPR = 3.0.

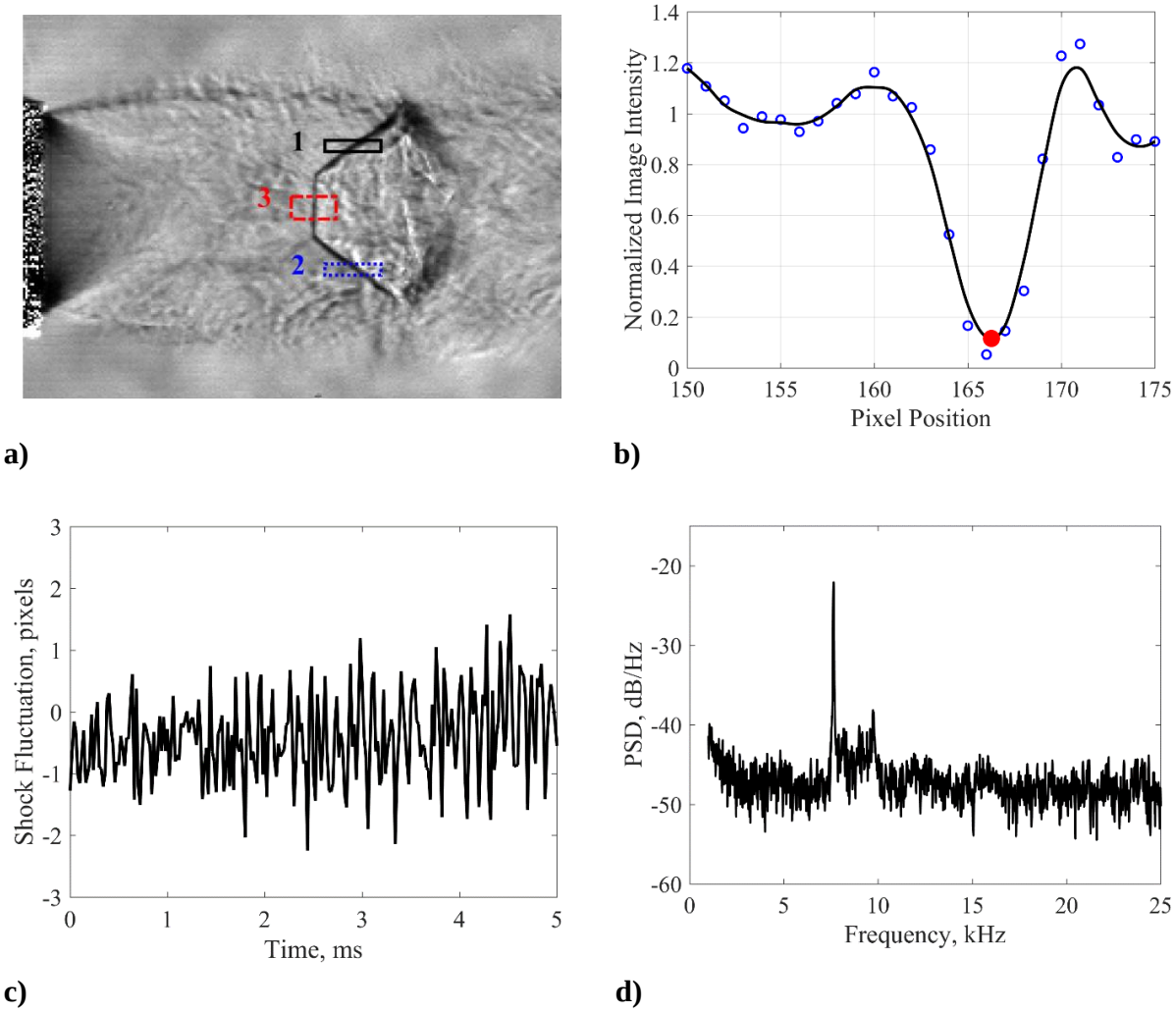

Figure 38. A description of the shock-position tracking analysis procedure.

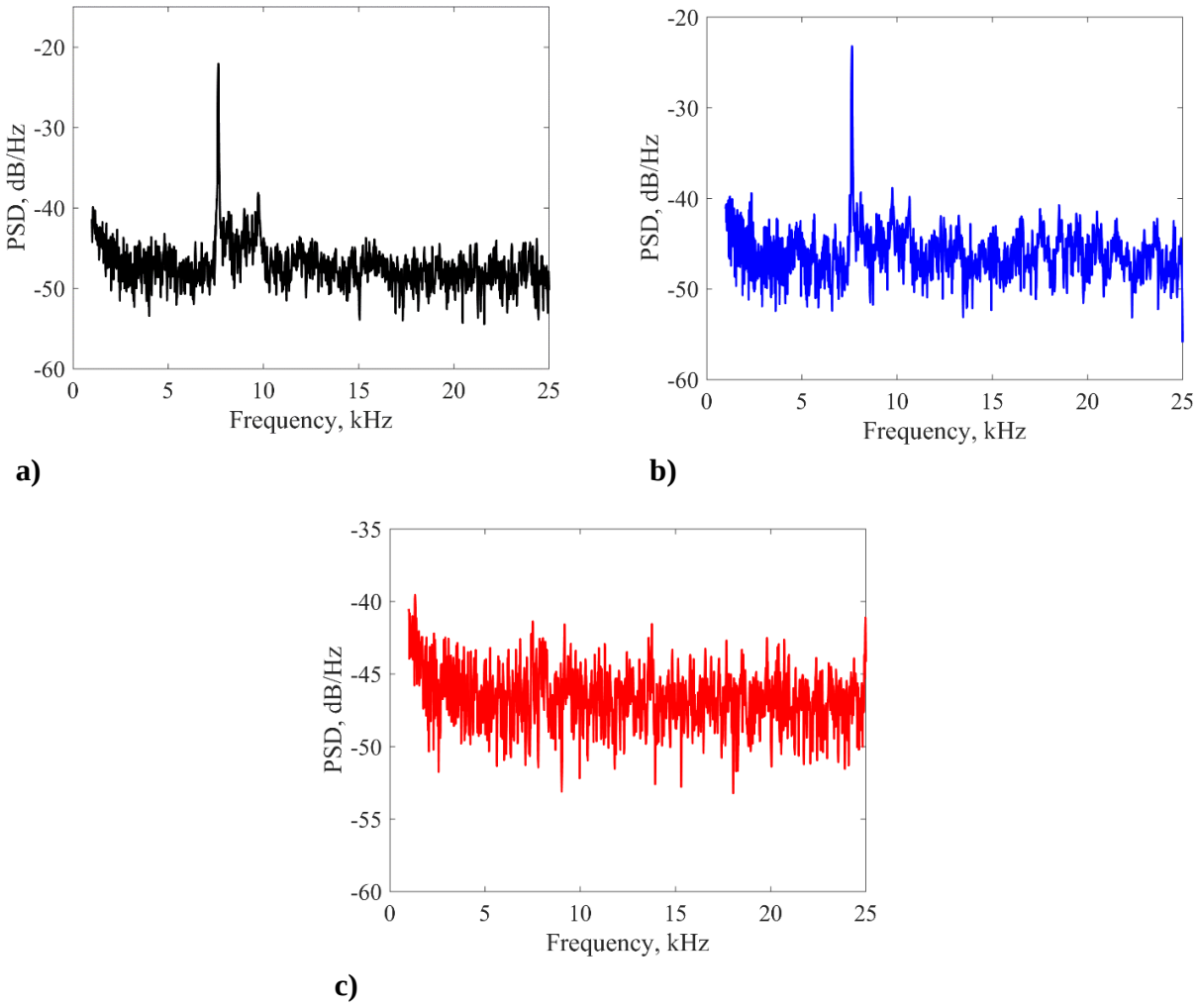

Figure 39. Shock-position tracking power spectral density curves for the NPR = 5.0 isolated jet for the a) upper reflected shock, b) lower reflected shock, and c) Mach disk.

Similar results were observed for the *NPR* = 4.0 and 3.0 cases, although the peaks were located at higher frequencies (8150 Hz and 11730 Hz, respectively). The *NPR* = 4.0 case seems to have a strongly active shock-oscillation cycle, as a harmonic frequency was also observed (Figures 40a and b), and the fundamental peak frequency was also active in the Mach-disk PSD (Figure 40c). The *NPR* = 3.0 PSDs display results similar to those obtained for the *NPR* = 5.0 case (Figure 41). In order to gain more insight into this shock-oscillation phenomenon, acoustic data were obtained for the isolated jet.

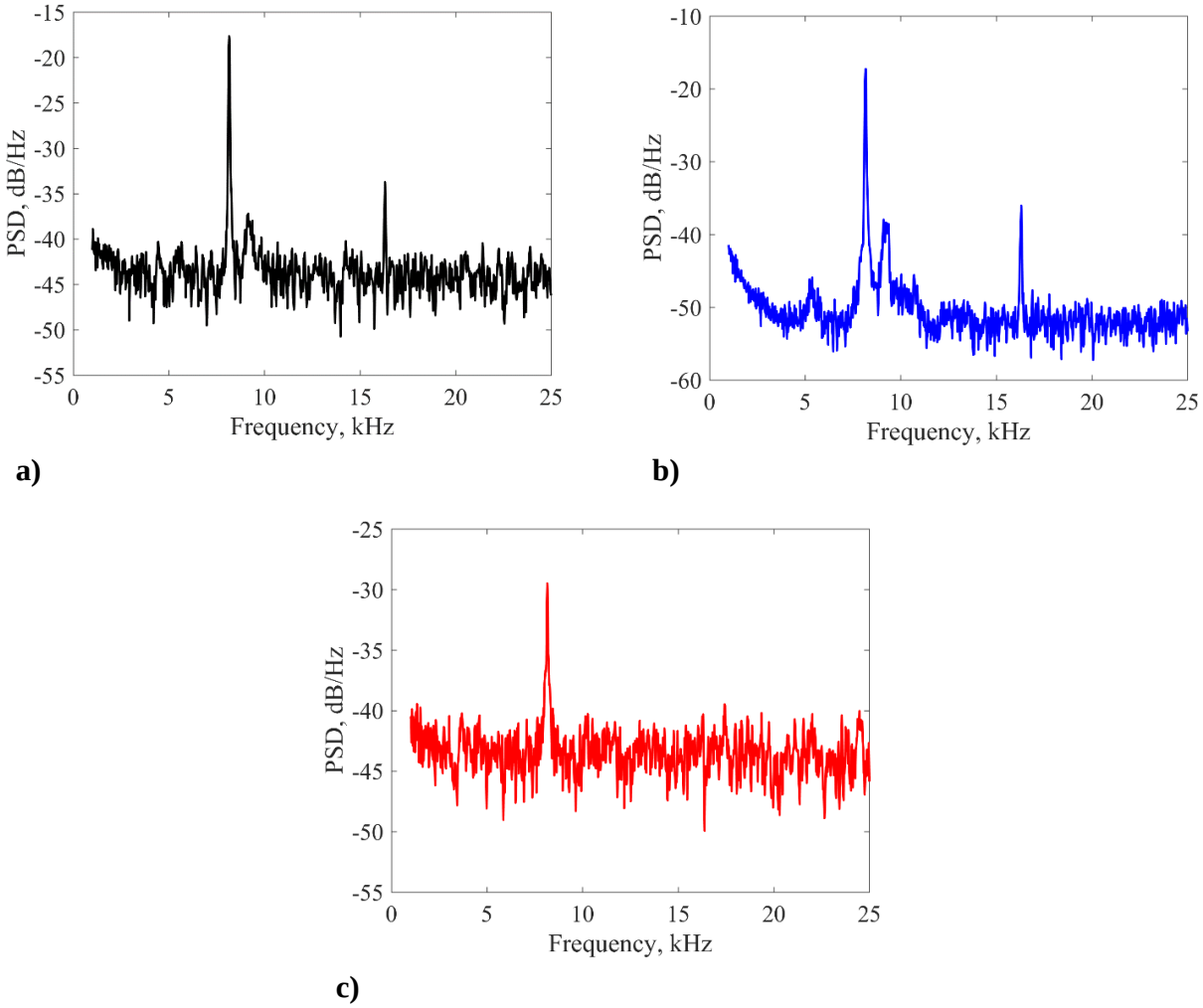

Figure 40. Shock-position tracking power spectral density curves for the NPR = 4.0 isolated jet for the a) upper reflected shock, b) lower reflected shock, and c) Mach disk.

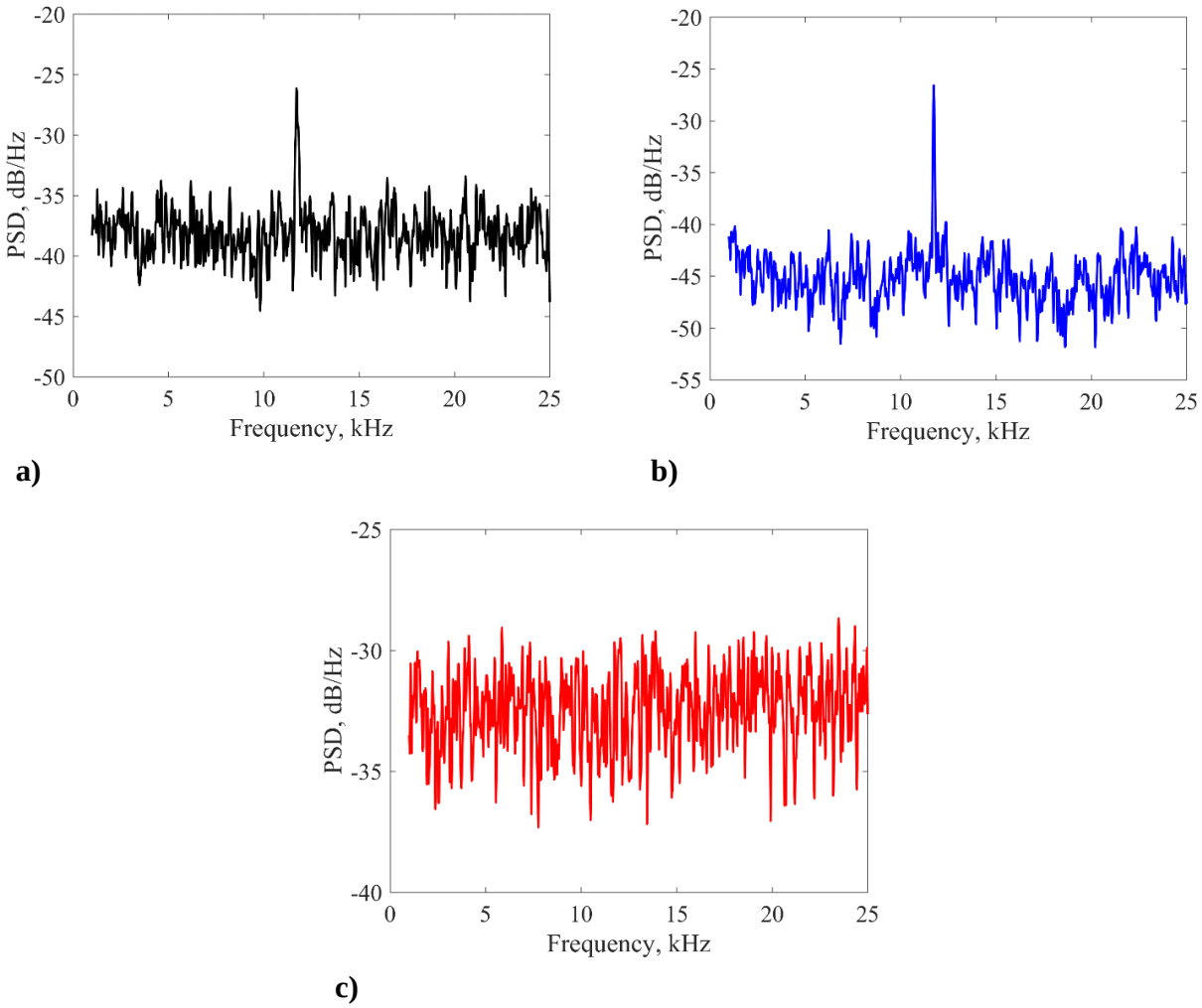

Figure 41. Shock-position tracking power spectral density curves for the NPR = 3.0 isolated jet for the a) upper reflected shock, b) lower reflected shock, and c) Mach disk.

3.2 Acoustics

3.2.1 *NPR* = 5.0 Acoustic Spectra

Far-field acoustic spectra were obtained using microphones placed at five different angular locations, ranging from 30° (downstream propagation) to 110° (upstream propagation) relative to the downstream axis. See Section 2.1 for a description of the experimental setup.

There are three primary sources of noise associated with high-speed jet flows: turbulent mixing, broadband shock noise, and screech.[12] Turbulent mixing noise (self-explanatory mechanism) is generally broadband in nature. Shock noise is generated by the interaction of turbulent structures and shock cells, and its amplitude is therefore influenced by the jet operating

condition (*NPR*), which governs the shock-cell structure of the jet. Screech is a special type of shock noise that is characterized by a self-sustaining instability-driven feedback loop. The screech cycle is described by the formation of instabilities in the jet shear layer, their convection downstream, interaction with shock waves, and subsequent generation of acoustic waves that propagate upstream and ultimately produce the perturbation for the shear layer instability. Screech is characterized by a dominant frequency (and possible harmonics thereof) in the acoustic spectra, and the screech tone is dependent on the jet's dominant instability mechanism (which could be axisymmetric, flapping, helical, etc.). The relative strength of each type of jet noise is strongly dependent on the direction from which measurements are made. Turbulent mixing noise is dominant in the downstream direction, while broadband shock noise and screech are more dominant in the upstream directions.

Figure 42 shows the acoustic spectra obtained for the *NPR* = 5.0 isolated jet for all five microphones. As expected, the 30° spectrum's signal is largely made up of the low-frequency

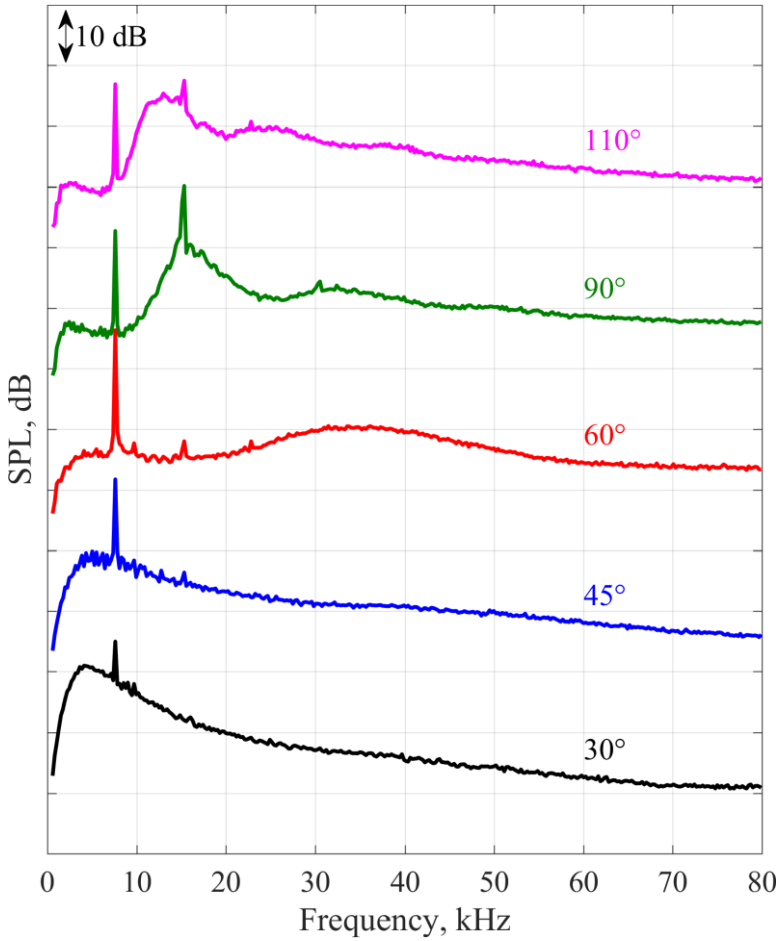

Figure 42. Acoustic spectra for the NPR = 5.0 isolated jet.

turbulent mixing component. The 110° plot shows contributions from three sources: low frequency broadband content attributed to turbulent mixing, higher frequency broadband content due to shock noise, and a very distinct peak that is characteristic of a screech tone. The fundamental screech tone occurs at 7605 Hz. Two harmonic peaks can also be seen. The fundamental screech tone peak is evident in all microphones. This result was unexpected, as screech is known to primarily propagate in the upstream direction. The downstream microphones may have recorded the screech tone due to reflection from the large diameter end face of the jet piping extending into the anechoic chamber.

3.2.2 *NPR* = 4.0 and 3.0 Acoustic Spectra

Acoustic spectra for the *NPR* = 4.0 and 3.0 cases are given in Figure 43. Similar trends were obtained for these operating conditions. The fundamental screech frequency for the *NPR* = 4.0 case was 8073 Hz. The *NPR* = 3.0 case shows several peaks that are too closely spaced to be harmonics. They are located at 9711, 10410, and 12750 Hz. It is believed that only one of these is a natural screech tone. The other tones may be screech-like tones driven by signal reflections of

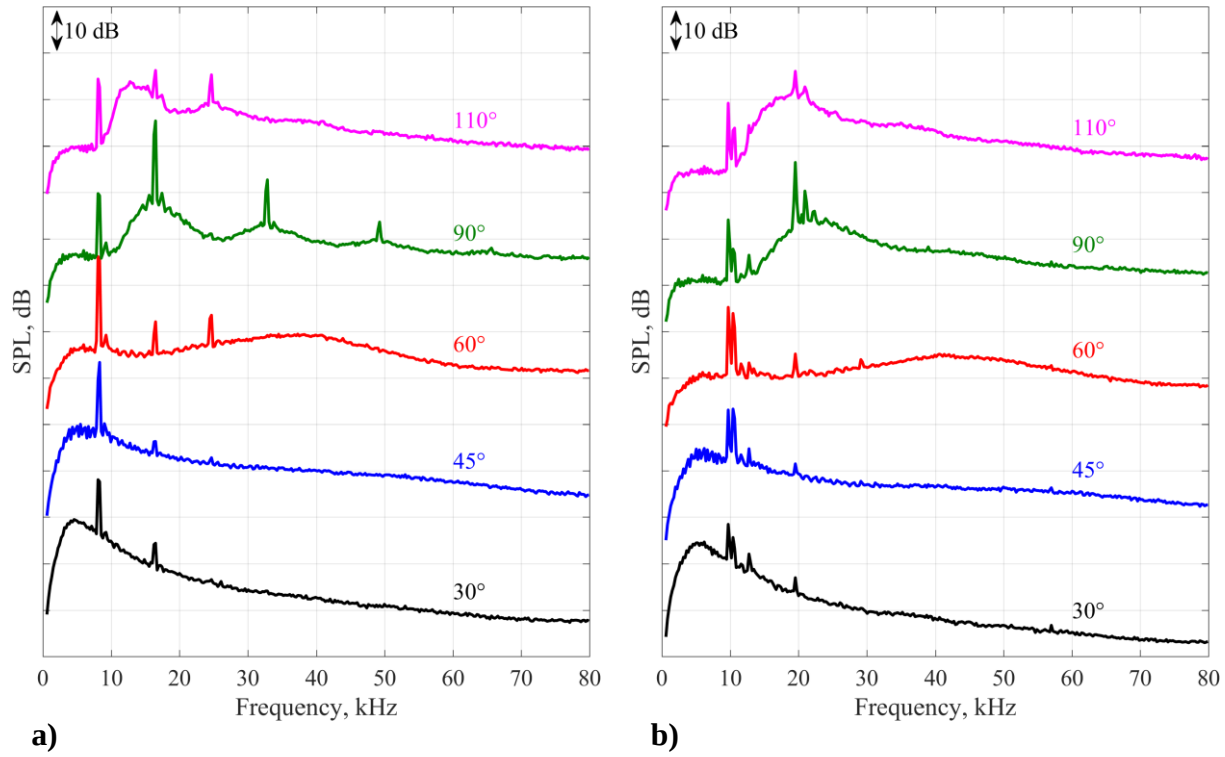

Figure 43. Acoustic spectra for the a) NPR = 4.0 and b) NPR = 3.0 isolated jet.

the natural tone from the end face of the large-diameter piping. Spectra for both *NPR*s show harmonics at higher frequencies (the fourth harmonic can be seen for the *NPR* = 4.0, 90° case).

3.2.3 Shock-Tracking Fundamental Frequency Association with Screech

It was immediately noticed that the dominant frequencies observed in the schlieren shock-position tracking analysis were very near those observed in the acoustic spectra, leading to the possibility that the shock-tracking analysis had identified the screech tone. In order to investigate this further, semi-empirical screech-tone prediction models were used to provide a third perspective. Tam, Seiner, and Yu[131] developed a screech-tone prediction model rooted in the assumption that the strongest acoustic waves generated by shock interactions must be directed upstream towards the nozzle lip, and empirical observations relating the convective and fully-expanded velocities as well as actual shock-cell spacing measurements to predictions from a vortex-sheet shock-cell model. They propose the following model:

$$\frac{f_s D_i}{U_i} \approx \frac{0.67}{\sqrt{M_i^2 - 1}}\left[1 + \frac{0.7 M_i}{\sqrt{1 + \frac{\gamma - 1}{2} M_i^2}}\sqrt{\frac{T_o}{T_\infty}}\right]^{-1} \quad \textbf{(5)}$$

$$\frac{D_i}{D_j} = \left[\frac{1 + \frac{\gamma - 1}{2} M_i^2}{1 + \frac{\gamma - 1}{2} M_d^2}\right]^{\frac{(\gamma+1)}{4(\gamma-1)}} \left(\frac{M_d}{M_i}\right)^{1/2} \quad (6)$$

Here, the screech fundamental frequency is f_s, the fully expanded jet diameter is D_i, the fully expanded Mach number and velocity are M_i and U_i, respectively, the jet total temperature is given by T_0, and the ambient temperature is T_∞. The fully expanded jet diameter is related to the nozzle exit diameter, D_j, by a conservation of mass relation as shown in Equation 6, where the subscript *d* indicates design conditions.

The model developed by Tam, Seiner, and Yu is valid for a wide range of Mach numbers. Massey and Ahuja[132] developed an alternative screech prediction model that accounted for the differences induced by the active jet instability mode (axisymmetric for $1 \leq M_i \leq 1.35$ and helical for $1.2 \leq M_i \leq 1.8$). Their helical-mode model (relevant for M_i values in this study) is given in Equation 7.

$$\frac{f_s D_i}{U_i} \approx \frac{0.615}{1.1\sqrt[3]{M_i^2 - 1}}\left[1 + \frac{0.615 M_i}{\sqrt{1 + \frac{\gamma - 1}{2} M_i^2}}\sqrt{\frac{T_0}{T_\infty}}\right]^{-1} \quad (7)$$

The dominant frequencies obtained from the shock-position tracking analysis, the acoustic spectra, and both screech-tone prediction models are given in Table 11. Also included are the percent differences from the shock-tracking frequency measurements. The agreement, particularly for the *NPR* = 5.0 case is extremely good. For that *NPR*, the highest percentage difference was only 3.7%, and that was for the prediction model that failed to account for any variation in the jet-plume instability modes. Agreement for the *NPR* = 4.0 case was also very good, although with slightly larger percent differences. The level of agreement decreased for the *NPR* = 3.0 case, but the acoustic spectra obtained there contained more than one peak frequency and M_i for this case approaches an instability mode-transition regime (axisymmetric to helical).

Since these three sources of data all align very well with each other, it can be concluded that the isolated jet undergoes an oscillatory cycle characterized by a positional oscillation of the shock waves located on the outside of the jet plume (specifically, the reflected shocks). That oscillatory cycle is related to jet screech as shown by the acoustic spectra and the screech-tone prediction models. It remains unclear whether the shock-position oscillation induces screech, if the screech cycle induces shock-motion, or if they are both a result of yet a third phenomenon.

Table 11. Comparison of various measurements of the isolated jet screech tones.

NPR	M_i	Shock Position PSD Freq. (Hz)	Acoustic Spectra Screech Tones		Screech-Tone Prediction Models			
					Tam, Seiner, & Yu		Massey & Ahuja, Helical mode	
			Freq. (Hz)	% Diff.	Freq. (Hz)	% Diff.	Freq. (Hz)	% Diff.
3.0	1.358	11743	9711 10410 12750	20.9 12.8 -7.9	12215	3.9	10472	-12.1
4.0	1.559	8148	8073	0.93	9364	13.0	8809	7.5
5.0	1.709	7642	7605	0.49	7934	3.7	7861	2.8

3.3 Planar PIV

In general, the isolated jet flowfield agrees with expectations and is very symmetric. Mean velocity and turbulent statistics are presented first, followed thereafter by a sampling of the

instantaneous results. Emphasis is given to the *NPR* = 5.0 case, but a summary of the results obtained for the other nozzle pressure ratios is also given. All reported planar PIV mean velocities and turbulent statistics are based on at least 1000 images. Refer to Section 2.6.2 for details regarding the experimental setup and image processing.

3.3.1 *NPR* = 5.0

The mean velocity and Mach number results for the isolated jet planar PIV are presented first. Data are presented from $0.1 \leq x/D_j \leq 10$ with a radial/spanwise extent sufficiently wide to view the entire jet structure ($z/D_j \leq \pm 1.25$). The velocity field is dominated by the mean streamwise component, $\bar{U}$, as shown in Figure 44a. The flow accelerates throughout the first shock cell. The maximum observed $\bar{U}$ is ~575 m/s and occurs along the jet centerline, just prior to the Mach disk. The Mach disk and two reflected shocks can be easily discerned, and the flow decelerates upon passage through the shock waves. The typical isolated jet shock-cell structure can be clearly seen. Subsequent shock cells grow progressively weaker. The shear layer, initially very thin at the nozzle exit, thickens with increasing x/D_j. Viscous effects in the jet, coupled with the decreasing magnitude of the under- and over-expansions, lead to the merging of high-speed zones on either side of the low-speed central core flow (shock cells two and three) into a single, centrally positioned, high-to-low speed variation (shock cells five and six).

Inspection of the mean *w* velocity component, $\bar{W}$, shown in Figure 44b, shows the strong outward radial velocity component within the first shock cell. Within the first shock cell, the radial velocity component is observed to initially increase as it passes through the nozzle-lip expansion fan, but then decreases in magnitude afterward; presumably, reflected compression waves then begin to reduce the $\bar{W}$ component. A sign reversal occurs within the last third of the first shock cell, coinciding with the change in curvature of the outer shear layer – again due to the presence of the reflected compression waves. A thin region of non-zero $\bar{W}$ can also be seen at the edge of the first shock-cell shear layer, extending to the same point. $\bar{W}$ is very symmetric in magnitude throughout the jet flowfield. The maximum observed $\bar{W}$ is ~ ±110 m/s. Since the Mach disk is a vertically-oriented normal shock, there is no evidence of its presence in the $\bar{W}$ results. However, the location of the reflected shocks, which do incur a change in $\bar{W}$, is very clear.

Throughout the remainder of the flowfield, $\bar{W}$ is observed to smoothly transition from one sign to the other, depending on the relative location within the shock cells. The lone exception is at the transition from the second to third shock cells (x/D_j ~ 3.25) where there appears to be a weak

shock wave. Along the jet axis, the flow is nearly entirely axial throughout the imaged region, where $\bar{W}$ is negligible. The jet's tendency towards flow entrainment is shown by the mild inward radial velocity component observed in the ambient air on either side of the jet.

The mean Mach number, calculated using the velocity magnitude and the adiabatic energy equation, is presented in Figure 44c. Streamlines, overlaid on the figure, show the outward-radial velocity component within the first shock cell, the purely streamwise component along the jet axis, and the flow's entrainment field. As expected, the jet over-accelerates in the first shock cell as the expansion fans from the other side of the jet reflect through to the opposite side. The maximum observed Mach number, located along the jet axis just prior to the Mach disk, is ~2.48. As with the $\bar{U}$ figure, the Mach disk and reflected shocks are prominently featured. The normal-shock relations predict a post-shock Mach number of 0.51; the actual data agree with that prediction very well. The Mach number plot also shows that the first two shock cells each contain a region of subsonic flow. The second shock cell is not strong enough to generate another Mach disk, but as the $\bar{W}$ figure indicated (and the Mach number plot agrees), there could be two oblique shocks at the beginning of the second shock cell. Within the jet plume, the remainder of the measurement domain is supersonic.

The PIV results were further validated and inspected in the reflected shock region using the oblique shock relations. Several locations were selected at positions upstream of the reflected shock wave and the local Mach number and flow angle were calculated at these pre-shock positions. After measuring the angle between the incoming flow and the reflected shock wave, the oblique shock relations could be used to predict the theoretical turning angle of the flow on the opposite side of the shock wave. In addition, the pre- and post-shock Mach numbers as well as the normal and tangential components thereof, could also be compared between the PIV results and the theoretical expectations.

In order to ensure that appropriate positions were taken for comparison across the reflected shock, streamlines passing through each pre-shock position were calculated, as shown in Figure 45. Then, the post-shock quantities, (M_2, the normal component of Mach number, M_{2n}, and the turning angle, δ) were tabulated at post-shock positions along the streamline. The specific point for comparison was selected as the one that best matched the observed and theoretical M_{2n}. Then, M_2 and δ were also compared. Results for one comparison are shown in Figure 45.

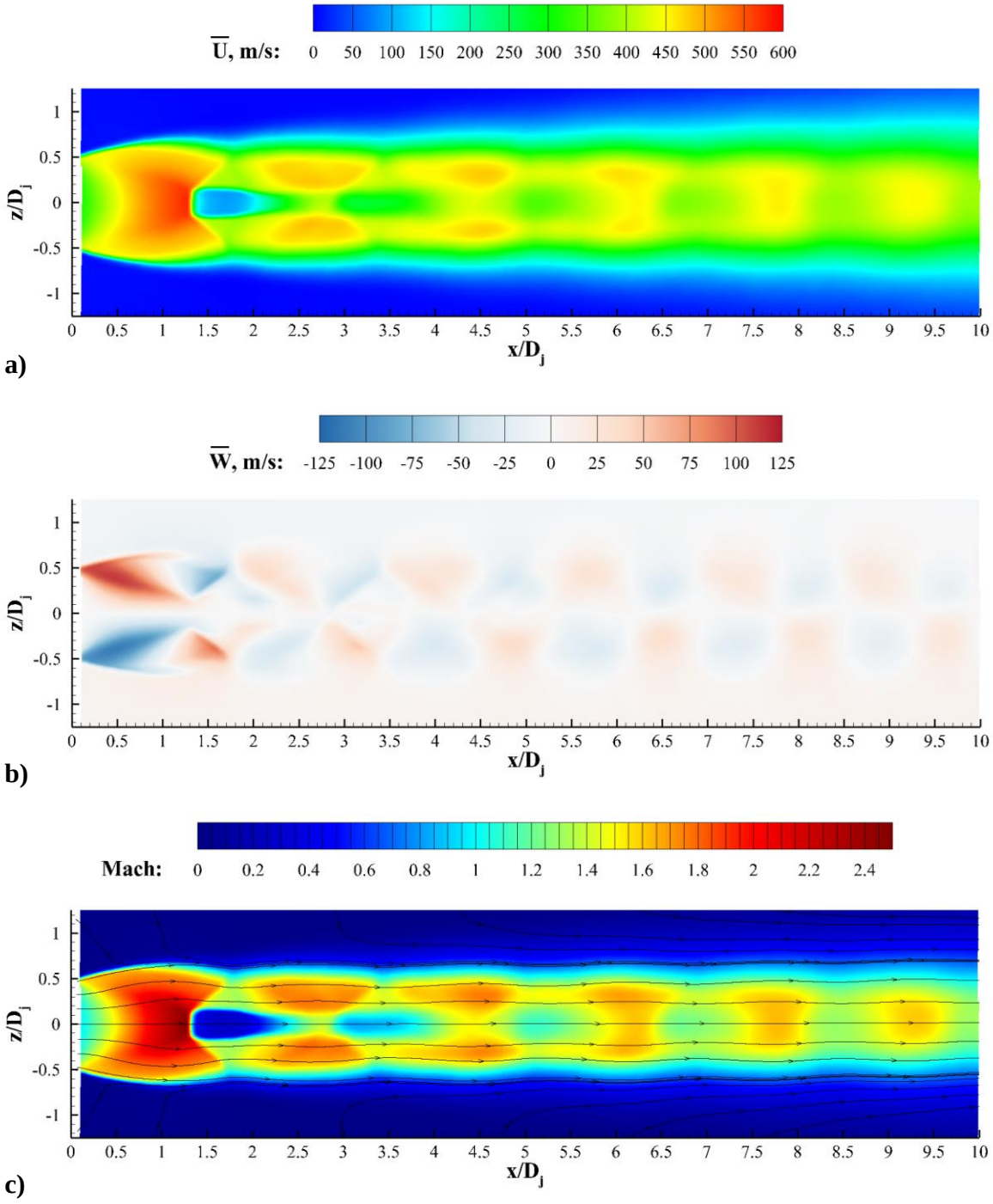

Figure 44. Mean PIV results for the NPR = 5.0 isolated jet showing a) streamwise velocity component, b) radial velocity component, and c) Mach number color contours with overlaid streamlines.

The comparison between the theoretical and actual results is shown in Table 12 for the position under consideration. The post-shock Mach numbers, M and M_{2n}, compare very well with the expected results. The turning angle, δ, differs from the expected angle by approximately 3 degrees. Although the agreement is not perfect, this exercise clearly shows that the PIV flowfield data are consistent with the oblique shock relations. As positions nearer to the jet axis are inspected, the deviations in the comparison metrics grow slightly larger.

Table 12. Change in flow conditions across reflected shock: PIV vs. expectations.

	Pre-shock	**Post-shock**	
	PIV	**PIV**	**Expected**
Local Flow Inclination, deg	-8.96	-5.05	-
M	1.69	1.35	1.36
M_n	1.16	0.86	0.87
***δ*, deg**	-	3.92	6.86

Several possible explanations for the deviations exist. First, the flow under consideration is not uniform on either side of the reflected shock; the shock-cell nature of the flow means that the flow is continually experiencing expansions or compressions of locally varying and unknown strength, and the specific effects of these are difficult to predict exactly on the flow. Second, this flow is highly three-dimensional, allowing unknown out-of-plane components and/or three-

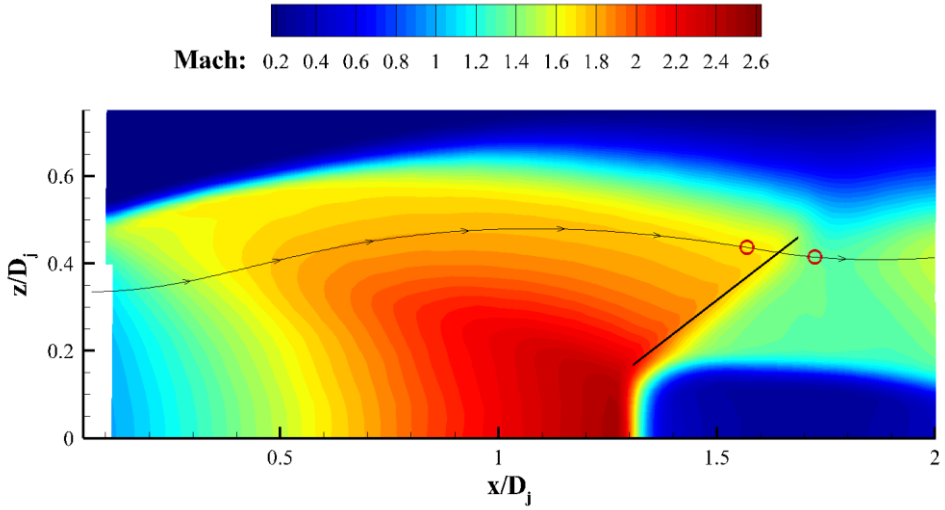

Figure 45. The change in conditions across the oblique reflected shock is calculated between two locations (red circles) along a streamline.

dimensional relief effects to influence the flow. A third possibility is that the line-integration effect of the schlieren imagery caused inaccuracies in the shock angle measurement, leading to subsequent inaccuracies.

The mean Reynolds shear stress, $\overline{u'w'}$, is presented in Figure 46a. Turbulence is concentrated within the shear layer. The strongest turbulence is found within the jet shear layer local to the first shock cell, where it is still quite thin. The mean Reynolds shear stresses are found to be nearly symmetric in magnitude with maximum values of ~ ±3700 m^2/s^2. Less strong turbulence can also be found within the slip-line shear layers generated by the Mach disk within the core of the jet. The fact that the slip-line shear layer turbulence was captured in these data point to the high data quality, uniform seeding density, and accurate PIV-processing correlations.

The streamwise and radial-direction normal Reynolds stresses are shown in Figures 46b and c, respectively. The $\overline{u'u'}$ figure better highlights the location of the slip lines within the core of the jet plume. Regions of mildly increased $\overline{u'u'}$ are found within each of the shock cells, due to the alternating acceleration and deceleration. The $\overline{w'w'}$ figure also allows for the visualizations of both the primary and slip-line shear layers. A pattern of angled lines of increased $\overline{w'w'}$ within the plume highlights the boundaries of the shock cells, likely due to plume (and, for thin lines, shock wave) unsteadiness. The fact that the presented data were obtained by merging two fields of view is most evident in the $\overline{w'w'}$ figure, where two vertical bands outlining the overlapping region are present at approximately x/D_j = 4.75 and 5.4.

A sample instantaneous velocity magnitude snapshot is shown in Figure 47 for $x/D_j \leq 5.0$ and Figure 48 for $x/D_j \geq 5$. Vectors (every 8th streamwise and every 3rd radial) are overlaid on the figures. The shear layer displays evidence of instability waves and vortex rollup within the first shock cell (notice especially the negative-*z* shear layer). The shear layer appears to thicken rapidly beyond the widest part of the first shock cell. The turbulent nature of the plume's primary shear layer is apparent, as is that of the interior slip-line shear layers. The high-speed flow regions, both in the first shock cell and within subsequent shock cells, contain relatively uniform and smoothly turning flow. As x/D_j increases (see Figure 48), the shear layer thickens, the edges of the high and low-speed regions become less well-defined, and speed uniformity within these regions also decreases. All of these features are characteristic of the more turbulent nature of the downstream region.

Note several very small low-speed regions (dark blue, usually within shear layers) in the figures. These are missing vectors that were removed during PIV vector post-processing and usually represent no more than 2-3 contiguous vectors. The vector post-processing filter used for these data is considered very aggressive; the low count of missing vectors speaks to the quality of the flow seeding, imaging system, processing steps employed, and overall data quality. These small gaps in the vector fields could easily be filled via interpolation, but are shown as-is here to provide visual confirmation of the data quality. Missing vectors were not counted towards mean or statistical quantities.

Also notice that there is no evidence of vector field stitching (the boundaries of the overlapping region are $x/D_j \approx 4.8$ and 5.4) in the instantaneous flowfield images.

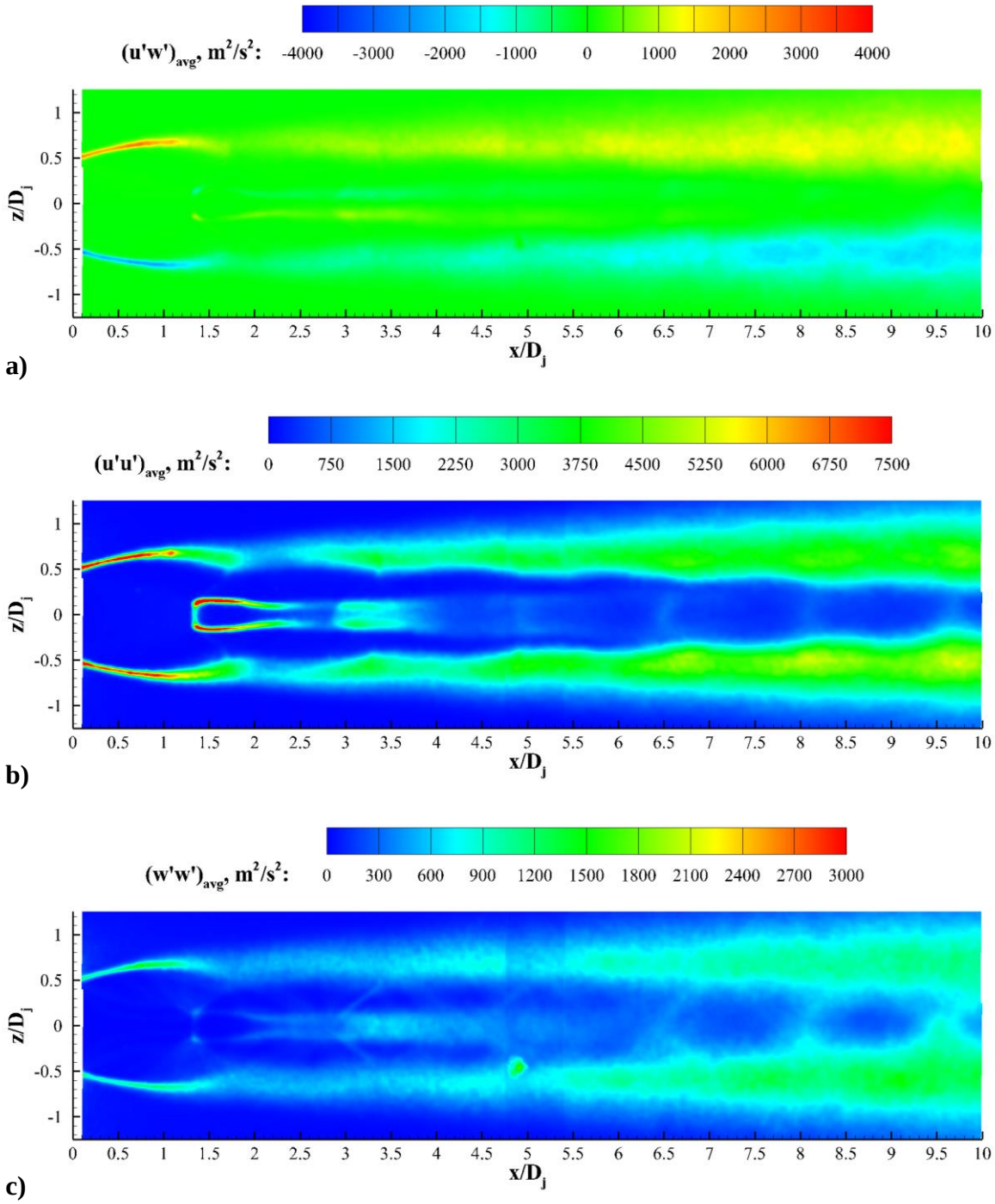

Figure 46. Mean turbulence quantities for the isolated jet (NPR = 5.0) showing a) Reynolds shear stress, b) streamwise Reynolds normal stress, and c) radial Reynolds normal stress.

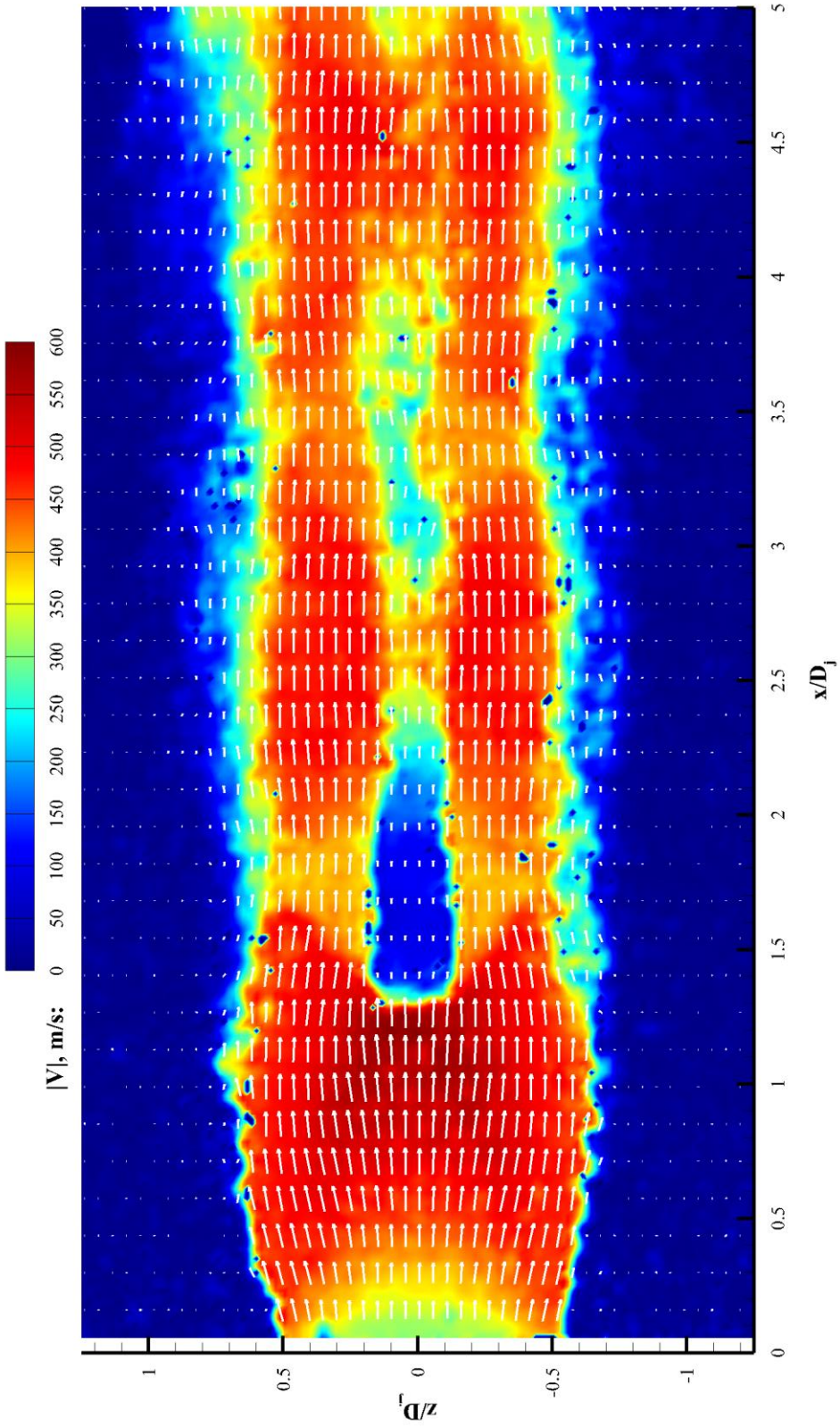

Figure 47. A sample instantaneous velocity magnitude image of the upstream region ($x/D_j \leq 5$) with overlaid vectors.

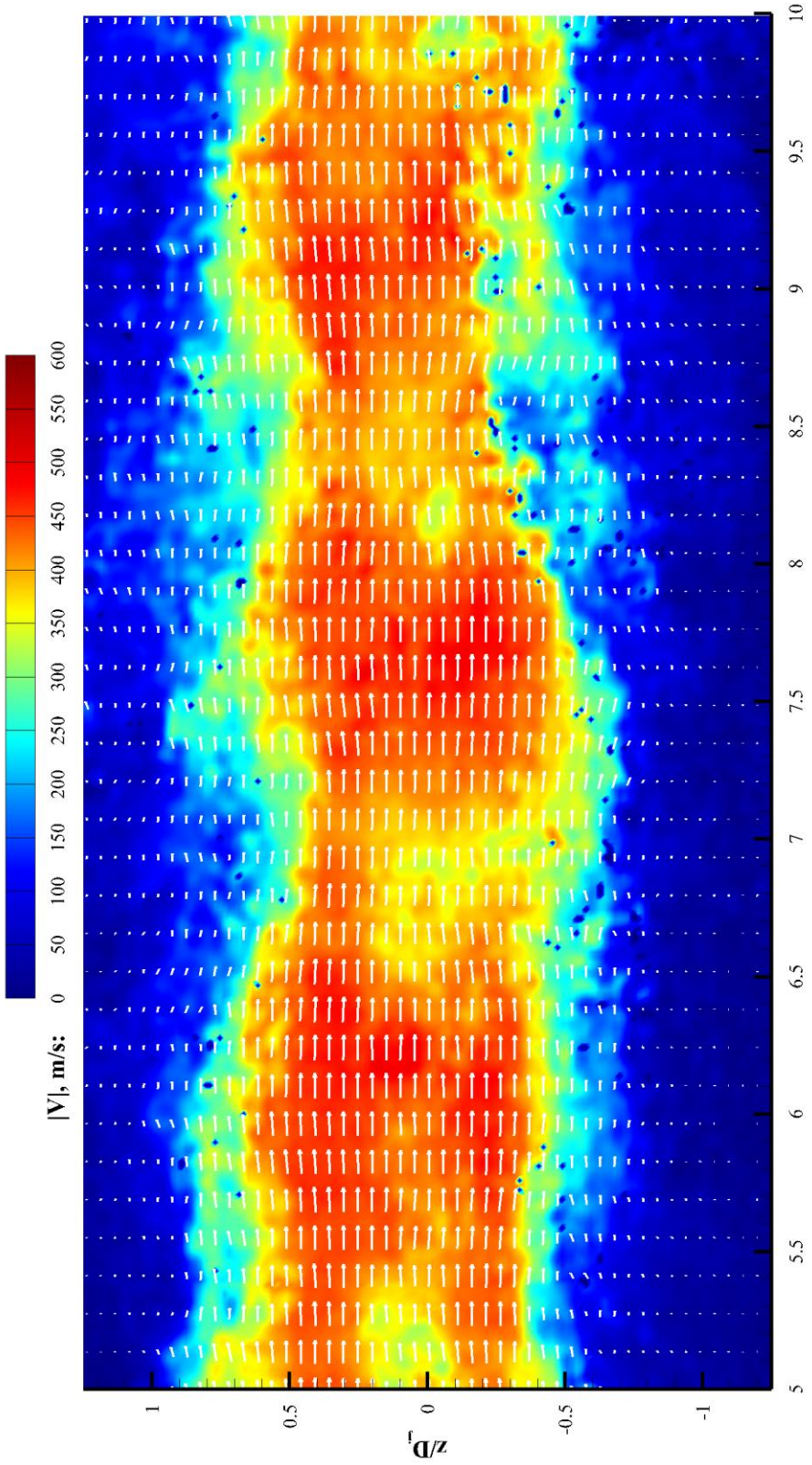

Figure 48. A sample instantaneous velocity magnitude image of the downstream region ($x/D_j \geq 5$) with overlaid vectors.

3.3.2 *NPR*= 4.0

The mean velocity magnitude for the *NPR* = 4.0 case is shown in Figure 49. Again, the flowfield shows a high degree of symmetry both in terms of shape and magnitude. The maximum observed mean velocity magnitude for the *NPR* = 4.0 case is ~530 m/s. In comparison to the *NPR* = 5.0 case, the decreased shock-cell length is readily apparent. The mean PIV flowfield is dominated by two oblique shocks that appear to intersect near the jet axis. The mean flowfield shows no subsonic-flow region(s) within the core of the jet plume, indicating that there is no Mach disk formation. Without the dual supersonic/subsonic flow streams within the jet plume, the velocity variation from one shock cell to the next is much smoother and uniform across the width of the jet. Six shock cells are readily apparent. Thereafter, viscous effects become strong enough to blend the shock cells. The maximum observed Mach number is ~2.1, while the ideally expanded Mach number for this operating condition is 1.56. The mean radial velocity component displays most of the same features found in the *NPR* = 5.0 case, but at reduced magnitudes; the maximum $\bar{W}$ magnitude for the *NPR* = 4.0 case is approximately ±72 m/s.

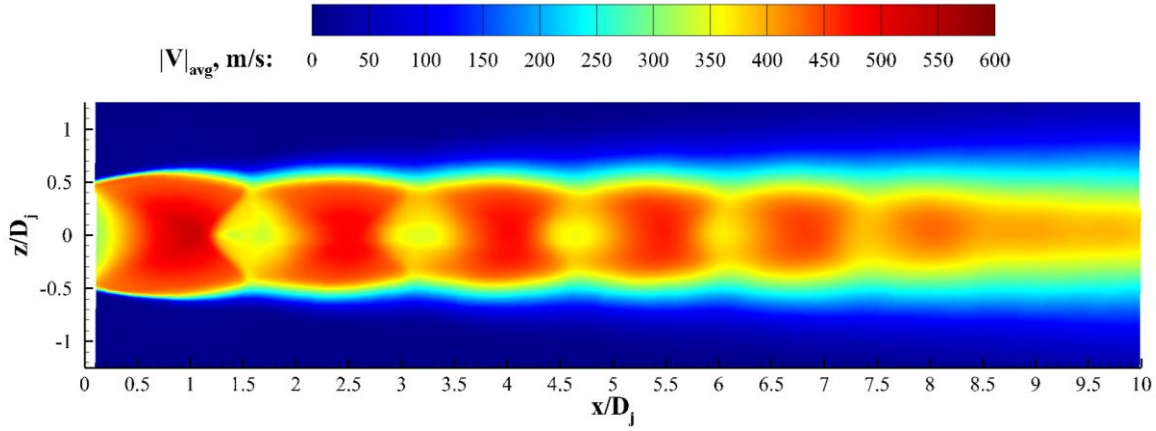

Figure 49. Mean velocity magnitude for the NPR = 4.0 isolated jet.

The mean turbulence quantities have the same general characteristics as the *NPR* = 5.0 case, but with two differences to note. As before, turbulence is concentrated within the shear layer, which is initially thin and thickens with x/D_j. The *NPR* = 4.0 case, however, contains higher amplitudes for all three turbulence quantities within the jet plume shear layers for $x/D_j \geq 6.25$, as compared to the *NPR* = 5.0 case. Second, since there is no mean subsonic core flow region, there are no strong interior slip-line shear layers, and the turbulence quantities are therefore remarkably

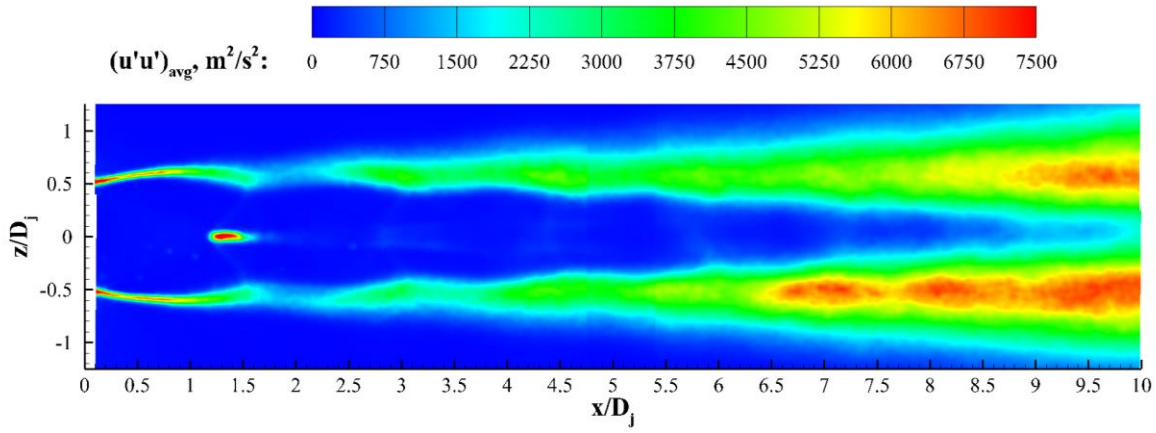

Figure 50. Mean streamwise Reynolds normal stress for the NPR = 4.0 isolated jet.

uniform within the core jet plume. One exception is $\overline{u'u'}$, (shown in Figure 50), which has a small high-intensity region directly downstream of the oblique shock wave intersection point. The increased "turbulence" at this location is believed to be primarily a result of compressible wave-structure unsteadiness. Although a Mach disk (and corresponding subsonic region after it) does not exist in the mean, it may present itself instantaneously. This would induce a locally high standard deviation from the mean, and thereby large perceived fluctuations and high "turbulence" levels. The source of the increased turbulence within the primary jet shear layer is uncertain. One possibility is that the shock-cell structure at this operating condition generates a more slug-flow like core flow, which forces all of the turbulent mixing to occur in the primary shear layer and very little to occur within the core. Such a redistribution may account for the increased shear layer turbulence seen for this case.

Note that the schlieren imagery for this operating condition (see Figure 35a), indicates that there is a small diameter Mach disk at these conditions. Close inspection of instantaneous snapshots from the schlieren imagery shows that the overall flowfield wave-structure is maintained within the dataset during the course of data acquisition. The exact reasoning for the difference in flow structure is unclear, as these data were obtained at the same operating condition using the same facility and nozzle.

It is possible that this *NPR* happens to occur near a transition point in the overall flowfield structure and that that makes it difficult to exactly replicate the same flowfield structure. Recall that the shock-tracking analysis unexpectedly identified a dominant frequency within the Mach disk (Figure 40c). Such a peak was *only* found for the *NPR* = 4.0 case, perhaps indicating that the

NPR = 4.0 operating condition is uniquely inconsistent or phenotypically unstable. The apparent shock wave unsteadiness seen in the PIV data hints that the jet is operating near a transitional state as well, as might the increased shear layer turbulence.

3.3.3 NPR = 3.0

The *NPR* = 3.0 data agree well with the schlieren imagery and display many of the same characteristics seen in the higher *NPR* operating conditions. The mean velocity magnitude (Figure 51) is symmetric and nine shock cells can be identified. The shock cell length and spacing is decreased as compared to the *NPR* = 5.0 and 4.0 cases. By x/D_j = 10, the primary plume shear layer has expanded to reach the center of the jet plume and the velocity profile through the jet width takes on a symmetric single-peak shape. The ideally expanded Mach number is 1.36, while

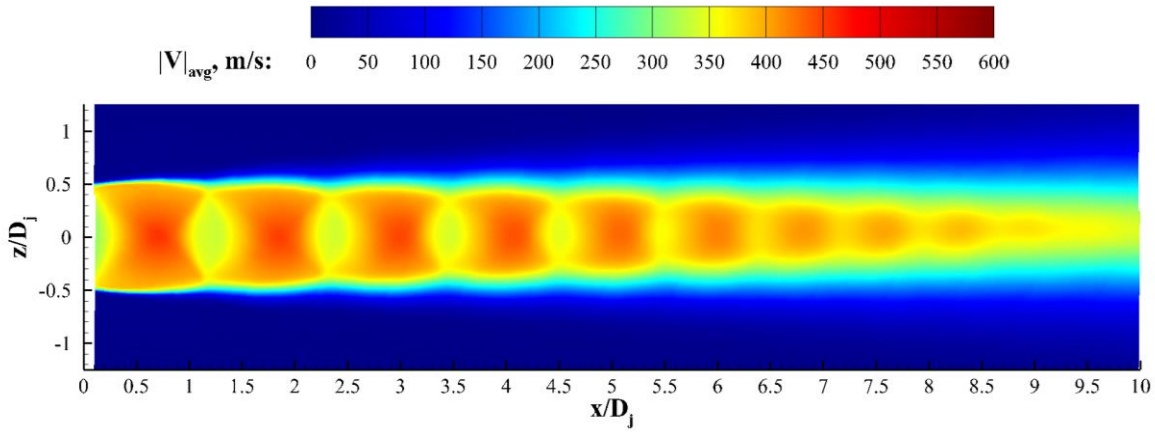

Figure 51. Mean velocity magnitude for the NPR = 3.0 isolated jet.

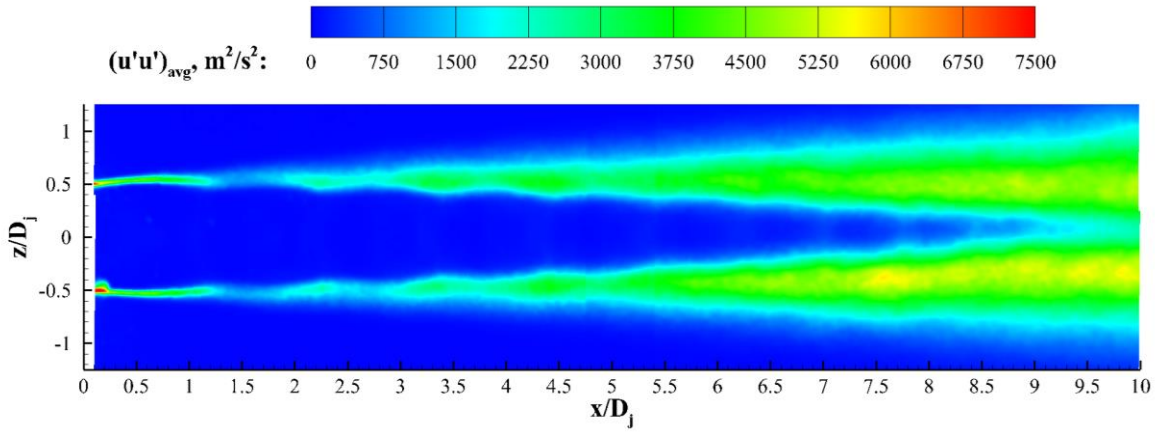

Figure 52. Mean streamwise Reynolds normal stress for the NPR = 3.0 isolated jet.

the maximum observed Mach number is approximately 1.63. The decreased degree of underexpansion is clear based on the minimal plume expansion upon exiting the nozzle. The maximum observed mean velocity magnitude is 456.5 m/s. $\overline{W}$ is approximately symmetric with a range of ~ ±48 m/s.

The turbulence quantities are reduced in magnitude. Figure 52 displays $\overline{u'u'}$ for the $NPR = 3.0$ isolated jet. As before, the maximum turbulence is found within the shear layer, and very little turbulence is found within the core of the jet. Profiles taken through the width of the jet at $x/D_j = 10$ are bimodal in nature, with approximately symmetric peaks on either side of $z/D_j = 0$, indicating that the primary jet shear layers have met, but are not yet fully merged.

3.4 Tomographic PIV

Three-component, volumetric velocity data were obtained using tomographic PIV for the isolated jet. These data provide a very realistic sense of the overall, three-dimensional structure of the flow, particularly, when the mean velocity components are considered. Mean velocity data, obtained from subsets of 250 snapshots, are presented first. Turbulence quantities, such as the Reynolds stresses, typically have not converged for such small sample sizes, so these quantities are not offered here using the volumetric data. Instead, refer to the planar PIV data (Section 3.3), for turbulence statistical quantities. One of the most attractive attributes of three-component, volumetric data, such as that obtained via tomographic PIV, is the ability to examine the instantaneous structure of the flow in terms of velocities and vorticity, and in terms of coherent structures (i.e., vortices) within the flow. To this end, instantaneous isolated jet tomographic PIV data are presented next. These volumetric data are presented using multiple planar slices, and, more powerfully, with isosurfaces. Isosurfaces are three-dimensional surfaces of some constant parameter, such as velocity or Q-criterion.

Tomographic PIV data are presented for all three tested operating conditions ($NPR = 5.0$, 4.0, and 3.0). Refer to Section 2.6.4 for a description of the experimental setup. The reader is reminded that data were obtained for half of the jet flowfield in the tomographic PIV experiments and that data were obtained beginning approximately 5 mm ($x/D_j \geq 0.39$) downstream of the nozzle exit plane. Assuming a symmetric flow, the experimental domain could be mirrored to see the entire jet. However, for purposes of visualization, showing only the true data domain is preferable, as it allows for insight into the interior of the volume.

For consistency, all tomographic PIV data (isolated jet as well as jet-and-surface configurations) are presented using the same viewpoint. Refer to Section 2.3 for a reminder of the coordinate system. Data are presented for the lower half of the jet, and the presented view is isometric, *as if viewing the jet from above and behind (i.e., through) the rigid or compliant surface*. From this perspective, the nozzle is located at the bottom right in the images, and the streamwise flow direction is upward and to the left. The *z*-axis is positive away and to the right, which allows for the placement of the test (rigid or compliant) surfaces at constant *z*-planes at *z* = -0.5, -0.55, or -0.60. Since the only the lower half of the jet was imaged, only the negative *y*-axis is shown. The viewpoint is not very important for the isolated jet case, as the flow is symmetric. However, knowledge and understanding of the viewpoint for the jet-and-surface configuration is critical due to the strong influence that the surface has on the overall flowfield.

3.4.1 *NPR* = 5.0

The shock-cell structure of an isolated jet is well understood, and the previously presented planar PIV data clearly show the alternating velocities in the streamwise direction and the radial expansion and compression of the jet. Using isosurfaces of constant mean streamwise velocity, $\bar{U}$, the three-dimensional structure can also be visualized and investigated.

Figure 53 displays increasing numbers of constant $\bar{U}$ isosurfaces, beginning with a single, high-velocity, isosurface, and progressively adding additional surfaces of lower constant $\bar{U}$. In Figure 53 a), a single $\bar{U}$ = 525 m/s, isosurface is shown; within the isosurface, $\bar{U}$ exceeds 525 m/s. This high-speed bubble is located within the first shock-cell expansion region. An additional, $\bar{U}$ = 500 m/s contour is shown in Figure 53 b), showing three distinct surfaces, one within each of the first three shock cells. Each isosurface is clearly seen to have an annular shape, hinting at the low-speed regions near the jet core between the high-speed regions. The $\bar{U}$ = 450 m/s isosurface, shown in Figure 53 c), begins to bridge the separate shock-cells, and also confirms that there are at least two low-speed regions within the core of the jet. As isosurfaces are added in Figures 53 d) – h), the jet primary shear layer and the low-speed jet-interior regions become more and more defined.

Figure 54 displays additional $\bar{U}$ isosurfaces, using the same color contours as the previous figure. The first low-speed region contains more nested isosurfaces, indicating that its lowest velocity is lower than that of the second shock cell. This observation agrees with the planar PIV data, as the smallest $\bar{U}$ value was observed downstream of the Mach disk, which was only present in the first shock cell. The primary jet shear layer is evident, and it can be seen to grow with

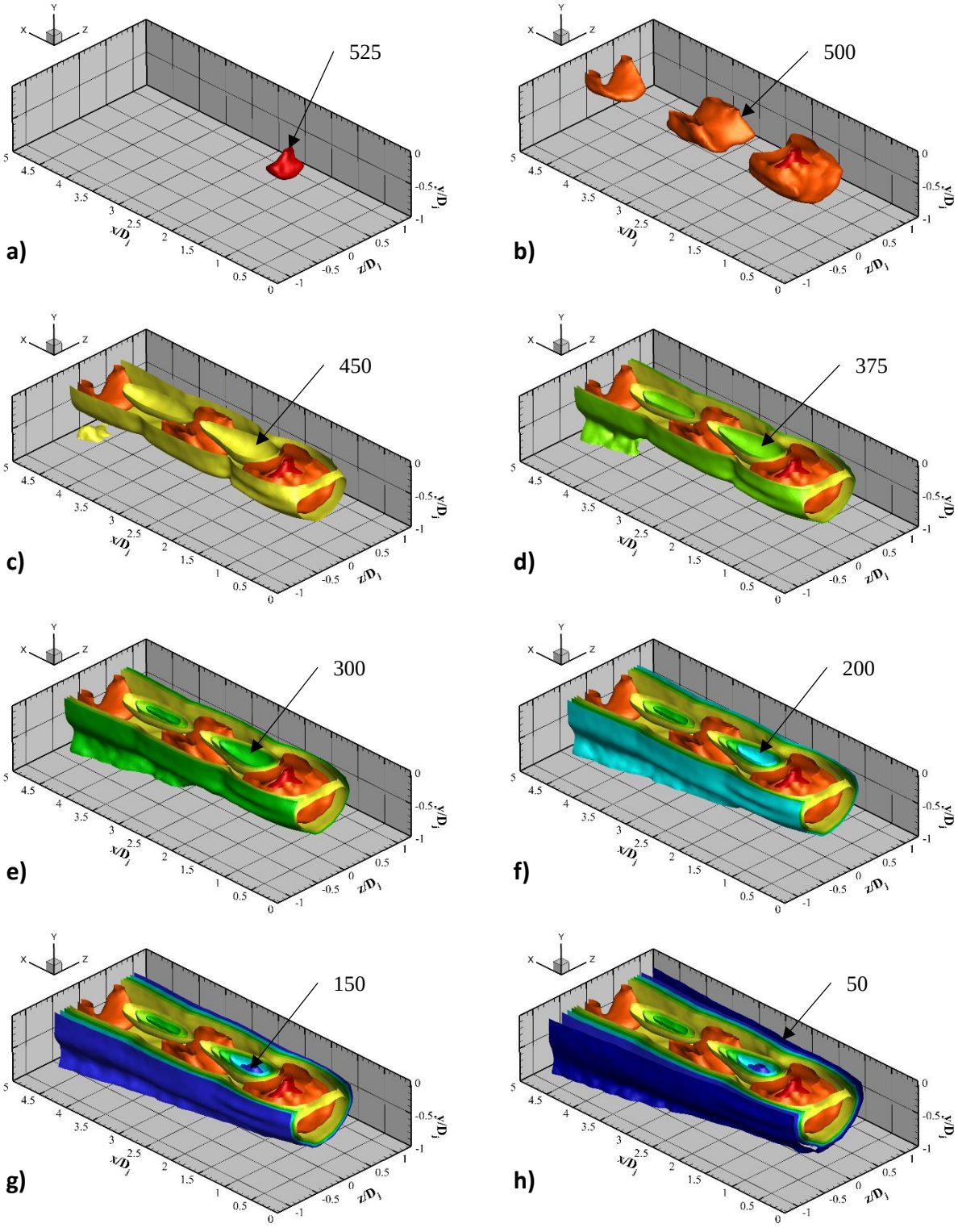

Figure 53. Increasing numbers of constant $\bar{U}$ isosurfaces (m/s) for the NPR = 5.0 isolated jet.

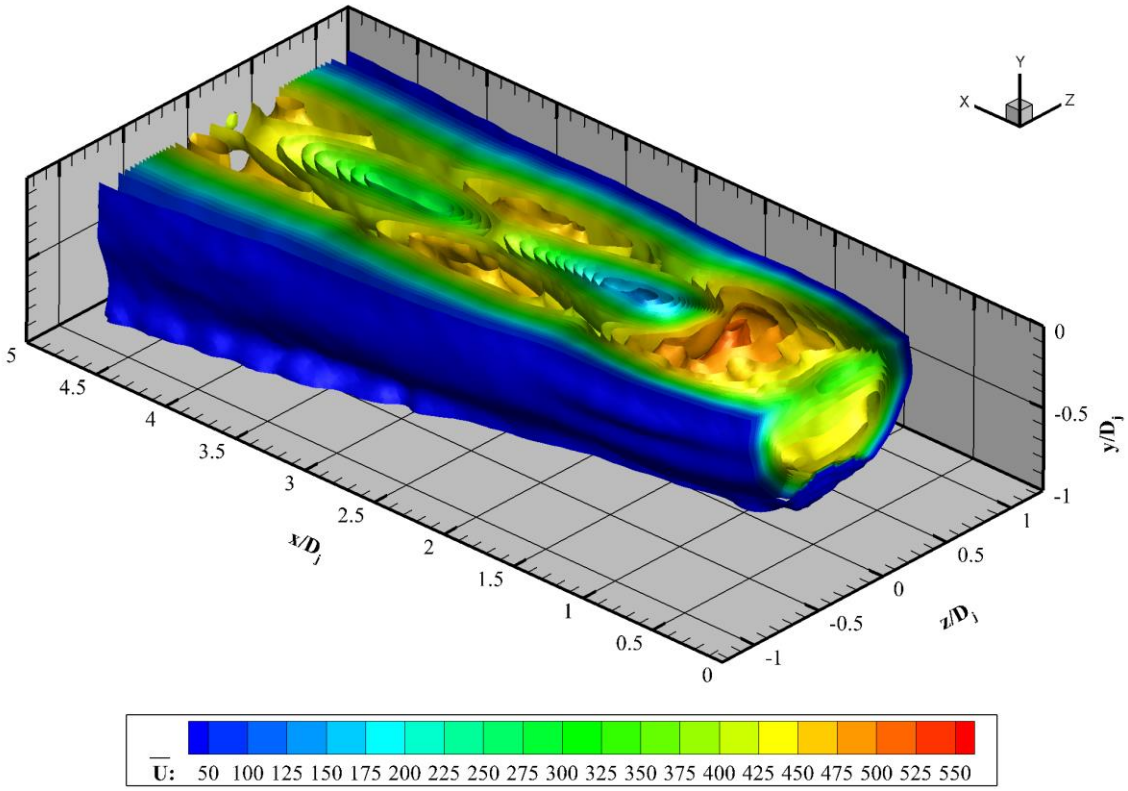

Figure 54. Constant $\bar{U}$ isosurfaces (m/s) for the NPR = 5.0 isolated jet show the typical shock-cell structure of the jet.

increasing x/D_j, as the isosurfaces spread farther apart. Additionally, it can be seen that the cross-sectional shape of the jet is round, especially near the nozzle exit.

Isosurfaces are an ideal way to explore $\bar{U}$ because the surfaces are primarily oriented in the streamwise direction, but this is not the case for $\bar{V}$ and $\bar{W}$, making their interpretations more difficult. Instead, planar slices are used to inspect $\bar{V}$ and $\bar{W}$. Figures 55 a) and b) present slices of $\bar{V}$ and $\bar{W}$, respectively, taken along constant y-planes, where the y coordinate has been stretched in order to facilitate visualization of all slices. As expected, both velocity components have very similar magnitude ranges, allowing for the use of a common scalebar in the figure. From these figures, the jet's radial expansion and compression shock-cell structure is clearly seen. Near the jet axis, both $\bar{V}$ and $\bar{W}$ are small. Inspection of the slices within Figure 55 a) shows that, within the first shock cell, as y/D_j decreases (radial distance increases), $\bar{V}$ becomes increasingly more negative as the jet expands outwards. This persists until the jet plume has been exited, whereupon the magnitude of $\bar{V}$ becomes small once again. Within the second shock cell, $\bar{V}$ has opposite sign, as

this is a jet radial-compression region, but with slightly lower magnitude. Similarly, $\bar{W}$ increases in magnitude within the first shock cell as distance from the center increases, allowing the jet to expand in *z*, as shown in Figure 55 b). Within the second shock cell, the sign of $\bar{W}$ corresponds with a radially-compressing jet. Figure 55 b) also shows that the distribution of $\bar{W}$ is symmetric about the centerline.

Figures 56 a) and b) present slices of $\bar{V}$ and $\bar{W}$, respectively, taken along constant *z*-planes, where the *z* axis has been stretched. The symmetry in $\bar{V}$ about the jet center is shown in Figure 56 a), as slices equidistant from $z/D_j = 0$ are very similar. Slices equidistant from the centerline in $\bar{W}$, shown in Figure 56 b), show the same trends and magnitudes, but in opposite directions, as expected.

The maximum $\bar{U}$ observed in the tomographic PIV data was 542 m/s, which compares favorably (less than 6% difference) with the measurement obtained from the planar PIV (576 m/s). The minimum $\bar{U}$ found in the tomographic PIV data was 112.5 m/s, which also agrees well with the previously described planar PIV data, and also agrees with shock-table estimates. The level of agreement is especially encouraging when considering that the mean for this case was obtained using a sample size of only 250 snapshots. The measurement domain allows for the measurement of maximum and minimum $\bar{W}$, which were found to be 82.5 and -105 m/s, respectively. These measurements differ in magnitude by approximately 20%. However, $\bar{W}$ is expected to reach minimum and maximum values at the top of the measurement domain. The discrepancy could be caused by a) misalignment of the jet and measurement domain, or b) lesser quality data near the edge of the illumination volume. The minimum recorded $\bar{V}$ was -115 m/s, which compares favorably with the min/max measured $\bar{W}$. $\bar{V}$ was not measured on the opposite side of the jet, as the measurement domain only measured the lower half of the jet. When $\bar{V}$ and $\bar{W}$ maximum magnitudes are normalized by $\bar{U}_{max}$, they correspond to approximately 0.15 – 0.20.

Some factors to consider when comparing tomographic PIV results to those obtained using planar PIV are spatial resolution and spatial averaging. Planar PIV data were obtained at a fine spatial resolution, with approximately 0.22 mm between adjacent vectors. The tomographic PIV data have a comparable spacing of approximately 0.33 mm between adjacent vectors. However, planar PIV data were obtained from smaller correlation windows, with each vector representing the spatial average of an approximately 0.44 mm by 0.44 mm 2D-planar window (approximately 1 mm thick). For the tomographic PIV results, however, each vector is obtained from a three-

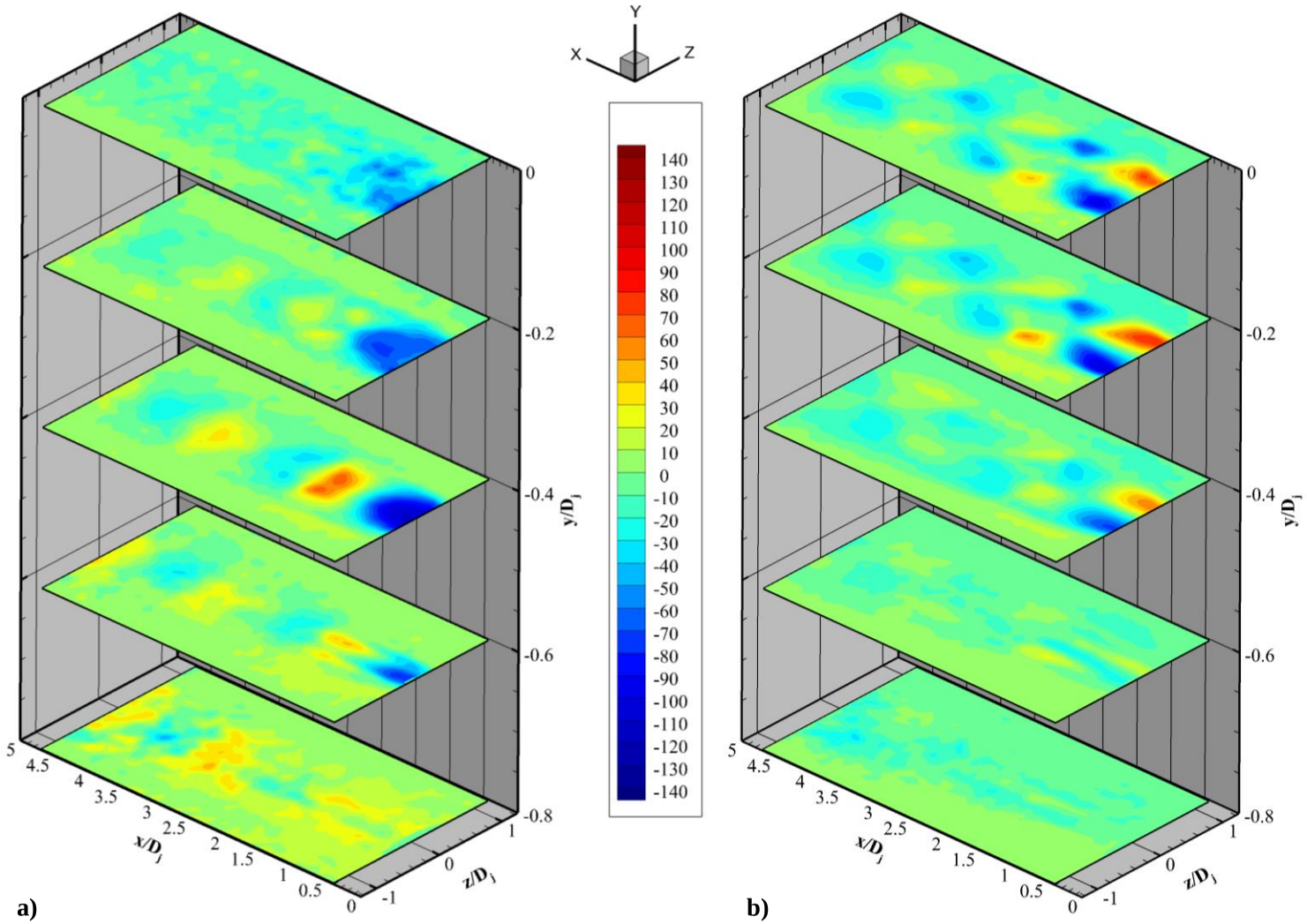

Figure 55. Constant-y planes showing a) $\bar{V}$ and b) $\bar{W}$ contours of velocity (m/s) for the NPR = 5.0 isolated jet. The figures share a common color scale.

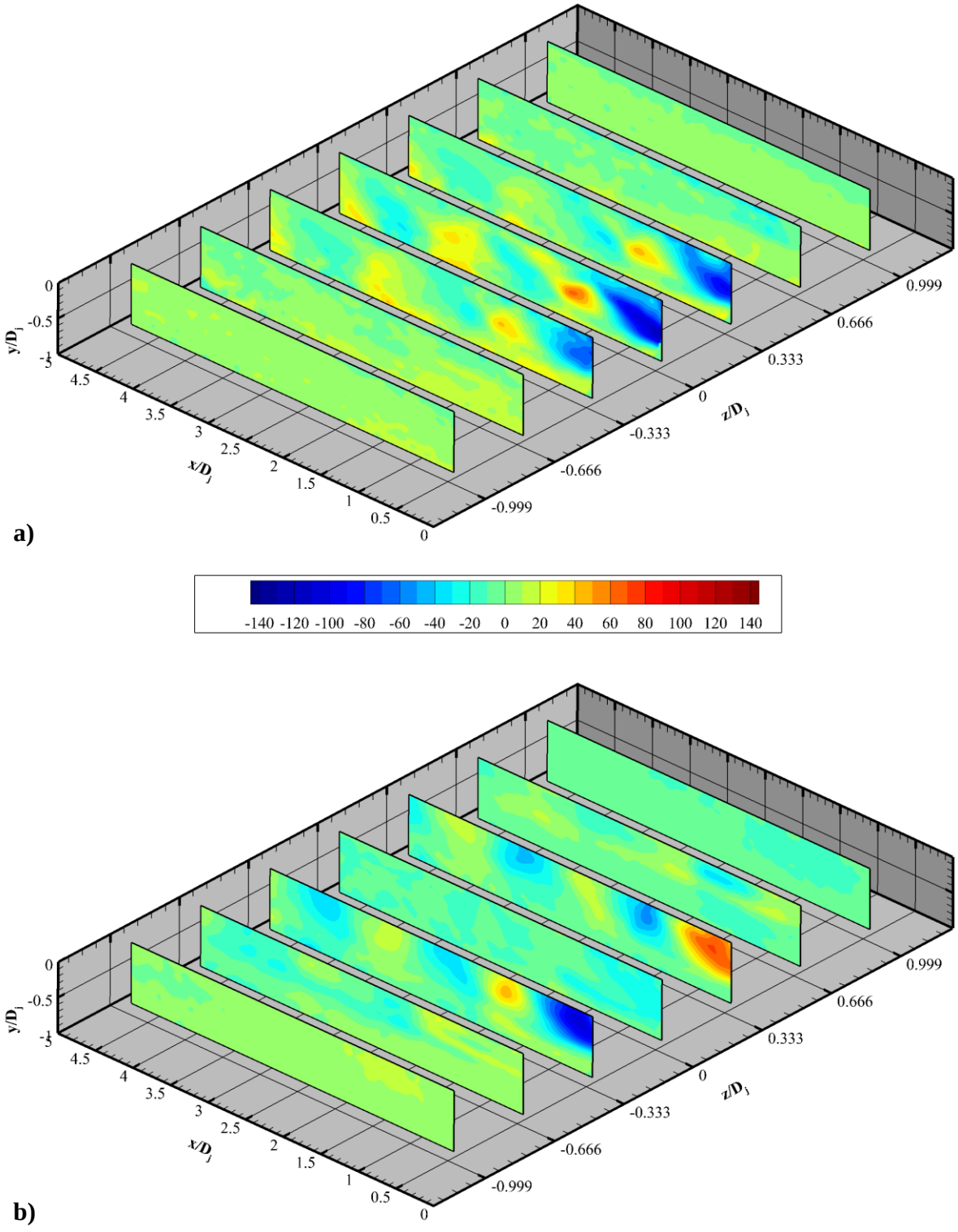

Figure 56. Constant-z planes showing a) $\bar{V}$ and b) $\bar{W}$ contours of velocity (m/s) for the NPR = 5.0 isolated jet. The figures share a common color scale.

dimensional cube (called a voxel) with approximately 1.31-mm long sides. The net effect is an increased spatial averaging that necessarily biases each vector by the larger surrounding correlation window, influencing both the velocity magnitudes and spatial velocity gradients, despite the similar distances between adjacent vectors.

A representative instantaneous flowfield for the *NPR* = 5.0 isolated jet is shown in Figure 57. As expected, the instantaneous velocities exhibit much more variation than the mean fields in magnitude as well as spatially, resulting in very complex, highly three-dimensional, isosurfaces. Still, the overall shape and structure of the jet is evident as the first shock-cell acceleration and subsequent deceleration post Mach disk can be clearly seen. In addition, the second low-speed region is also apparent, as is the jet's tendency to broaden as the shear layer thickens with increasing x/D_j. Instantaneously, the velocity variation is much greater than that seen in the time-averaged results, leading to numerous high- and low-speed bubble-like isosurfaces. Inspection of the other two velocity components shows that the instantaneous variation in these directions is also

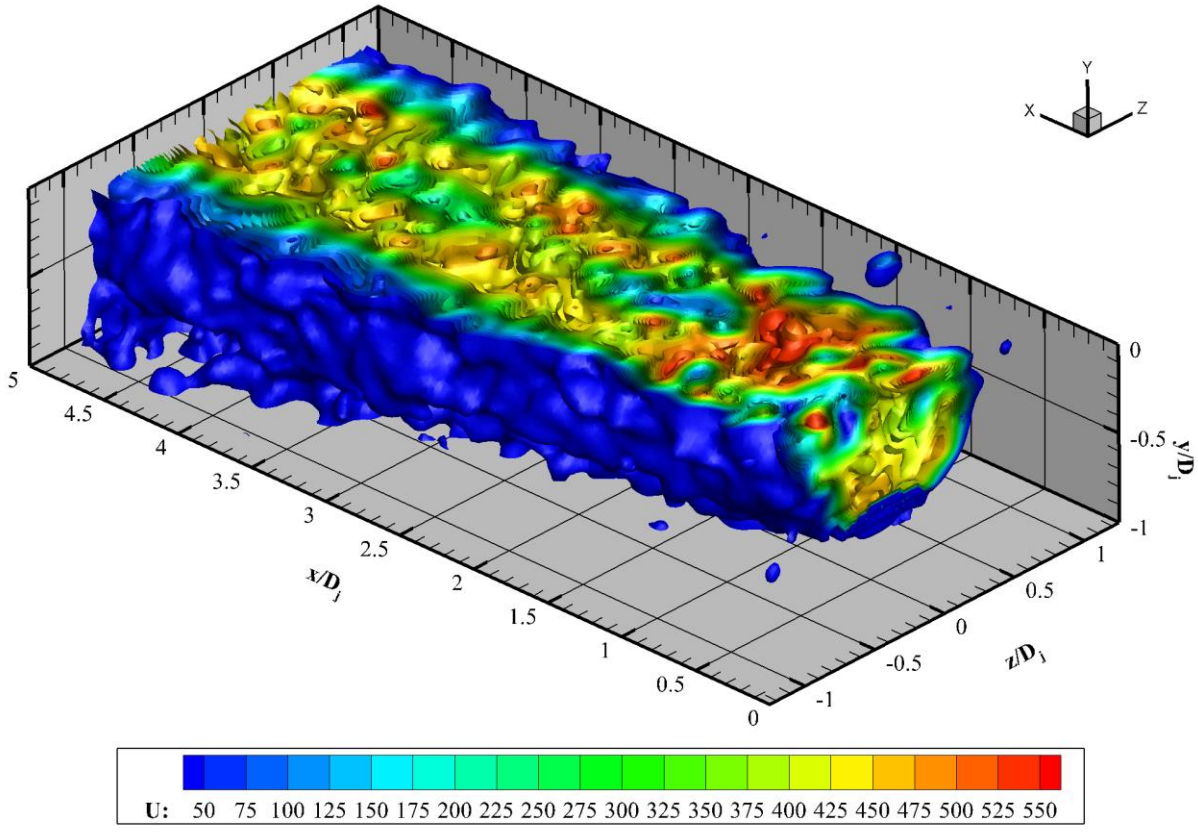

Figure 57. Instantaneous U velocity component isosurfaces for the NPR = 5.0 isolated jet exhibit large variations in both magnitude and space.

very high, especially near the y/D_j domain limits. These planes are simultaneously near the edge of the laser illumination window, far from the ideally-focused imaging region, and at the limits of the tomographic volume self-calibration region. These factors combine to affect the tomographic calibration and to increase the noise in the data in these regions, particularly in the *y* direction.

The tomographic PIV spatial averaging effect is further compounded by the small length scales of the flow under consideration in the current study, especially with regards to the identification of instantaneous coherent structures. Assuming that an identifiable structure requires a vector reversal, a minimum of two non-overlapping windows would be required. This represents an approximate minimum distance of 1.31 mm, and gives an indication as to the smallest identifiable coherent structures. Coherent structure identification is further complicated by the high degree of overlap between correlation windows which smoothes the velocity gradient across it. The flow currently under investigation has a nominal length scale set by the jet diameter, D_j = 12.7 mm, limiting the smallest measurable structures to those with length scales of approximately 1/10 D_j. However, the flow under consideration is a high-Reynolds number, compressible, turbulent jet, and the expected range of length scales will far surpass the minimum resolvable tomographic-PIV structures. Therefore, coherent structure identification using the data obtained from tomographic PIV in the current setup is only expected to allow for the identification of the very largest structures.

3.4.2 *NPR* = 4.0

Isosurfaces of $\bar{U}$ for the *NPR* = 4.0 isolated jet are presented in Figure 58, using the same color scales as those used for the *NPR* = 5.0 data shown previously. The surfaces are generally smooth, indicating that a sufficient number of instantaneous snapshots were obtained in order to accurately estimate the mean conditions. In comparison to the *NPR* = 5.0 case, the velocity magnitudes exhibit a narrower range, as the degree of under- and over-expansion within each shock cell is decreased. As seen in the planar PIV data, the shock cells for this operating condition are smaller and more closely spaced. The jet width is also decreased as compared to the *NPR* = 5.0 case.

Figures 59 a) and b) present slices of $\bar{V}$ and $\bar{W}$, respectively, taken along constant *y*-planes, and Figures 60 a) and b) do the same along constant *z*-planes. For consistency, the same color scales have been employed for these figures as the corresponding *NPR* = 5.0 case figures. Again, both velocity components have very similar magnitude ranges. The outward radial velocities are evident within jet expansion regions, while inward radial velocities are predominant within jet

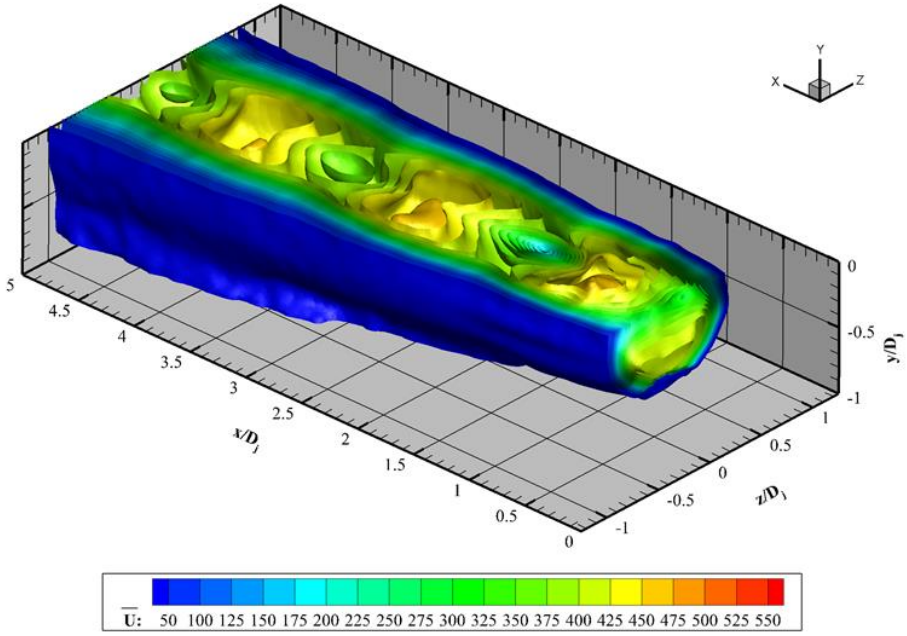

Figure 58. Constant $\bar{U}$ isosurfaces (m/s) for the NPR = 4.0 isolated jet.

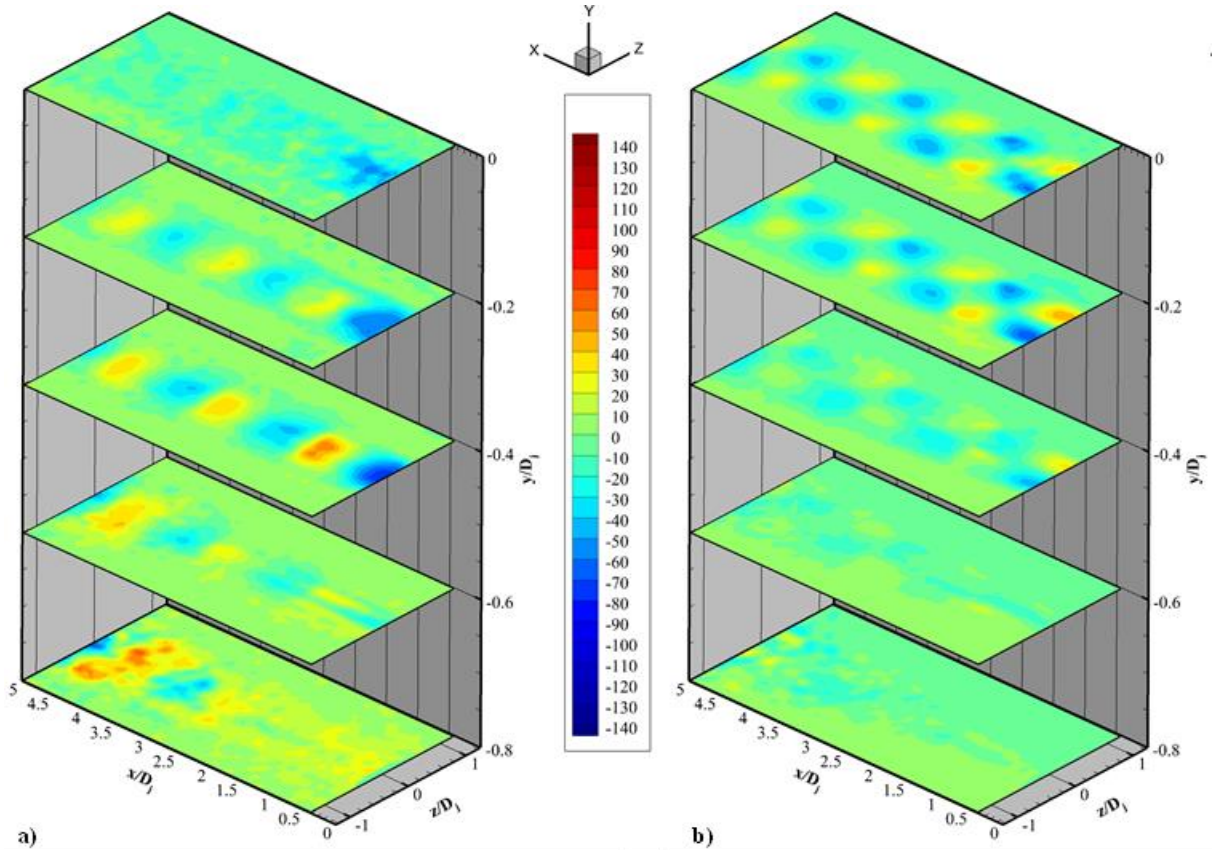

Figure 59. Constant-y planes showing a) $\bar{V}$ and b) $\bar{W}$ contours of velocity (m/s) for the NPR = 4.0 isolated jet. The figures share a common color scale.

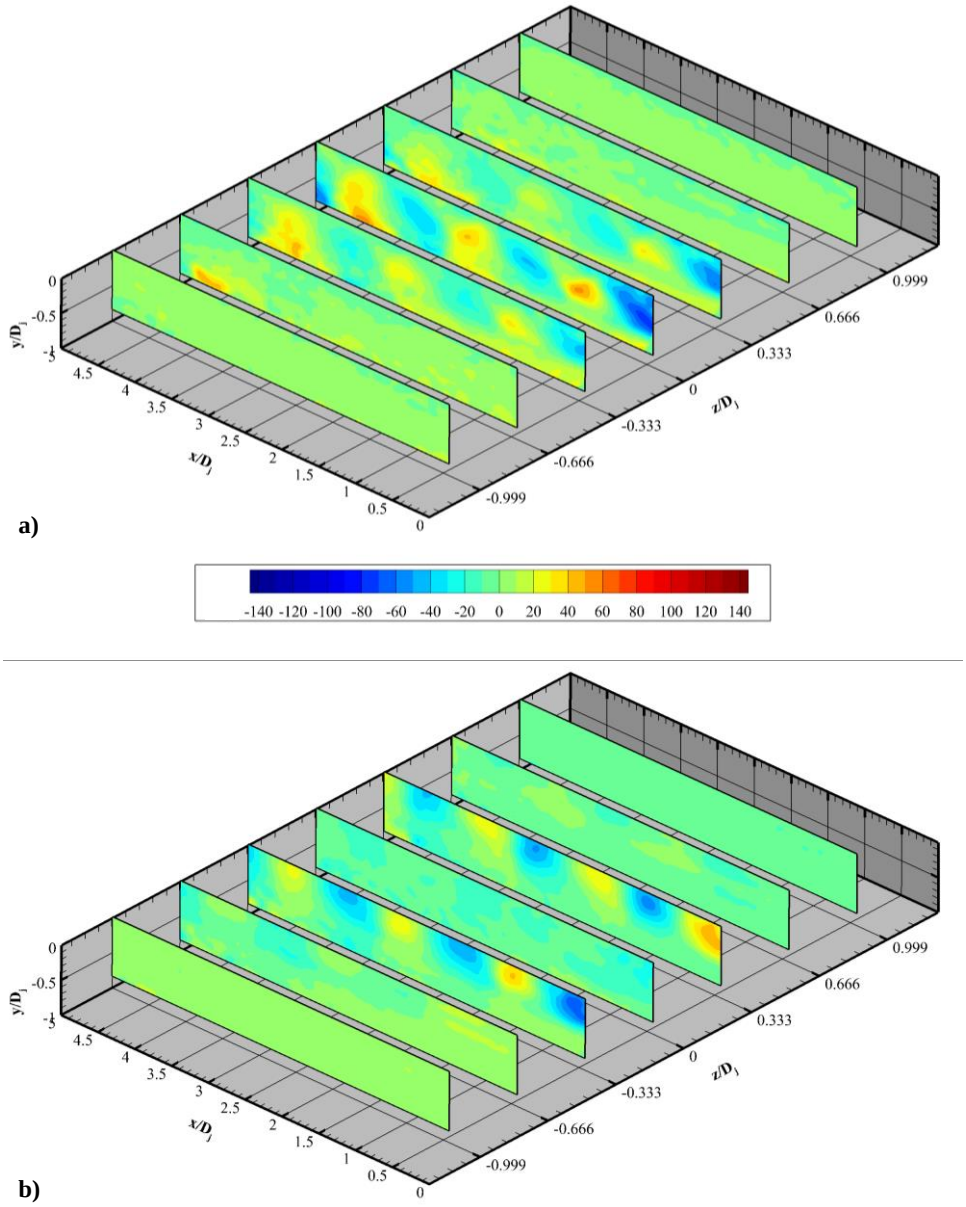

Figure 60. Constant-z planes showing a) $\bar{V}$ and b) $\bar{W}$ contours of velocity (m/s) for the NPR = 4.0 isolated jet. The figures share a common color scale.

compression zones. Overall, the $\bar{V}$ and $\bar{W}$ velocity data show that the flowfield is nearly axisymmetric. The mean velocities agree with the values obtained from the planar PIV data, to within the expected degree based on the tomographic PIV spatial averaging effect previously discussed.

3.4.3 *NPR = 3.0*

Isosurfaces of $\bar{U}$ for the *NPR* = 3.0 isolated jet are presented in Figure 61. Compared to the *NPR* = 5.0 and 4.0 cases, the velocity magnitudes exhibit an even narrower range. The shock cells at this operating condition are yet smaller and more closely spaced. The jet width is also decreased as compared to the other operating conditions.

Figures 62 and 63 present slices of $\bar{V}$ and $\bar{W}$, respectively, taken along constant *y*- and *z*-planes, as before. These figures show how symmetric the jet flowfield is, and, once again, highlight the jet shock-cell structure. As with the NPR = 5.0 and 4.0 cases, the mean velocities agree with the values obtained from the planar PIV data.

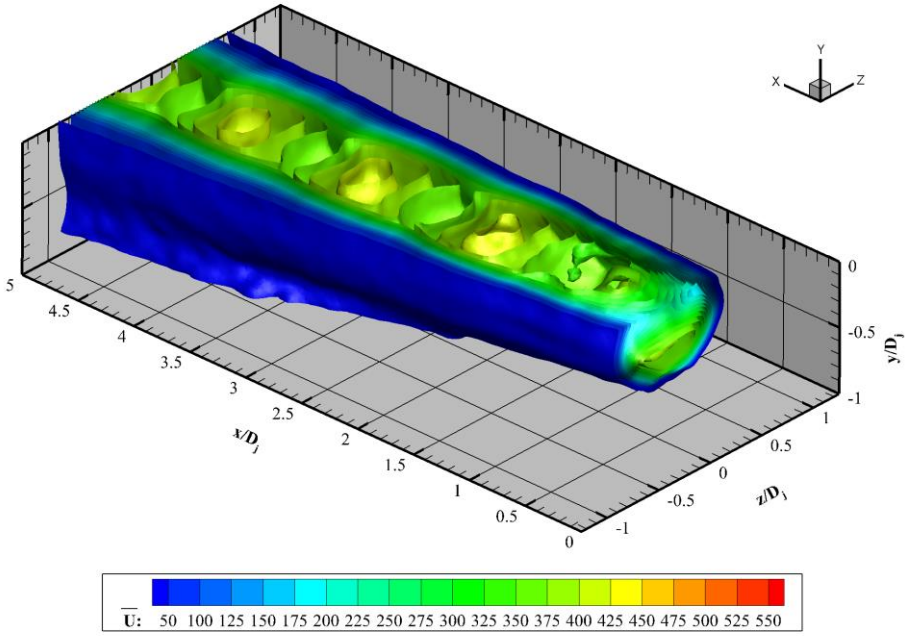

Figure 61. Constant $\bar{U}$ isosurfaces (m/s) for the NPR = 3.0 isolated jet.

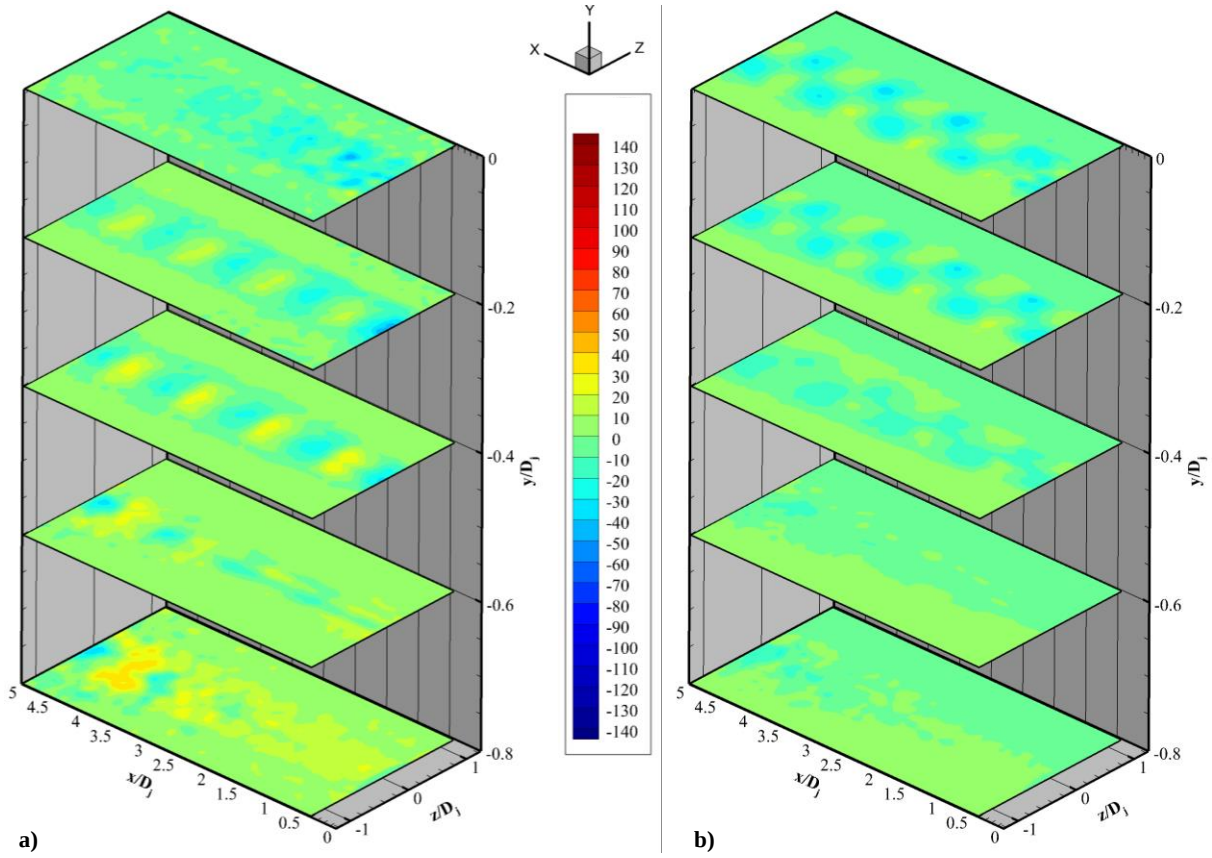

Figure 62. Constant-y planes showing a) $\bar{V}$ and b) $\bar{W}$ contours of velocity (m/s) for the NPR = 3.0 isolated jet. The figures share a common color scale.

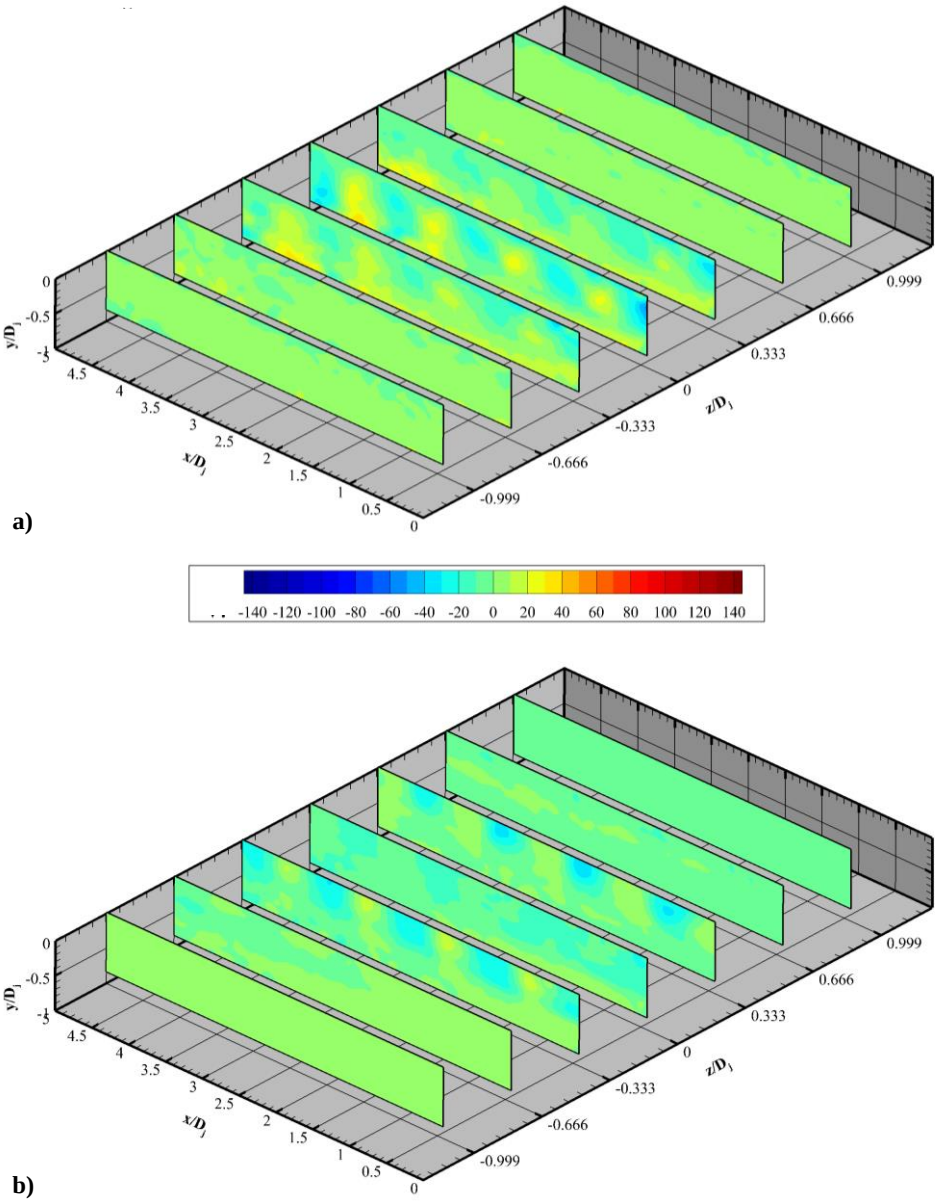

Figure 63. Constant-z planes showing a) $\bar{V}$ and b) $\bar{W}$ contours of velocity (m/s) for the NPR = 3.0 isolated jet. The figures share a common color scale.

Chapter 4 Jet/Rigid-Surface Results

Jet and rigid-surface configuration results are described in this chapter. Results, in the form of high-speed schlieren imagery, planar and tomographic PIV, steady PSP, and oil flow visualization are presented. In this study, emphasis was placed on the h/D_j = 0.50, *NPR* = 5.0 case, and so most of the discussion centers on this case. Data were obtained for h/D_j = 0.50, 0.55, and 0.60 and for *NPR* = 5.0, 4.0, and 3.0, and so these results are discussed as well, although in less detail. Just as the isolated jet results (Chapter 3) provide a reference jet-flow state, the jet/rigid-surface results presented in this chapter provide a baseline for comparison for the jet/compliant-surface case experiments and results discussed in the following chapter (Chapter 5).

4.1 High-speed Schlieren

Schlieren imagery provides an ideal initial inspection of the jet flowfield in the presence of an adjacent rigid planar surface and is therefore presented first. A large field-of-view, time-averaged image, is shown in Figure 64 for the h/D_j = 0.50, *NPR* = 5.0 case, while Figure 65 presents an instantaneous image of the first shock cell region. The mean image shows that, in comparison to the isolated jet case, the surface greatly alters the shock-cell structure of the flowfield. Within the first shock cell, the shock waves are well-defined and crisp, while farther downstream they are less clear. This is a result of a more steady (or at least a decreased amplitude of oscillation) flow state in the first shock cell and increased unsteadiness farther downstream. Figure 65, which has been annotated, highlights the more obvious effects within the first shock cell, as well as shows the instantaneous turbulent nature of the flowfield.

The surface's presence disrupts the flowfield in two primary ways. First, an apparent oblique shock forms on the near-surface side of the jet from the nozzle exit. The natural outward flow

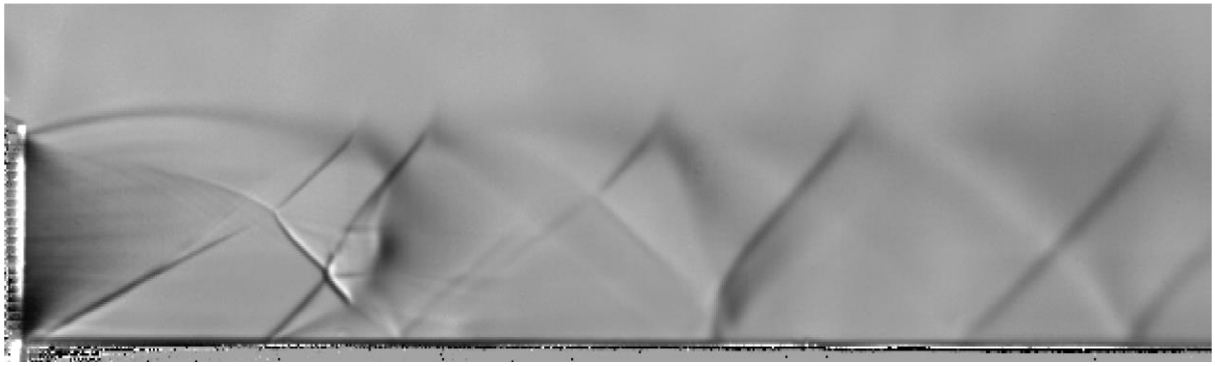

Figure 64. Mean schlieren image for the h/D_j = 0.50, NPR = 5.0 rigid-surface case.

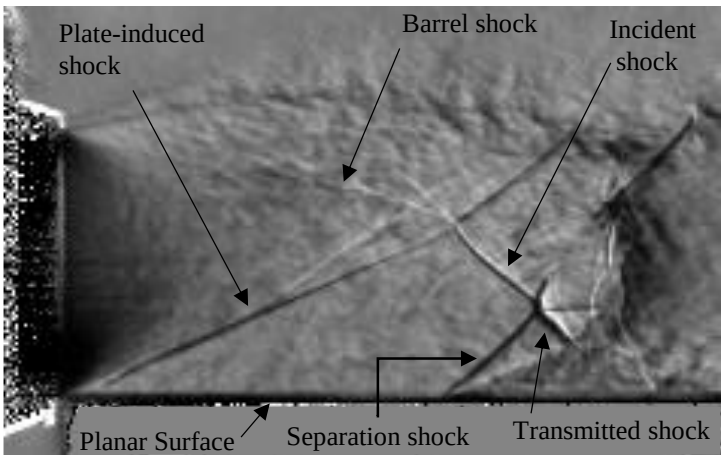

Figure 65. An instantaneous schlieren image for the $h/D_j = 0.50$, NPR = 5.0 rigid-surface case.

expansion is constrained due to the no-penetration boundary condition induced by the surface, leading to the formation of this wave. This wave, henceforth termed the "plate-induced shock", projects into the core of the jet, disrupting the plate-side barrel shock formation, destroying the Mach disk, and generating a new shock interaction instead (with the jet far-side barrel shock).

Second, the constant-pressure free surface shear layer nearest the surface transforms into a wall-bounded flow. The plate-induced shock intersects with the jet far-side barrel shock and generates two additional shock waves, one of which projects back towards the surface and becomes the incident shock for a shock/boundary layer interaction (SBLI). Following the naming conventions from Babinsky and Harvey,[133] the SBLI is characterized by the incident shock, a separation shock, a transmitted shock, and a region of boundary layer thickening (and flow separation); each of these is identified in Figure 65.

Using the high-speed schlieren images, the same type of shock-position tracking analysis as described for the isolated jet (see Section 3.2.3) was carried out, for which case it was shown that dominant shock-fluctuation frequencies directly coincide with the screech tone observed in the far-field acoustic data. Shock-tracking analyses carried out for the jet/rigid-surface case, for which there are no acoustic data, allow for insight into whether or not the rigid surface affects the jet screech cycle.

Three shock waves were investigated as shown in Figure 66 a), corresponding to the oblique reflected shock, the SBLI incident shock, and the SBLI separation shock. These shock waves were selected for analysis due to their persistent nature in all of the schlieren images, their relatively large size, steep angle, and fact that they were relatively isolated (thereby minimizing the chance of losing the intended shock during time-series analysis). The resulting PSDs, which are shown in Figures 66 b) - d), are all broadband in nature. Since no distinct peaks were observed as a result of this shock fluctuation analysis, it was concluded that the presence of the plate disrupts the generation of the screech cycle. This was an expected result; other screech studies for similar configurations have also reported inhibited screech cycles for jets in the presence of surfaces, likely due to altered jet-column modes.[36,61,62] No acoustic data were obtained for the jet-and-surface

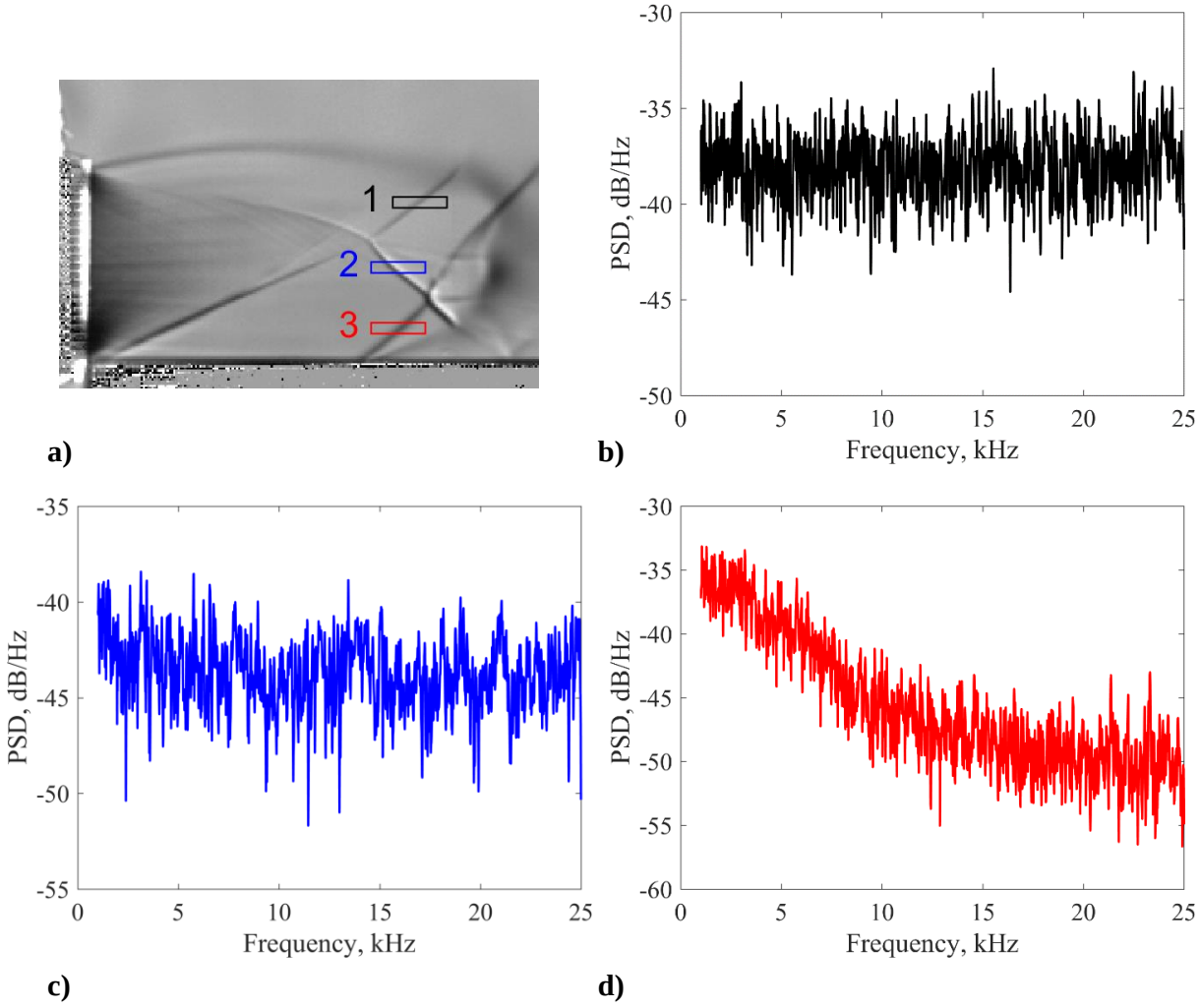

Figure 66. Shock axial-position time-series analyses, conducted for three shock waves, show broadband frequency responses at all inspected positions for the rigid-surface h/D_j = 0.50, NPR = 5.0 case.

configuration, due to the non-ideal relative positions between the jet/rigid-surface and microphones, and the large amount of surfaces and instrumentation (optical table, model support structure, traverse, etc.) within the anechoic chamber that could interfere with the measurements. Therefore, no supporting evidence for this theory can be found in acoustic measurements.

The broadband frequency response observed in the SBLI separation shock is also notable for another reason. Movies of the instantaneous high-speed schlieren data, taken at a variety of frame rates (including 500 Hz), show that the SBLI position is remarkably steady. The distinct shocks in the mean schlieren image confirm the temporal stability of the SBLI shock waves. This is in contrast to traditional SBLIs, which typically exhibit low-frequency oscillations, for reasons which are still under debate.[134] The unusual SBLI temporal stability observed in this study is likely related to the fact that the SBLI forms in a jet flow; perhaps the three-dimensionality of the jet, or the under/over expansion characteristic of the flowfield are responsible.

4.2 Planar PIV

In this chapter, contour plots are used to present the PIV results in a primarily fullfield manner. In selected instances, profiles through the jet are used to provide additional quantitative insight into the results, as well as to show the measurement uncertainties. Chapter 5 presents many additional rigid-surface case data profiles while comparing results with those obtained for the compliant-surface case.

Mean PIV contour plots for the streamwise velocity, $\bar{U}$, wall-normal velocity, $\bar{W}$, and velocity magnitude, $\overline{|V|}$, are shown in Figure 67 for the h/D_j = 0.50, NPR = 5.0 case. Each plot uses a different color contour scheme to facilitate comparison between other figures.

As expected, $\bar{U}$ is the dominant velocity component. $\bar{U}$ increases from approximately sonic conditions at the nozzle exit until it encounters the shocks and SBLI at the end of the first shock cell. $\bar{U}$ achieves a maximum value of 576 m/s within the first shock cell, just upstream and above the SBLI. This value is identical to that observed for the isolated jet (at least to the current measurement precision), although the location differs slightly. As the flow passes through the shock waves, $\bar{U}$ undergoes a sudden deceleration, and then begins to accelerate again. This pattern persists through the remaining shock cells, with increasingly less severe oscillations. The shock-cell structure can be clearly seen at the interior shear layer boundary, where clear kinks can be found in the $\bar{U}$ contours.

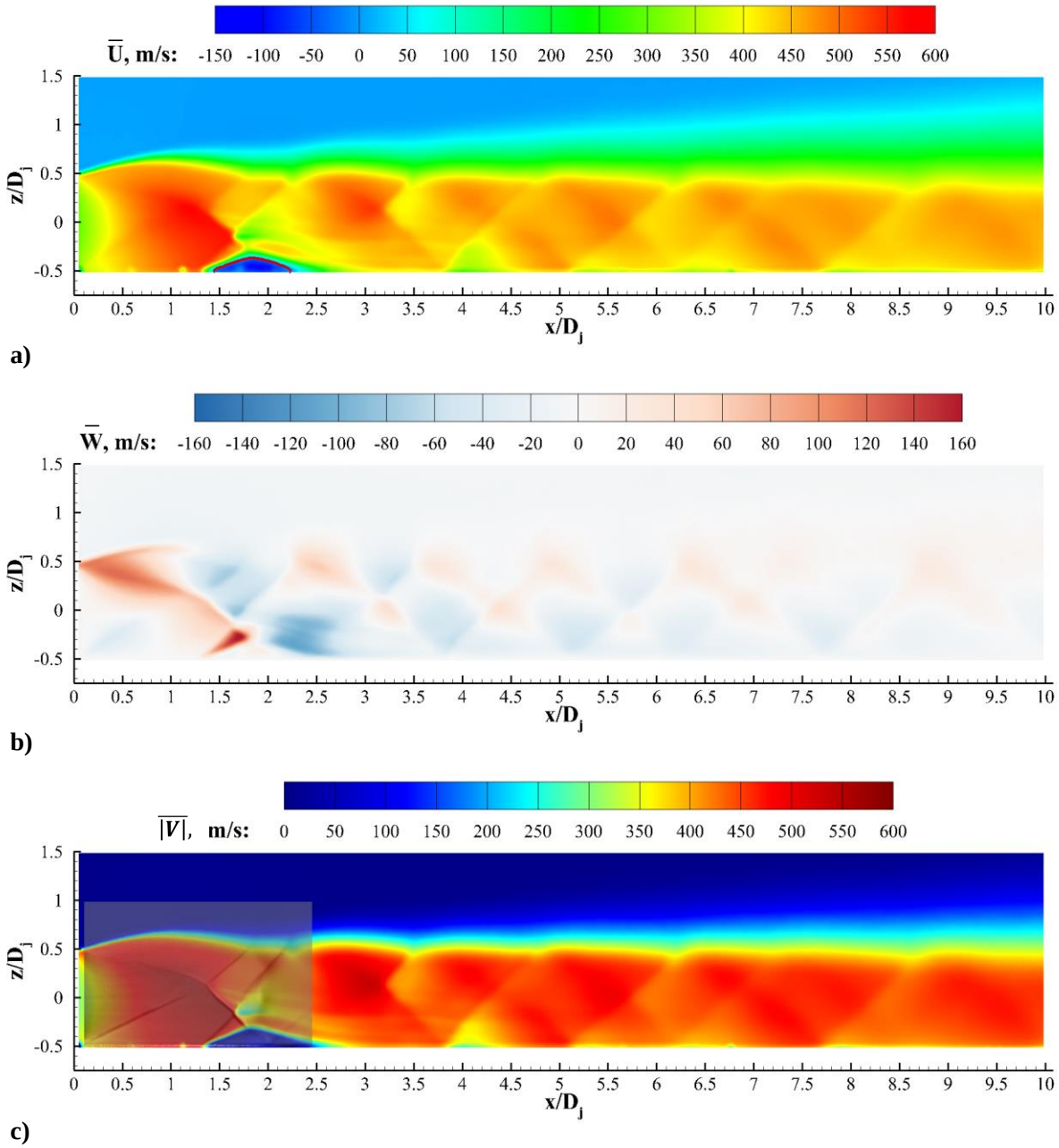

Figure 67. Mean PIV results for the h/D_j = 0.50, NPR = 5.0 rigid-surface case showing a) the streamwise velocity component, $\bar{U}$, with $\bar{U}$ = 0 m/s isocontour (in red) highlighting the flow reversal region, b) the wall-normal component, $\bar{W}$, and c) velocity magnitude, $|\overline{V}|$, with overlaid mean shock locations as obtained by schlieren imagery.

The red line in Figure 67 a) near x/D_j = 2 is a $\bar{U}$ = 0 isocontour and shows that there is mean flow reversal within the SBLI. The maximum speed of the reversed flow is approximately 125 m/s. The ability to capture reversed flow within the SBLI indicates that measurements were obtained very close to the surface and that the grazing laser illumination technique was effective at minimizing laser surface reflections.

However, due to the high freestream velocity and short distance over which it can develop, the boundary layer is exceedingly thin and is therefore not fully captured by the PIV. A calculation of the local Reynolds number, Re_x, (Equation 8) across the PIV measurement domain reveals that Re_x crosses the typical flat-plate transition point (Re_x = 5 x 10^5) at $x/D_j \approx 0.5$ and exceeds 1 x 10^6 at $x/D_j \approx 1.0$. Therefore, we can safely assume that upward of 90% of the measurement domain has a turbulent boundary layer, which, due to its greater proportion of near-wall momentum, makes it even more difficult to capture in the data. Instantaneous high-speed schlieren images support a turbulent flow state.

$$Re_x = \frac{\rho \bar{U}_{max} x}{\mu} \tag{8}$$

$$\delta = \frac{0.37x}{Re_x^{1/5}} \tag{9}$$

The boundary layer thickness, δ, was estimated using Prandtl's flat plate turbulent boundary layer power-law relation shown in Equation 9.[135] For simplicity, it was assumed that the freestream velocity was 575 m/s and that there was no pressure gradient (which, as evidenced by the presence of the SBLI, is not true). Just upstream of the SBLI separation shock location at x/D_j = 1.25, δ was estimated at less than 0.4 mm, which is on the order of the size of the PIV interrogation windows and is therefore too small to be effectively captured. At the downstream end of the measurement domain (near x/D_j = 10), δ was estimated at approximately 2 mm, which represents approximately 4 – 5 non-overlapping interrogation windows (and 8 – 10 windows with 50% overlap).

Inspection of Figures 67 a) and c) clearly shows that by the end of the measurement domain, the boundary layer has become substantially thicker than it had been in the first shock cell. In addition, the boundary layer can be seen to thicken slightly in regions corresponding to flow deceleration (adverse pressure gradient) within the shock cells. This observation is, of course, expected.

The jet's tendency to expand at the nozzle exit can be seen upon inspection of the wall-normal velocity component, $\overline{W}$, (Figure 67 b). The jet is allowed to freely expand in the wall-normal direction (red region above the jet axis in the first shock cell), but expansion towards the wall is clearly restricted (lack of dark blue coloration below the jet axis in the first shock cell) due to the no-penetration boundary condition imposed by the surface. The maximum $\overline{W}$ observed within the freely expanding region of the first shock cell is ~115 m/s, which agrees very well with that seen in the same region for the isolated jet case (~110 m/s). The wall-normal velocity component also shows the flow lifting, caused by the SBLI separation shock, as well as the tendency toward reattachment on the downstream side of the SBLI. Within the SBLI separation region, $\overline{W}$ is nearly zero. The maximum $\overline{W}$ is found behind the SBLI separation shock, where $\overline{W}_{max}$ = 164 m/s, and the minimum is found in the reattachment region behind the SBLI region.

A time-averaged schlieren image of the first shock-cell is overlaid on the velocity magnitude plot shown in Figure 67 c). The two data sets align nicely. Stronger shocks (such as the SBLI incident and separation shock waves) are accompanied by larger drops in velocity magnitude. Velocity magnitude changes across weak shocks and slip lines are accordingly more subtle.

A dominant feature in the schlieren imagery is the plate-induced wave, which appears to be an oblique shock wave. However, the PIV data do not show a clear velocity or Mach number change at the apparent shock location in the contour plots, nor do the streamlines appear to bend appreciably upon passage through the shock. However, the Mach number contours do show a clear kink at the location of the shock wave. Further investigation of the data using profiles through the jet revealed noticeable bends in the profiles at the shock location, especially for $x/D_j \lesssim 0.60$. For instance, wall-normal ($\overline{W}$) velocity profiles through the jet show a slope reversal near the shock location.

The fact that the flow is undergoing a local expansion helps explains why the plate-induced shock is not more obvious in the PIV data. The expansion facilitates the development of out-of-plane velocity components (these are not captured in the planar PIV data), which may be preferred over remaining in the plane, passing through the shock wave, and incurring those losses. These effects are anticipated to be strongest for small x/D_j, due to the aggressive local expansion and small/short opportunity for the development of out-of-plane components. Farther downstream, flow-expansion and 3D-relief effects are more likely to occur due to the additional area in which the flow may divert, and the increased time/length over which out-of-plane velocity components

have developed. This explains why evidence of the plate-induced shock becomes more difficult to discern in the PIV data beyond $x/D_j \approx 0.60$. Further, the line-integrating nature of schlieren, coupled with shock curvature and the sideline view, may create the impression that the plate-induced shock is stronger than it really is.

The mean turbulence quantities (Reynolds stresses) provide further insight into the flowfield. As expected, a great deal of turbulence is found within the shear layer, where levels compare favorably to those observed in the isolated jet case. Within the core of the jet, turbulence levels are low, except for some elevated levels near the shock-cell boundaries (likely due to shock unsteadiness effects and not turbulence). Inspection of $\overline{u'u'}$ and $\overline{u'w'}$ in Figures 69 a) and c), respectively, clearly shows that turbulence is also generated within the shear layer formed over the SBLI separation region. The $\overline{w'w'}$ plot (Figure 69 b) reveals increased turbulence intensity directly behind the SBLI separation shock (possibly due to flow unsteadiness), which is clearly distinct from the increased levels within the SBLI separation region shear layer. Turbulence generation (or general flow unsteadiness) in Figure 69 b) also reveals the location of the slip line (see arrow annotation) created at the primary SBLI shock intersection. In general, $\overline{u'u'}$ is 3 – 5 times greater than $\overline{w'w'}$, showing that the turbulence field has a high degree of anisotropy.

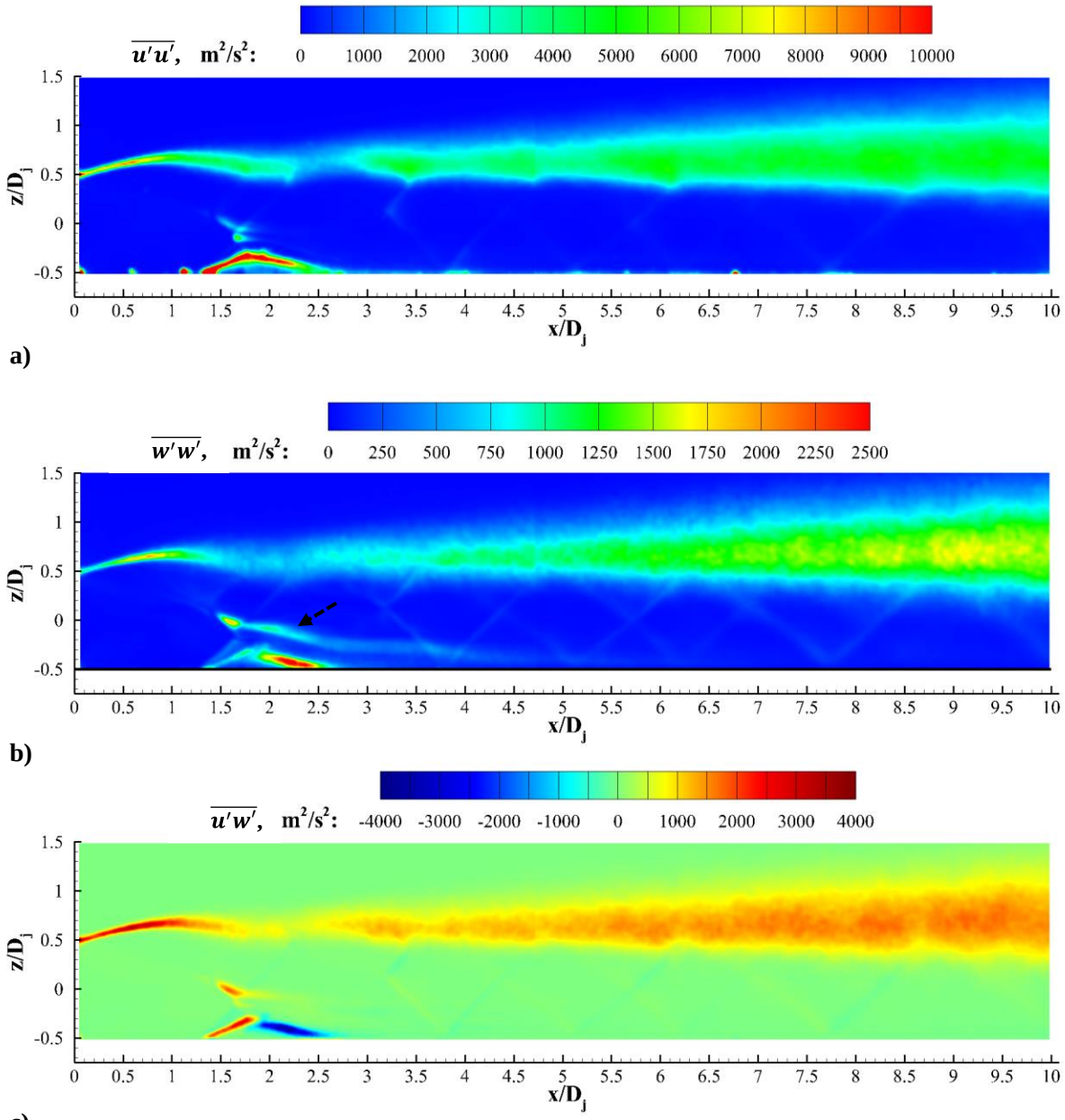

Figure 68. Mean PIV turbulence quantities for the h/D_j = 0.50, NPR = 5.0 rigid-surface case showing a) $\overline{u'u'}$, b) $\overline{w'w'}$, and c) $\overline{u'w'}$.

An instantaneous PIV vector field, colored by velocity magnitude, $|V|$, is shown in Figure 70 for $0 \leq x/D_j \leq 5$ and Figure 71 for $5 \leq x/D_j \leq= 10$. Vectors (every 8th streamwise and every 3rd wall-normal) are overlaid on the figures. Within the first shock-cell, the vectors on the free-shear layer side of the jet undergo a much greater degree of turning as compared to streamlines on the wall-bounded side of the jet. As with the mean results, the plate-induced shock is not readily apparent within this instantaneous velocity field. However, many of the other shock waves, including the SBLI incident and separation shocks and weaker shocks within later shock cells, are visible. Inspection of the instantaneous and mean PIV data also confirm (just as with the high-speed schlieren) that the SBLI position is remarkably steady. Within the SBLI, the instantaneous velocity field also exhibits true flow reversal within the SBLI, as marked by the area inside the single red line contour ($u = 0$ isocontour). There are also some regions of instantaneous reversed flow outside of the primary jet (i.e., in the "ambient" region), especially for $x/D_j \leq 5$. These regions become less frequent as x/D_j increases, the shear layer thickens, and the ambient air transitions from a quiescent state to a state of entrainment. The turbulent nature of the jet flow is apparent, particularly within the primary shear layer for larger x/D_j.

PIV measurement uncertainties have been estimated for the $h/D_j = 0.50$, $NPR = 5.0$ rigid-surface case. The reader is referred to Section 2.6.3 for uncertainty estimations for instantaneous and mean velocities, as well as those for mean turbulence quantities like the Reynolds normal and shear stresses.

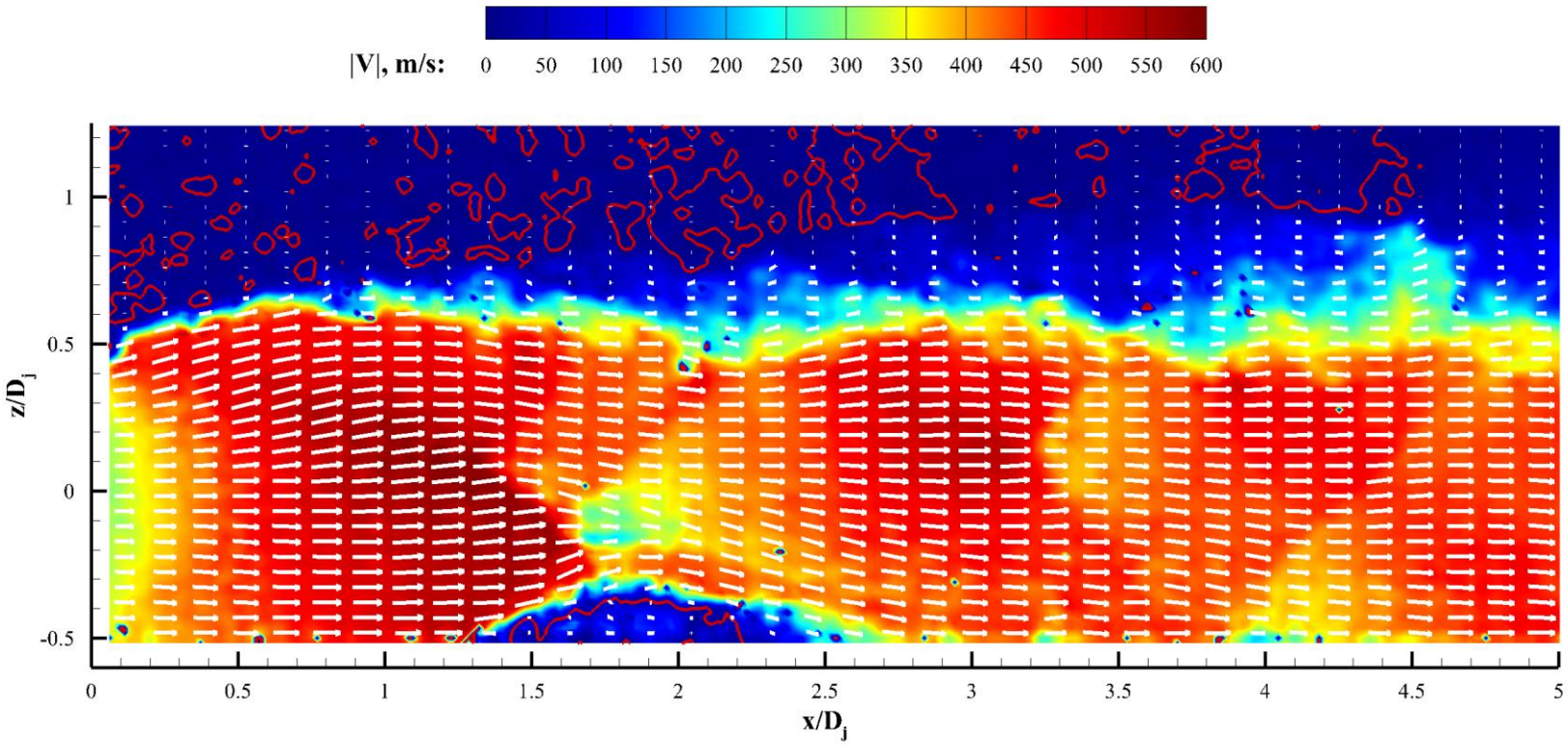

Figure 69. A sample instantaneous velocity magnitude image of the upstream region ($0 \leq x/D_j \leq 5$) with overlaid vectors.

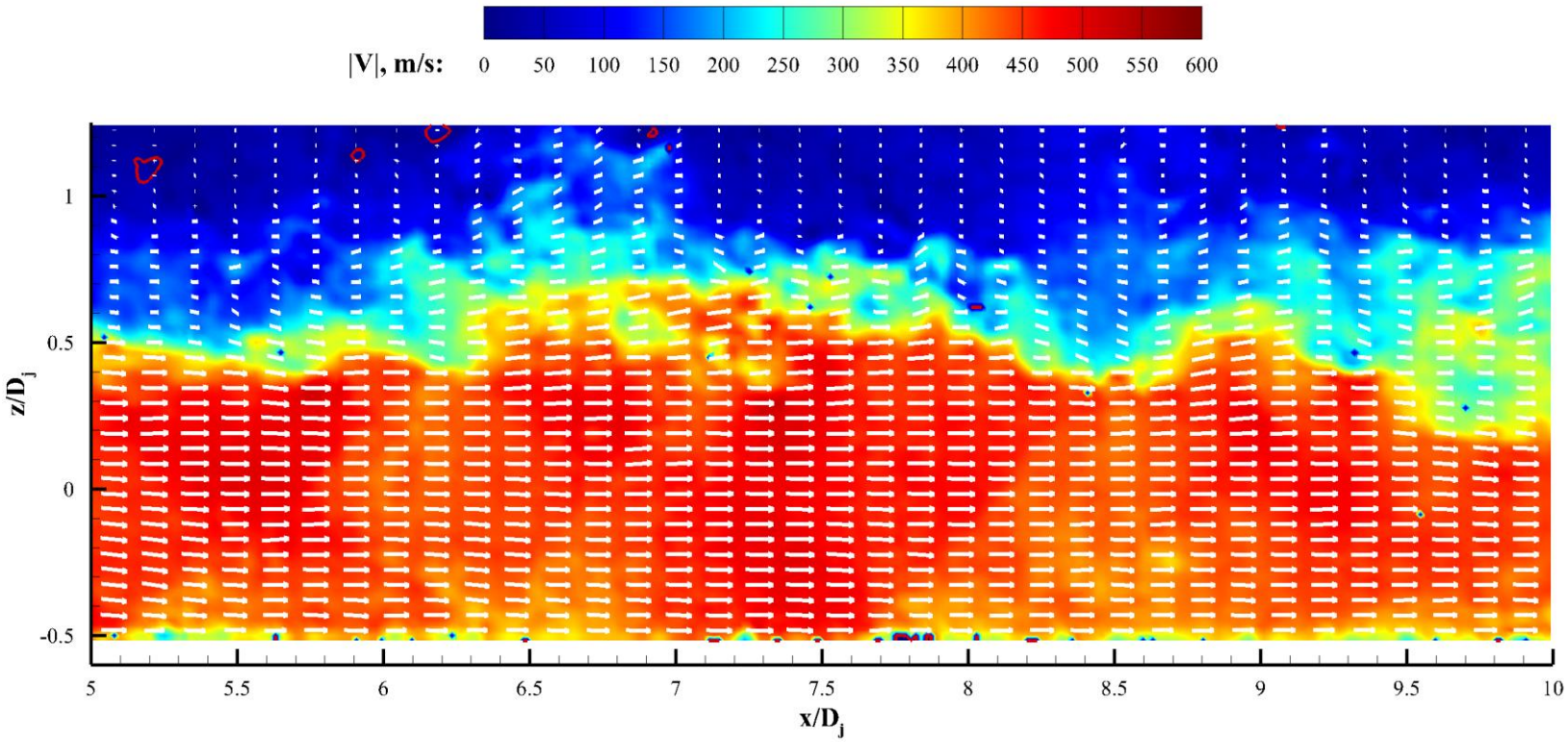

Figure 70. A sample instantaneous velocity magnitude image of the downstream region ($5 \leq x/D_j \leq 10$) with overlaid vectors.

4.3 Steady PSP

Steady pressure-sensitive paint measurements were obtained on the rigid surface. Refer to Section 2.7.1 for details regarding the experimental setup, paint calibration, data acquisition parameters, and measurement uncertainty estimations. The mean pressure ratio, P/P_{ref}, obtained from 500 images is shown in Figure 72 for the $h/D_j = 0.50$, $NPR = 5.0$ rigid-surface case. The full imaging region, which extends from $0 \leq x/D_j \leq 9.25$ and $y/D_j \leq \pm 4.5$, is shown in this figure to illustrate the entire field-of-view. Subsequent PSP data are trimmed to a more relevant field-of-view. It should be noted that the reference pressure condition, P_{ref}, corresponds to the no-flow case (i.e., ambient conditions where $P = P_{amb}$). As a result, P/P_{ref} is a direct measure of the pressure differential across the thickness of the surface, where $P/P_{ref} \geq 1$ corresponds with an inward (away from the jet flowfield) deflection of the surface, while $P/P_{ref} \leq 1$ corresponds with an outward (into the jet flowfield) deflection of the surface.

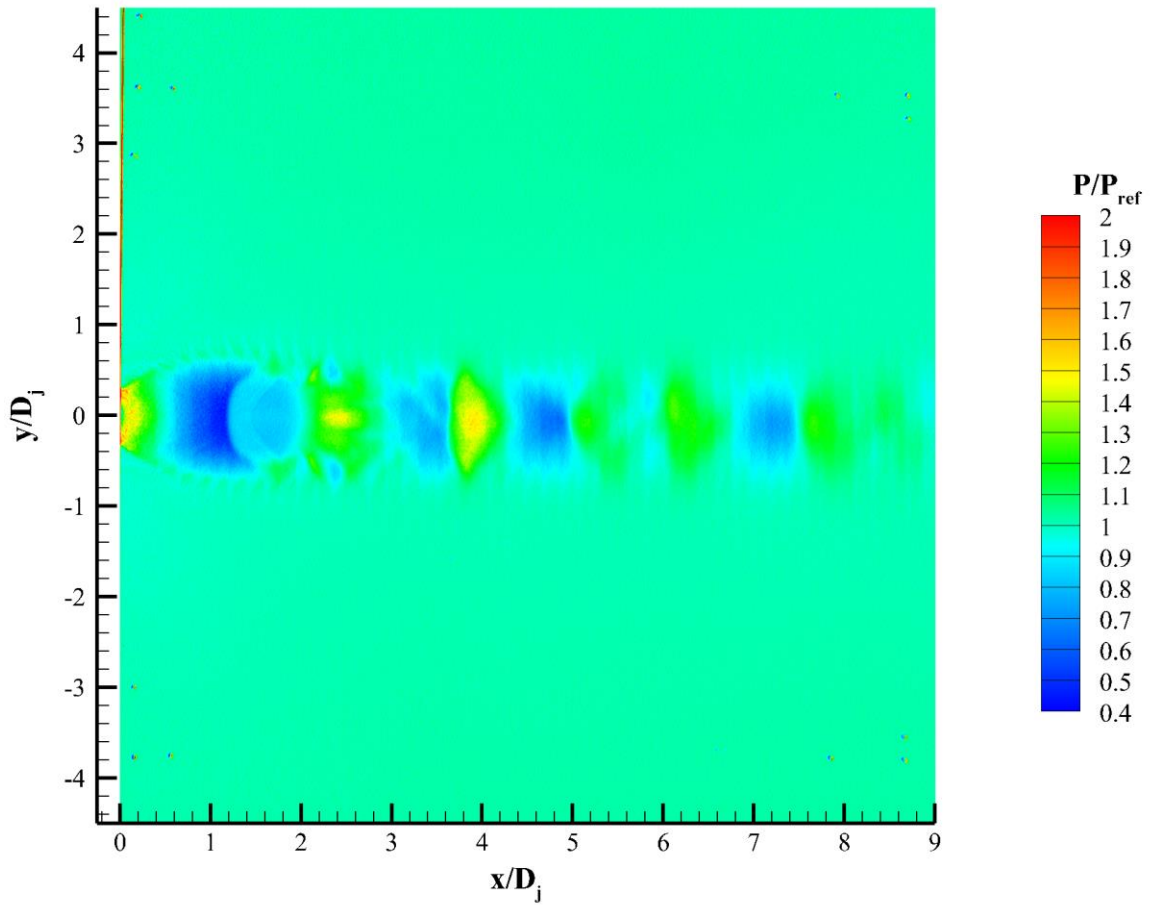

Figure 71. Mean steady pressure ratio for the $h/D_j = 0.50$, NPR = 5.0 rigid-surface case.

Figure 73 presents the pressure distribution along the symmetry plane ($y/D_j = 0$). Immediately at the jet nozzle exit, P/P_{ref} approaches 1.5. This is a result of near-stagnation conditions as the flow expands outward at the nozzle exit or, possibly, increased pressure behind the plate-induced shock. P/P_{ref} achieves its maximum value at $x/D_j = 0.12$. The location of the maximum pressure is important to note, particularly in reference to the upstream edge of the compliant surface, which is located at $x/D_j = 0.27$. Thus, a large portion of the first pressure peak is actually positioned on the model support frame instead of on the compliant surface. P/P_{ref} remains greater than unity until $x/D_j = 0.48$, at which point the pressure begins to induce an upward (into the jet) deflection.

As x/D_j increases, P/P_{ref} decreases as the flow accelerates within the first shock cell, where it reaches a minimum of approximately 0.45. While accelerating, the footprint of the jet increases in width, which is consistent with an expanding supersonic flow. P/P_{ref} undergoes a step increase at $x/D_j \approx 1.13$, and enters a region of nearly constant pressure which extends until $x/D_j \approx 2$. Within that region, $P/P_{ref} \approx 0.80$, which is slightly below ambient conditions. Thus, P/P_{ref} is less than unity nearly everywhere within the first shock cell. This is an important observation as it indicates that there is a unidirectional pressure differential across the thickness of the plate everywhere within the first shock cell (since conditions on the back side of the plate are approximately ambient, $P/P_{ref} \approx 1$ there). This finding may have important ramifications for the compliant-surface case in terms of the direction of surface deflection. The pressure increase, and subsequent region of

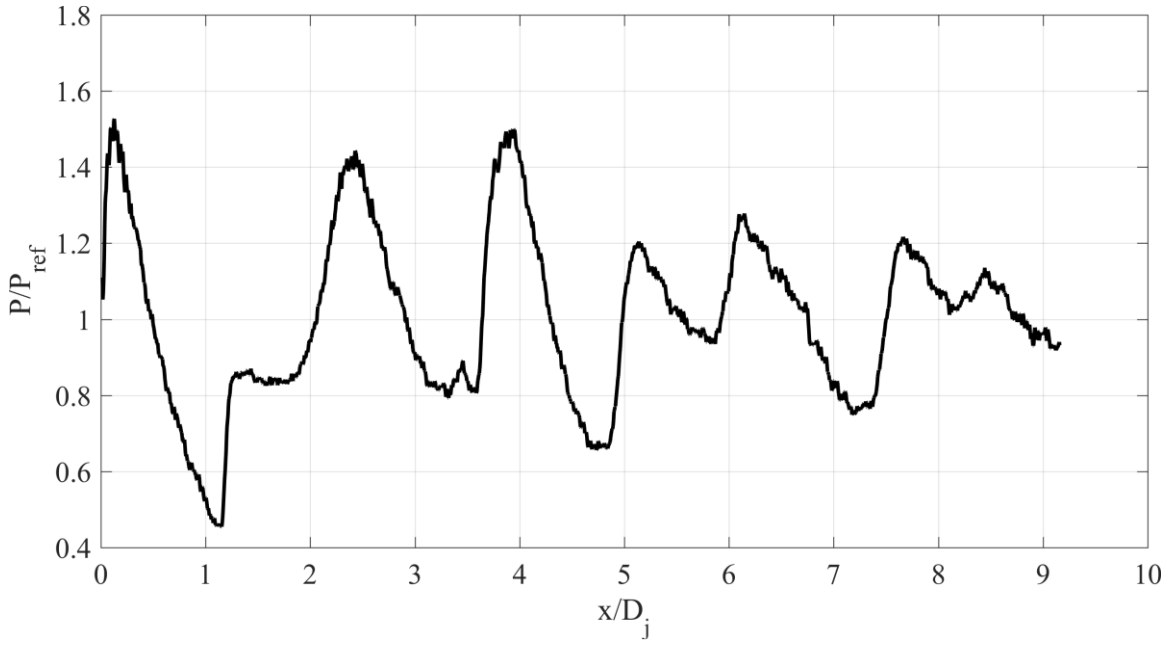

Figure 72. The pressure distribution along the centerline of the jet flowfield.

approximately constant pressure, are due to the SBLI separation shock and boundary-layer separation regions, respectively.

At approximately $x/D_j \approx 2$, P/P_{ref} increases again, reaching a local maximum of $P/P_{ref} \approx 1.35$ at $x/D_j = 2.4$. This high pressure region is relatively small in width. From this point on, the alternating pattern of decreasing pressure (flow acceleration) followed by regions of increased pressure (flow deceleration) continues through the remainder of the measurement domain. In general, the amplitude of pressure oscillation decreases as x/D_j increases. However, there are several important characteristics to point out. One is a particularly high-pressure region found near $x/D_j = 3.85$ where $P/P_{ref} \approx 1.55$. Also note that P/P_{ref} undergoes regions with two smaller amplitude pressure rises on either side of a slight pressure decrease. This occurs twice; once from $5 \leq x/D_j \leq 6.5$ and then again $7.5 \leq x/D_j \leq 8.75$. This pattern is due to the altered shock-cell spacing of the jet/rigid-surface configuration, which now has a more staggered shock-cell structure instead.

Due to the very low speeds and the low PSP signal-to-noise ratio at these pressures, the pressure ratio is nearly unity at all locations for which $y/D_j \geq \pm 1$, as shown in Figure 72. For this reason, all subsequent PSP images no longer display the entire imaging area.

The extremely small dots near the corners of the imaging region in Figure 72 are the registration marks used to ensure alignment between the wind-on and wind-off images. A slight vertical banding effect can been seen in the PSP data, particularly near the edges of the jet footprint. These bands are artifacts of the rigid-surface model manufacturing and machining process.

4.4 Surface Oil Flow Visualization

Surface oil flow visualization (SOFV) experiments were carried out on the rigid surface. A description of the experimental setup, data acquisition parameters, and image post-processing can be found in Section 2.7.2. It is important to note that oil flow visualization is a qualitative technique and yields little quantitative data. The images obtained using SOFV are greatly influenced by the consistency of the mixture used, its application prior to testing, as well as the duration over which the pattern is allowed to develop. For this reason, inferences based on the distance traveled by the oil mixture should be avoided. However, SOFV is useful for the insight it provides into the flow structure in terms of separated versus attached flow, and in the identification of recirculation regions and/or vortex locations.

A single oil flow image, obtained after several minutes of running the jet, is shown in Figure 74 for the h/D_j = 0.50, *NPR* = 5.0 rigid-surface case. The imaging region extends from $0 \leq x/D_j \leq 9$ and $y/D_j \leq \pm 3$. The SOFV image clearly demonstrates the underexpanded nature of the flow exiting the nozzle, as the streaklines have a significant outward (*y*-direction) component everywhere except along the $y/D_j = 0$ symmetry line. A prominent oil separation line denotes the position of the SBLI separation shock at $x/D_j \approx 1.1$. Two counter-rotating recirculation regions positioned on either side of $y/D_j = 0$ are located behind the oil separation line. There is clear flow reversal within the recirculation region. A flow reattachment point is located at the aft end of the recirculation region at $x/D_j \approx 2.4$, and flow emanates outward from it in both the upstream and downstream directions. The downstream-facing streaklines continue in a mostly axial direction until they encounter a second oil separation line at $x/D_j \approx 3.6$, which marks the second shock cell. Subsequent shock cells become less prominent due to the decreased shock strength, but the flow's tendency to expand and contract is evident in the figure. The lack of complete symmetry in the

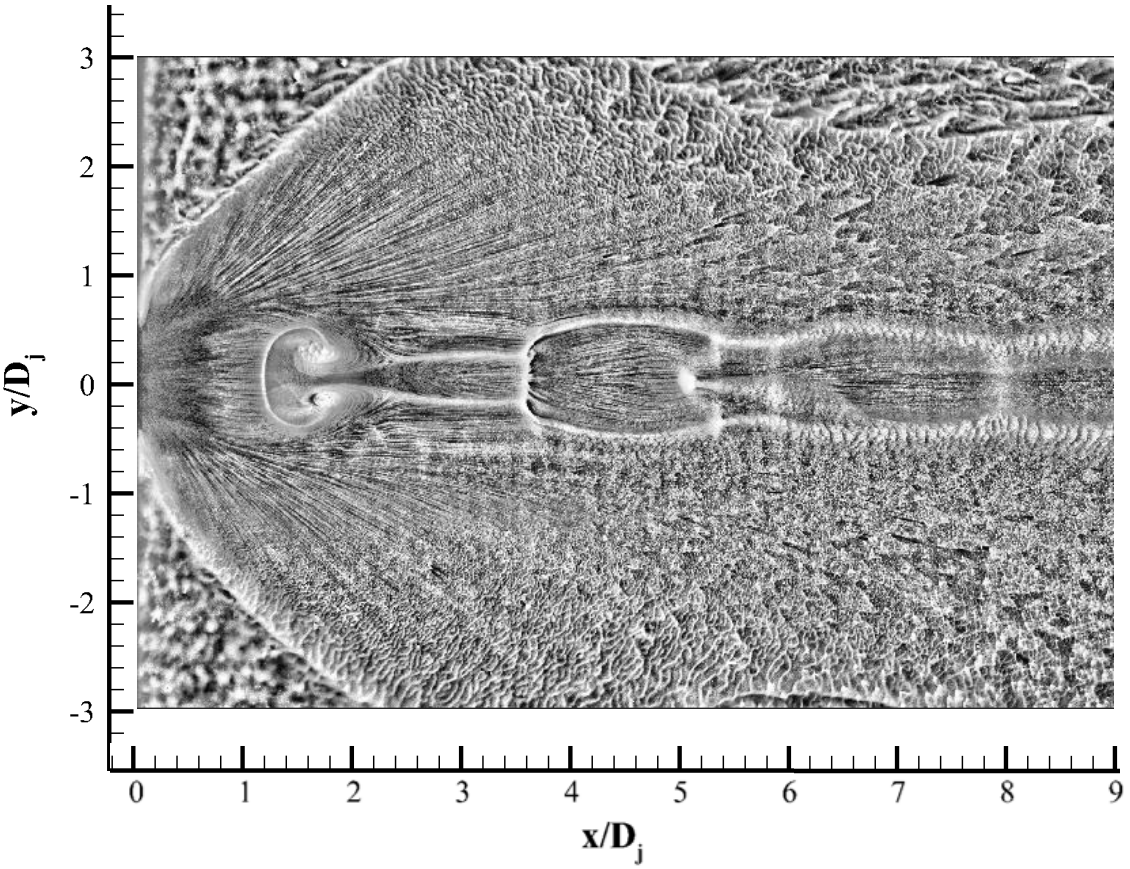

Figure 73. An instantaneous surface oil flow image for the h/D_j = 0.50, NPR = 5.0 rigid-surface case.

image is likely due to differences in the oil mixture consistency and application thickness, and is not an indication of an asymmetric flowfield.

4.5 Further Investigation of the SBLI

The schlieren imagery, planar PIV, pressure-sensitive paint (PSP), and surface oil flow visualization (SOFV) all indicate that a strong shock/boundary layer interaction (SBLI) exists within the h/D_j = 0.50, NPR = 5.0 flowfield, and that it is strong enough to induce complete boundary layer separation and flow reversal. A more complete understanding of the flowfield can be obtained by combining these forms of data. Figure 75, via image overlay and alignment, presents schlieren imagery, planar PIV, PSP, and SOFV data in qualitative form. All data types corroborate each other as there is good alignment and consistency between results.

The SOFV image shows a large teardrop-shaped separation region (approximately bounded by the dashed red line). The upstream boundary of the recirculation region is defined by a separation oil flow line (labeled "S" in the figure) that forms near the location of the SBLI separation shock. Within the separated region, two primary vortices induce strong flow recirculation, as illustrated by the blue arrows. The SBLI separation region reattachment point, labeled by the letter "R" in the figure, acts as a source from which streaklines radiate outwards. Farther downstream, the flow is primarily oriented in the streamwise direction. The second shock cell, identified by a second oil separation line, is evident, after which the flow again appears to expand and accelerate. Additional shock cells can also be seen, becoming less and less pronounced.

The PSP, planar PIV, and schlieren data corroborate the above flowfield description based on the SOFV. For instance, the pressure can be seen to decrease within the first shock cell, and it coincides with spreading oil streaklines, which indicate supersonic flow acceleration and expansion. The minimum pressure is observed just before the oil separation line, and the PIV data confirm the continual flow acceleration within the first shock cell.

The beginning of the SOFV recirculation region aligns with the SBLI separation shock observed in the schlieren and with the accompanying velocity drop in the PIV. In addition, the pressure undergoes a step increase at the same location due to passage through the shock wave. Within the recirculation region, the PIV data confirm that the flow is reversed, as observed in the oil flow streaklines. The low velocity magnitudes point to a nearly constant pressure, which is

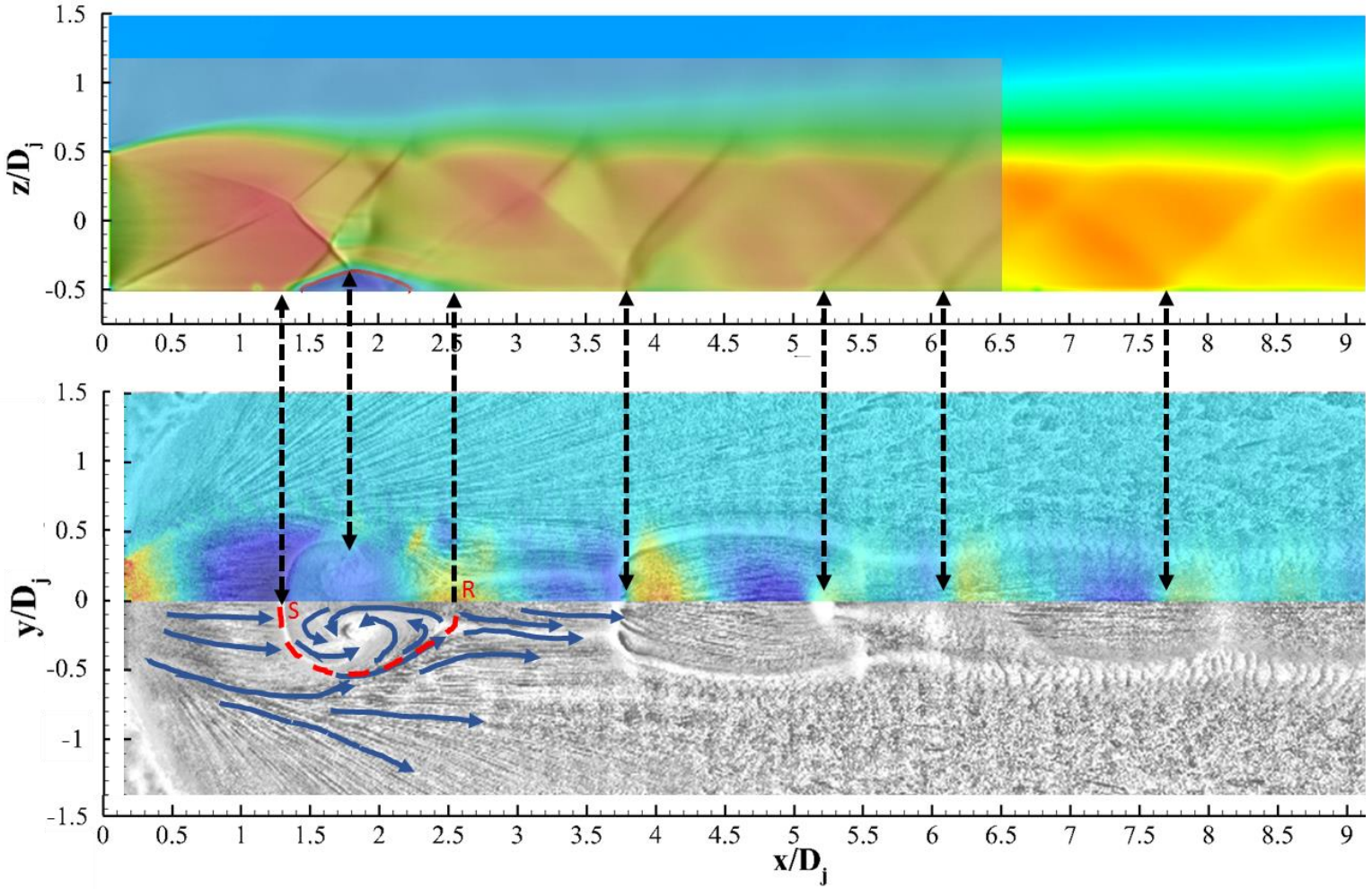

Figure 74. A joint view of schlieren, planar PIV, pressure-sensitive paint, and surface oil flow visualization shows strong agreement and alignment of the primary flow features including the separation shock, recirculation region, reattachment location, and shock positions in later shock cells.

exactly what the PSP data show, and is consistent with the boundary-layer theory expectations for a separation region.

The PSP data show a region of increased pressure at the aft end of the separation region, coinciding with the reattachment point identified in the SOFV image. Alignment of the reattachment location with the schlieren image indicates that the separation region extends farther downstream than the schlieren imagery alone might suggest. However, the true reattachment location agrees quite well with where the PIV data suggest it may be.

Downstream of the reattachment point, the SOFV streaklines are oriented in a primarily streamwise direction. The decreasing pressure within that region points to a flow acceleration/expansion. The PIV data also show a velocity acceleration with in this region.

The streaklines then encounter a second separation oil line, which is observed to align nicely with a shock-cell induced (nearly) normal shock and the corresponding PIV-velocity decrease. The pressure increases at the shock location, as expected. Post shock, the streaklines again show outward flow expansion and the pressure within this region decreases accordingly. The pattern continues through the remaining visible shock cells, although with decreasing amplitudes. For instance, schlieren and/or PIV shocks impinging on the surface in the third through fifth shock cells align well with the SOFV.

Together, the schlieren imagery, planar particle image velocimetry, pressure-sensitive paint, and surface oil flow visualization data provide a thorough and consistent description of the flowfield. The position and extent of the shock/boundary layer interaction region are apparent, as is the jet's shock-cell structure. Additionally, regions of flow expansion and acceleration can be identified using the oil flow, surface pressure data, and the velocimetry data.

4.6 Tomographic PIV

Tomographic PIV data were obtained for the h/D_j = 0.5, NPR = 5.0 rigid-surface case. For information regarding the experimental setup, calibration, and data processing, the reader is referred to Section 2.6.4. As described in Section 3.4, all isometric tomographic PIV results are presented using the same perspective: *as if viewing the jet from above and behind (i.e., through) the rigid or compliant surface.* This perspective allows for a line of sight into the interior of the flowfield, as well as for convenient inspection of the near-wall region and the shock/boundary layer interaction. The nozzle is located at the lower right in the figures, and the streamwise

direction is upward and to the left. The lower half of the jet is imaged, so the upper face of the measurement volume is located near the jet symmetry plane. The rigid surface is oriented vertically (in the *xy*-plane) at z/D_j = -0.50. Near-wall values have been blanked out so as to allow for a line-of-sight into the flowfield.

Mean tomographic PIV results, obtained using 250 instantaneous velocity snapshots, are shown in Figure 76 using both 2D-slice contour plots and isosurfaces of $\bar{U}$. Figure 76 a) presents 2D-slice contour plots at the y/D_j = 0 and z/D_j = -0.50 planes. The figure confirms that the flow accelerates within the first shock cell, and that the jet expands in both the *z* and *y* directions. A low-speed region can be seen near x/D_j = 2. In the isolated jet case, the low-speed region was the subsonic flow found behind the Mach disk and was consequently found along the jet axis (z/D_j = 0). In this case, however, the low-speed region is created by SBLI-induced boundary-layer separation and so it is found near the wall (z/D_j = -0.5) instead. The contour plots show that the flow accelerates as it either a) *diverts around* the SBLI, as shown in the constant-*z* plot, or b) *passes over* the SBLI, as shown in the constant-*y* plot.

In Figures 76 b) – d), the planar contour plots are shown with increasing amounts of transparency, so as to incrementally reveal the $\bar{U}$ isosurfaces within the measurement volume. This approach is used because it facilitates understanding of the three-dimensional nature of the isosurfaces, and in identifying which isosurfaces open on which face of the volume.

Figure 76 e) shows the fully revealed mean $\bar{U}$ isosurfaces. The structure is similar to that seen for the isolated jet in that there are clear nesting of isosurfaces in regions of high- and low-speed flow. As previously mentioned, the location of the low-speed region changes from a position at the jet axis for the isolated jet, to one at the rigid-plate surface for the rigid-surface case. In this experimental setup, the tomographic PIV data do not effectively capture shock waves or reversed

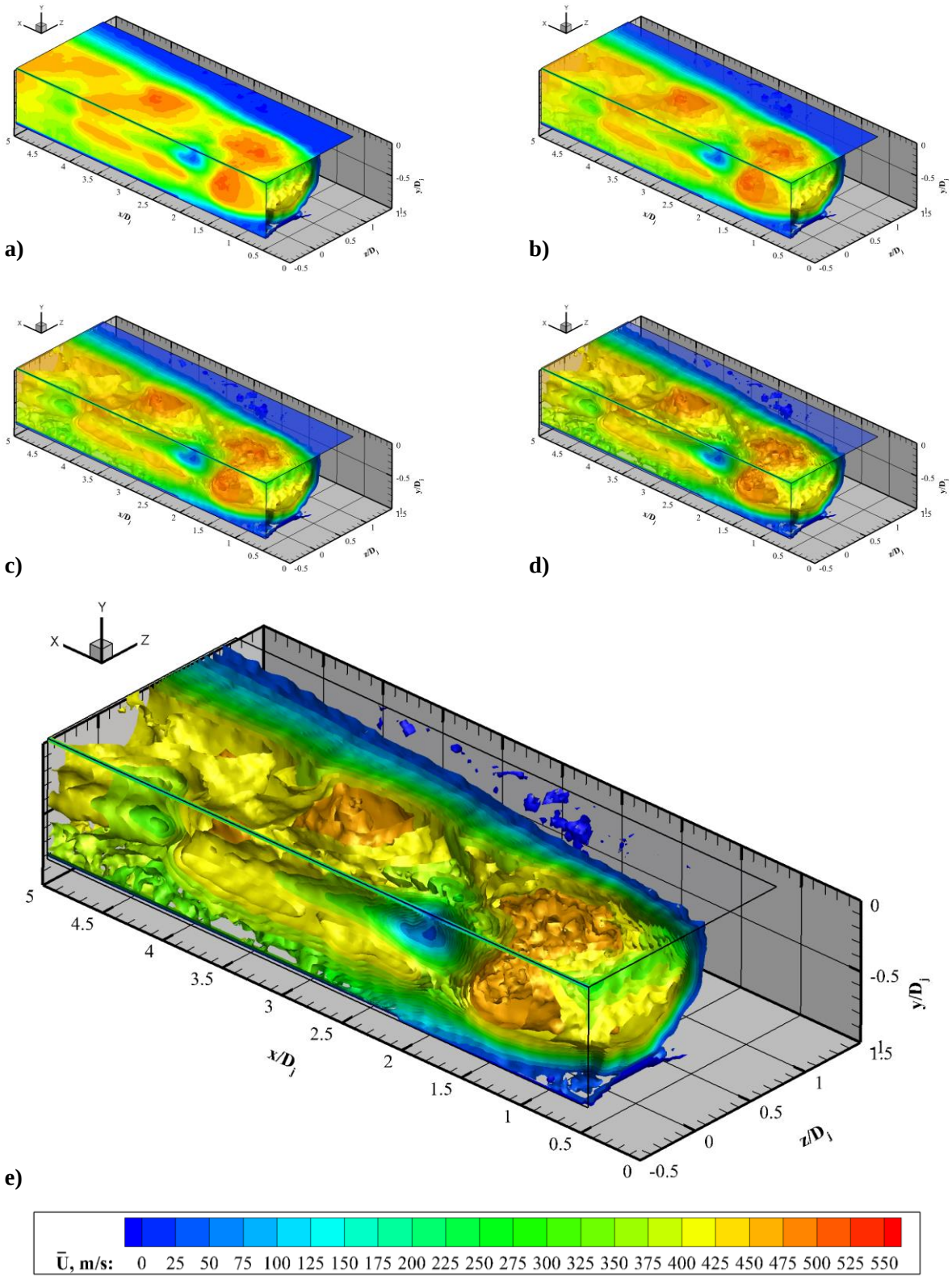

Figure 75. $\bar{U}$ contour plot and isosurfaces within the tomographic PIV measurement domain for the h/D_j = 0.50, NPR = 5.0 rigid-surface case. In a) – e), the contour plots become increasingly more transparent, providing context for the velocity isosurfaces within the volume.

flow within the SBLI recirculation region. The shock waves are difficult to capture due to their unsteady nature and the spatial averaging caused by the three-dimensional interrogation windows. Mean flow reversal within the SBLI recirculation region was not obtained due to proximity to the surface and also the effects of spatial averaging. The planar PIV data indicate that the $\bar{U} = 0$ region extends approximately 2.5 mm from the surface. The tomographic PIV voxels are only slightly smaller than this (1.31 mm cubes), and so only few voxels can be expected to contain reversed flow. Challenges with laser surface reflections and effectively imaging the near-wall region further contributed to the difficulties in imaging the reversed flow. However, $\bar{U}$ values as low as 25 m/s were observed in the near-wall region, and the high standard deviation in $\bar{U}$ at that location indicate that many instantaneous snapshots do contain flow reversal.

Elsewhere, the $\bar{U}$ values observed in the tomographic PIV results compare favorably with those seen in the planar PIV data for the rigid-surface case. After the SBLI low-speed region, the flow accelerates again in the second shock cell. The second low-speed region is found at

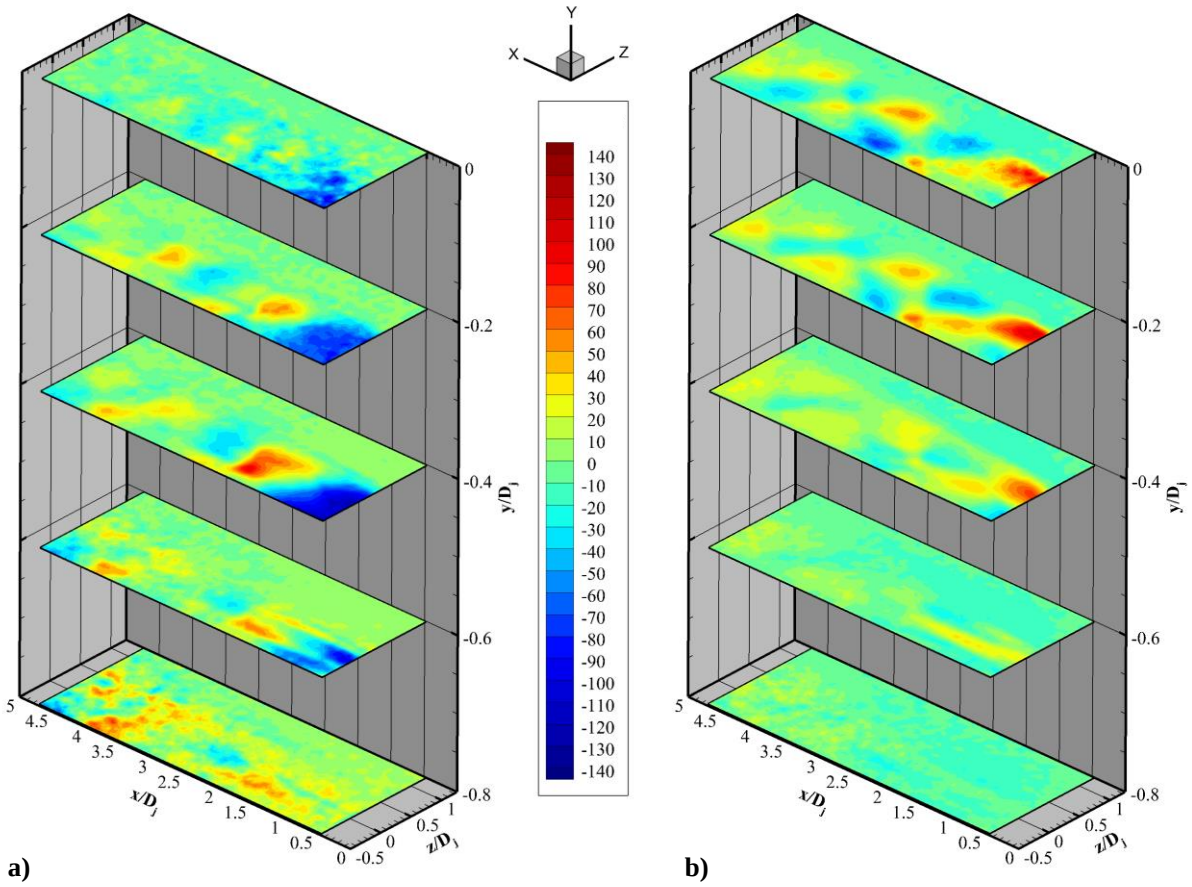

Figure 76. Constant-y planes showing a) $\bar{V}$ and b) $\bar{W}$ contours of velocity (m/s) for the $h/D_j = 0.50$, NPR = 5.0 rigid-surface case. The figures share a common color scale.

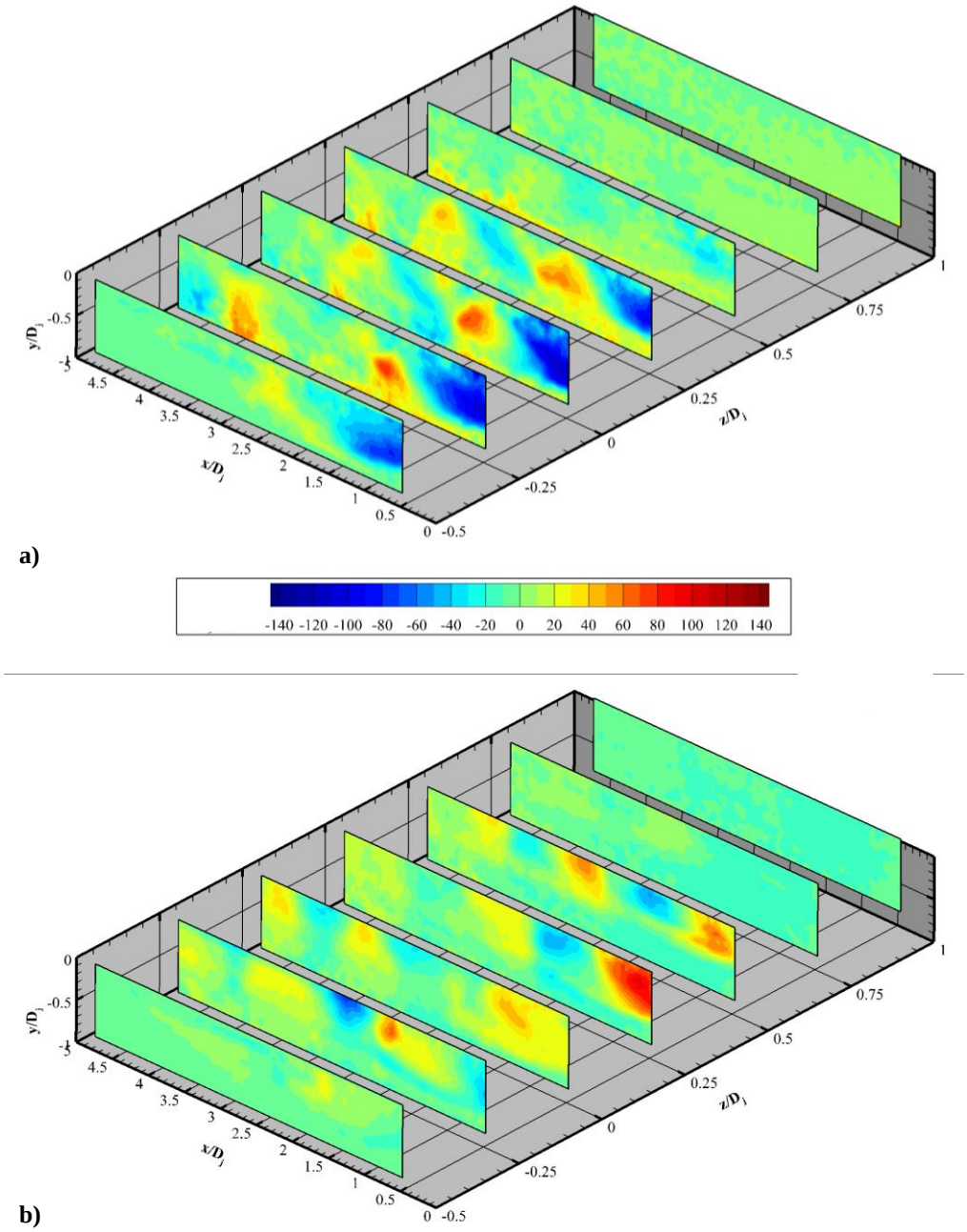

Figure 77. Constant-z planes showing a) $\bar{V}$ and b) $\bar{W}$ contours of velocity (m/s) for the h/D_j = 0.50, NPR = 5.0 rigid-surface case. The figures share a common color scale.

approximately x/D_j = 4.5. The shear layer can be seen to thicken in the positive z direction. Shear layer thickening is not as easily observed in the y-direction due to the finite measurement volume thickness and the viewing direction.

$\bar{V}$ and $\bar{W}$ contour slices are shown in Figures 77 and 78 using intentionally stretched axes to allow for complete viewing of the data. The data confirm that the jet undergoes alternating

expansion and compression regions, wherein the plume broadens and contracts, respectively. $\overline{V}$ and $\overline{W}$ experience similar velocity magnitudes. The highest magnitudes are typically experienced near the nozzle lip, at y/D_j = -0.5 and z/D_j = 0.5, for $\overline{V}$ and $\overline{W}$, respectively, while near the jet axis, both $\overline{V}$ and $\overline{W}$ are small.

The effect of the presence of the rigid surface can also be observed in the figures. For instance, Figure 78 b) shows that magnitude of $\overline{W}$ within the first shock cell on the z/D_j = -0.25 plane is noticeably less than that experienced on the opposite of the jet on the z/D_j = 0.25 plane. This is a direct consequence of the limited flow expansion on the plate-side of the jet. The z/D_j = -0.25 plane of the same figure also shows flow lifting and reattachment on either side of x/D_j = 2; this is likely flow passing over, and then reattaching behind, the SBLI separation region. Similarly, the z/D_j = -0.5 plane in Figure 78 a) shows the flow diverting around the SBLI region through $\overline{V}$.

4.7 Variation in h/D_j

The effect of variation in h/D_j was investigated for the NPR = 5.0 case. Data were obtained at h/D_j = 0.50, 0.55, and 0.60 using high-speed schlieren, PIV, PSP, and surface oil flow visualization. The shock position fluctuation time-series analysis used to confirm jet screech in the isolated jet case was carried out for all three separation distances. As with the h/D_j = 0.50 case that was previously discussed, the resulting PSDs for the h/D_j = 0.55 and 0.60 cases, shown in Figure 79, show that the shock motion was broadband in nature, without any dominant frequency bands.

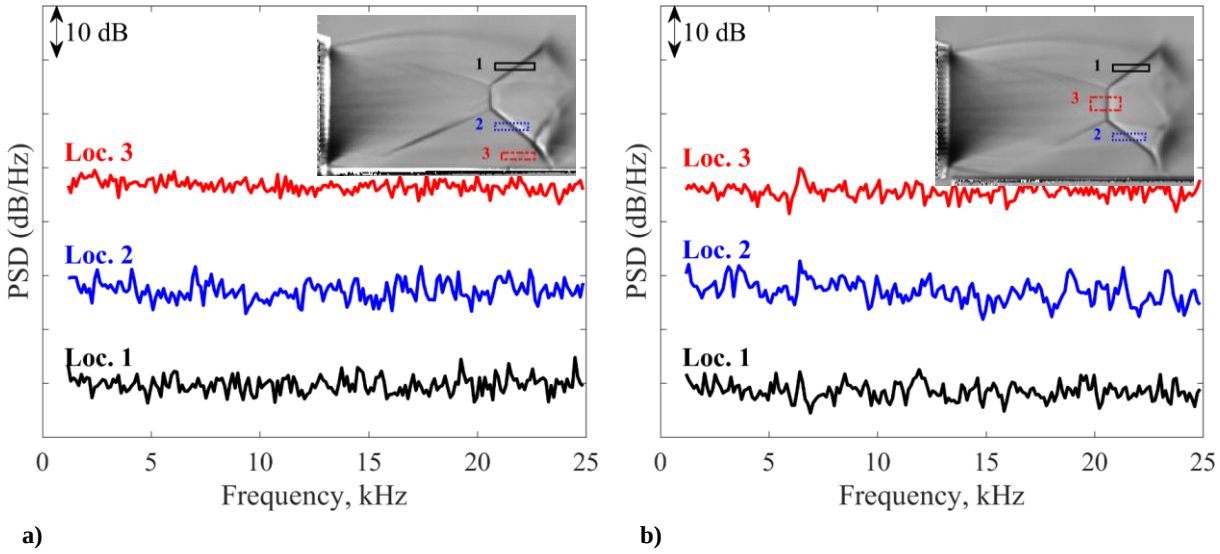

Figure 78. Shock-tracking time-series analyses conducted for the a) h/D_j = 0.55 and b) h/D_j = 0.60 rigid-surface cases at NPR = 5 show broadband responses.

A weak frequency peak may exist for the h/D_j = 0.60 case (Figure 79 b) near 6525 Hz, but its presence is uncertain; the peak amplitude in each curve is not substantially greater than others, and it is unclear if the peaks would have been identified if viewed individually. The isolated jet screech tone was observed near 7640 Hz (shock-tracking analysis) and 7605 Hz (acoustic spectra); these values differ from than seen in Figure 79 b) by approximately 15%. Data obtained at larger h/D_j (= 0.75 and 0.80, not shown) definitely did not exhibit any dominant frequencies. These results indicate that the presence of the surface inhibits the screech cycle, as previously shown by Wlezien[62] and others; hence, these results are expected. However, it is interesting to note that screech inhibition was also seen for the h/D_j = 0.60 case, despite the fact that the mean and instantaneous schlieren and PIV flowfield data appear nearly identical to those observed in the isolated jet case (which does undergo screech).

Mean PIV results for each h/D_j are given in Figure 80 for both the streamwise ($\bar{U}$, left column) and wall-normal ($\bar{W}$, right column) velocity components for the first shock-cell. Moving the plate from h/D_j = 0.50 to 0.55 (a distance of 0.635 mm) results in minor flow structure changes. The height of the recirculation region decreases, as does its streamwise extent and the velocity magnitude of the reversed flow within. Inspection of the wall-normal velocity component shows that the magnitudes of the lifting and reattaching flow before and after the SBLI are decreased.

With the increase in h/D_j, some degree of local flow expansion is allowed to occur near the nozzle lip, as evidenced in the wall-normal velocity component figures (Figure 80, right column). The schlieren data (see the insets in Figure 79) show that this local expansion results in a less prominent plate-induced shock, and it no longer extends all the way down to the plate surface.

Further increasing h/D_j to 0.60, as shown in Figure 80 c), causes large changes in flow structure and is characterized most obviously by the reformation of the Mach disk, and the subsequent subsonic region behind it. The SBLI region is greatly reduced in size, and only a little evidence of it remains in the $\bar{W}$ plot. At this larger separation distance, the flow's ability to expand on the near-surface side is even more pronounced, but it is clear from the figure that expansion towards the surface is still much less than that on the other side of the jet. The reformation of the Mach disk and reduced extent of the SBLI region decrease the length of the first shock cell, as highlighted by the arrows in Figure 80 (left column), causing an upstream shift in the position of the rest of the shock cells as compared to smaller values of h/D_j. The shortened first shock cell

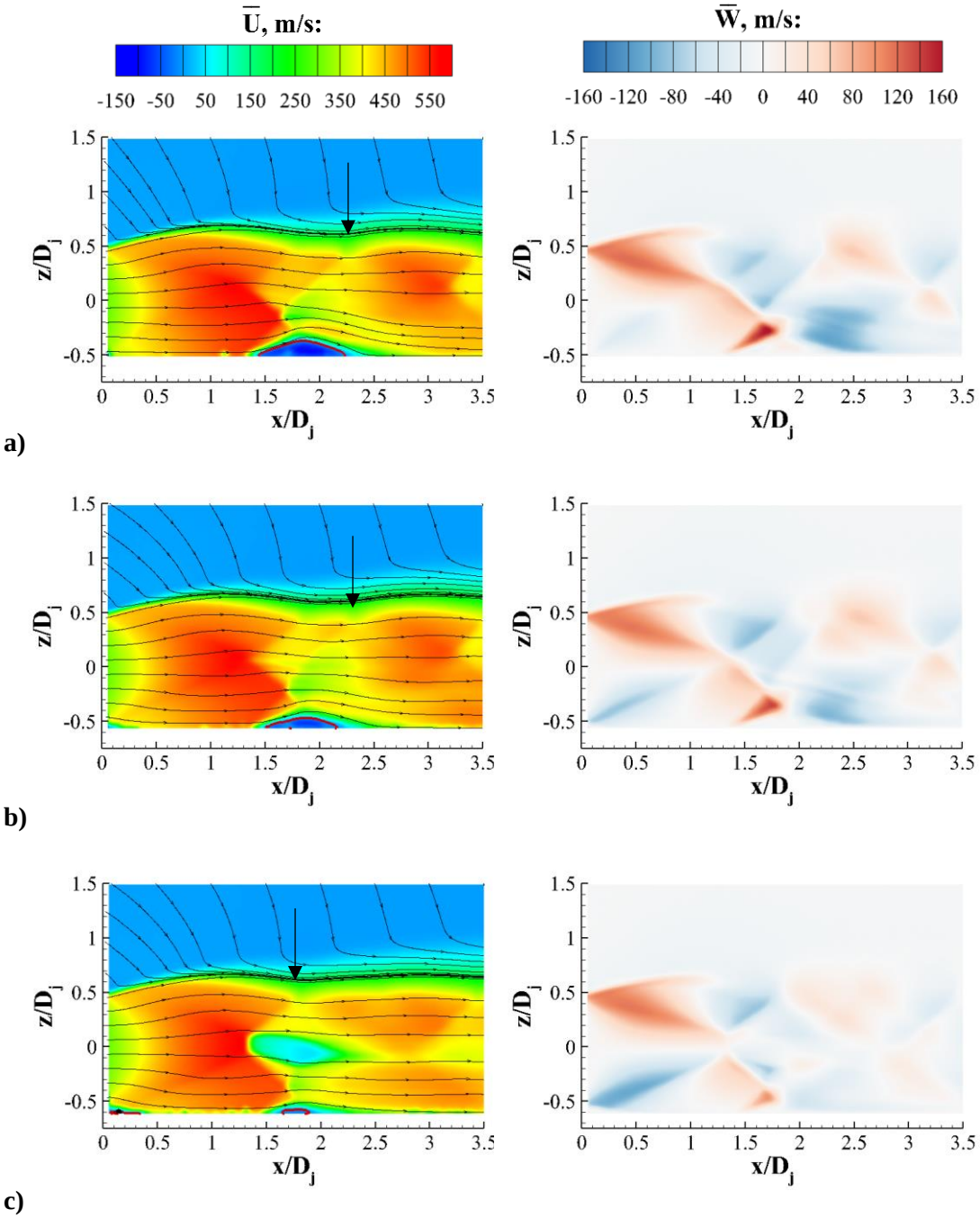

Figure 79. Mean streamwise velocity, $\bar{U}$, (left column) and wall-normal velocity, $\bar{W}$, (right column) PIV results for h/D_j = a) 0.50, b) 0.55, and c) 0.60, NPR = 5.0 rigid-surface cases. Arrows identify the approximate length of the first shock cell.

length can also be seen in the surface pressure results discussed later. In addition, at this separation distance, the previously primarily wall-bounded low-speed regions of the shock-cell structure raise from the surface and are now primarily located within the main jet flow.

The effect of variation in h/D_j can be quantitatively assessed through the use of profiles through the jet. Figures 81 – 83 present $\overline{U}$, $\overline{W}$, and M profiles, respectively, at four x/D_j locations before the SBLI for the three h/D_j under consideration. Measurement uncertainties are included for the h/D_j = 0.50 case. Uncertainties for the other cases are expected to be similar. The $\overline{U}$ and M profiles show that there is little difference between the different h/D_j cases for any of the x/D_j values under consideration within the jet primary shear layer or within the upper half of the flowfield. Near to the wall, however, significant differences exist. At x/D_j = 0.50, $\overline{U}$ and M are increased for the larger separation distance cases, and the amount of increase is related to h/D_j. This is a direct effect of the reduction in flow expansion restriction caused by the larger separation distances. This effect is confirmed upon inspection of the $\overline{W}$ profiles at x/D_j = 0.50, which also show larger velocity magnitudes for increasing h/D_j. As x/D_j increases, the region of increased $\overline{U}$ and M moves farther into the jet, and by x/D_j = 1.25, there is a near-wall deficit (as compared to the h/D_j = 0.50 case) for the larger jet/surface separation distances. In this region, the $\overline{W}$ profiles show mildly positive (away from the wall) values. The decreased Mach numbers in the near-wall region just before the SBLI for the larger h/D_j cases lead to decreased shock strengths within the

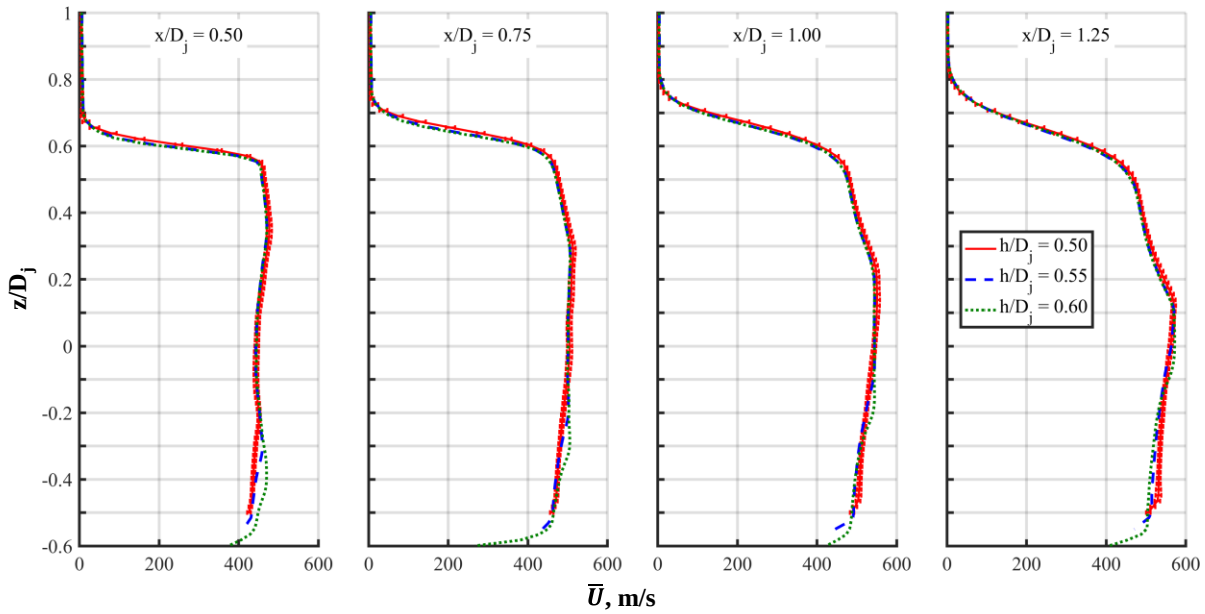

Figure 80. Profiles of $\overline{U}$ at selected x/D_j positions in the first shock cell (before the SBLI).

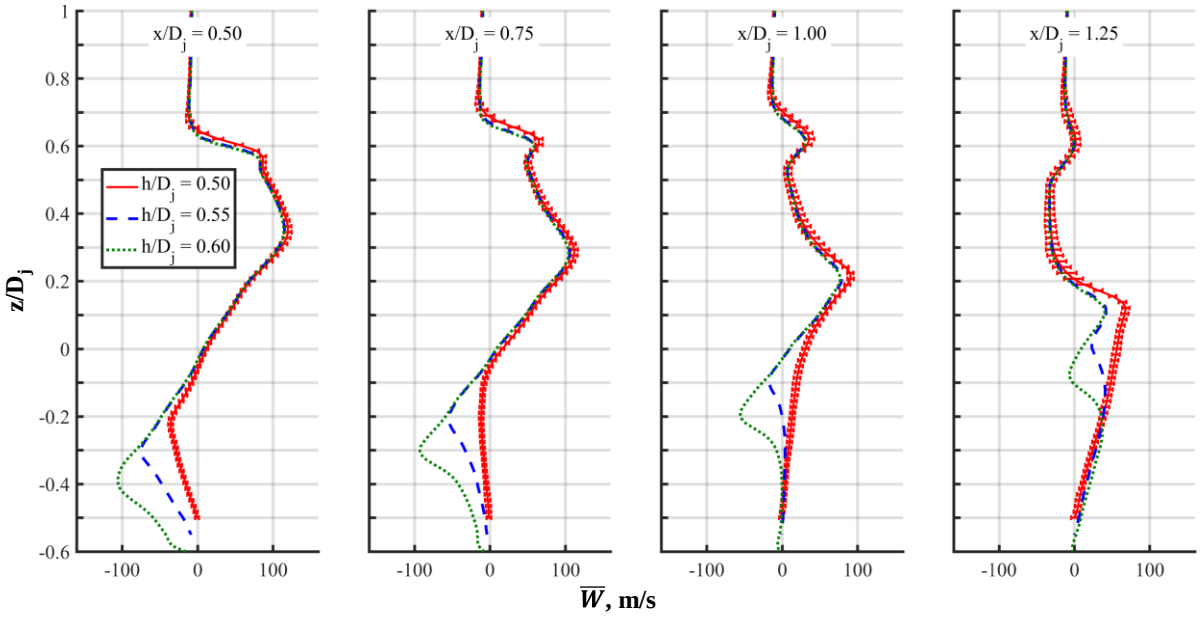

Figure 81. Profiles of $\overline{W}$ at selected x/D_j positions in the first shock cell (before the SBLI).

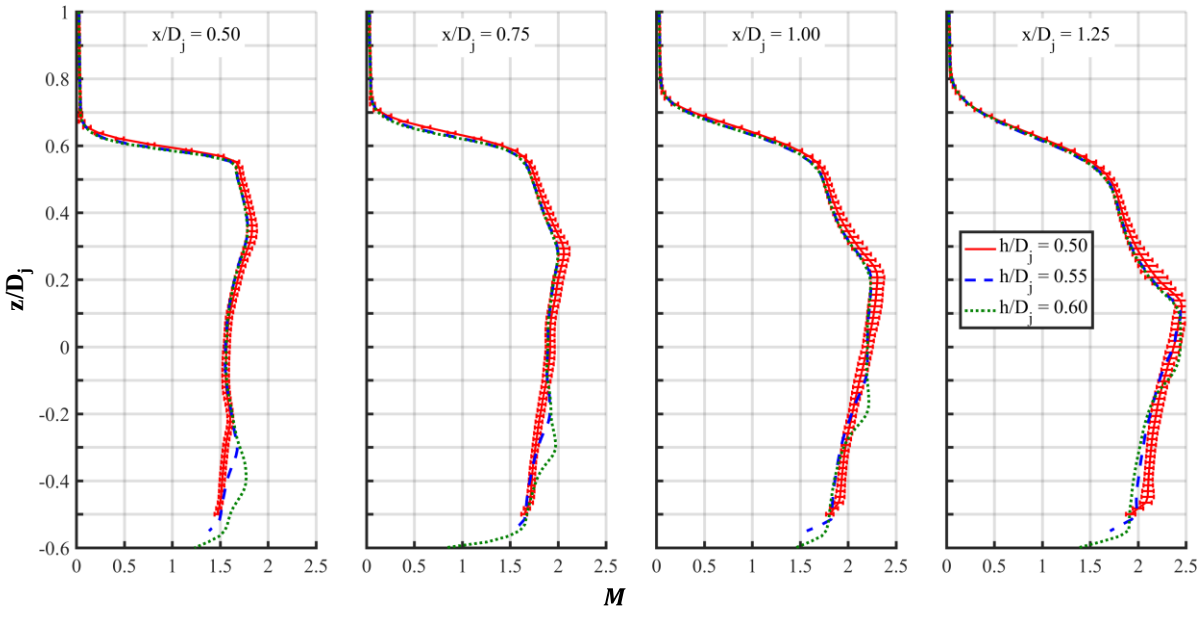

Figure 82. Profiles of M at selected x/D_j positions in the first shock cell (before the SBLI).

SBLI. This is accompanied by smaller and weaker SBLI separation regions and relatively increased near-wall velocities and Mach numbers on the other side of the SBLI.

The mean turbulence quantities also show the effect of variation in the plate-to-surface separation distance. Figure 84 displays how variation in h/D_j (rows) affects $\overline{w'w'}$ (left column) and $\overline{u'w'}$ (right column). For $h/D_j = 0.50$, the maximum observed $\overline{w'w'}$ is found in the separation-region shear layer recompression region. Increasing h/D_j to 0.55 reduces the maximum observed value by nearly a factor of two. As with the $h/D_j = 0.50$ case, the shock-cell boundaries and slip line shear layers are clearly seen. Similarly, maximum and minimum values of $\overline{u'w'}$ observed within the SBLI separation region shear layer are greatly reduced with increased h/D_j. Further increasing h/D_j to 0.60 allows for the visualization of the turbulence production regions defined by the slip lines formed behind the Mach disk in both turbulence parameters. Despite the small size of the SBLI region for the $h/D_j = 0.60$ case as compared to the $h/D_j = 0.50$ and 0.55 cases, the characteristic SBLI turbulence signature remains, but with accordingly decreased magnitudes.

PSP and SOFV measurements corroborate the velocity-field data as shown in Figures 85 – 87, respectively. As h/D_j increases, the width of the jet footprint decreases, particularly within the first shock cell as shown by the PSP data. Careful inspection of the oil flow streaklines allows for the delineation of the first shock-cell boundaries, and shows its varying extent as h/D_j increases. The size and position of the recirculation region, as viewed by both the PSP data and the oil flow streaklines, change in the same manner as that predicted by the schlieren and PIV data. The width of the high-pressure region at the jet exit decreases and the oil flow streaklines clearly show a greatly decreased spanwise component as h/D_j increases. The minimum observed pressure is approximately constant across all tested h/D_j; this can be confirmed upon inspection of the PSP calibration curves (see Section 2.7.1). The PSP data show that within the first shock cell (and the SBLI separation region), the pressure is less than ambient for all three h/D_j cases. This may have

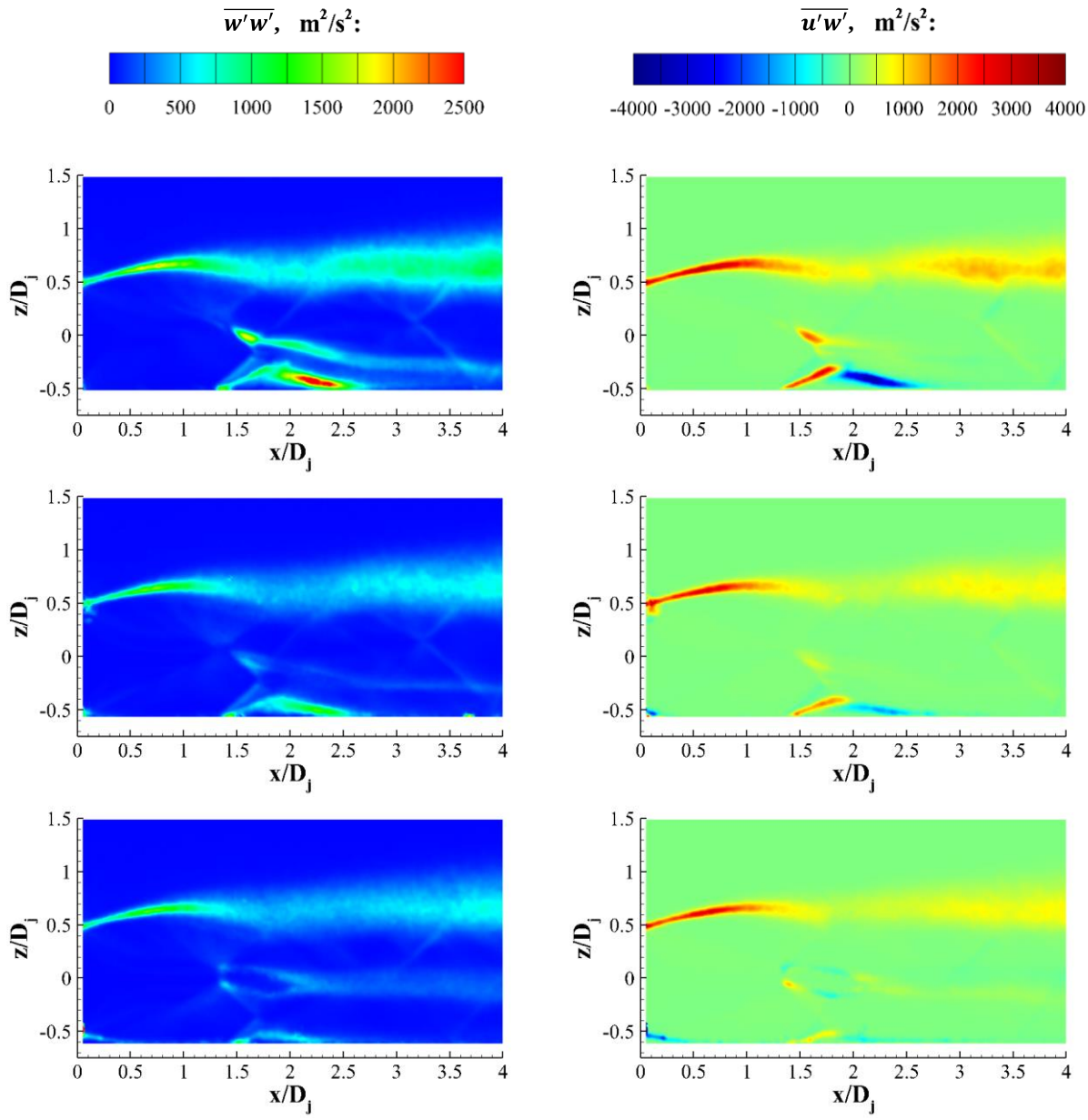

Figure 83. Mean turbulence quantities for $\overline{w'w'}$ (left column) and $\overline{u'w'}$ (right column) for h/D$_j$ = 0.50 (top row), 0.55 (middle row), and 0.60 (bottom row), NPR = 5.0 rigid-surface cases.

important implications for the compliant-surface case to be studied later, as it implies that there will be a pressure differential across the plate thickness within the first shock cell. A slight vertical banding effect can again be seen in the PSP data; these bands are artifacts of the surface manufacturing and machining process.

It was expected that the observed pressure range would decrease as h/D_j increases. This is true for the h/D_j = 0.60 case, but the h/D_j = 0.55 case exhibits greater measured pressures than either

of the other cases. This is true for all of the high-pressure regions (between shock cells), and is an unexpected observation. Since all PSP data were obtained within several hours of each other, it is unlikely that day-to-day variations caused the discrepancy. PSP calibrations were conducted using pressure taps, but the placement of the taps was optimized for the $h/D_j = 0.50$ case, leaving the possibility that the calibration was either inaccurate or required excessive extrapolation for the other cases. However, a unique calibration was generated for each run, and they all achieved very strong R^2 values (in excess of 0.99), as shown in Section 2.7.1. Additionally, the measured pressures obtained via the pressure taps were also noticeably higher for the $h/D_j = 0.55$ case than for the other two cases. Further, the intensity ratio histogram indicates that there was no more extrapolation used in the $h/D_j = 0.55$ case than for the 0.50 case. This leads to the conclusion that the increased pressure observed in the $h/D_j = 0.55$ case is indeed a real flowfield phenomenon. This is perhaps not so surprising after all; Wlezien observed coherent pressure loading at "intermediate" separation distances, which he attributed to an enhanced wall-normal flapping screech mode.[62]. Wlezien's "intermediate" separation distances were significantly larger than that observed in this study, but the nozzle geometry and nozzle pressure ratios considered in this study are also different.

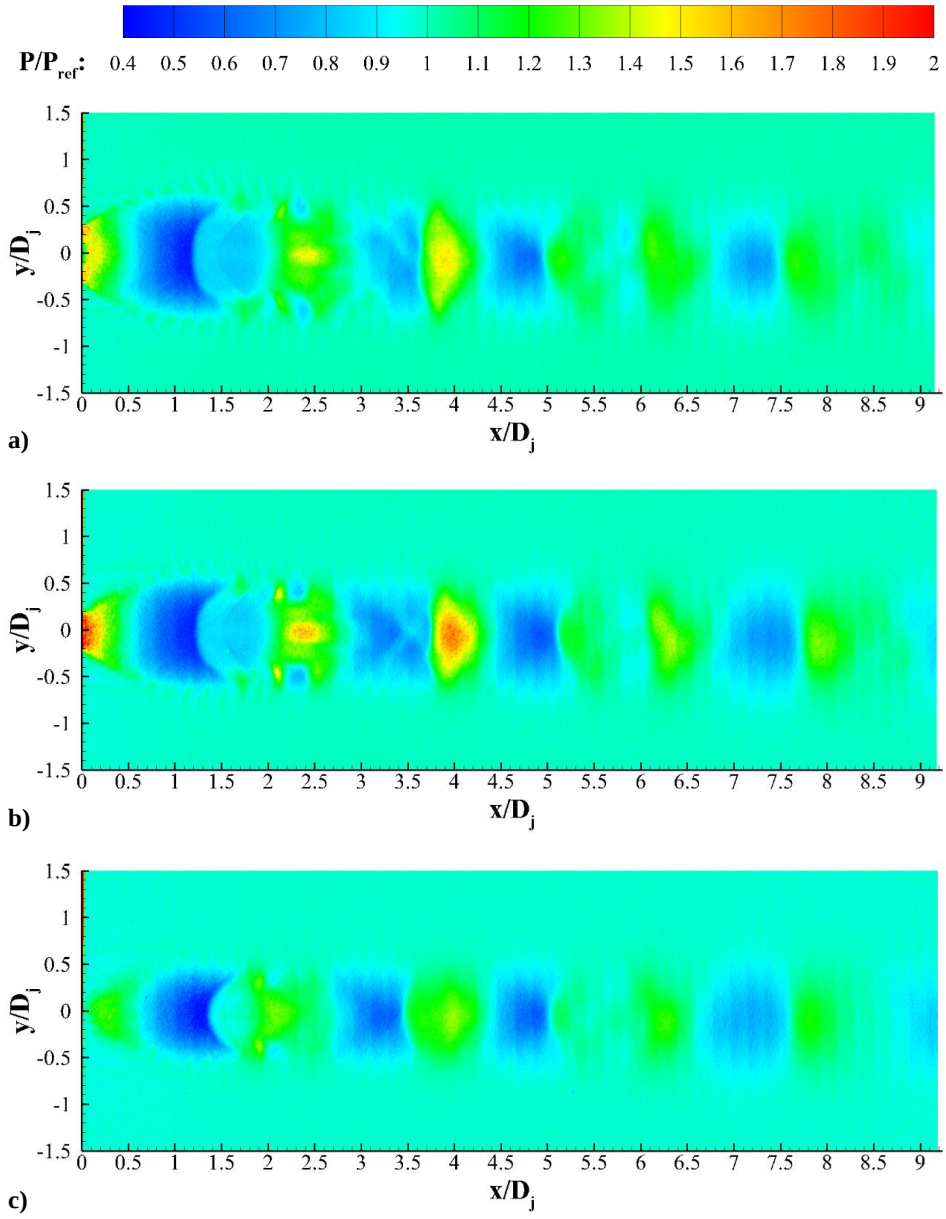

Figure 84. Mean pressure-sensitive paint results for h/D_j = a) 0.50, b) 0.55, and c) 0.60 with NPR = 5.0 rigid-surface case.

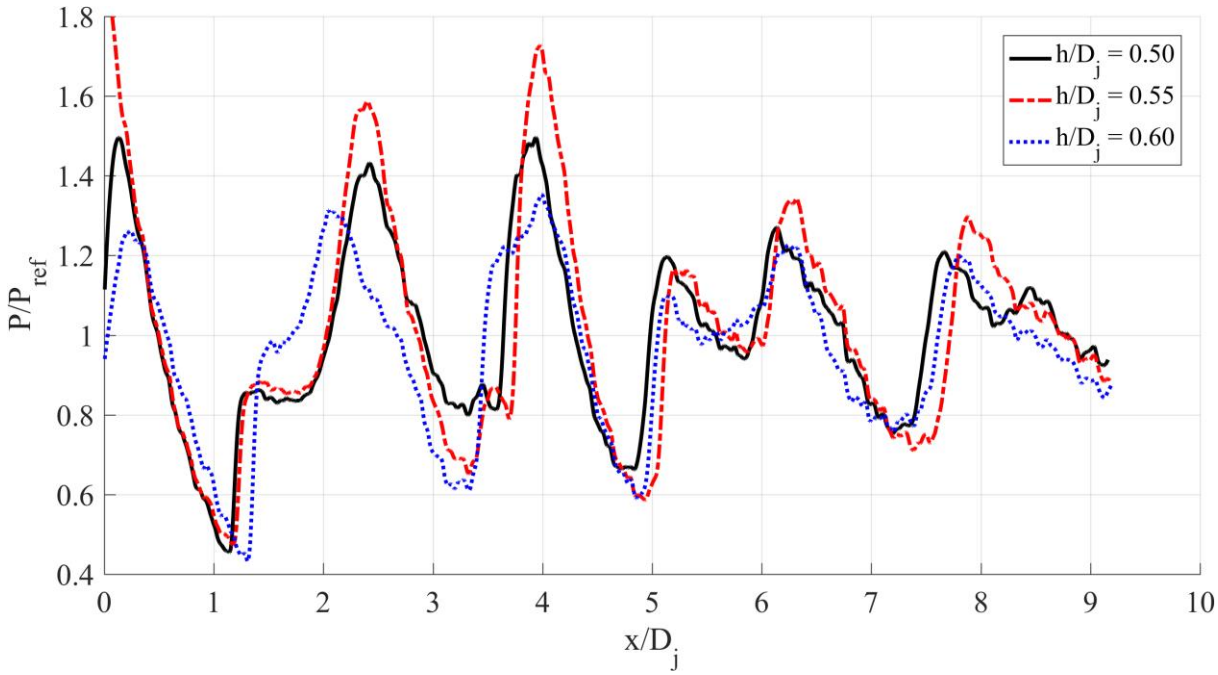

Figure 85. The pressure distribution along the symmetry line ($y/D_j = 0$) for various h/D_j at NPR = 5.0 for the rigid-surface case.

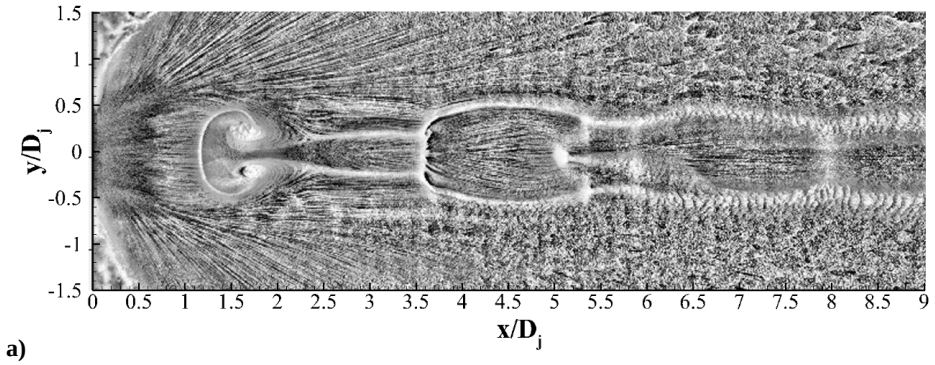

a)

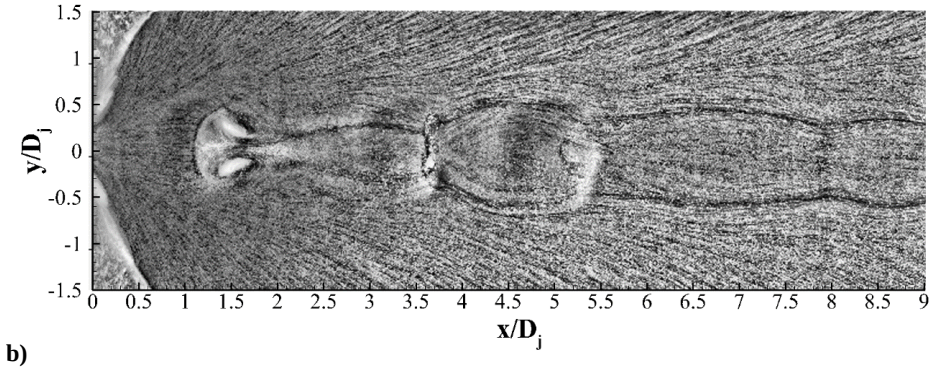

b)

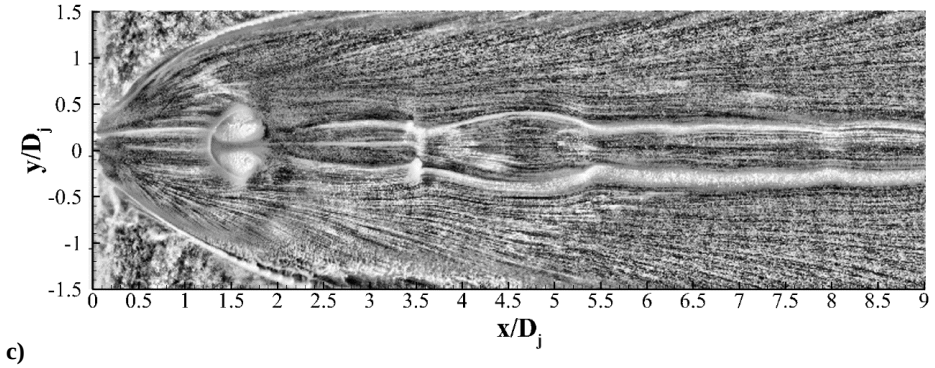

c)

Figure 86. Instantaneous surface oil flow images for h/D_j = a) 0.50, b) 0.55, and c) 0.60 with NPR = 5.0 rigid-surface case.

4.8 Variation in *NPR*

In addition to the primary dataset obtained at *NPR* = 5.0, data were also obtained at *NPR* = 4.0 and 3.0. Results obtained at these *NPR*s are briefly presented here for the h/D_j = 0.50 case. For reference and ease of comparison, the *NPR* = 5.0 results are shown in the figures, and each figure shares a common legend.

Mean streamwise velocity component, $\overline{U}$, contour plots are shown in Figures 88 a) – c) for *NPR* = 5.0, 4.0, and 3.0. The similarity between the flowfield is very evident between the *NPR* = 5.0 and 4.0 cases; the same characteristics (SBLI shock waves, SBLI separation region, downstream shock cell structure) are observed. The velocity magnitudes, the size of the SBLI separation region, and the length of the shock cells are decreased for the lower *NPR* operating condition. For the *NPR*= 3.0 case, the characteristic SBLI structure is no longer visible, and there is no apparent region of flow reversal. Consequently, the flowfield is noticeably more symmetric for this operating condition. This is due to the fact that the degree of underexpansion is significantly less at this operating condition, leading to a much narrower jet plume, which does not interact as strongly with the adjacent surface. This explanation also accounts for the low-speed flow near the surface, which is believed to be the jet plume shear layer and not a wall-induced boundary layer. Inspection of the Mach number contours (Figure 89), further illustrates these observations. Approximately nine shock cells can be seen for the *NPR* = 3.0 case, while only about four can been seen for the *NPR* = 5.0 case.

The turbulence quantities all show similar trends within the jet primary shear layer, as shown in Figures 90 a) – c) for the wall-normal Reynolds normal stress, $\overline{w'w'}$. As expected, the magnitudes decrease with decreasing *NPR*. As with the velocities, the *NPR* = 4.0 case exhibits similar turbulence distributions near the SBLI shock waves and separation region. The location of the downstream shock waves are also apparent for the two higher operating conditions. The *NPR* = 3.0 case, however, does not exhibit any noticeable evidence of the SBLI, and the locations of the shock waves are not as clearly discerned. However, surface oil flow visualization (not shown) does show that there is a small and weak recirculation region, even for this lowest operating condition.

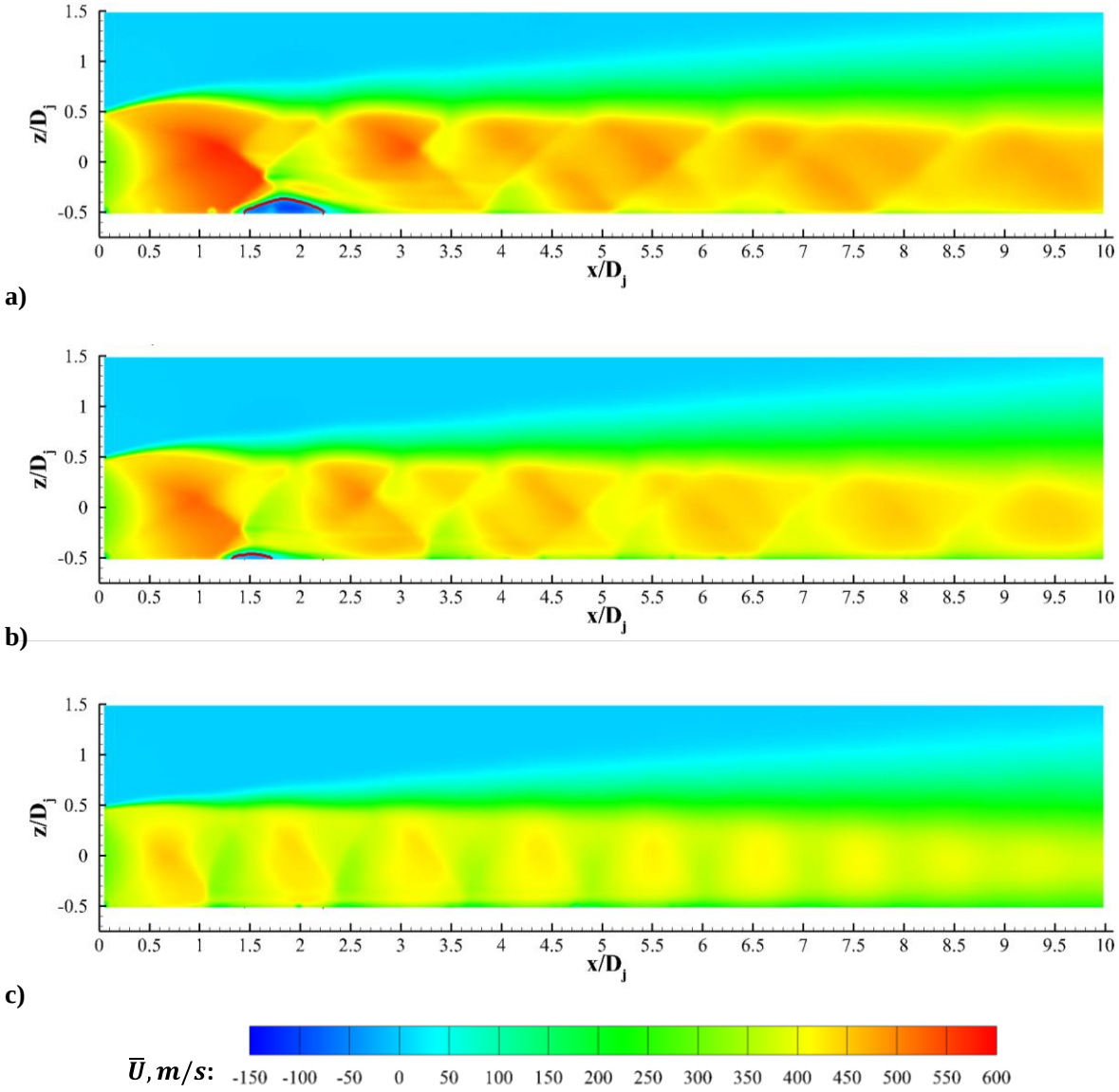

Figure 87. Mean streamwise velocity component results for the h/D_j = 0.50 case with NPR = a) 5.0, b) 4.0, and c) 3.0.

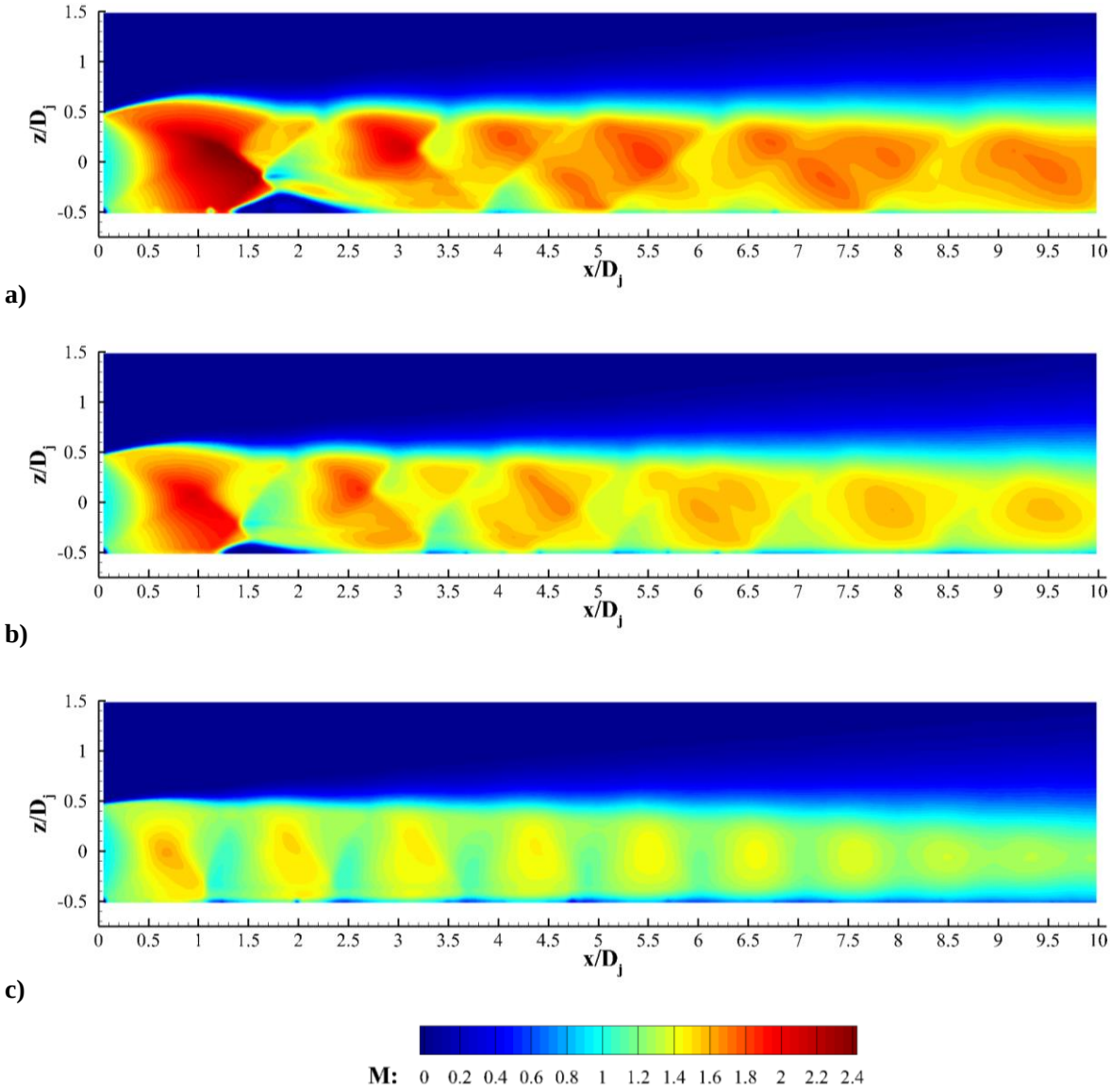

Figure 88. Mean Mach number results for the h/D_j = 0.50 case with NPR = a) 5.0, b) 4.0, and c) 3.0.

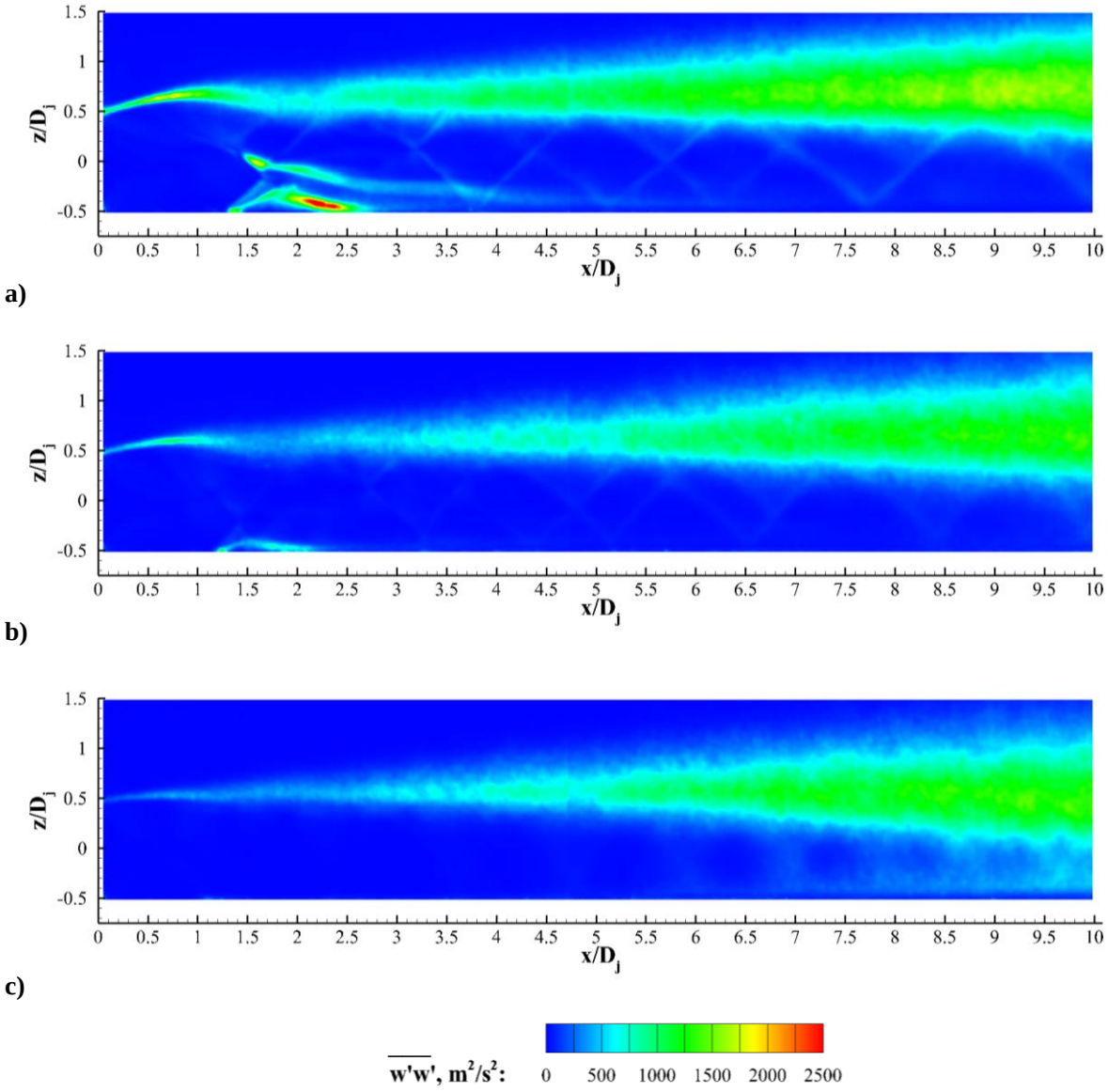

Figure 89. Mean wall-normal direction Reynolds normal stress results for the h/D_j = 0.50 case with NPR = a) 5.0, b) 4.0, and c) 3.0.

Chapter 5 Jet/Compliant-Surface Results

The results obtained for the compliant-surface case are presented next. Unless otherwise stated, the results presented within this chapter are obtained for the h/D_j = 0.50, NPR = 5.0 operating condition. The chapter begins with a brief review of the governing principles for fluid dynamics and structural mechanics to illustrate the complexities that FSI studies present. Next, the processing steps used to bring the sDIC data to a useful state are discussed. This is followed by a cross-validation of the synchronized experiments. The sDIC results, taken along the symmetry plane, are presented first; the deflected surface response is analyzed in terms of the measurement noise floor, as well as the relative importance between the time-averaged and instantaneously varying surface response. This is followed by a presentation of the PIV results. The compliant-surface flowfield is described in a full-field manner first, and then compared to the rigid-surface case using quantitative methods. Differences between the two are noted, and the reasons for these discrepancies are proposed. The discussion of the primary case of interest (h/D_j = 0.50, NPR = 5.0) concludes with a presentation of the fullfield surface response. The chapter concludes with a brief overview of the results obtained for the other operating conditions.

5.1 Review of the Governing Principles

A brief review of the physics governing both the fluid and structure are provided here. There are numerous references that provide a much more thorough investigation into these, both individually and combined.[1-4,114,135,136] The reader is referred to these for additional information. The major challenge with the study of fluid-structure interactions is the sheer number of modes by which they can act. This is illustrated by the equations; both the fundamental equations of fluid dynamics and structural mechanics are nonlinear partial differential equations, and depending on the degree of interaction, may or may not be coupled in a similar manner.

5.1.1 Fluid Dynamics

There are multiple formulations for the equations describing the motion of fluids, but all can be expressed using the conservation of mass, momentum, and energy.[135] The Navier-Stokes equations (Equation 10) are the most general form, and are valid for unsteady, viscous, compressible flows of perfect gases. Here, ρ is density, u_i are the three velocity components, p is pressure, E is energy, q_j is heat addition, and τ_{ij} is the stress tensor.

$$\frac{\partial \rho}{\partial t} + \frac{\partial}{\partial \mathrm{x}_i}(\rho u_i) = 0$$

$$\frac{\partial \rho u_i}{\partial t} + \frac{\partial}{\partial \mathrm{x}_i}\left(\rho u_i u_j + p\delta_{ij} - \tau_{ij}\right) = 0 \tag{10}$$

$$\frac{\partial \rho E}{\partial t} + \frac{\partial}{\partial \mathrm{x}_j}\left[(\rho E + p)u_j + q_j + u_i \tau_{ij}\right] = 0$$

5.1.2 Structural Dynamics

Love's equations govern the deflections and stresses of shells. When applied to plates (which are shells without curvature), Equations 11 – 15 are obtained.[114] This set of five equations governs the in- and out-plane dynamic motion of a flat plate (curvature terms have been removed) in response to any general dynamic (or static) load. Here, subscript *i*, is 1 and 2 in the in-plane directions, and 3 in the out-of-plane direction. α is the coordinate axis, *N* is force/unit length along the surface, A_i is the cross-sectional area normal to direction *i*, ρ_m is the material density, *h* is the material thickness, u_i is the displacement/deflection, q_i is a distributed load applied along direction *i*, Q_{ij} is the transverse shear force/unit length, M_{ij} is the bending moment/unit length, and time derivatives are expressed using the over-dot notation.

$$-\frac{\partial(N_{11}A_2)}{\partial \alpha_1} - \frac{\partial(N_{21}A_1)}{\partial \alpha_2} - N_{21}\frac{\partial A_1}{\partial \alpha_2} + N_{22}\frac{\partial A_2}{\partial \alpha_1} + A_1 A_2 \rho h \ddot{u}_1 = A_1 A_2 q_1 \tag{11}$$

$$-\frac{\partial(N_{12}A_2)}{\partial \alpha_1} - \frac{\partial(N_{22}A_1)}{\partial \alpha_2} - N_{21}\frac{\partial A_2}{\partial \alpha_1} + N_{11}\frac{\partial A_1}{\partial \alpha_2} + A_1 A_2 \rho h \ddot{u}_2 = A_1 A_2 q_2 \tag{12}$$

$$-\frac{\partial(Q_{13}A_2)}{\partial \alpha_1} - \frac{\partial(Q_{23}A_1)}{\partial \alpha_2} + A_1 A_2 \rho h \ddot{u}_3 = A_1 A_2 q_3 \tag{13}$$

$$Q_{13} = \frac{1}{A_1 A_2}\left[\frac{\partial(M_{11}A_2)}{\partial \alpha_1} + \frac{\partial(M_{21}A_1)}{\partial \alpha_2} + M_{12}\frac{\partial A_1}{\partial \alpha_2} - M_{22}\frac{\partial A_2}{\partial \alpha_1}\right] \tag{14}$$

$$Q_{23} = \frac{1}{A_1 A_2}\left[\frac{\partial(M_{12}A_2)}{\partial \alpha_1} + \frac{\partial(M_{22}A_1)}{\partial \alpha_2} + M_{21}\frac{\partial A_2}{\partial \alpha_1} - M_{11}\frac{\partial A_1}{\partial \alpha_2}\right] \tag{15}$$

The nonlinear version is given in Equation 16 for a Cartesian coordinate system using more commonly used notation. Here, u_3 is the deflection in the out-of-plane direction, ρ_m is the material density, *t* is the plate thickness, Δp is the aerodynamic pressure applied across the surface, *D* is the plate bending (or flexural) rigidity, *E* is the material Young's Modulus, and *v* is the material Poisson ratio.

$$D\left(\frac{\partial^4 u_3}{\partial x^4} + 2\frac{\partial^4 u_3}{\partial x^2 \partial y^2} + \frac{\partial^4 u_3}{\partial y^4}\right) + \rho_m t \frac{\partial^2 u_3}{\partial t^2} = \Delta p$$

$$D = \frac{Et^3}{12(1-\nu^2)} \tag{16}$$

Boundary conditions, typically either simply-supported or clamped edges, are required. Clamped edges are employed in this study, for which the boundary conditions are u_3 = 0 and $\partial u_3/\partial x = \partial u_3/\partial y = 0$. There are numerous theories that are derived from Love's equations. One of those, called Kirchoff-Love theory, is commonly used for thin plates, and often used in flutter studies[85]. Kirchoff-Love theory is notable because it allows for the separate definition of tensile forces within the plate/shell due to preloading or those induced by large out-of-plane deformations. Beam functions can be used to calculate the expected natural frequencies of vibration for selected geometries and boundary conditions.[114] The expected natural frequencies for the first several modes of the compliant-surface model used in the current study were calculated as part of the compliant-surface characterization (see Section 2.5.2).

5.2 Initial Surface State

All sDIC analyses are conducted relative to a reference image. Traditionally, this is an image obtained prior to conducting the test. All motion (and strains) are computed relative to the initial reference condition. The reference condition is composed of three-dimensional surface coordinates ($\mathcal{X}_{\text{ref}}$, $\mathcal{Y}_{\text{ref}}$, and $\mathcal{Z}_{\text{ref}}$) within a defined coordinate system. As described in Section 2.7.3, the sDIC coordinate system was defined to align with that used in the current study. This was accomplished via coordinate transformation from the "Camera0" in VIC3D.

In the course of sDIC processing, the deflections ($\mathcal{U}$, $\mathcal{V}$, $\mathcal{W}$) are calculated relative to the reference positions. The instantaneous deflected surface contour, defined by $\mathcal{X}$, $\mathcal{Y}$, and $\mathcal{Z}$, can then be constructed using the reference location and the deflection, as shown in Equation 17 (analogous equations are used for $\mathcal{Y}$ and $\mathcal{Z}$).

$$\mathcal{X} = \mathcal{X}_{ref} + \mathcal{U} \tag{17}$$

In the current study, a single data run yielded approximately 260 instantaneous measurements of simultaneous planar PIV and sDIC. In order to accumulate a significant number of instantaneous measurements, multiple data runs were required. However, over the course of data collection, the

initial contour of the compliant surface between tests was found to vary from one run to the next. For this reason, all data runs used the same reference image (one obtained from an early test). Figure 91 presents the reference state ($\mathcal{Z}_{ref}$) used for the h/D_j = 0.50, NPR = 5.0 runs. It is evident that the surface is not strictly flat; the maximum discrepancy is approximately 0.36 mm (ranging from -0.3 to 0.06 mm). This is in contrast to the compliant surface model as originally manufactured, where $\mathcal{Z}_{ref}$ ranged from approximately -0.1 to 0.05 mm. However, because the compliant model underwent several speckle-pattern touchups, the originally-constructed model surface image could not be used as the sDIC reference state.

For the purposes of the current study, it is primarily the comparison to the flat (rigid) surface state that is of interest. Since the sDIC results are computed within the coordinate frame used for the study, the instantaneously deflected surface positions ($\mathcal{X}$, $\mathcal{Y}$, and $\mathcal{Z}$) are still the positions relative to the rigid-model surface, despite the sDIC-reference images not corresponding to the same condition. Hence, the reference state with the non-ideal curvature can be used for sDIC processing.

The consequence, however, is that the sDIC-derived deflections are not relative to the rigid-surface location, but to the reference-state instead. This means that the sDIC-derived strains are also computed relative to the reference-state, and not the ideal-rigid surface condition. The consequences and implications of the methods used here are important to keep in mind when considering the sDIC data and results.

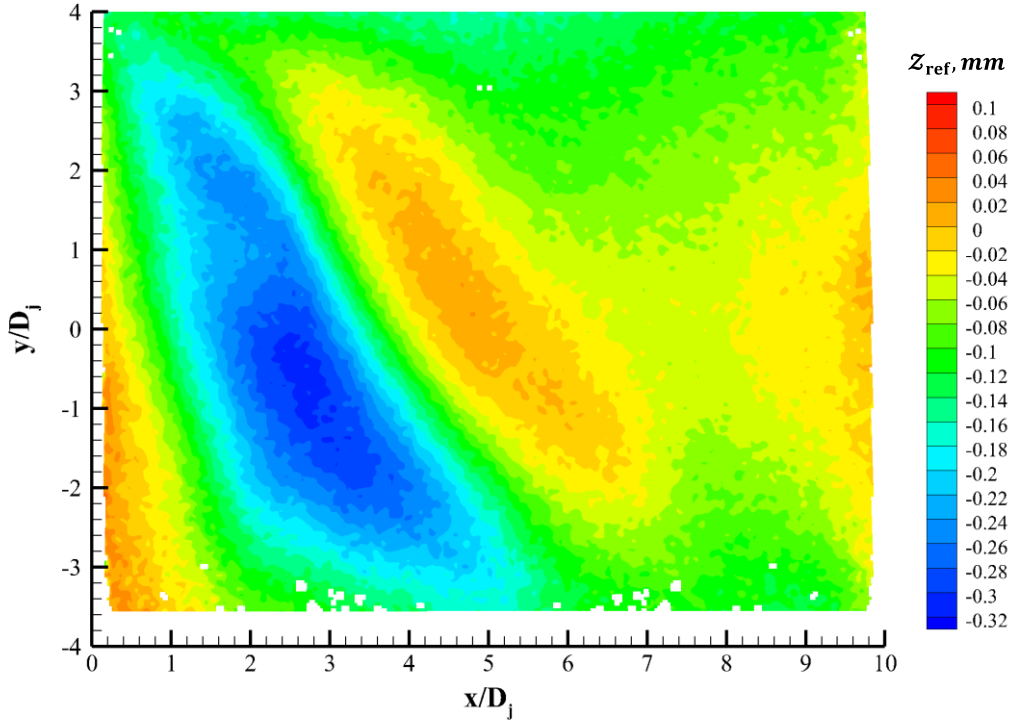

Figure 90. The initial (reference) state of the compliant surface used for sDIC processing.

It should be noted that the deflected surface positions, $\mathcal{X}$and $\mathcal{Y}$, are essentially equal to *x* and *y* since the model motion is dominated by the out-of-plane motion, and there is very little in-plane motion. Therefore, these notations are used interchangeably.

5.3 Accounting for Rigid Frame Motion

In addition to obtaining sDIC data for the compliant surface, data were also obtained for a region of the support frame. The data obtained in this region were used to correct the compliant surface motion for instantaneous rigid model deflection. The reference region was approximately 12.5 mm by 126 mm large, and supplied in excess of 9000 individual measurements. The mean out-of-plane displacement, $\mathcal{W}_{frame}$, for each instantaneous measurement was used to correct the measurement obtained for the rigid surface as shown in Equation 18.

$$\mathcal{Z} = \mathcal{Z}_{ref} + \mathcal{W} - \mathcal{W}_{frame} \tag{18}$$

A record of $\mathcal{W}_{frame}$, for all instantaneous measurements was saved. A histogram and pdf is shown in Figure 92 for all 1068 measurements obtained for the h/D_j = 0.50, *NPR* = 5.0 case. For this run condition, the model deflects towards the surface by a mean value of approximately 42

μm with a standard deviation that is approximately half of the mean. The histogram indicates that although the mean deflection is quite small, there is a relatively large degree of variation between measurements. The rigid frame motion in the *x*- and *y*-directions were considered negligible and so no similar corrections were made for them.

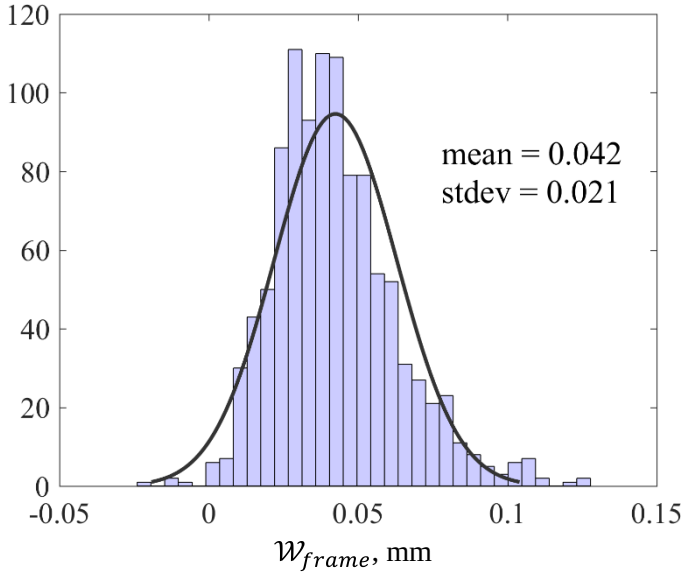

Figure 91. A histogram (and overlaid Gaussian distribution fit) of the rigid motion of the frame in the out-of-plane direction.

5.4 Instantaneous Cross-Experimental Validation

Data validation is an important aspect of any experimental study. For the author, planar PIV represents a commonly used and well-understood technique. A great deal of validation can be achieved during the course of data processing or via the uncertainty estimation process, as discussed in Section 2.6.3 and Appendix B. However, sDIC is a technique that the author is not as familiar with and so every opportunity for data validation was utilized. Section 2.7.3 discusses sDIC validation using linear traverse testing with and without PIV seeding particles, as well as estimation of the measurement uncertainty.

The raw planar PIV images, obtained simultaneously with the sDIC images, present another opportunity for sDIC data validation. Due to the grazing laser illumination, the compliant surface can be seen in the PIV images. This allows for the extraction of instantaneous sDIC data along the laser illumination line ($y/D_j = 0$), and overlaying it on the PIV images.

This is shown in Figure 93, where the red line is the processed sDIC result. The agreement is very good. The sDIC is very close to the expected location ($y/D_j = -0.5$) at both the beginning

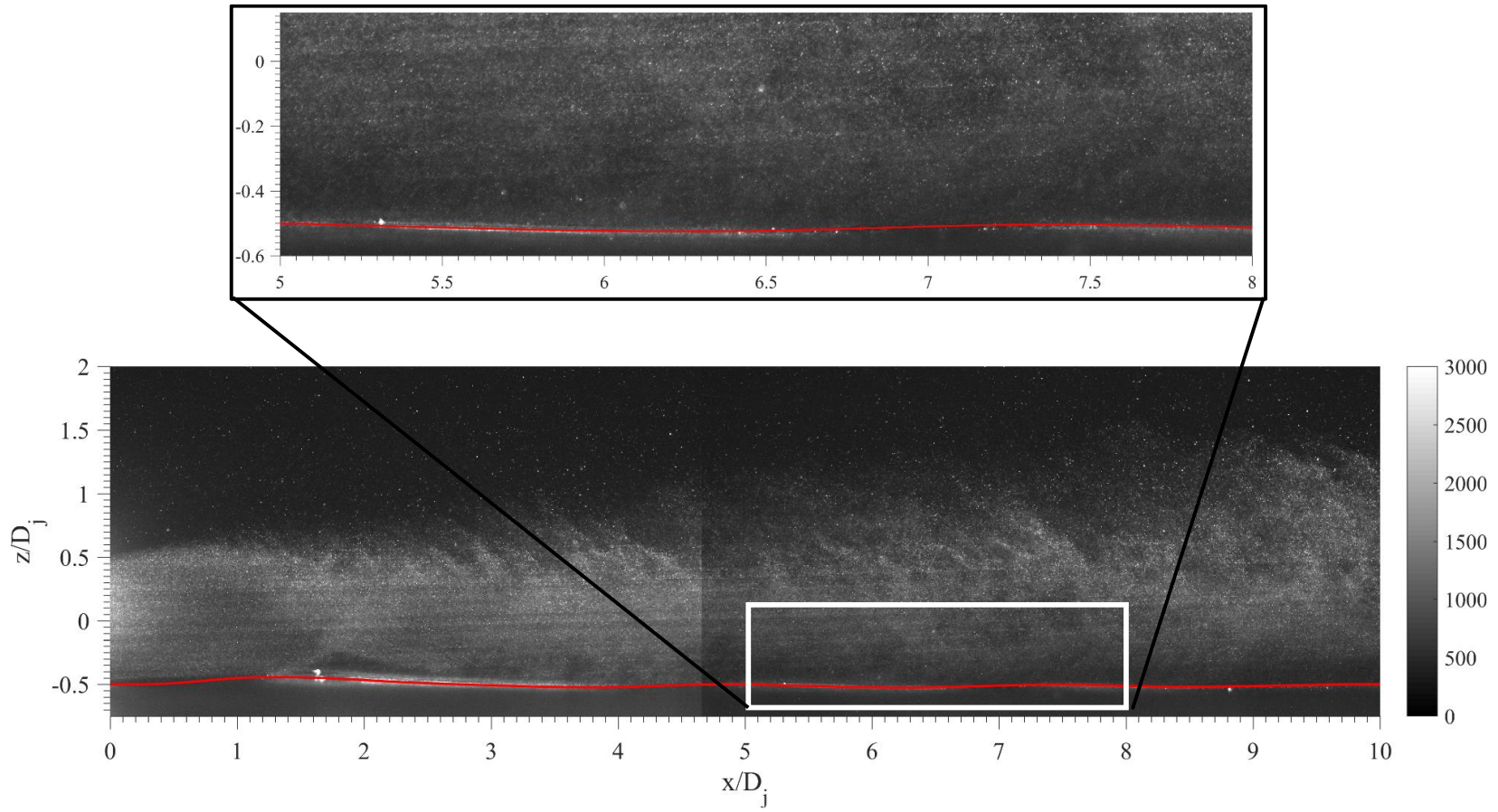

Figure 92. The centerline sDIC-derived deflected surface contour (red line) aligns exceedingly well with the surface as illuminated in the raw PIV particle image.

and end of the imaging domain. A large jetward deflection is evident near $x/D_j = 1.5$, followed by three to four additional wave-like deflections of smaller magnitude. The figure inset shows a zoomed in view near $5 \leq x/D_j \leq 8$. Here, the direction of laser illumination can be observed, as there is a clear shadowing effect of the surface on the upstream side of the local deflection wave (see especially at $x/D_j \approx 7$). The strong agreement between the sDIC results and the PIV laser illumination line gives further confidence in the proper calibration of both experiments, as well as their synchronization. It should be noted that the results shown in Figure 93, are for a single instantaneous snapshot; however, the figure is representative of the larger dataset.

Figure 93 also allows for an inspection of the PIV particle images. Particle seeding density is obviously increased within the jet. This is due to the fact that particles are seeded into the jet directly and their increased diameter as compared to the particles used for the entrained flow. The SBLI separation region can be seen near $x/D_j \approx 1.75$, as evidenced by the slightly reduced particle seeding within it. The particles also show the jet's flow expansion near $z/D_j = 0.50$ upon exiting the nozzle. Some vortex rollup, which are perhaps Kelvin-Helmholtz waves, can be seen in the upper shear layer near $2 \leq x/D_j \leq 4.5$. Farther downstream, the fact that the shear layer has substantially thickened is apparent. Also note the horizontal streaks within the seed particles. These are due to seed-particle residue accumulating on the window that shields the laser illumination optics (which are located within the jet at about $x/D_j = 50$). The streaking does not have a substantial effect on the PIV processing as the sliding background intensity-removal image-preprocessing step accounts for the varying intensities.

5.5 Symmetry Plane Structural Response

The structural response along the symmetry plane ($y/D_j = 0$) is considered first, as that is the data most directly relevant to the PIV data. The fullfield surface deflection results are discussed in Section 5.7.

Figure 94 a) presents the deflected surface position, normalized by the panel thickness, for 100 instantaneous results. Figure 94 b) displays the normalized mean deflection obtained using all 1068 instantaneous measurements, with additional curves offset above and below by one standard deviation. Finally, Figure 94 c) presents the standard deviation from the mean deflection, again normalized by the panel thickness. The traces begin at $x/D_j = 0.27$, which corresponds to the edge of the frame and extend to the opposite edge of the frame, located at $x/D_j = 10$.

The instantaneous variation can be assessed by the spread of the thin colored lines in the first figure. The first item to note in Figure 94 a) is that the variation between instantaneous results occurs predominantly in the *z*-direction. This means that surface deflection waves are in-phase with each other, and that the general surface deflection takes a standing-wave shape. Since the measurements were obtained at random time intervals, the observed phase-agreement is not due to aliasing or temporal phase-locking.

Since the deflected surface takes a standing-wave shape, the shape of the mean deflection curve, shown in Figure 94 b), is fairly representative of the true time-averaged state of the surface. The mean deflection is dominated by a very large displacement into the jet, which attains a maximum of $\mathcal{Z}/t$ = 9.13 at x/D_j = 1.3. Thereafter, the surface deflects in the opposite direction, moving away from the jet, and reaches a minimum of $\mathcal{Z}/t$ = -4.44 at x/D_j = 3.8. Beyond $x/D_j \geq 3.8$, the surface deflection takes a more uniform amplitude wave shape, but the oscillation takes place about a negative $\mathcal{Z}/t$ location, with the maximum jetward deflected states nearing the original surface location. Only about two full wavelengths can be seen in this region, but the amplitude does decrease as x/D_j increases. At the beginning of the third wave cycle, the downstream plate boundary is approached, and the surface deflects upward to return to the original position.

Visual inspection of the instantaneous measurements shows that, in comparison to the edges, there is increased variation in the *z*-direction near the center of the panel. This is an entirely expected observation; the clamped-edge boundary conditions restrict the compliant-surface motion near the edges, and a stronger perturbation is required to induce equivalent responses. The standard deviation of out-of-plane deflection plot, shown in Figure 94 c), corroborates these observations. The figure also contains several additional points of interest.

First, note that the standard deviation in deflection at both the leading and trailing edges of the compliant surface approaches a non-zero value of approximately 0.1 panel thicknesses, or 7.6 μm. This is approximately three times larger than the expected sDIC out-of-plane measurement accuracy (2.3 – 2.6 μm). Therefore, this non-zero value is taken to indicate that there is a noise-floor in the measurement accuracy. It is believed that this noise floor is due to frame out-of-plane deflection. This effect was already taken into account, correcting the results by a mean rigid-frame deflection of 42 μm. However, the standard deviation in that measurement was large, making the correction inexact and thereby allowing for the currently observed measurement noise floor.

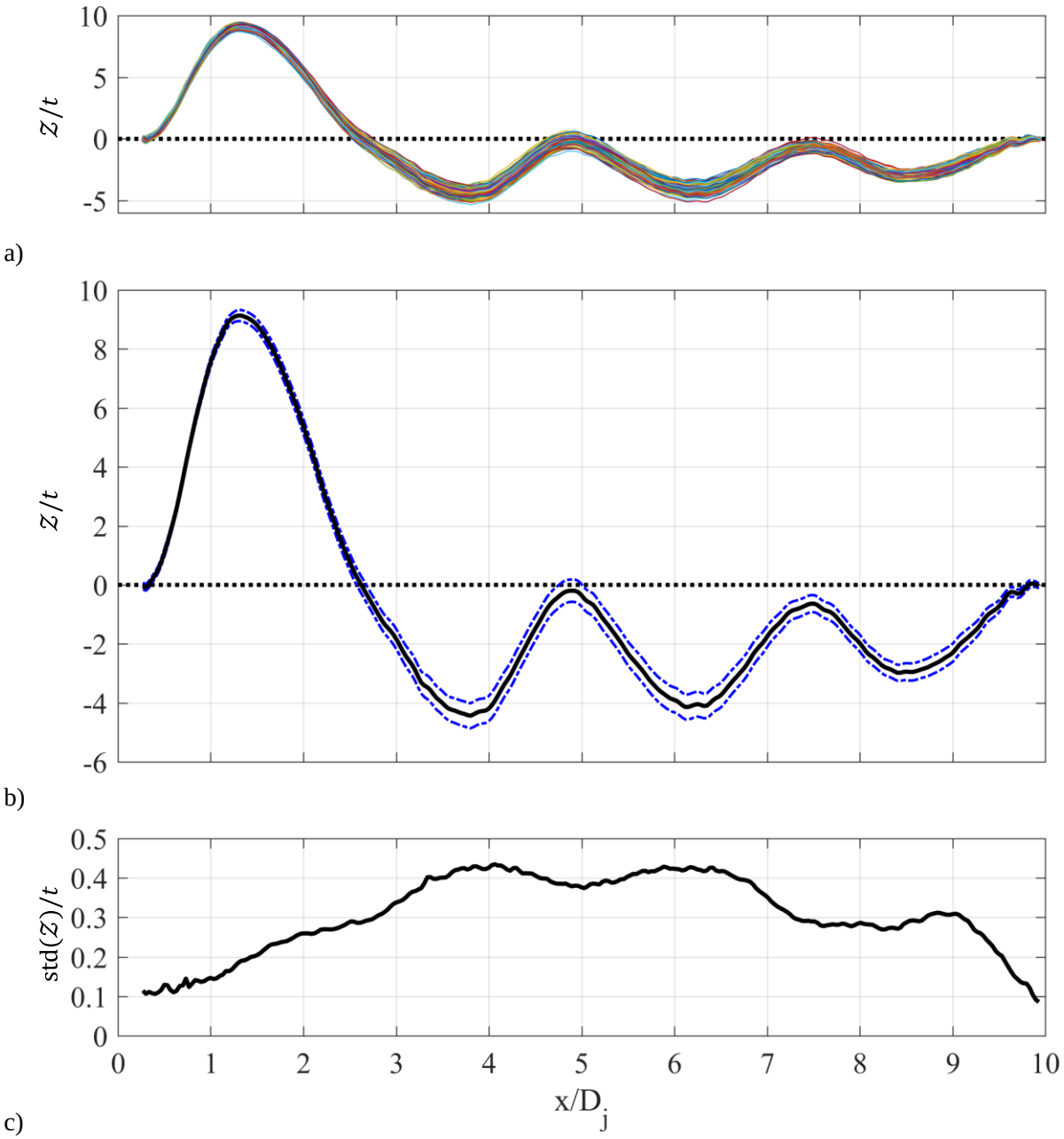

Figure 93. Centerline (symmetry plane) compliant surface results showing a) 100 deflected-contour instantaneous snapshots, b) the mean deflected surface and uncertainty bounds, and c) the standard deviation about the mean deflected position. All results are normalized by the compliant surface thickness, t.

Second, Figure 94 c) shows that the standard deviation increases more slowly on the upstream end of the surface than it does on the downstream end, particularly in the range $0.27 \leq x/D_j \leq 2.5$. The location of decreased slope in the standard deviation curve corresponds to the region with the large jetward deflection, which, as already noted, is at least three times larger in amplitude than

the wave nearest the downstream end of the surface. Thus, the degree of stretching experienced by the surface is much greater near the upstream end of the surface due to the comparatively larger deflection. This added strain increases the local tensile load, which in turn decreases the surface's dynamic response to an equivalent external forcing. The net result is a decreased variation in the measured deflection.

It is important to define the amplitude of oscillation (standard deviation) in terms of physical space as well as in the framework of the PIV interrogation windows. As shown in Figure 94 c), a conservative estimate of the maximum standard deviation about the mean deflected position is 0.45*t*, which corresponds to a physical deviation of ±0.0343 mm. Allowing for two standard deviations (which encompasses 95% of the measurements for a normally distributed parameter), corresponds to ±0.0686 mm. This corresponds to a maximum deviation in the surface position of approximately ±2.5 pixels in the PIV imaging system. In terms of PIV interrogation windows, the surface-positional deviation represents less than 16% of the smallest windows (16 x 16 pixels). Since the exact location of the surface within PIV measurement interrogation windows is unknown, and interrogation windows overlap by 50%, a conservative estimate is that the two vectors nearest the surface may be influenced or otherwise affected by the surface position.

Figures 95 a) – b) display histograms of the variation about the mean deflected position for x/D_j = 0.27 and 7.5, respectively. It is clear that the histograms are approximately normally distributed, validating the use of the standard deviation as a symmetric (two-sided) confidence

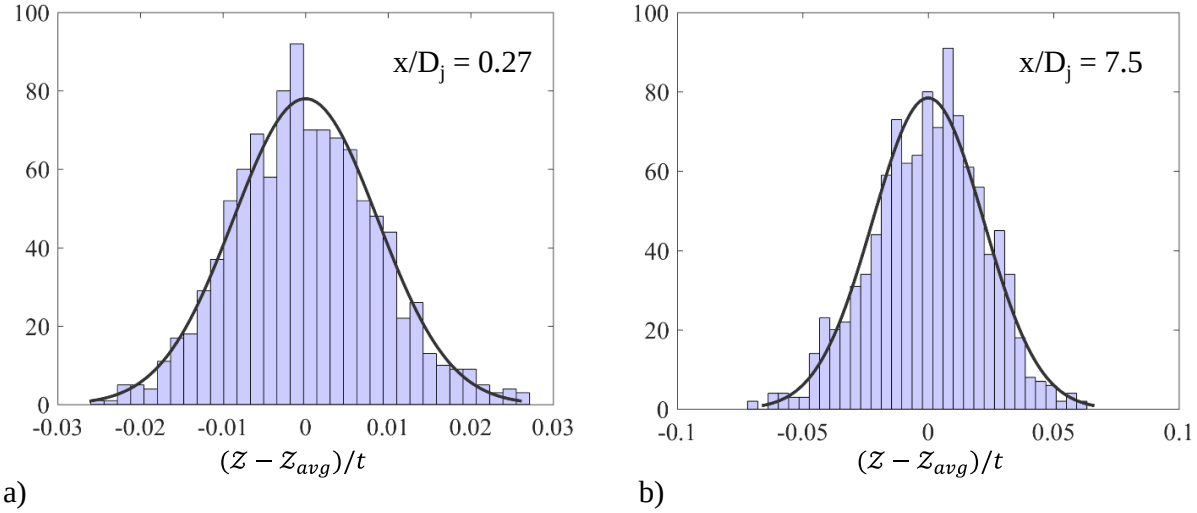

Figure 94. Histograms taken at locations along the centerline of the deflected compliant surface show that the variation about the mean deflected position take approximately normal distributions.

margin estimate. This observation validates the bounding curves in Figure 94 b) as well as the out-of-plane deflection noise floor estimation.

The combined knowledge that a) the deflected shape of the compliant surface takes a quasi-static "standing wave" form, b) the oscillation about the deflected shape occurs primarily in the *z*-direction, and c) that the oscillation is small with respect to the PIV interrogation windows, justifies the analysis of the mean and statistical PIV results in addition to the instantaneous vector results. However, the oscillations about the mean deflected surface may extend as far as two vectors into the velocity field; this fact should be kept in mind during the interpretation of the near-wall velocity vectors.

5.6 Planar PIV

The mean PIV results are considered first. The presented data were obtained using approximately 1000 instantaneous snapshots. Whenever possible, the same color palettes and ranges are used for the compliant-surface results as were employed in the rigid-surface case. The mean deflected-surface contour, taken along the symmetry plane, is also shown in the figures. Figures 96 a) – c) present $\bar{U}$, $\bar{W}$, and M for the $h/D_j = 0.50$, $NPR = 5.0$ compliant-surface case. In general, the compliant-surface case flowfield looks similar to that observed for the rigid-surface case. The shock structure is similar, the SBLI still exists, and the boundary layer within the SBLI also separates. As before, there is a clear shock-cell structure farther downstream.

However, the compliant-surface case flowfield does display a number of clearly discernible differences as compared to the rigid-surface case. In order to highlight these differences, the flowfield for the compliant-surface case is described in a fullfield manner first. Notable differences between the compliant- and rigid-surface cases are discussed, and explanations regarding the differences are proposed when possible. The rigid- and compliant-surface cases are compared more directly by making use of profiles through the flowfield at selected *x* and *z* positions. These profiles serve to present the differences in a quantitative sense, and also include measurement uncertainty windows (for the rigid-surface case) to assess whether these observed differences are statistically significant. The quantitative data also provide further evidence and additional support for the proposed reasons for the differences between the rigid- and compliant-surface cases.

In general, the flowfield description is broken up into a) the nozzle exit plane to the shock/boundary-layer interaction (SBLI) shock waves, b) the flow through the SBLI region, c) the

SBLI separation zone d) the shock cell structure of the remainder of the jet plume, e) the near-wall boundary layer, and f) farfield conditions.

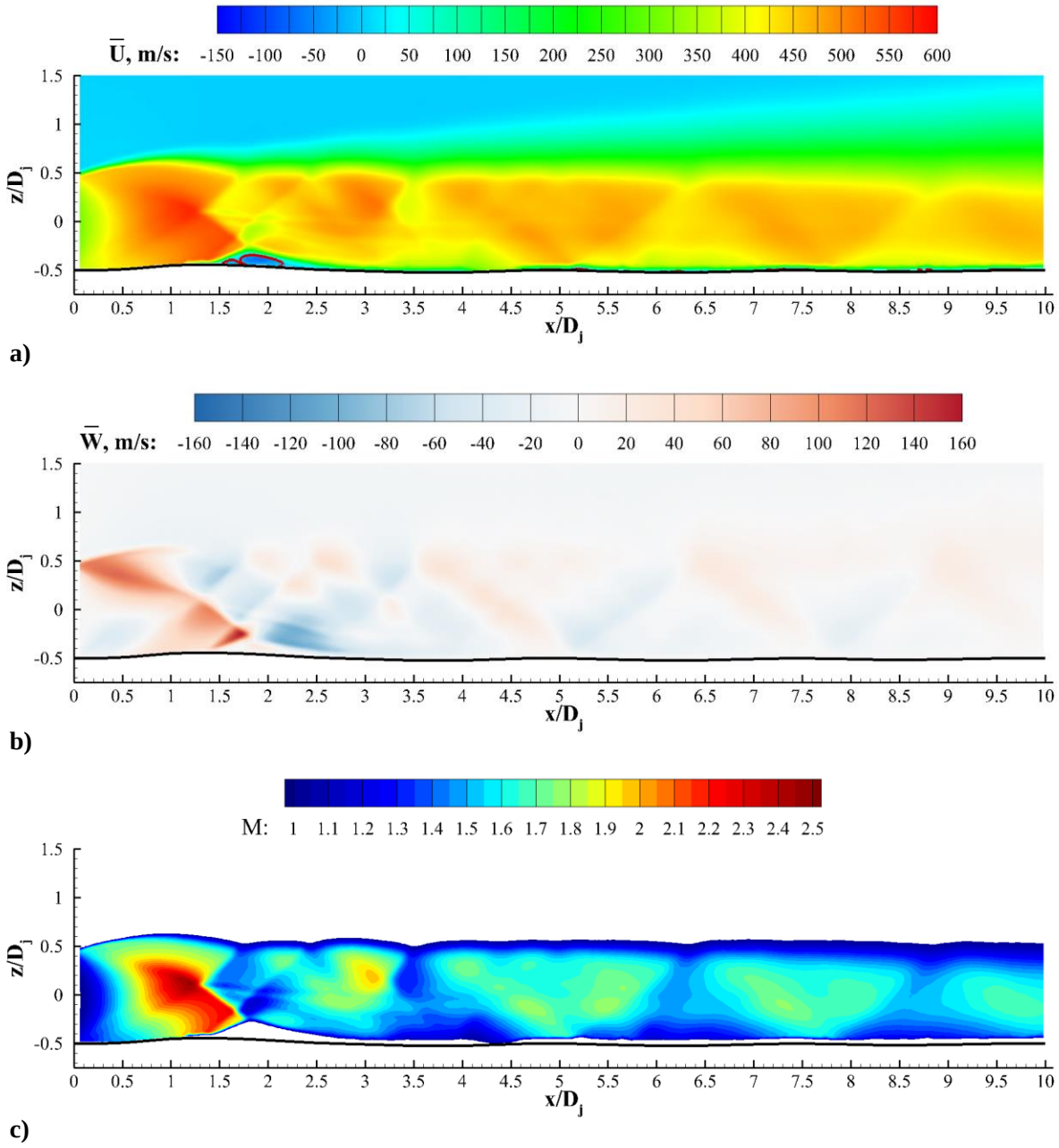

Figure 95. Mean compliant-surface case PIV results showing a) streamwise velocity component, $\bar{U}$, b) wall-normal velocity component, $\bar{W}$, and c) Mach number, M (M < 1 is masked out).

5.6.1 Nozzle Exit to SBLI

The compliant-surface case flowfield description begins in the first shock cell, spanning from the nozzle exit plane to the SBLI shock waves. The region above the jet axis is discussed first, and is followed by the near-wall region (below the jet axis). Then, profiles are utilized to more thoroughly illustrate the differences.

We begin on the side of the jet flowfield far from the surface. As with the rigid-surface case (as well as the isolated jet), the flow accelerates radially outward upon exiting the nozzle. This expansion occurs freely on the side of the jet flowfield far from the surface ($z/D_j \geq 0$), resulting in the formation of a free shear layer. As the flow passes through the expansion fan centered about the nozzle lip, it accelerates, leading to increasing $\bar{U}$ and $\bar{W}$ within this region, as shown in Figures 97 and 98 a), respectively. Based on the fullfield images, the flowfield for the compliant-surface case is nearly identical to that for the rigid-surface case in this region, as shown in Figures 97 and 98 b), respectively. The velocities and Mach number (shown in Figure 99) are also similar, as is the placement and thickness of the shear layer.

On the side of the jet flowfield nearer to the surface ($z/D_j \leq 0$), the flow initially accelerates in a nearly purely axial manner; the surface prevents outward radial expansion leading to negligible $\bar{W}$ near the nozzle exit. A region of positive $\bar{W}$ (away from the wall) begins to form near the surface, beginning near $x/D_j = 0.4$, as shown in Figure 98 a).This region of flow 'lifting' grows in thickness rapidly and also increases in magnitude. The region of near-wall positive $\bar{W}$ extends downstream until it encounters the SBLI incident and separation shock waves. The x/D_j location corresponding

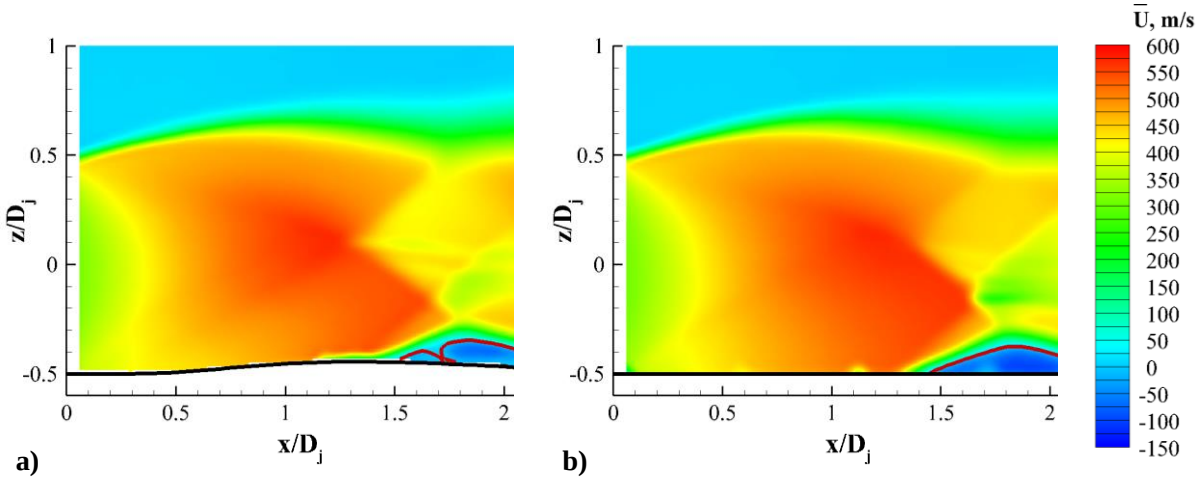

Figure 96. Mean streamwise-direction velocity component, $\bar{U}$, for a) the compliant-surface case, and b) the rigid-surface case.

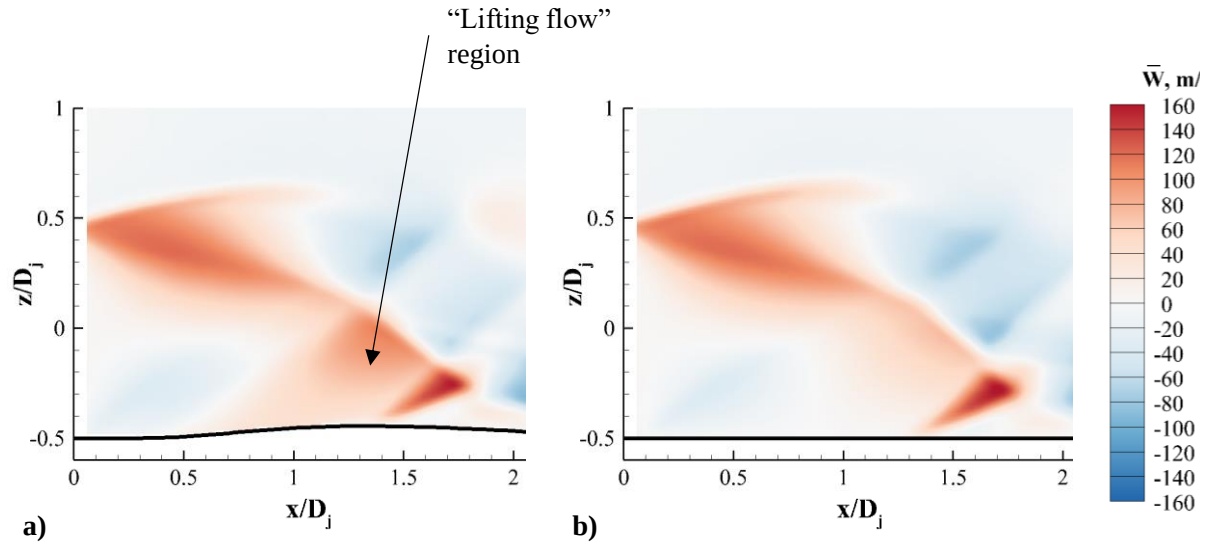

Figure 97. Mean wall-normal direction velocity component, $\bar{W}$, for a) the compliant-surface case, and b) the rigid-surface case.

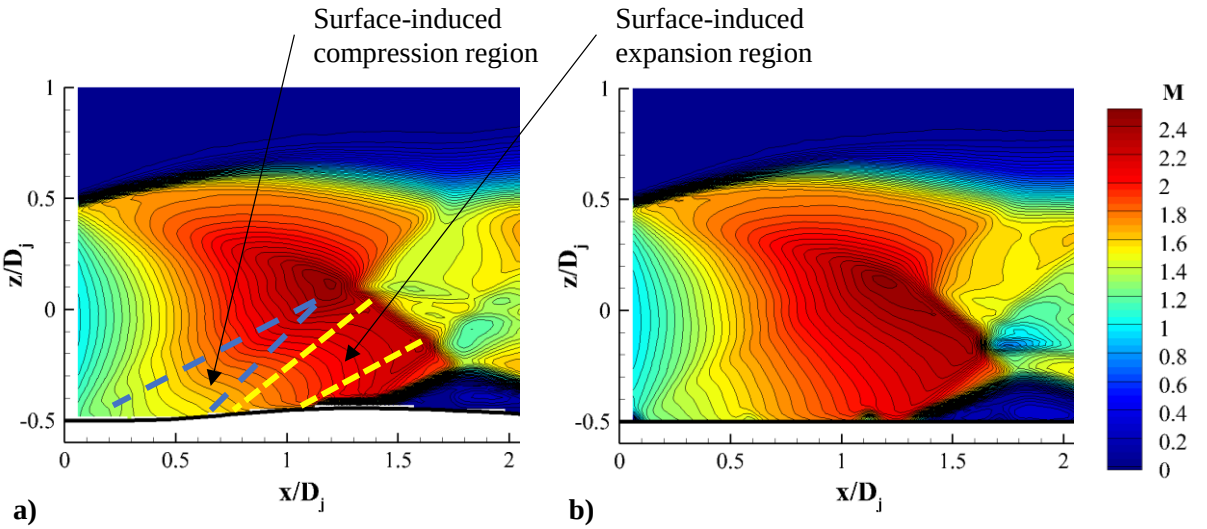

Figure 98. Mean Mach number contours, M, for a) the compliant-surface case, and b) the rigid-surface case.

to the origin of the 'lifting flow' region is near the position where the compliant surface begins its deflection into the flowfield. Figure 97 appears to indicate that $\bar{U}$ is reduced within the lifting flow region. Extremely close to the wall, the compliant-surface case shows a region of reduced $\bar{U}$ that extends farther upstream (to x/D_j = 1.1) than the position of the SBLI separation shock. This is believed to be due to boundary-layer thickening due to the adverse pressure gradient incurred in the subsonic boundary layer beyond the inflection point in the deflected surface contour. Thus, the

deflection of the compliant surface into the flowfield has the effect of inducing flow diversion up and over it.

Figure 100 presents profiles of $\bar{U}$ and $\bar{W}$ at eight positions ranging between $0.2 \leq x/D_j \leq 1.6$. Both the rigid- and compliant-case profiles are shown. Uncertainties in the mean are included for the rigid-surface profiles. The uncertainty bars can be used to assess whether the rigid- and compliant-surface cases are statistically different. Uncertainties were not calculated for the compliant-surface profiles, but the rigid-surface case results are believed to be representative of the measurements obtained for the compliant-surface case as well. Thus, the profiles should be separated by approximately two (rigid-surface) error bar widths in order for the difference to be statistically significant.

Figure 100 confirms that the velocity profiles are exceedingly similar for $x/D_j \leq 0.6$. The two cases have similarly positioned jet primary shear layers and rates of acceleration in $\bar{U}$. There is little to no evidence of the near-wall boundary layer in either profile in the first several presented profiles. This is not unexpected; due to the large freestream velocity and the short length over which it can grow, the boundary layer is expected to be extremely thin and likely not measureable with PIV. The compliant-surface case profile begins to show the boundary layer at $x/D_j = 1.2$; this, as previously discussed, is expected to be evidence of thickening of the boundary layer due to the adverse pressure gradient experienced by the subsonic portion of the boundary layer beyond the inflection point in the deflected surface profile. The last profiles presented in the figure are located at positions that capture the SBLI-induced boundary-layer thickening (and, for the last profile, boundary-layer separation). The vertical offset of the boundary-layer profiles at the last few locations is due to the deflection of the surface into the flowfield for the compliant-surface case; the overall height of the boundary-layer/separation regions are approximately equivalent between the two cases.

The $\bar{W}$ profiles confirm that the flow expansion in the wall-normal direction is much smaller than that on far side of the jet. The 'lifting flow' region, which begins to form at $x/D_j = 0.4$, can be seen to grow in the profiles for the compliant-surface case. Then, as the profiles pass through the SBLI separation shock, strong near-wall regions of positive $\bar{W}$ are formed. On the far side of the jet, regions of positive $\bar{W}$ are found, resulting from the upper nozzle lip expansion fan. The region of positive $\bar{W}$ separates into two; one broader region is in the interior of the jet and the other is a thinner layer located in the jet primary shear layer.

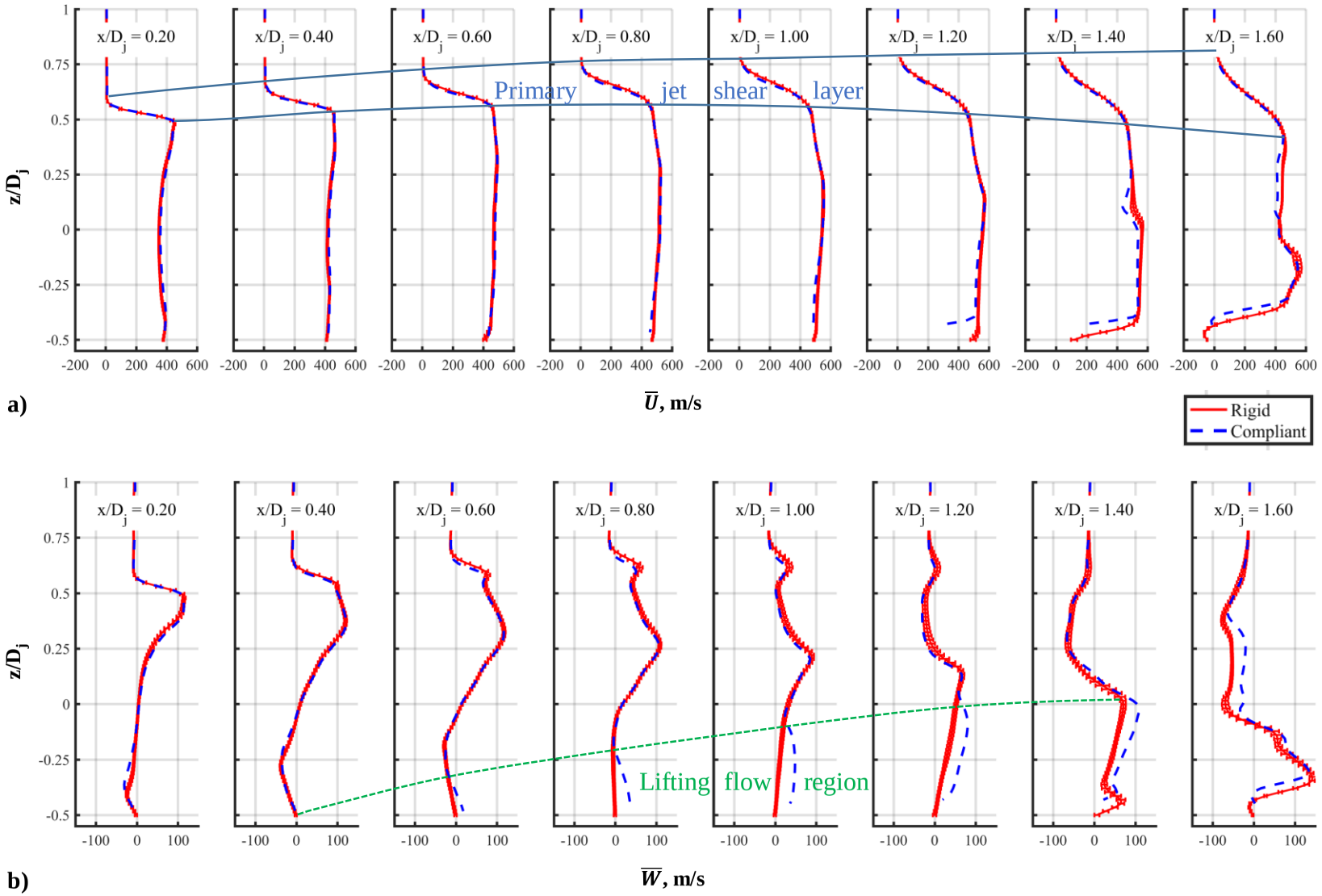

Figure 99. Mean profiles of a) $\bar{U}$, and b) $\bar{W}$ at various x/D_j positions between the nozzle exit and the SBLI shock waves.

Since the deflected surface induces an “into the flow” turn of this supersonic flow, it was expected that the Mach number contours would show characteristics of a compression-like flow. However, inspection of the Mach contours, shows a highly curved distribution in this region and reveals that the flow continues to accelerate as it is diverted around the deflected surface. Figure 99 presents the Mach number contour plots, where solid black lines are used to emphasize the contour boundaries. The increased separation distance between isocontours shows that the acceleration is much weaker than before, but does not indicate true supersonic compression (that is, a reduction in Mach number). There are several reasonable explanations. First, the fact that there the flow is continually going through under- and over-expansion cycles, makes it much more difficult to identify a compression. It is possible that the surface, being compliant, takes a contour that corresponds to an isentropic-like compression, which would make the deceleration much more subtle than that for a sharp-cornered compression ramp. In addition, the actual compression region is relatively short since it only extends from the initial point of surface deflection (x/D_j = 0.3) to the upstream inflection point of the into-the-flowfield surface deflection wave (x/D_j = 0.75). Beyond the inflection point, the flow experiences an expansion region instead as the wall effectively “turns away from” the flow. Thus, it is possible that the Mach contours do not clearly show a compression region because the compression is subtle, occurs over a short span, and is immediately followed by a flow expansion. The highly-curved Mach contours may suggest both compression and expansion with the onset of curvature corresponding to the compression region, while the primary curvature is associated with the expansion. These regions are highlighted in Figure 99 a) by the blue and yellow lines, respectively.

5.6.2 The SBLI

Although both cases display a prominent SBLI, there are notable differences between them, as highlighted in Figure 101 and 102. In general, the inflow conditions for the compliant-surface case correspond to lower Mach numbers, as shown by the first profile in Figure 102 a). This has ramifications through the entire SBLI, as well as for the outflow conditions. The decreased inflow Mach numbers lead to weaker shock waves and altered shock-shock interactions. For instance, the SBLI incident shock wave takes a shallower angle in the compliant-surface case (35.8° relative to horizontal) than in the rigid-surface case (39.3° relative to horizontal). This change leads to an altered SBLI incident/separation shock interaction. In the rigid-surface case, a small normal shock is also associated with this shock interaction, but in the compliant-surface case, it does not exist.

The presence of the normal shock leads to greatly reduced Mach numbers near the wall at the SBLI outflow in the rigid-surface case as compared to the compliant-surface case.

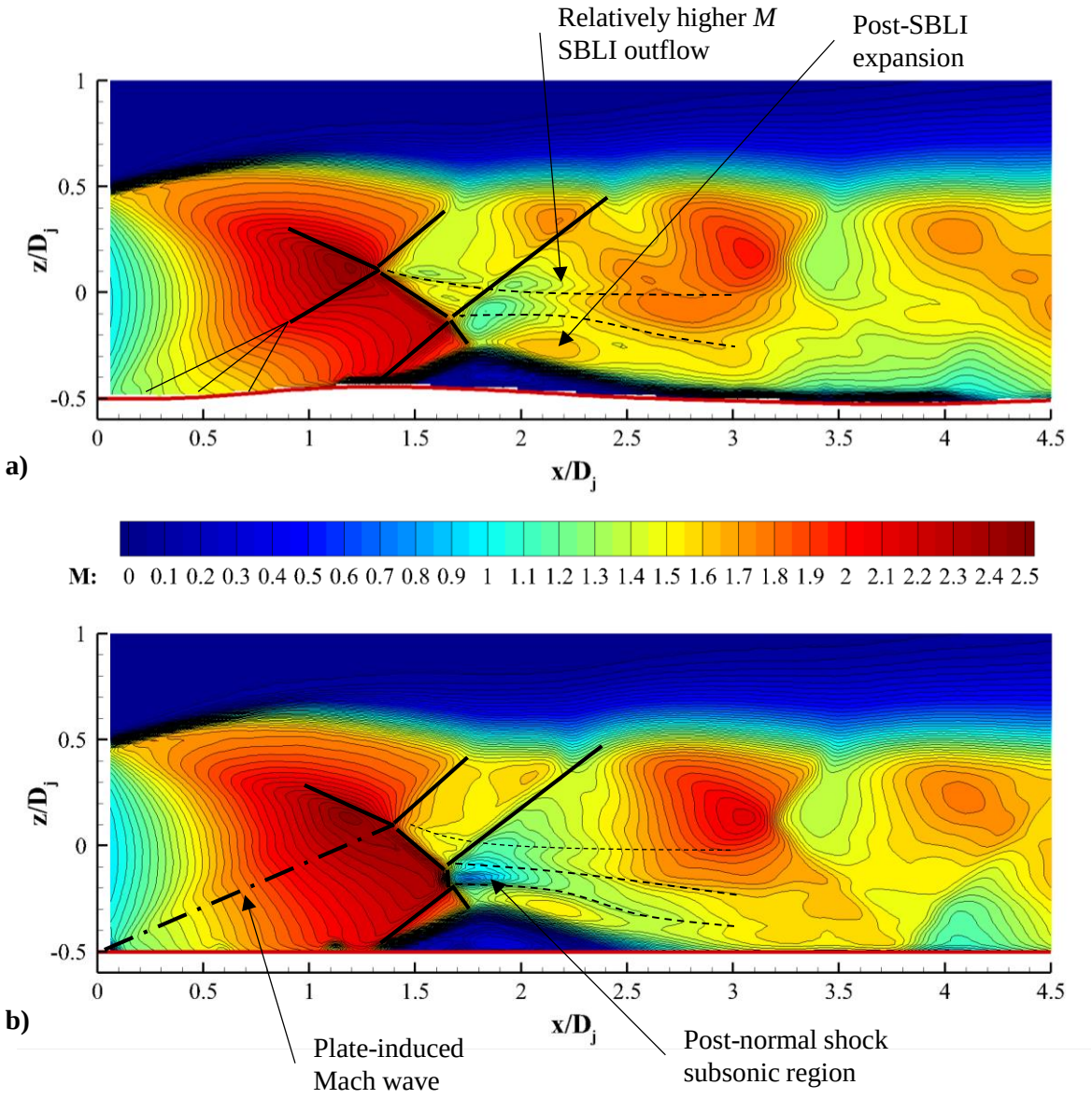

Figure 100. Mean Mach number contours within the SBLI regions for a) the compliant-surface case, and b) the rigid-surface case.

The decreased compliant-surface case inflow Mach number is also important for the far side of the jet, where it also leads to decreased Mach numbers in the region between the two reflected shock waves. The compliant-surface case does contain a region of increased Mach number near the jet shear layer, just upstream of the SBLI reflected shock. This higher-speed region is coupled

with an increased jet plume width for the compliant-surface case, as shown in Figure 101 and by the M profiles at x/D_j = 2.0 and 2.2 in Figure 102 a).

Thus, it can be generally said that the SBLI shock system is weaker for the compliant-surface case as compared to the rigid-surface case and that the compliant-surface case results in higher Mach number outflow conditions. This is true despite the increased geometrical blockage incurred in the compliant-surface case (since the surface deflects into the flow). The compliant-surface case also results in fewer slip line shear layers since there are fewer shock wave interactions. However, the increased shock strengths in the rigid-surface case lead to more clearly visible shock cells in Figure 101.

Profiles of M and $\bar{U}$ through the SBLI region at specific x/D_j locations, shown in Figure 102 a) and b), respectively, further illustrate the differences between the compliant- and rigid-surface cases. The first profile is located near the intersection of the barrel shock and the plate-induced shock (x/D_j = 1.4) and the profiles show that the wave interaction is shifted slightly upstream in the compliant-surface case (see deficits near z/D_j = 0.125).

The next two profiles are placed on either side of the SBLI incident and separation shock interaction (x/D_j = 1.6 and 1.7). For the rigid surface case, this interaction also includes the normal shock (discussed previously) near z/D_j = -0.125. The increased M uncertainties near the Mach disk for the x/D_j = 1.6 profile are likely due to particle lag effects and shock positional unsteadiness. The normal shock leads to a rigid-surface case deficit on the downstream side (profiles for $x/D_j \geq$ 1.7). The profiles at x/D_j = 2.0 and 2.2 illustrate the increased Mach number and jet plume width just before the SBLI reflected shock for the compliant-surface case. The last profile, located at x/D_j =2.4, illustrates that the SBLI outflow conditions correspond to increased Mach numbers and speeds for the compliant-surface case.

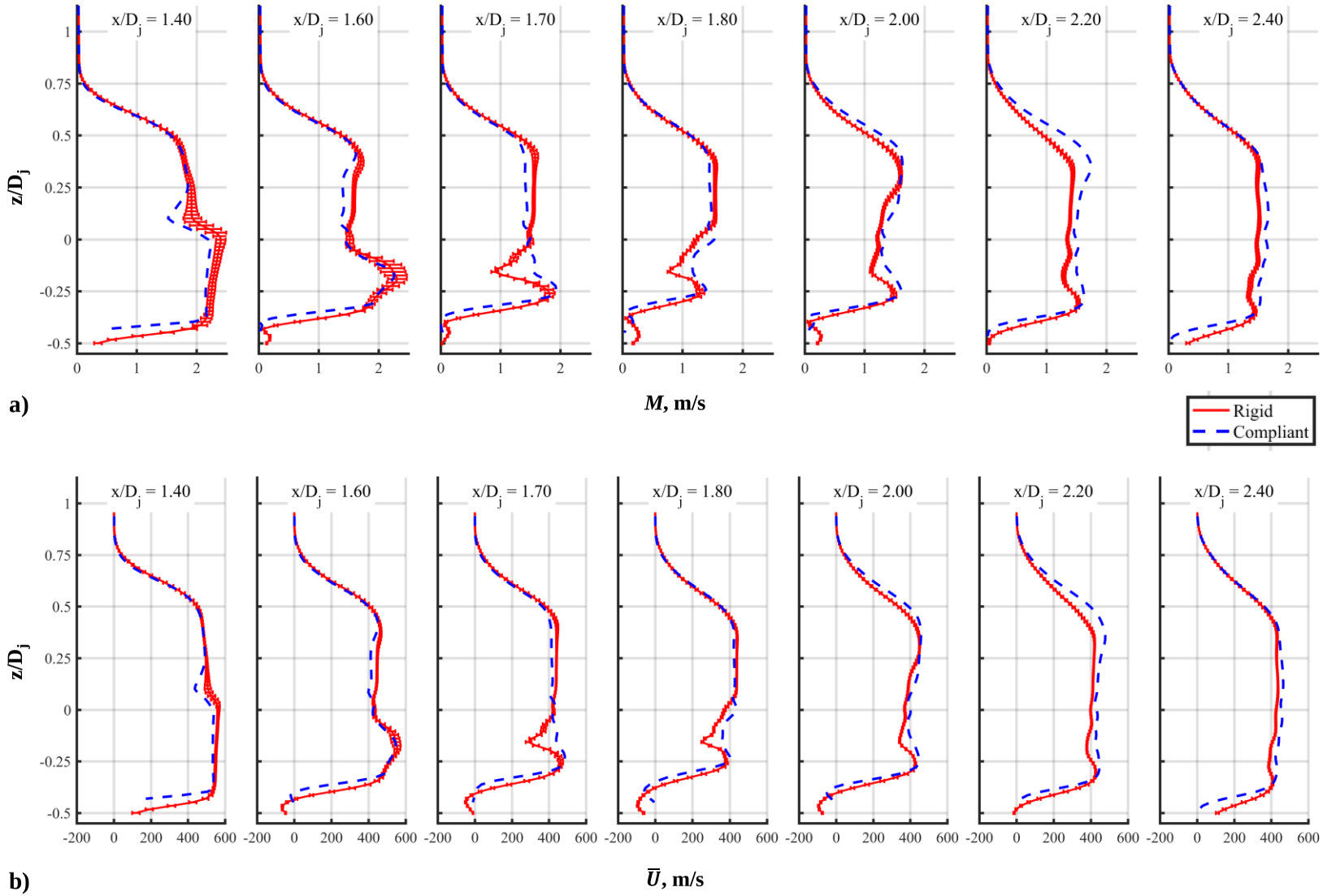

Figure 101. Mean profiles of a) Mach number and, b) $\bar{U}$ through the SBLI.

5.6.3 The SBLI Separation Region

The compliant-surface case also results in an altered SBLI separation region in addition to affecting the shock wave structure. In order to better investigate the SBLI separation region, boundary layer profiles were utilized. In order to facilitate the comparison, the velocity profiles are plotted using distance from the surface on the vertical axis, d_w, thereby removing the varying vertical offset created by the deflected surface contour. Figure 103 presents these $\bar{U}$ profiles at various x/D_j locations within the SBLI separations region.

The first profile, obtained at x/D_j = 1.3, has a plainly visible low-momentum region nearest the wall for the compliant-surface case. This is believed to be due to boundary-layer thickening caused by an adverse pressure gradient incurred in the subsonic portion of the boundary layer beyond the inflection point in the deflected surface contour. The boundary layers thicken and separate near x/D_j = 1.45 and 1.55 for the rigid- and compliant-surface cases, respectively. Although some of the profiles are difficult to interpret because there is no uniform freestream, it is still clear that the SBLI separation region in the rigid-surface case is thicker than that in the compliant-surface case. The maximum separation-region thickness is on the order of 3 mm and occurs near x/D_j = 1.8. The compliant-surface case maximum thickness is found at a similar location, but is approximately 2.5 mm. The magnitude of flow reversal is greater for the rigid-surface case, reaching a maximum magnitude of approximately 100 m/s, compared to approximately 65 m/s for the compliant-surface case. Boundary-layer reattachment occurs near x/D_j = 2.2 for both cases, resulting in a longer separated region for the rigid-surface case.

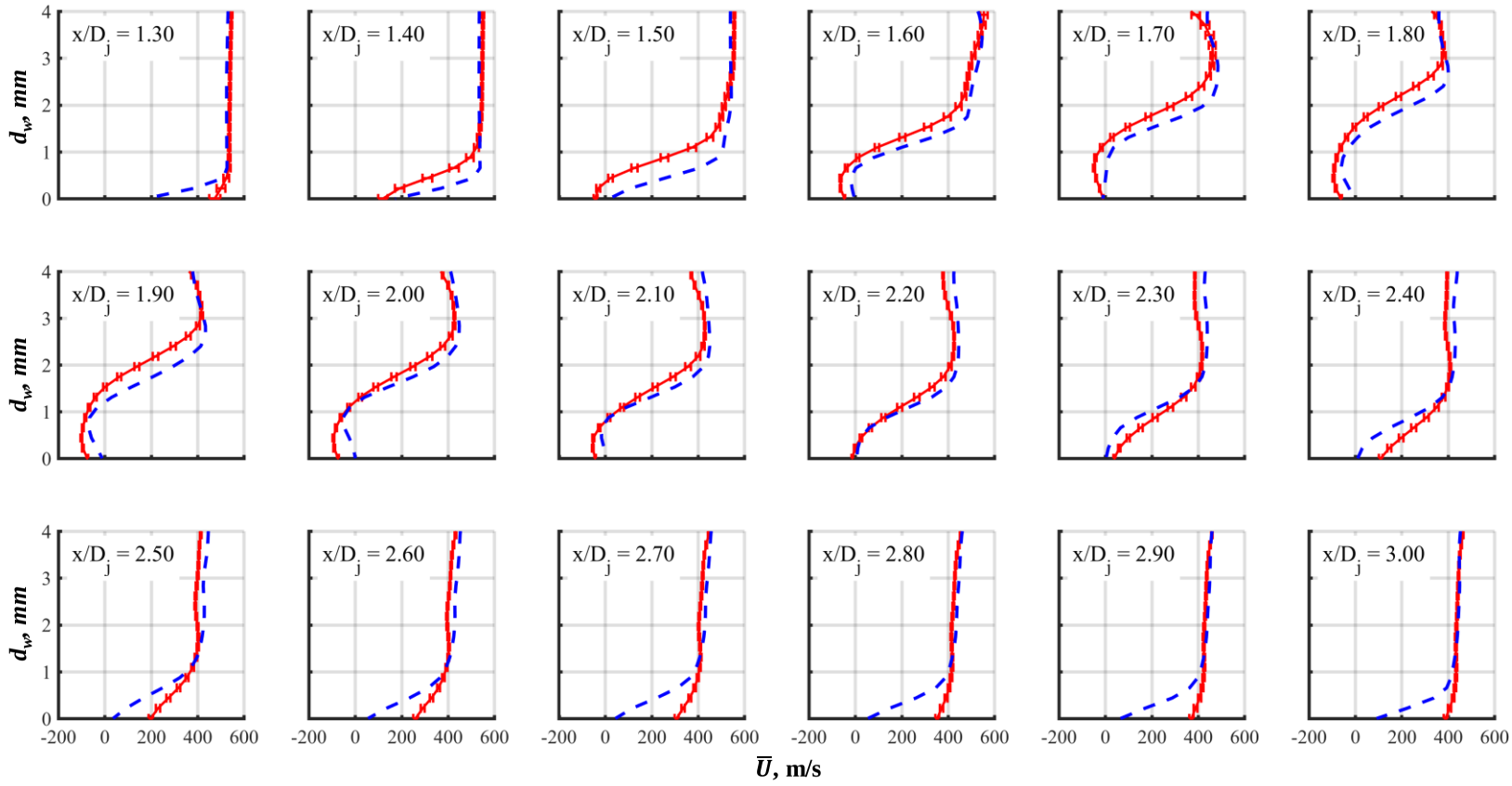

Figure 102. Boundary layer profiles throughout the SBLI separation region.

5.6.4 Downstream Shock-Cell Structure

Mean Mach contour plots of the entire measurement domain for both cases are shown in Figure 104. The wave structure in the first shock cell region is similar for both cases, with the only notable differences being those described previously (the inclination of the SBLI incident shock and the presence of the small normal shock above the SBLI separated region). However, farther downstream, the shock-cell structures of the two flowfields differ significantly. In the rigid-surface case, the second shock cell is much more clearly defined than it is in the compliant-surface case, as highlighted by the overall crisper features in the high-speed region, near the oblique shock wave, and the near-wall low-speed region (see within $2.5 \lesssim x/D_j \lesssim 4.5$).

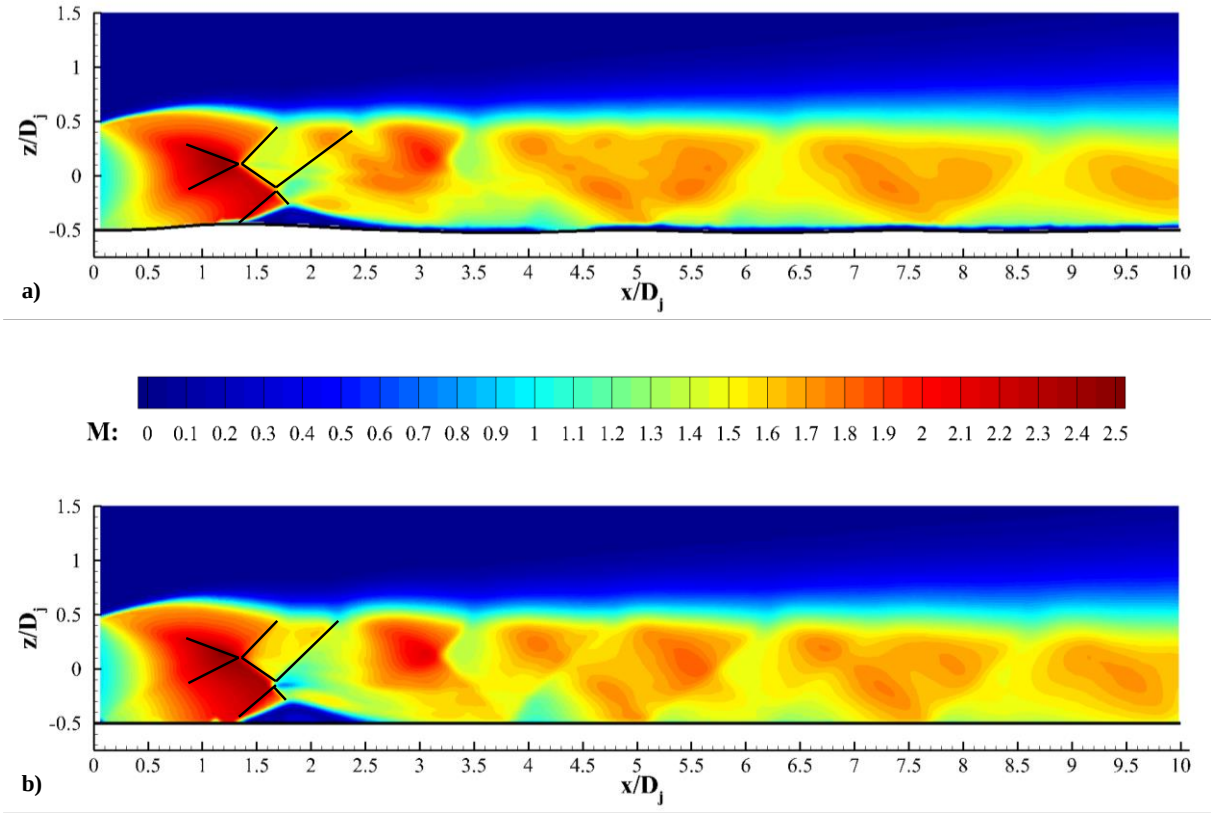

Figure 103. Mach contours for a) the compliant-surface case, and b) the rigid-surface case, reveal differences in the shock-cell structure within shock cells 3 – 5.

There are also large-scale changes in the later shock cells. The shocks take a crossing configuration in the rigid-surface case, but one of the shock trains seems to be more dominant than the other. This is evidenced both by the Mach contour plot shown in Figure 104 b) as well as by the schlieren imagery obtained previously and described in Section 4.1 (where some of the waves were much less defined than others). In the compliant-surface case, the weaker shock train appears

to be further reduced, leading to a well-defined zig-zag pattern in Figure 104 a). This reduction in wave strength may be due to altered shock strengths farther upstream, by the much thicker near-wall boundary layer, or by both.

5.6.5 The Boundary Layer

Immediately downstream of the SBLI separation region, the compliant-surface case boundary layer is noticeably thicker than that for the rigid-surface case, as can be seen in Figures 101 a) and b). This trend continues throughout the remainder of the measurement domain, as confirmed by Figures 104 and 105. Figure 105 presents boundary layer profiles at a variety of x/D_j locations between the SBLI reattachment point and the end of the measurement domain ($x/D_j \approx 10$). The first profile obtained at $x/D_j = 2.50$, is beyond the SBLI reattachment point, but near enough to still

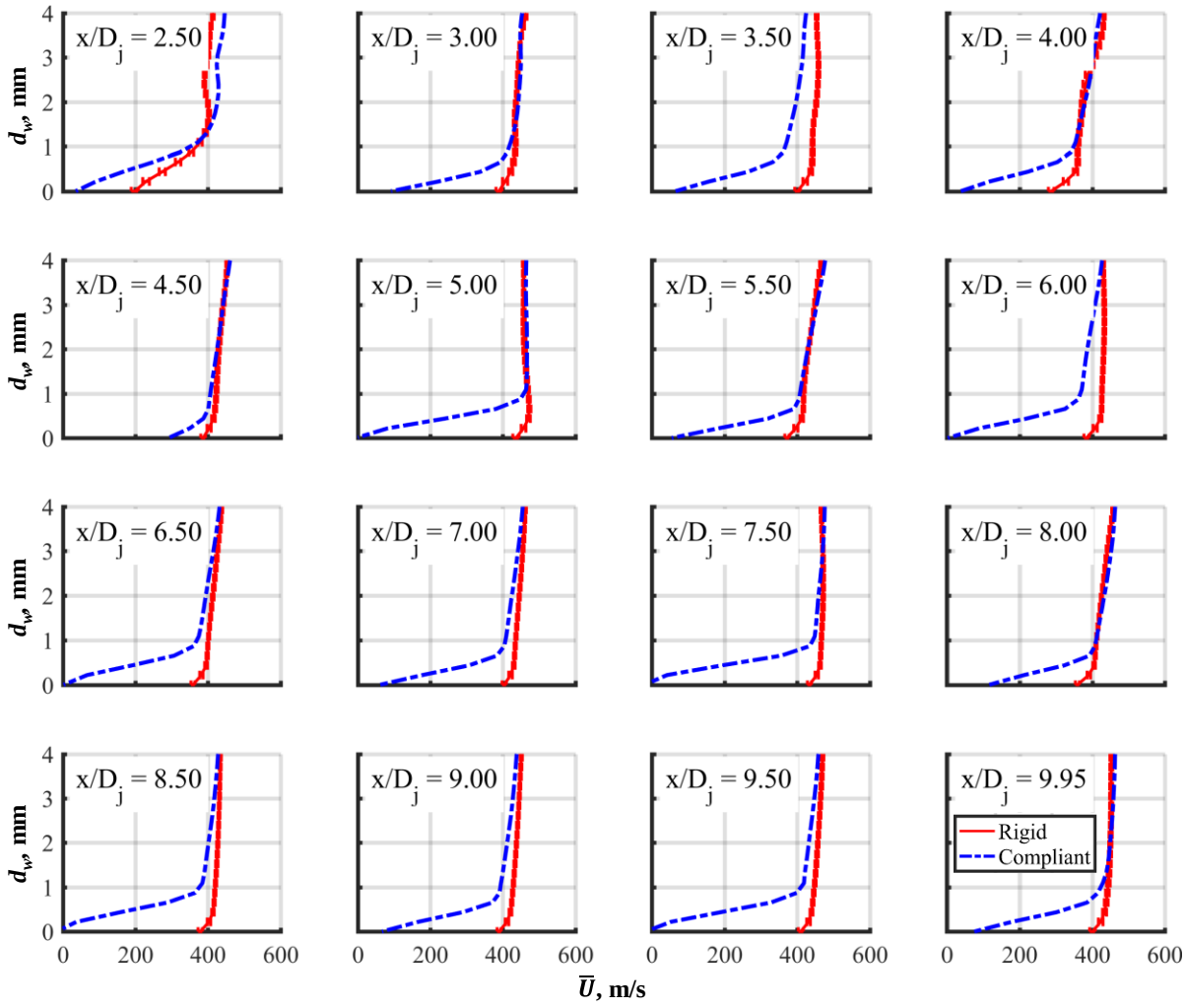

Figure 104. Boundary layer profiles at selected locations between the SBLI reattachment point and the end of the measurement domain.

have clearly thickened boundary layers for both the rigid- and compliant-surface cases. Throughout the remaining profiles, the boundary-layer thickness, δ, remains relatively constant in the rigid-surface case. The compliant-surface profiles, in contrast, show varying boundary-layer thicknesses. The profiles obtained at x/D_j = 4.5, 5.5, and 8.0, for instance, have thinner boundary layers than those at x/D_j = 5.0, 7.5, and 8.5. The compliant-surface case boundary layer is also much thicker (3-4 times, in some cases) than that of the rigid-surface case.

The fluctuation in δ in the compliant-surface case does not appear to be correlated to the direction of surface deflection, but may be related to the magnitude of local surface-contour slope, as the local deflection maxima and minima coincide with locations of comparatively thicker δ. Another possibility is that δ is related to the local surface pressure. Surface pressure data were previously discussed for the rigid-surface case using pressure-sensitive paint (see Section 4.3). An obvious correlation does not exist between the compliant-surface case δ and the rigid-surface case surface pressure distribution, but the compliant-surface case pressure distribution may be significantly different from that of the rigid-surface case. Further work is needed in this area; either through more thorough correlation analyses and/or compliant-surface case pressure data acquisition (the latter presents significant experimental challenges).

5.6.6 Farfield Conditions

Conditions in the latter half of the measurement domain were surveyed and compared as well. Of particular interest here were the shear layer location, its thickness, and the turbulence statistics within. Profiles through the flowfield were inspected at x/D_j locations corresponding to both high-speed (5.0, 7.5, and 9.75) and low-speed (6.25 and 8.75) regions.

The $\bar{U}$ profiles presented in Figure 106 clearly show that the rigid- and compliant-surface case shear layers are very similar. The compliant-surface case shear layer may be slightly wider than that of the rigid-surface case, but since the difference is only slightly larger than the rigid-surface case measurement uncertainties, this cannot be verified unequivocally. Profiles of the Reynolds shear stress, $\overline{u'w'}$, are presented in Figure 107. Again, the distributions through the jet are very similar, with a relatively symmetric peak located in the middle of the shear layer. Unfortunately, the rigid-surface case measurement uncertainties are too large to identify any clearly discernible differences between the rigid- and compliant-surface cases. This is due to the relatively modest number of instantaneous measurements (N = 1000 – 1200) that contribute to the turbulence statistics. The uncertainty is a function of $1/\sqrt{N}$ (see Ref. 119), so approximately 4000 snapshots

should be obtained in order to halve the uncertainty. In any case, the farfield profiles do show that the jet primary shear layer behaves similarly between the rigid- and compliant-surface cases.

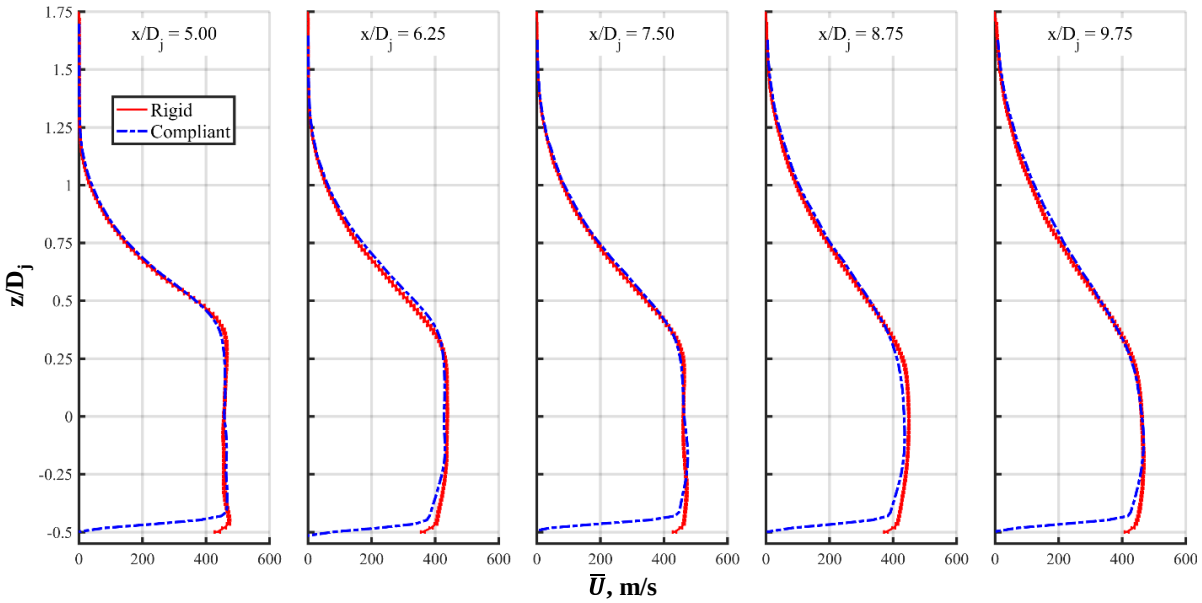

Figure 105. $\bar{U}$ profiles at selected farfield positions show extremely similar shear layer growth rates.

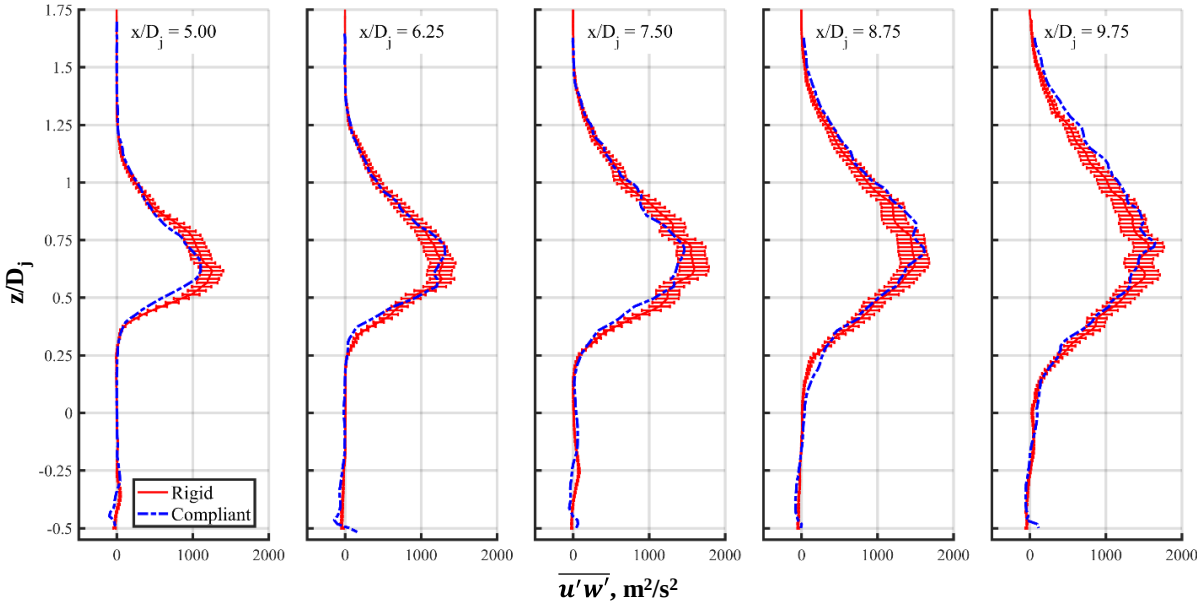

Figure 106. Reynolds shear stress profiles at selected farfield positions show similar turbulence profiles.

5.7 Fullfield Structural Response

Over 1000 instantaneous sDIC snapshots were obtained for the compliant-surface case. These fullfield data were analyzed for the out-of-plane deflection and the in-plane strains in both instantaneous and averaged senses, as discussed in the following sections.

5.7.1 Out-of-Plane Deflection

Figure 108 presents the deflected surface-position ($\mathcal{Z}$) contour maps for four randomly selected instantaneous measurements. The data are presented in dimensional form, where $\mathcal{Z} = 0$ corresponds to the rigid-surface planar condition. Positive values correspond to deflection into the jet flowfield. All of the surface contour maps look qualitatively similar, indicating that the deflected surface may have a quasi-static surface response that is characterized by a standing wave pattern along the jet axis. The wave response has the largest magnitudes along the jet axis, as expected. The largest deflection is on the order of 0.7 mm, is directed towards the jet, and occurs within the first shock cell. The deflection decreases in magnitude with x/D_j. The surface deflects both into and away from the jet. A more detailed analysis of the deflected surface state along the jet axis can be found in Section 5.5.

The instantaneous results presented in the figure are fairly symmetric about the jet axis ($y/D_j = 0$). As distance from the axis increases, the magnitude of the surface deflection becomes smaller. One area that does display some asymmetry can be found on the downstream end of the initial jetward deflection region, near $x/D_j = 1.75$, $y/D_j = \pm 3.5$. The surface deflects farther away from the jet on the positive-y side of the axis than it does on the negative-y side. This is not believed to be a result of the jet loading on the compliant surface, which is symmetric (as confirmed upon inspection of the rigid-surface case steady pressure-sensitive paint results, shown in Section 4.3). Instead, the asymmetry may be caused by local variation in the boundary condition along the positive-y edge of the compliant surface. Inspection of the model did not show bonding failure or material separation in that area. Unfortunately, further inspection was not possible with the model-assembly process used in this study, so the reduction in bond strength could not be confirmed or quantified. In the future, ultrasonic damage and delamination instruments/tests may provide a method by which the boundary conditions could be inspected. It should be noted that the initial

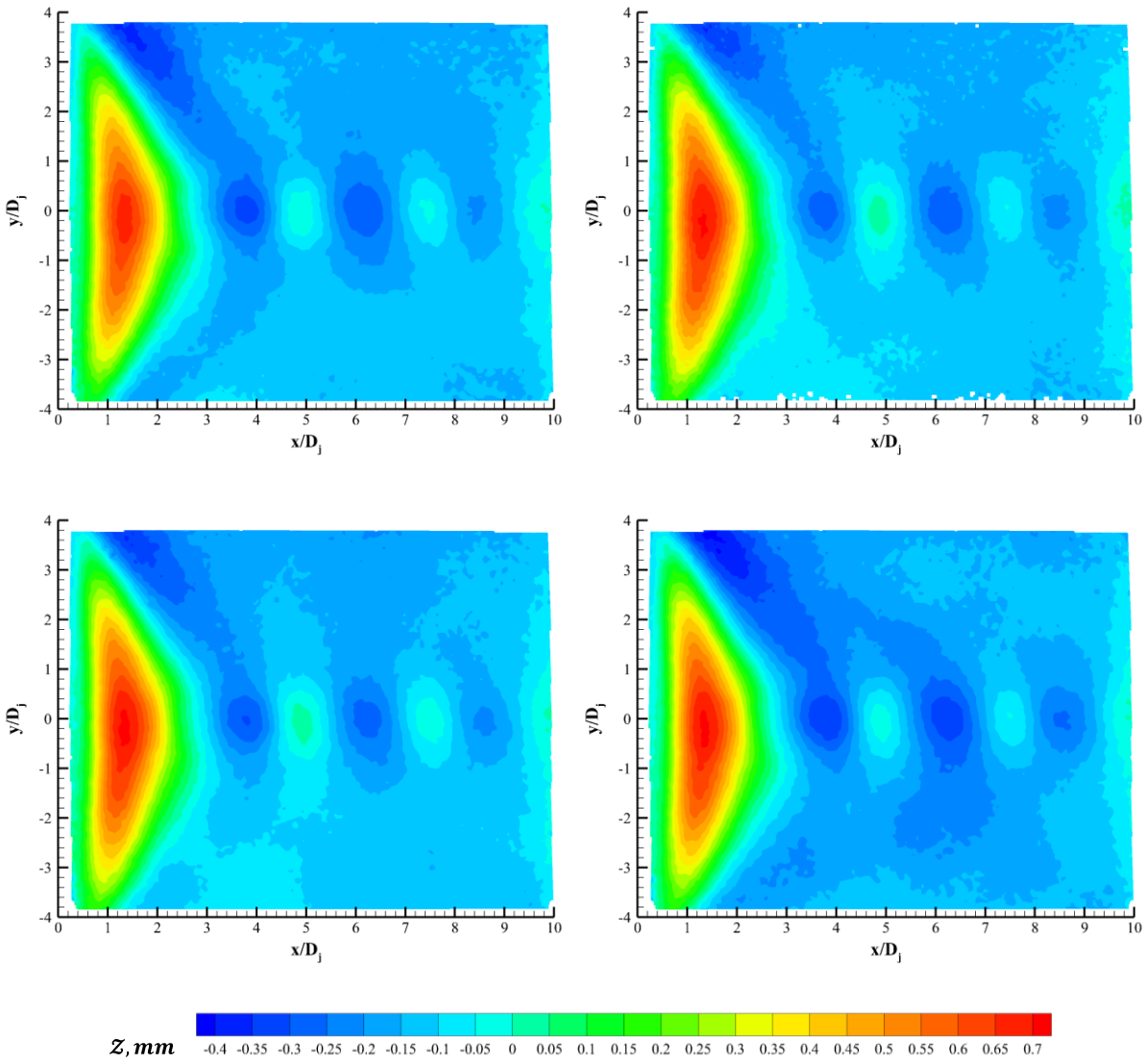

Figure 107. Instantaneous deflected surface-position contours for four instantaneous snapshots.

surface condition (the sDIC reference state) did contain a ripple, and that it was positioned in a similar location and angle, as discussed in Section 5.2.

Since the sDIC images were obtained from the back side of the model, the thickness of the model-support frame prevented image capturing to the ±*y* edges of the compliant surface with both cameras. This limited the sDIC processing window to $y/D_j \leq \pm 3.8$, while the model edge was at $y/D_j = \pm 4.92$. Thus, the surface deflection conditions along these edges, and a corresponding assessment of the boundary condition application, could not be conducted.

However, the clamped boundary conditions could be assessed on the leading and trailing edges of the compliant-surface model as these regions were imaged by both cameras. Inspection

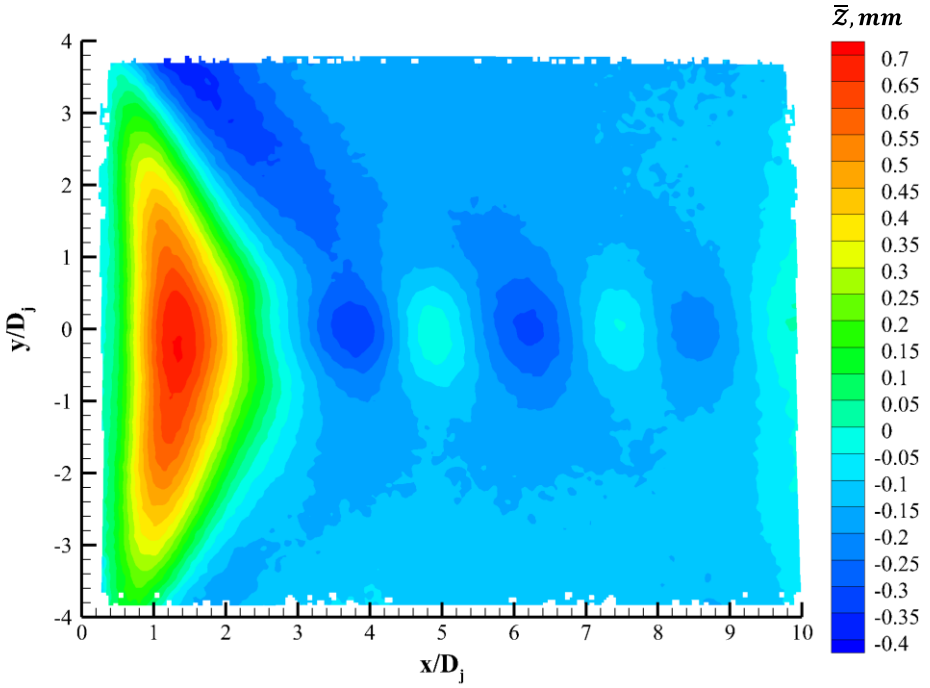

Figure 108. The mean deflected surface-position contour.

of the leading and trailing edges of the deflected compliant surface contours, depicted in Figure 108, show that $\mathcal{Z}$ approaches zero, as expected. Recall that the leading edge of the compliant surface is located at $x/D_j = 0.27$ so as to allow for a compliant surface model with clamped edges on all sides.

The mean fullfield deflected surface state is shown in Figure 109. From this figure, it is clear that the instantaneous snapshots shown previously are representative of the mean deflected state. This can be quantified by inspecting the standard deviation about the mean deflected state, $\sigma_{\mathcal{Z}}$, which is shown in dimensional form in Figure 110 a). Except for several very small regions near the downstream edge of the compliant surface (the darkest blue regions in the figure), all of these measurements exceeded the previously determined measurement noise floor of $0.1t = 7.62$ μm. In general, $\sigma_{\mathcal{Z}}$ is small near the edges of the compliant surface due to the clamped-edge boundary condition, and increases with increasing distance from the edges. $\sigma_{\mathcal{Z}}$ is relatively small within the initial jetward deflected region, but increases noticeably in the region following the first surface deflection wave, leading to a “)”-shaped distribution. However, the increase is not as large along the jet centerline, leading to the formation of local $\sigma_{\mathcal{Z}}$ maxima near $x/D_j = 3.5$, $y/D_j = \pm 2.0$ of approximately 0.425 mm. This type of distribution indicates that the surface condition is more

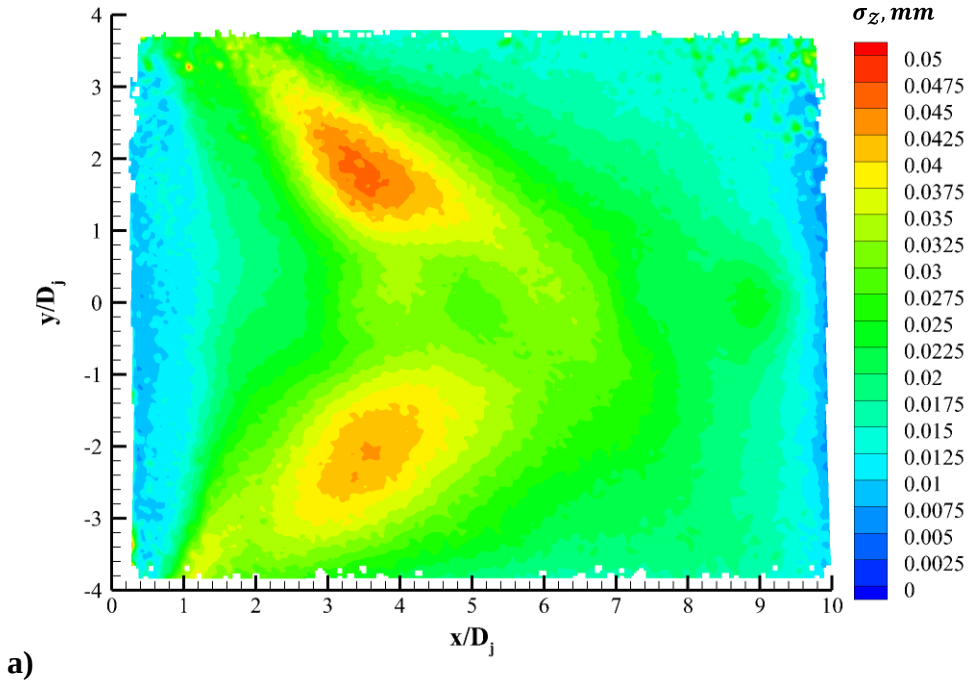

a)

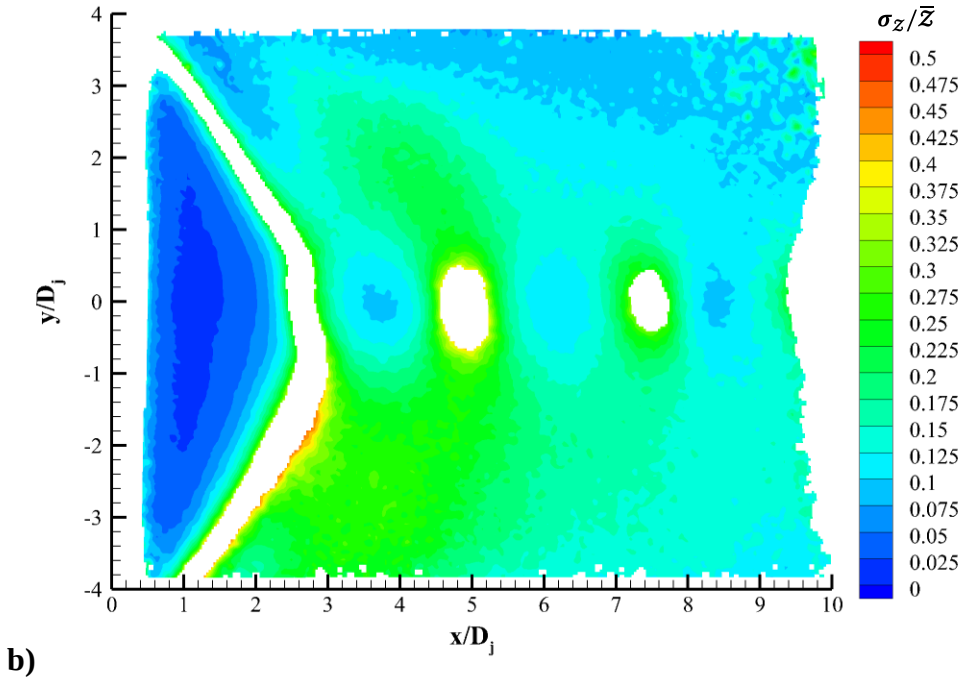

b)

Figure 109. a) Contour map of the standard deviation about the mean deflected surface-position, b) normalized by the mean deflected surface-position. Regions of small deflection have been masked out to avoid undefined values.

stable along the jet axis, leading to less variation, as compared to farther away from the jet axis. The stability in the surface condition near $y/D_j = 0$ is believed to be due to the relatively steady operation of the jet; it applies a load to the surface that is composed of a predominantly static/steady component and a comparatively smaller unsteady/dynamic component, thereby leading to smaller deviations from the mean deflected position. The imposed load is dominated by the steady/static component within and near the jet footprint, which explains why the region of decreased $\sigma_{\mathcal{Z}}$ is approximately bounded by $y/D_j = \pm 1$.

The standard deviation is normalized by the local surface deflection in Figure 110 b). Regions where $\bar{\mathcal{Z}} < 0.075$ mm have been masked out in the figure because $\sigma_{\mathcal{Z}}/\bar{\mathcal{Z}}$ approaches $\pm\infty$ for small $\bar{\mathcal{Z}}$. Presentation of the data in this manner allows for the assessment of the relative importance of the steady/static deflected component (the mean state, $\bar{\mathcal{Z}}$) as compared to the unsteady/dynamic component ($\sigma_{\mathcal{Z}}$) of the deflection. The figure shows that the steady/static component is generally significantly more important than the unsteady/dynamic component. Excluding regions of small $\bar{\mathcal{Z}}$, the dynamic component is maximally 30% of the steady/static component. Within the first, large amplitude, jetward deflection wave, the dynamic component is very small compared to the steady/static component; values in this region are as low as 0.018. Along the centerline, $\sigma_{\mathcal{Z}}/\bar{\mathcal{Z}}$ is also relatively small; here, the steady/static component is at least 10 times greater than the unsteady/dynamic component (once again neglecting regions where $\bar{\mathcal{Z}}$ is small).

In summary, an analysis of the instantaneous and statistical fullfield sDIC results show that the compliant surface takes on a quasi-static deflected shape. This description of the deflected state of the compliant surface is based on an analysis of the mean and standard deviation of $\bar{\mathcal{Z}}$, which shows that the mean (steady) state contributes much more than the standard deviation (dynamic) state. Along the centerline, the deflected shape takes on a "standing-wave" type form, with a large-amplitude jetward deflection wave in the first shock cell of the jet. Thereafter, the waves become smaller in amplitude, with deflections both into and out of the jet. As distance from the jet axis increases, the out-of-plane deflections become smaller. The dynamic motion of the surface becomes a larger contributor just after the large-amplitude jetward deflection wave ($x/D_j \approx 3.5$), and approximately halfway between the jet axis and the clamped edges ($y/D_j \approx 2 - 3$).

5.7.2 In-plane Strain

In addition to the out-of-plane deflection, sDIC can also be used to investigate the in-plane strain (which, after all, was among the original uses of the DIC technique). Several things should be noted when considering the in-plane strain results. First, the reader is reminded that the sDIC measurements were obtained on the underside of the compliant surface, and that the out-of-plane deflection measurements were presented as if viewing from the flow side of the compliant surface. This was achieved based on an assumption that the thickness of the compliant surface was uniform, even in a deflected state. However, that approach is not valid for the strain measurements because the surface experiences both curvature and uniform (mid-plane) strain. These cannot be separated using the sDIC results alone. Therefore, the strain results discussed in the following figures correspond to the strain on the underside of the compliant surface and are presented as if viewing from the underside of the compliant surface. This leads to the placement of the origin on the right side of the figures, with x increasing to the left.

Second, the reader is reminded that strains are computed relative to the initial reference state of the surface, which was not perfectly planar (see Section 5.2). Thus, the strains reported here are not relative to the rigid-surface (perfectly planar, zero strain everywhere) case.

The in-plane normal strains, ε_{xx} and ε_{yy}, are presented in Figures 111 a – b) for an instantaneous snapshot. Near $x/D_j = 0$, the axial strain on the underside of the compliant surface is tensile as the surface bends into the jet (appearing convex from the underside). Then, as x/D_j increases, the strain changes sign to a compressive state as the out-of-plane deflection reaches a maximum and the surface curvature becomes concave. Since these strain features are due to the curvature of the compliant surface in response to the surface deflection, they take a distribution similar in shape to $\mathcal{Z}$. Farther along the jet axis, the axial strain continues to alternate between weak tensile and compressive states, according to the local surface curvature. The strains in the transverse direction, ε_{yy} and shown in Figure 111 b), also exhibit a curvature-dependent distribution. In this case, regions of weak tensile strain are observed along the jet axis near $x/D_j = 3.8$, 6.0, and 8.5, corresponding with regions of convex curvature (as viewed from the underside of the compliant surface). These regions of tensile strain are surrounded by regions of weakly compressive strains, corresponding to the concave curvature experienced beyond the inflection points.

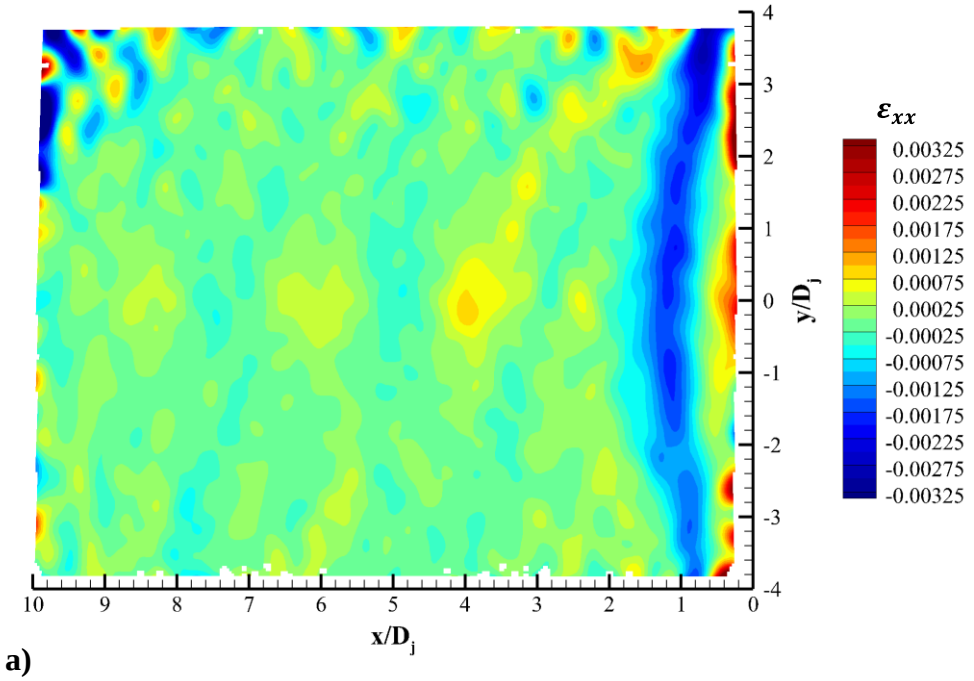

a)

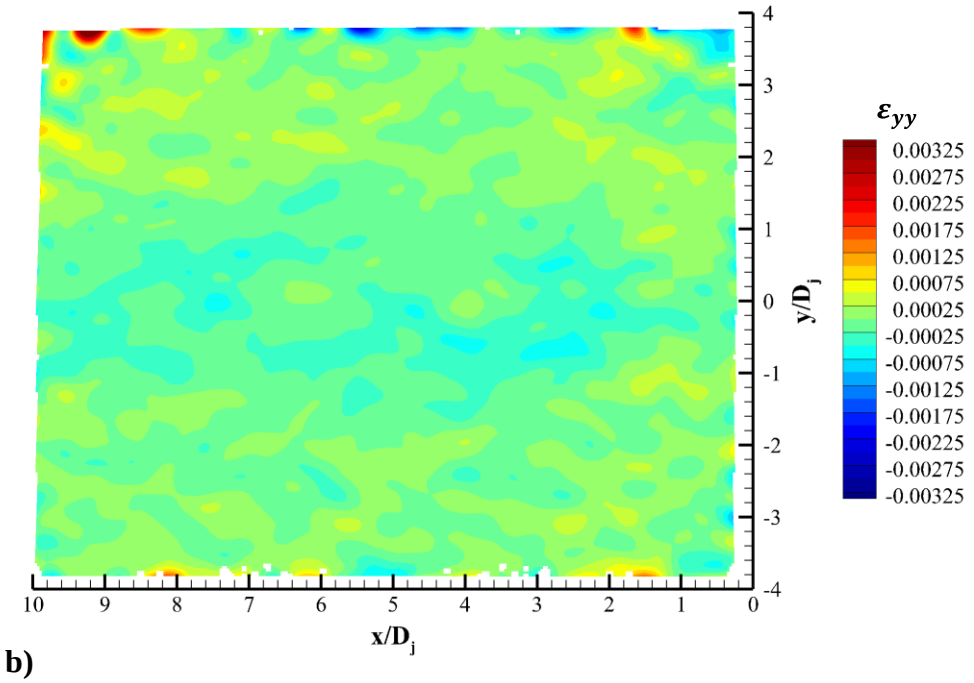

b)

Figure 110. a) Contour map of instantaneous a) axial-direction in-plane normal strain, and b) transverse-direction in-plane normal strain as measured on the sDIC imaging surface (the underside of the compliant surface).

Just as with the out-of-plane deflection, the instantaneous results were found to be fairly representative of the mean in-plane strains, $\overline{\varepsilon_{xx}}$ and $\overline{\varepsilon_{yy}}$, which are shown in Figures 112 a – b). In this case, the assessment is limited to a visual qualitative comparison because the analysis performed previously (using the mean and standard deviation) becomes intractable due to the very small measurement values. Figure 113 presents the mean in-plane strain measurements obtained along the jet centerline. The abscissa axis is reversed to emphasize the fact that these results correspond to the backside of the compliant surface. From the figure, it is immediately apparent that the axial (*x*-direction) strains are much larger in magnitude than those in the transverse direction. The axial strain is highly tensile in the initial jetward deflection wave, but decreases and changes sign to reach a minimum (compressive) strain near the location of maximum out-of-plane deflection. Farther downstream, the axial strain alternates signs according to a relatively regular waveform, which correlates well with the out-of-plane surface deflection, $\bar{z}$, as expected. Along the jet centerline, the transverse-direction strain is mildly compressive everywhere, with oscillations that also correlate well with $\bar{z}$.

The in-plane strains can be rotated to their principal axes so as to minimize the shear strain. These principal strains, ε_1 and ε_2, are shown in Figure 114 for the mean in-plane strains discussed previously, and the measurements obtained along the jet centerline are shown in Figure 115. The principal strains represent the maximum (and minimum) strains incurred by the compliant surface along any two orthogonal directions (and thereby zero shear strain). The principal strains can be used to verify whether the deflected-surface-state induced strains fall within the material elastic regime. The material elastic strain limit, ε_y, was estimated using the material's elastic modulus, *E*, and the yield stress, σ_y = 651.5 MPa, (obtained from the material traceability report; see Appendix A) according to Equation 19.

$$\varepsilon_y = {}^{\sigma_y}/_{E} \tag{19}$$

The elastic strain limit was determined to be ε_y = 0.00326. Beyond this threshold, the compliant surface may enter the plastic deformation regime, where the deformations become permanent. Assuming that ε_y is valid in both tension and compression, inspection of Figure 114 shows that the strain on the underside of the compliant surface approaches, but does not exceed, ±0.003. Although the exact values for the strain on the flowfield-facing surface of the compliant surface are unknown, it is believed that the compliant surface experienced stresses and strains that were relegated to the elastic (or linearly proportional) regime of the material used.

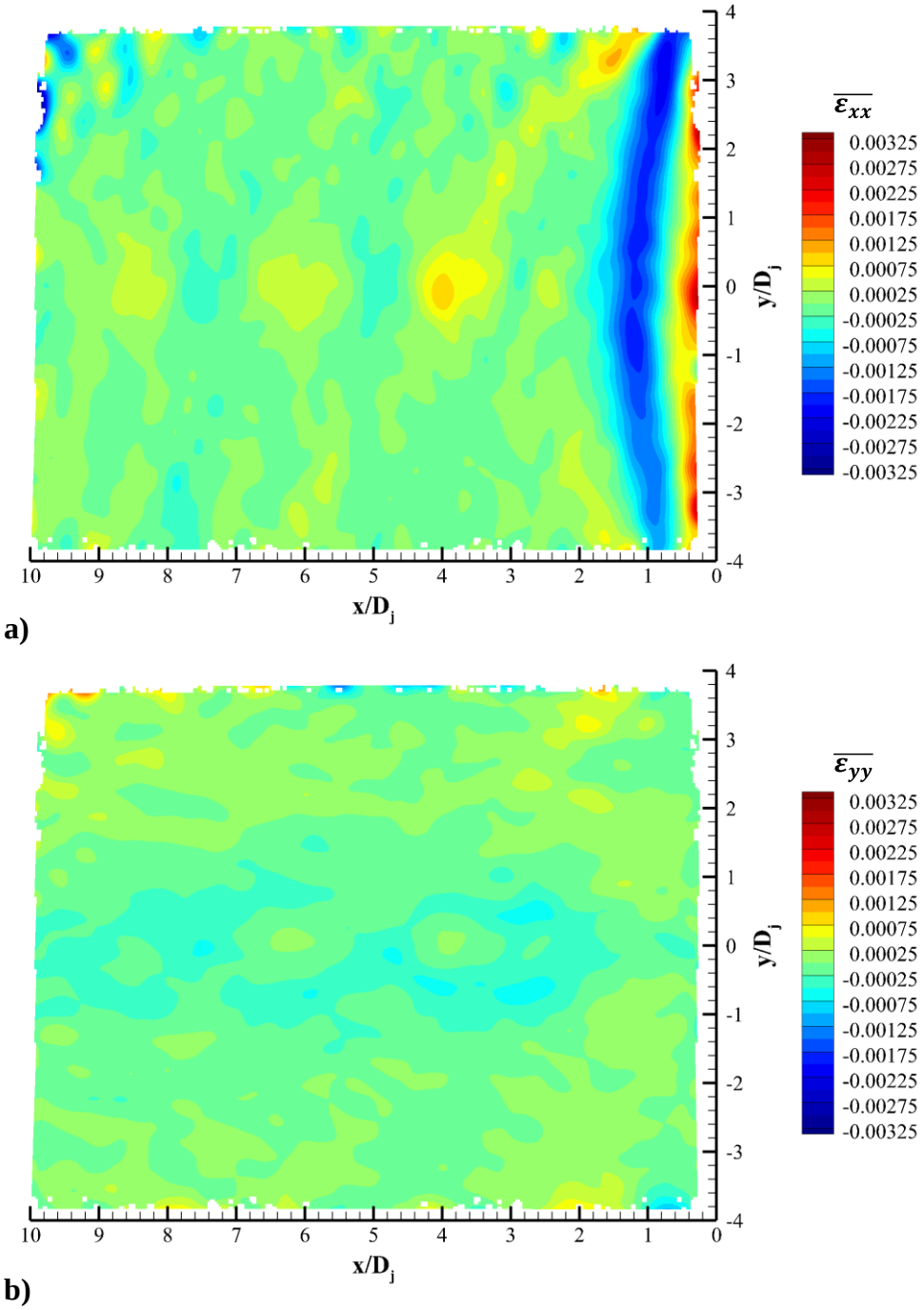

Figure 111. a) Contour map of a) the mean axial-direction normal strain, and b) the mean transverse-direction normal strain as measured on the sDIC imaging surface (the underside of the compliant surface).

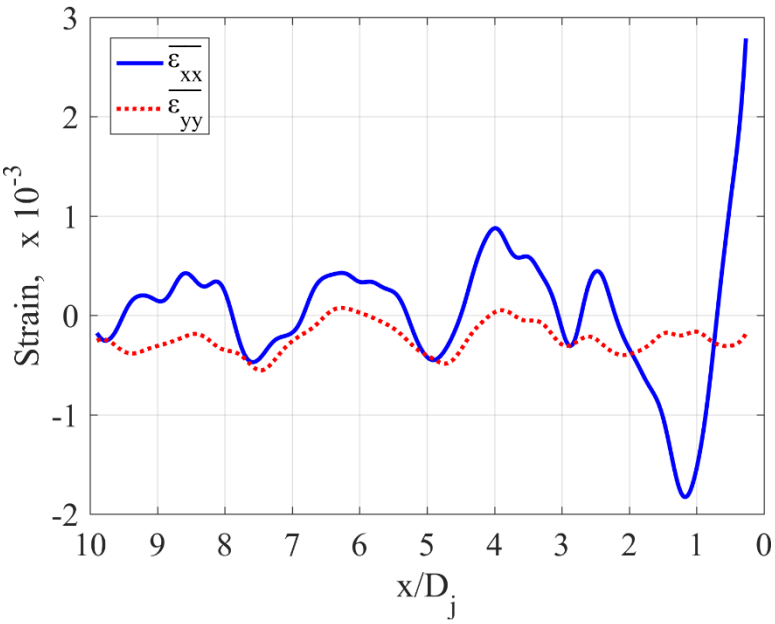

Figure 112. Mean in-plane strains along the jet centerline.

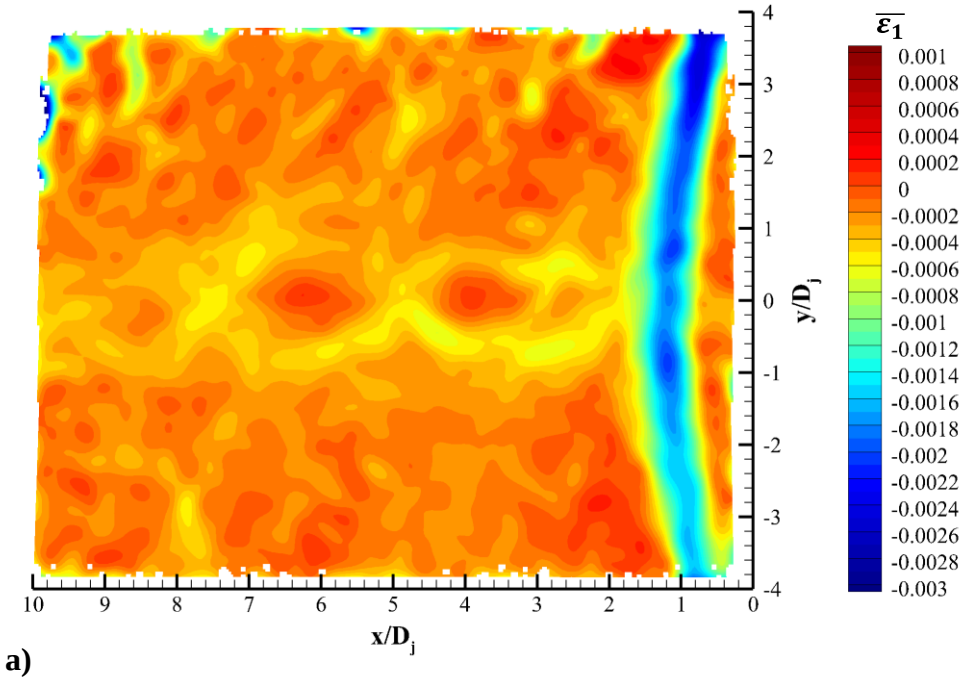

a)

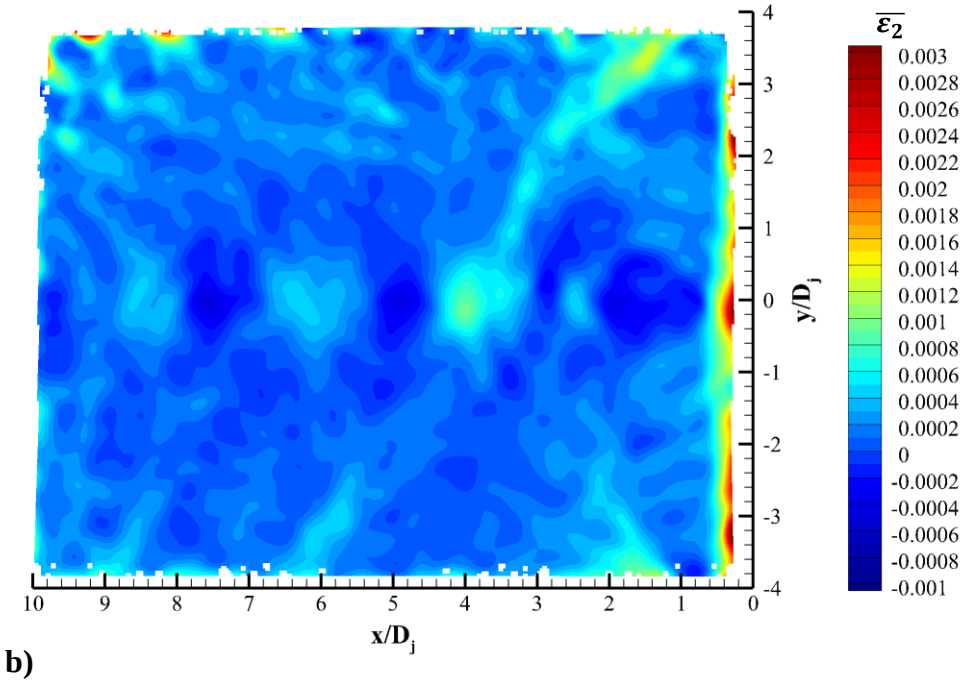

b)

Figure 113. a) Contour maps of the mean principal in-plane strain as measured on the sDIC imaging surface (the underside of the compliant surface), where a) and b) are orthogonal.

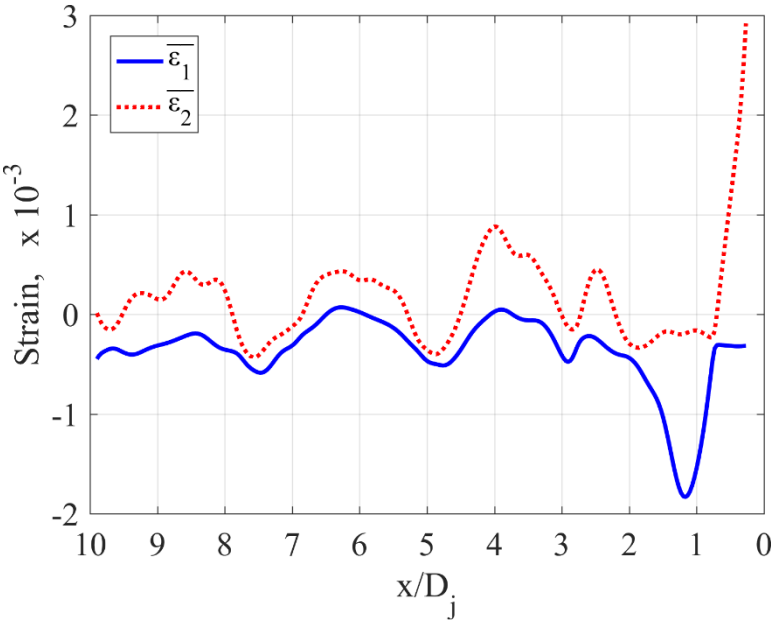

Figure 114. Mean in-plane principal strains along the jet centerline.

Chapter 6 Conclusions and Recommendations

6.1 Research Summary and Conclusions

The current work characterizes, in detail, the flowfield and surface state of the relatively little-explored problem of an underexpanded axisymmetric jet flowing across an adjacent parallel surface, in both rigid-surface and compliant-surface configurations. The problem has significance due to the many fluid-mechanical phenomena present in this turbulent flow in both the rigid- and compliant-surface configurations. These include unusual compressible-wave interactions, shear layers, boundary layers, and shock/boundary layer interactions, any of which may be unsteady in nature, as well as the fluid-structure interactions that may occur in the compliant-surface case. Real-world applications for this type of flow may include engine exhausts and nearby airframe surfaces and carrier decks.

To date, the vast majority of the rigid-surface case literature has been generated by the acoustics community, and so, while much of the data and results obtained in those studies are dynamical in nature, they are largely rooted in pointwise (acoustic) measurements. This has left the flowfield, which obviously plays an integral part in other areas of interest for the problem (including the acoustics), largely undocumented. The compliant-surface literature for the scenario under investigation is extremely limited, all studies having been conducted by a single author and his colleagues. Those studies are again motivated by acoustics, and therefore emphasize the dynamics of the structural interaction in those terms, once again leaving the flowfield little explored. Meanwhile, in recent years there has been a growing interest in the area of fluid-structure interactions as we continue to push technological, engineering, and operational boundaries towards lighter and stronger structures at increasingly high speeds, pressures, and temperatures.

It is the purpose of this work to document and experimentally characterize the rigid- and compliant-surface flowfields, and their corresponding surface states, towards the goal of improving the understanding of the fluid-structure interactions involved. The study takes a multi-step approach. First, the isolated jet, which is the fundamental flow involved, is characterized in both a flowfield-velocimetry and unsteady manner at a nozzle pressure ratio, *NPR*, of 5.0 (with some additional experiments at 4.0 and 3.0). Next, the rigid-surface case is considered, and the flowfield and accompanying surface conditions are documented in detail, so as to provide a baseline for comparison for subsequent compliant-surface case experiments. Several jet/surface

separation distances, h/D_j, were considered (0.50, 0.55, 0.60) for NPR = 5.0. Then, the simultaneous acquisition of instantaneous velocity fields and surface deflection data are demonstrated for the compliant-surface case under the same operating conditions (NPR and h/D_j). Until now, obtaining these fullfield data, in mutually consistent and high-quality forms, for such a supersonic flowfield has, to the author's knowledge, not yet been demonstrated. Last, the compliant-surface case data are explored in both a mean and instantaneous sense, and conclusions are drawn regarding the fluid-structure interaction involved via a comparison to the rigid-surface case.

6.1.1 Isolated Jet

The isolated underexpanded jet, being a canonical compressible flow, has a long tradition of research, and the characteristic shock-cell structure is well understood. Far-field acoustic spectra revealed narrow-band dominant frequencies that were believed to be associated with jet screech tones. This theory was corroborated by comparison to established screech-tone semi-empirical prediction models. High-speed schlieren imagery were used to investigate the positional-fluctuation of shock waves within the first shock cell, and the spectral peaks identified in the resulting time-series analyses were found to match closely with those obtained from acoustic spectra, and screech-tone prediction models found in the literature. Thus, it was concluded that high-speed schlieren can be used to identify screech within a jet flow.

Velocimetry data were obtained on a plane passing through the jet axis in the form of two-component planar PIV, and the instantaneous and mean velocity fields and turbulence quantities were described. Then, a newly acquired tomographic PIV system was used to obtain three-component velocimetry data within a volume that spanned approximately half of the jet flowfield. These mean data revealed the shock-cell structure of the isolated jet in a 3D manner, allowing for the visualization of the first several shock cells, axisymmetric flow acceleration and radial growth in regions of flow expansion, deceleration and contraction in regions of flow compression, a Mach disk and post-shock subsonic core, and a growing turbulent shear layer. The schlieren imagery, planar PIV, and tomographic PIV were all found to be consistent with each other.

6.1.2 Jet/Rigid-Surface Interaction

Next, the jet and rigid-surface case were considered. The high-speed schlieren imagery immediately revealed that the presence of the surface greatly altered the flowfield, especially for

the h/D_j = 0.50, NPR = 5.0 case. The flow exits the nozzle at an underexpanded condition, but is prevented from expanding (turning/bending) outward due to the no-penetration boundary condition imposed by the surface. Schlieren imagery reveals the presence of an oblique shock wave leading from the nozzle lip/plate leading edge into the interior of the jet flow at an angle of approximately 24° (relative to the horizontal). The velocimetry data confirm the presence of this wave, which is called the "plate-induced shock." The plate-induced shock alters the isolated-jet compressible wave structure, resulting in the destruction of the Mach disk, and instead yielding a two-oblique shock interaction (the other shock being a barrel shock). Two reflected oblique shocks are formed downstream of the shock interaction, one of which is directed towards the surface. This shock becomes the incident shock of a shock/boundary-layer interaction (SBLI). The SBLI is a prominent feature in both the schlieren and velocimetry data, inducing boundary layer separation. The surface conditions, both in and outside of the SBLI separation region, were investigated using pressure-sensitive paint and surface oil-flow visualization.

In addition to the obvious changes in the first shock cell, the remaining flowfield showed significant changes in terms of the shock-cell structure of the jet. These are in part due to the changes in the first shock cell, but are also largely governed by the presence of the surface itself, leading to a wall-dominated flowfield on that side of the jet.

In the absence of far-field acoustic data, high-speed schlieren data for the rigid-surface case were used to assess whether or not the screech cycle had been affected by the presence of the surface. Shock-tracking time-series analyses of the instantaneous schlieren imagery for all three separation distances yielded broadband spectra, indicating that acoustic screech had been suppressed at all three considered h/D_j. This finding was consistent with those of other studies.

The acquisition of high-quality near-wall velocimetry data using PIV is traditionally a great experimental challenge due to particle seeding and laser reflection issues, as well as challenges in optimally imaging the region, and with conducting data processing in a manner that isolates the flowfield from the surface. The current study utilized a unique approach in which the laser illuminated the surface from a position downstream of the jet in a grazing manner. This approach decreased the amount of beam divergence required and thereby conserved laser power, while also decreasing laser surface reflections since only a small portion of the beam actually impinged against the surface. The resulting planar PIV dataset is considered to be of high quality due to the

high spatial resolution, expansive field of view, and the ability to obtain data very near to the model surface, including the reversed flow within the SBLI recirculation region.

Steady pressure-sensitive paint (PSP) and surface oil flow visualization (SOFV) data were used to assess conditions on the rigid-model surface. The characteristics of both the flowfield and surface data are mutually consistent with each other. Regions of flow acceleration correspond to decreasing surface pressure, and expanding oil streaklines. Oil separation lines are formed at the location of the SBLI separation shock, and there is a corresponding surface pressure increase as well. Within the recirculation region, both the flowfield velocimetry data and the oil streaklines show reversed flow, characterized by two counter-rotating vortices positioned symmetrically about the jet centerline, and the surface pressure corroborates boundary-layer separation due to the approximately constant pressure within. Notably, the pressure everywhere within the first shock cell, even within the separation region, is lower than the ambient pressure. This results in a net unidirectional pressure differential across the plate thickness within the first shock cell. For the compliant-surface configuration, this type of pressure differential induces deflection of the surface into/towards the jet.

Mean tomographic PIV data were also obtained for the rigid-surface case. These data are consistent with those of other measurements, although volumetric spatial averaging limited the ability to resolve shock waves, and data could not be obtained near enough to the surface so as to capture reversed flow within the SBLI separation region. The tomographic PIV data, therefore, did not provide further insight into the three-dimensional structure of the plate-induced shock at the spatial resolution employed in the current study.

The effect of variation in the jet/surface separation distance was studied for the rigid-surface case at $NPR = 5.0$ at $h/D_j = 0.50$, 0.55, and 0.60. The SBLI region was observed to become smaller and appeared to be less strong for the $h/D_j = 0.55$ case. Increasing to $h/D_j = 0.60$ resulted in a significant reduction in the SBLI strength in the PIV data, while the schlieren imagery contained negligible evidence of the SBLI's presence. The PSP and SOFV results, however, indicate that the SBLI does still exist, and that the effect on the boundary layer is still strong enough to induce separation in addition to boundary-layer thickening.

6.1.3 Jet/Compliant-Surface Interaction

Data were then obtained for the compliant-surface case, emphasizing the $h/D_j = 0.50$, $NPR = 5.0$ case. Instantaneous planar PIV measurements were synchronized with stereo/3D DIC (sDIC)

measurements to capture both the flowfield velocities and the out-of-plane surface deflection. To the author's knowledge, this is the first time that these types of data were obtained simultaneously for a high-speed flow; the measurements obtained in this study therefore represent an important experimental precedent for future work.

The experimental setups and resulting measurements had to be rigorously validated prior to data acquisition. For instance, the sDIC calibration and measurement accuracy were validated using a linear-traversing test to make sure that the measured deflections agreed with those that had been applied mechanically. Additionally, tests were performed to quantify the measurement noise error and to investigate whether the sDIC measurements were sensitive to the presence of the PIV seed particles (they were not). Planar PIV measurements were validated using previously obtained data in addition to comparisons to theoretical/analytical expectations.

Since the surface was illuminated by the PIV laser, it could be seen in its deflected state in the PIV images. This allowed for a cross-experimental validation, where the deflected surface contour was obtained from sDIC and then plotted on the raw PIV images. They were found to be mutually consistent. Using the instantaneous sDIC results, local deflected-position envelopes were determined using statistics, and were found to affect, at most, the two nearest-wall velocity vectors in the PIV data, validating the analysis of the mean flowfield data. Great care was exercised to ensure proper synchronization, and to protect all equipment from damage. Data were obtained at random intervals so as to maximize the number of independent measurements and avoid potential aliasing in the data.

The compliant-case surface response was considered in a fullfield sense as well as along the flow symmetry plane. Instantaneous deflected-surface results were found to be representative of the mean deflected condition in most locations. The compliant surface was observed to have a quasi-static response characterized by series of waves along the jet centerline. The largest out-of-plane deflections were observed within the first shock cell, where the surface deflected into the jet by 9.13 surface thicknesses (~0.70 mm). Thereafter, the amplitude of the surface deflection waves became smaller, and acted primarily in the opposite direction (away from the jet), reaching a maximum deflection of -4.44 surface thicknesses (~0.34 mm). Approximately three surface deflection wavelengths were observed.

The surface deflections were largest along the centerline; the fullfield surface deflection maps showed decreasing amplitudes as distance from the centerline increased. The transverse

extent of deflections was, naturally, observed to be related to the magnitude of the deflection along the centerline. The quasi-static response appears to be most closely associated with a surface contour map similar to that expected for a (3,1) vibrational mode. The deflections at the leading and trailing edge boundaries were measured with sDIC and were found to approach the measurement noise floor, and indicate that the clamped-edge boundary conditions had been successfully implemented. Deflections at the transverse boundaries could not be measured due to camera field of view constraints.

In order to investigate the relative importance of the quasi-static/steady and dynamic/unsteady states, the standard deviation about the mean was normalized by the local mean deflection. This analysis revealed that the quasi-static response dominated the surface response, especially along the centerline, where the magnitude of the flowfield forcing is largest. This was especially true in the first shock cell, where the surface deflected very strongly into the jet flowfield. The dynamic response was found to be most important in a crescent shaped region located downstream of the first large jetward deflection and its associated reflexed region. Within this region the mean deflection is relatively small, thereby more easily allowing for a more important dynamic contribution. In this analysis, regions of very small mean deflection were not considered.

The deflected surface contour was found to be similar to the surface pressure distribution observed using PSP for the rigid-surface case. In particular, the low pressure region within the first shock cell agrees well with the observed jetward deflection. The correlation for the other surface deflection waves is less clear, but the rigid-surface case pressure distribution is undoubtedly different from that for the compliant-surface case. Surface pressure measurements could not be obtained for the compliant-surface case due to the difficulties incurred by the surface motion.

The compliant-surface case flowfield data were compared closely to the results obtained for the rigid-surface case. The comparisons were conducted both in a fullfield manner using contour plots, and in a more quantitative sense via the use of profiles through the jet. The two cases were compared on a region basis considering a) the nozzle exit plane to the shock/boundary-layer interaction (SBLI) shock waves, b) the flow through the SBLI region, c) the SBLI separation zone, d) the shock cell structure of the remainder of the jet plume, e) the near-wall boundary layer, and f) farfield conditions. Each of these are summarized in turn.

At the nozzle exit, velocity (and Mach number) profiles through the jet show that the flowfields are nearly identical. Both cases also exhibit very similar characteristics in the primary jet shear layer (on the side of the jet far from the surface) where the velocity distributions are similar, as are the shear layer position, thickness, and growth rate, and the turbulence statistics. Nearer to the surface, there are notable differences. The jetward surface deflection wave induces a compression-expansion effect on the flowfield; a supersonic compression is experienced before the inflection point in the surface contour and an expansion occurs beyond the inflection point. A region of wall-normal velocity was observed, which is consistent with a supersonic compression-ramp effect. Inspection of the local Mach number did not show a true decrease in the compression region, but that is likely due to the fact that the flowfield is undergoing under- and over-expansion cycles (the compression region effectively has no uniform free stream) and is highly three-dimensional. Schlieren imagery was not obtained for the compliant-surface case, but it is expected that the plate-induced shock would not be as visibly prominent due to the gradual compression. Supersonic acceleration was observed within the expansion region located downstream of the deflected-surface inflection point.

The flow through the shock/boundary-layer interaction (SBLI) region is also quite different for the compliant and rigid-surface cases. The SBLI incident shock wave was found to be weaker in the compliant-surface case, which altered the remaining shock wave structure, and prevents the formation of a normal shock, as seen in the rigid-surface case. In general, the SBLI in-flow Mach numbers are lower for the compliant-surface case due to the surface-induced compression-expansion, resulting in weaker shock waves, and higher out-flow Mach numbers, especially for the parts of the flowfield nearer to the surface. One counter example exists near the jet primary shear layer, where the compliant-surface case Mach number is lower, but it also results in a locally-expanded plume diameter.

Boundary layer profiles obtained through the SBLI separation region show that the boundary layer is thinner in the compliant-surface case than it is for the rigid-surface case. The compliant-surface case boundary layer separates earlier than in the rigid-surface case, but they share a common reattachment point. The magnitude of the reversed flow is smaller for the compliant-surface case.

The downstream shock cell structure is altered significantly by the nature of the compliant surface. Mach number contour plots reveal that the second shock cell is more clearly organized in

the rigid-surface case as compared to the compliant case. This is due to the differing SBLI out-flow conditions, for which the compliant-surface case was more uniform across the jet plume. Large differences also exist in the shock cells farther downstream. The rigid-surface case is characterized by a crossing-type shock cell pattern, but one of the shock trains appears to be stronger than the other. In the compliant-surface case, the weaker shock train is further reduced in strength, leading to a well-defined zig-zag pattern instead.

The boundary layer immediately downstream of the SBLI reattachment point is noticeably thicker for the compliant-surface case than it is for the rigid-surface case. This trend continues throughout the remainder of the measurement domain. However, in the compliant-surface case, the boundary layer shows varying thicknesses, while that for the rigid-surface case is approximately constant. The variation in boundary-layer thickness for the compliant-surface case does not appear to be correlated to the direction of surface deflection, but may be related to the magnitude of the local surface-contour slope, or, more likely with the local surface pressure.

Lastly, comparisons were made between the two cases across the jet width near the end of the measurement domain ($x/D_j \approx 10$). The velocity profiles were found to be very similar in both the jet core and within the shear layer. Turbulence statistics were also compared. However, due to the relatively modest number of instantaneous measurements obtained, the uncertainty in these measurements was quite high, making it difficult to discern statistically significant differences.

6.2 Suggestions for Future Work

It is clear that further research into fluid-structure interactions is needed in both experimental and computational frameworks. Fluid-structure interactions are extremely complex, as there are numerous mechanisms through which they can operate, and the relative importance of these mechanisms depends greatly on the characteristics and properties of the fluids and structures involved, as well as their respective operating conditions, geometry and boundary conditions, and the relevant length and time scales involved.

In terms of the current experimental investigation, there are several directions that future work can explore. The current study has identified a quasi-static surface deflection state and the corresponding flowfield, but was not able to deeply explore the temporal motion and interaction involved. However, the vast majority of interesting FSIs exhibit highly dynamic qualities, such as oscillatory or chaotic characteristics. Therefore, one of the first tasks recommended is to upgrade

the data acquisition systems to their high-speed counterparts. This would allow for the acquisition of time-resolved data and subsequent analysis in the temporal and frequency domains. Simultaneously-obtained time-series surface and flowfield data could be used to investigate temporal evolution via both space and time correlation analyses, and allow for the possible identification of periodicity or limit cycle oscillations. Time-resolved experimentation, especially for optical fullfield methods, has its own challenges, particularly with regard to storing, processing, and handling the tremendous datasets that are required for long-time data analyses, but these are challenges that some researchers have successfully addressed.[96]

In addition to capturing high-speed data of the flowfield velocities and surface deflection, other high-speed experiments would also be highly beneficial. For instance, high-speed schlieren and acoustics data may provide further insight into the relevant dynamical interactions, such as the presence/influence of the screech cycle, acoustic-pressure coherent loading, and others like those investigated by Maestrello.[71-73] Fast-response surface pressure data, ideally obtained using nonintrusive fullfield optical techniques would also provide further insight into the dynamics of the fluid-structure interaction. Fast-response pressure data were obtained in the current study for the rigid surface case with limited success (see Appendix C), but the radiometric method employed here was not suited to a dynamically deforming model. Therefore, for the compliant-surface tests, the recommendation would be to use the life-time calibration method, for which image registration is not needed (at the cost of decreased signal-to-noise ratio), instead of the radiometric method.

Although many aspects of the currently investigated jet/surface interaction have been adequately quantified, additional conditions and parameters should be quantified before these experiments can be truly considered a simulation-verification quality dataset. As the flow conditions have been characterized in detail, most of the additional quantification and validation are related to the structural aspects of the experiment. For instance, the natural frequencies of the compliant surface, the model support structure, and the completed assembly, should be independently verified using hammer-strike testing, time-resolved data (as discussed previously), or by other means. Similarly, the thermal response and characteristics of the model assembly should be more thoroughly investigated in terms of surface heat transfer and material thermal expansion (both of which may affect the surface dynamical response in terms of local pre-stress/strain loading). Ideally, this would be conducted based on knowledge of both the individual components' material properties and that of the assembled model (thereby taking into account the

effects of assembled components of varying materials and properties). The complete vibrational and thermal data required to accomplish these tasks go beyond the scope of those obtained in the current experiment (for instance, the steady surface temperature measurements described in Appendix C). This information should be used to verify that the desired boundary conditions were applied to the compliant surface model, and to ensure that motion and vibration of the model support structure are not falsely attributed to the motion of the compliant surface. In the current investigation, the instantaneous deflection of the rigid frame was used to correct the measured displacement of the compliant surface, but this correction is likely not sufficient for an assessment of the respective vibrational frequencies.

There are also several questions that the current experiments have raised which are yet to be definitively answered or explained. For instance, the increased surface pressures for the h/D_j = 0.55, NPR = 5.0 rigid-surface case are speculated to be due to coherent pressure loading, but the source of the coherence is unknown.

As proposed in Section 4.2, this wave is believed to be located in some other plane and its location, shape, and orientation are currently unknown. Further investigation into the three-dimensional nature of the flow, perhaps via the acquisition of PIV data at multiple planes or high spatial resolution tomographic PIV, could provide a definitive answer in this regard.

References

1 Anderson, J. D., *Modern Compressible Flow with Historical Perspective*, 3rd Ed., McGraw-Hill, New York, NY, 2003.

2 Shapiro, A. H., *The Dynamics and Thermodynamics of Compressible Fluid Flow, Vol. I*, Ronald Press Company, New York, NY, 1953.

3 Chapman, C. J., *High Speed Flow*, Cambridge University Press, Cambridge, United Kingdom, 2000.

4 Fox, R. W., Pritchard, P. J., McDonald, A. T., *Introduction to Fluid Mechanics*, 7th Ed., John Wiley & Sons, Inc., Hoboken, NJ, 2009.

5 Ffowcs Williams, J. E., "The Noise from Turbulence Convected at High Speed," Philosophical Transactions of the Royal Society of London. Series A, Mathematical and Physical Sciences, Vol. 255, No. 1061, pp. 469-503, 1963.

6 Plaschko, P., "Stochastic Model Theory for Coherent Turbulent Structures in Circular Jets," Physics of Fluids, Vol. 24, pp. 187 – 193, 1981.

7 Tam, C. K. W., Chen, P., "Turbulent Mixing Noise from Supersonic Jets," AIAA Journal, Vol. 32, pp. 1774 – 1780, 1994.

8 Seiner, J. M., Norum, T. D., "Experiments of Shock Associated Noise of Supersonic Jets," AIAA 12th Annual Fluid and Plasma Dynamics Conference, Williamsburg, VA, AIAA Paper No. 79-1526, 1979.

9 Powell, A., "On the Mechanism of Choked Jet Noise," Proc. Phys. Soc., Vol. 66, pp. 1039-1056, 1953.

10 Powell, A., "The Noise of Choked Jets," Journal of the Acoustical Society of America, Vol. 25, pp. 385 – 389, May 1953.

11 Norum, T. D., "Screech Suppression in Supersonic Jets," AIAA Journal, Vol. 21, pp. 235 – 240, 1983.

12 Tam, C. K. W., "Supersonic Jet Noise," Annual Review of Fluid Mechanics, Vol. 27, pp. 17 – 43, 1995.

13 Jordan, P., Colonius, T., "Wave Packets and Turbulent Jet Noise," Annual Review of Fluid Mechanics, Vol. 45, pp. 173 – 195, 2013.

14 Morris, P. J., "Jet Noise: A Perspective on Recent Developments and Future Directions," Proceedings of the Acoustics 2012 Nantes Conference, Nantes, France, 2012.

15 Plaschko, P., "Axial Coherence Functions of Circular Turbulent Jets Based on Inviscid Calculation of Damped Modes," Physics of Fluids, Vol. 26, pp. 2368 – 2372, 1983.

16 Tam, C. K. W., Hu, F. Q., "On the Three Families of Instability Waves of High-Speed Jets," Journal of Fluid Mechanics, Vol. 201, pp. 447 – 483, 1989.

17 Troutt, T. R., McLaughlin, D. K., "Experiments on the Flow and Acoustic Properties of a Moderate-Reynolds-Number Supersonic Jet," Journal of Fluid Mechanics, Vol. 116, pp. 123 – 156, 1982.

18 Parras, L., Le Dizes, S., "Temporal Instability Modes of Supersonic Round Jets," Journal of Fluid Mechanics, Vol. 662, pp. 173 – 196, 2010.

19 Fourguette, D. C., Mungal, M. G., Dibble, R. W., "Time Evolution of the Shear Layer of a Supersonic Axisymmetric Jet," AIAA Journal, Vol. 29, pp. 1123 – 1130, 1991.

20 Thurow, B., Samimy, M., Lempert, W., "Compressibility Effects on Turbulence Structures of Axisymmetric Mixing Layers," Physics of Fluids, Vol. 15, pp. 1755 – 1765, 2003.

21 Elliott, G. S., Crawford, J., Mosedale, A., "Enhancement of Large Scale Structures in Supersonic Axisymmetric Jets Using Laser Excitation," 36th AIAA Aerospace Sciences Meeting and Exhibit, AIAA Paper No. 1998-331, 1998.

22 Ibrahim, M. K., Kunimura, R., Nakamura, Y., "Spreading Enhancement of Axisymmetric Supersonic Jet by the Use of Micro Jets," 31st AIAA Fluid Dynamics Conference & Exhibit, Anaheim, CA, AIAA Paper No. 2001-3048, 2001.

23 Huffman, R. E., Elliott, G. S., Boguszko, M., "Turbulence Measurements Using FARRS in a Supersonic Axisymmetric Jet," 45th AIAA Aerospace Sciences Meeting and Exhibit, Reno, NV, AIAA Paper No. 2007-471, 2007.

24 Krothapalli, A., Strykowski, P. J., King, C. J., "Origin of Streamwise Vortices in Supersonic Jets," AIAA Journal, Vol. 36, pp. 869 – 872, 1998.

25 Arnette, S. A., Samimy, M., Elliott, G. S., "On Streamwise Vortices in High Reynolds Number Supersonic Axisymmetric Jets," Physics of Fluids, Vol. 5, pp. 187 – 202, 1993.
26 Krothapalli, A., Buzyna G., Lourenco, L., "Streamwise Vortices in an Underexpanded Axisymmetric Jet," Physics of Fluids, Vol. 3, pp. 1848 – 1851, 1991.
27 Adamson, T. C., Nicholls, J. A., "On the Structure of Jets from Highly Underexpanded Nozzles into Still Air," Journal of the Aerospace Sciences, Vol. 26, pp. 16 – 24, 1959.
28 Crist, S., Sherman, P. M., Glass, D. R., "Study of the Highly Underexpanded Sonic Jet," AIAA Journal, Vol. 4, pp. 68 – 71, 1966.
29 Addy, A. L., "Effects of Axisymmetric Sonic Nozzle Geometry on Mach Disk Characteristics," AIAA Journal Technical Note, Vol. 19, pp. 121 – 122, 1981.
30 Panda, J., "Shock Oscillation in Underexpanded Screeching Jets," Journal of Fluid Mechanics, Vol. 363, pp. 173 – 198, 1998.
31 DeOtte Jr., R. E., Morrison, G. L., Sewell, R. D., "LDV Measurements of the Velocity Field in an Underexpanded Supersonic Jet (Ma = 1.5)," 30th Aerospace Sciences Meeting & Exhibit, Reno, NV, AIAA Paper No. 92-0504, 1992.
32 Ewan, B. C., Moodie, K., "Structure and Velocity Measurements in Underexpanded Jets," Combustion Science and Technology, Vol. 45, pp. 275 – 288, 1986.
33 Yüceil, K. B., Ötügen, M. V., Arik, E., "Interferometric Rayleigh Scattering and PIV Measurements in the Near Field of Underexpanded Sonic Jets," 41st AIAA Aerospace Sciences Meeting, Reno, NV, AIAA Paper No. 2003-917, 2003.
34 Kuehner, J. P., "Simultaneous Acquisition of Pressure, Temperature, and Velocity Using Coherent Anti-Stokes Raman Scattering," Master's Thesis, Department of Mechanical Engineering, University of Illinois at Urbana-Champaign, 2000.
35 Woodmansee, M. A., Iyer, V., Dutton, J. C., Lucht, R. P., "Nonintrusive Pressure and Temperature Measurements in an Underexpanded Sonic Jet Flowfield," AIAA Journal, Vol. 42, pp. 1170 – 1180, 2004.
36 Seiner, J. M., Manning, J. C., Jansen, B., "Supersonic Jet Plume Interaction with a Flat Plate," SAE Technical Papers, Paper No. 872361, 1987.
37 Kwak, J., Lee, Y., "An Experimental Study on the Characteristics of Rectangular Supersonic Jet on a Flat Plate," *International Journal of Aeronautical and Space Sciences,* Vol. 17, No. 3, pp. 112 – 121, 2016.
38 Rainey, R. W., "Interference Effects Upon Fuselage Drag of a Jet Exhausting from a Wing-Mounted Nacelle," NACA RM L56A09, 1955.
39 Salmi, R. J., Klann, J. L., "Interference Effects at Mach 1.9 on a Horizontal Tail Due to Trailing Shock Waves from an Axisymmetric Body with an Exiting Jet," NACA RM E55J13a, 1956.
40 Englert, G. W., "Interaction Between Jets and Various Aerodynamic Surfaces," NACA Conference on Aerodynamics of High Speed Aircraft, pp. 229 – 241, 1955.
41 Englert, G. W., Wasserbauer, J. F., Whalen, P., "Interaction of a Jet and Flat Plate Located in an Airstream," NACA RM E55G19, 1955.
42 Wasserbauer, J. F., Englert, G. W., "Interaction of an Exhaust Jet and Elementary Contoured Surfaces Located in a Supersonic Air Stream," NACA RM E56A16, 1956.
43 Bressette, W. E., "Investigation of the Jet Effects on a Flat Surface Downstream of the Exit of a Simulated Turbojet Nacelle at a Free-Stream Mach Number of 2.02," NACA RM L54E05a, 1954.
44 Bressette, W. E., Faget, M. A., "An Investigation of Jet Effects on Adjacent Surfaces," NACA RM L55E06, 1955.
45 Bressette, W. E., "Some Experiments Relating to the Problem of Simulation of Hot Jet Engines in Studies of Jet Effects on Adjacent Surfaces at a Free-Stream Mach Number of 1.80," NACA RM L56E07, 1956.
46 Lan, C. E., Campbell, J. F., "A Wing-Jet Interaction Theory for USB Configurations," *Journal of Aircraft,* Vol. 13, No. 9, pp. 718 – 726, 1976.
47 Cornelius, K. C., Lucius, G. A., "Physics of Coanda Jet Detachment at High-Pressure Ratio," *Journal of Aircraft,* Vol. 31, No. 3, pp. 591 – 596, 1994.
48 Dash, S. M., Beddini, R. A., Wolf, D. E., Sinha, N., "Viscous/Inviscid Analysis of Curved Sub- or Supersonic Wall Jets," 16th Fluid and Plasma Dynamics Conference, AIAA Paper No. 83-1679, 1983.
49 Piesik, E. T., Koppang, R. R., Simkin, D. J., "Rocket-Exhaust Impingement on a Flat Plate at High Vacuum," *Journal of Spacecraft,* Vol. 3, No. 11, pp. 1650 – 1657, 1966.

50 Rochelle, W. C., Kooker, D. E., "Heat-Transfer and Pressure Analysis of Rocket Exhaust Impingement on Flat Plates and Curved Panels," *Journal of Spacecraft,* Vol. 6, No. 3, pp. 248 – 256, 1969.
51 Lengrand, J-C., Allegre, J., Raffin, M., "Interaction of Underexpanded Jets with Adjacent Flat Plates," *Rarefied Gas Dynamics,* pp. 447 – 458, 1977.
52 Dettleff, G., "Plume Flow and Plume Impingement in Space Technology," Progress in Aerospace Sciences, Vol. 28, pp. 1 – 71, 1991.
53 Ivanov, M. Y., Kraiki, A. I., Mikhailov, N. V., "A Method of Through Computation for Two- and Three-Dimensional Supersonic Flows," Translated from Zh. uychisl. Mat. mat. Fiz., Vol 12, No. 2, pp. 441 – 463, 1972.
54 Ivanov, M. Y., Nazarov, V. P., "'Lateral' Interaction of a Supersonic Underexpanded Ideal-Gas Jet with Surfaces of Different Shape," Translated from Izvestiya Akademii Nauk SSSR, Mekhanika Shidkosti i Gaza, No. 6, pp. 3 – 8, 1973 (Translated 1974).
55 Ivanov, M. Y., Nazarov, V. P., "Numerical Solution of the Problem of the 'Lateral' Interaction of Underexpanded Supersonic Jets of an Ideal Gas with a Plane and with One Another," Translated from Zh. uychisl. Mat. mat. Fiz., Vol. 14, No. 1, pp. 179 – 187, 1974.
56 Ivanov, M. Y., Kireev, V. N., "Calculation of Highly Underexpanded Supersonic Free Jets," Translated from Zh. uychisl. Mat. mat. Fiz., Vol. 16, No. 3, pp. 750 – 757, 1976.
57 Abrosimov, S. N., Polyakov, G. A., "Characteristics of the Action of an Underexpanded Jet on an Adjacent Surface," Translated from Zhurnal Prikladnoi Mekhaniki i Tekhnicheskoi Fixiki, No. 1, pp. 95 – 98, 1980 (Translated 1982).
58 Antokhin, V. M., Gerasimov, Y. I., Shokhov, V. A., Khomutskii, A. A., "Thermal Effect of a Freely Expanding Gas Jet on a Flat Plate," Translated from Izvestiya Akademii Nauk SSSR, Mekhanika Shidkosti i Gaza, No. 4, pp. 119 – 126, 1979 (Translated 1981).
59 Gerasimov, Y. I., "Dimensionless Numbers in the Problem of the Interaction of a Freely Expanding Jet with a Plate," Translated from Izvestiya Akademii Nauk SSSR, Mekhanika Shidkosti i Gaza, No. 2, pp. 169 – 173, 1979 (Translated 1981).
60 Powell, A., "On the Mechanism of Choked Jet Noise," *Proceedings of the Physical Society,* Vol. 66, pp. 1039 – 1056, 1953.
61 Ahuja, K. K., McCaulley, J. A., Tam, C. K. W., "Noise and Instability Wave in Supersonic Jets in the Proximity of Flat and Cylindrical Walls," 12th AIAA Aeroacoustics Conference, AIAA Paper No. 89-1136, 1989.
62 Wlezien, R., "Near-Field Acoustic Environment of a Supersonic Plume Adjacent to a Wall," 12th AIAA Aeroacoustics Conference, AIAA Paper No. 89-1137, 1989.
63 Ibrahim, M. K., Sawai, T., Obase, K., Mori, K., Nakamura, Y., "Experimental Investigation of Screech-Tone Characteristics of Jet Interaction with a Flat Plate," *AIAA Journal,* Vol. 47, No. 9, pp. 2031 – 2038, 2009.
64 Obase, K., Nakamura, Y., "Aerodynamic and Aeroacoustic Interactions of a High-Speed Jet with a Flat Plate," 2nd AIAA Flow Control Conference, AIAA Paper No. 2004-2404, 2004.
65 Brown, C. A., "Developing an Empirical Model for Jet-Surface Interaction Noise," 52nd AIAA Aerospace Sciences Meeting, AIAA Paper No. 2014-0878, 2014.
66 Clem, M. M., Brown, C. A., Fagan, A. F., "Background Oriented Schlieren Implementation in a Jet-Surface Interaction Test," 51st AIAA Aerospace Sciences Meeting, AIAA Paper No. 2013-0038, 2013.
67 Brown, C. A., Clem, M. M., Fagan, A. F., "Investigation of Broadband Shock Noise from a Jet Near a Planar Surface," *Journal of Aircraft,* AIAA Early Edition, 2014.
68 Brown, C. A., "Jet-Surface Interaction Test: Far-Field Noise Results," *J. Eng. Gas Turbines Power,* Vol. 135, Paper No. GTP-12-1222, 2013.
69 Brown, C., Wernet, M., "Jet-Surface Interaction Test: Flow Measurement Results," 20th AIAA/CEAS Aeracoustics Conference, AIAA Paper No. 2014-3198, 2014.
70 McLaughlin, D. K., Kuo, C. W., Papamoshou, D., "Experiments on the Effect of Ground Reflections on Supersonic Jet Noise," 46th AIAA Aerospace Sciences Meeting & Exhibit, AIAA Paper No. 2008-22, 2008.
71 Maestrello, L., "Active Control of Nonlinear-Nonstationary Response and Radiation of a Panel-Stringer Structure Near a Supersonic Jet," 15th AIAA Aeroacoustics Conference, AIAA Paper No. 93-4338, 1993.
72 Maestrello, L., "Control of Shock Loading from a Jet in the Presence of a Flexible Structure," AIAA Paper No. 99-1975, 1999.
73 Maestrello, L., "Control of Shock Loading from a Jet in a Flexible Structure's Presence," *AIAA Journal,* Vol. 38, No. 6, pp. 972 – 977, 2000.

74 Frendi, A., Maestrello, L., Bayliss, A., "Coupling Between Plate Vibration and Acoustic Radiation," AIAA 31st Aerospace Sciences Meeting, AIAA Paper No. 93-0603, Reno, NV, 1993.
75 McGreevy, J. L., Bayliss, A., Maestrello, L., "Interaction of Jet Noise With a Nearby Panel Assembly," *AIAA Journal*, Vol. 33, No. 4, pp. 577 – 585, 1995.
76 Fenno Jr., C. C., Bayliss, A., Maestrello, L., "Panel-Structure Response to Acoustic Forcing by a Nearly Sonic Jet," *AIAA Journal*, Vol. 35, No. 2, pp. 219 – 227, 1997.
77 Fenno Jr., C. C., Bayliss, A., Maestrello, L., "Interaction of Sound From Supersonic Jets with Nearby Structures," AIAA 35th Aerospace Sciences Meeting, AIAA Paper No. 97-0283, Reno, NV, 1997.
78 Fenno Jr., C. C., Bayliss, A., Maestrello, L., "Interaction of Sound From Supersonic Jets with Nearby Structures," *AIAA Journal*, Vol. 36, No. 12, pp. 2153 – 2162, 1998.
79 Bayliss, A., Maestrello, L., "Nonaxisymmetric Disturbances in a Jet and Their Effect on Structural Loading," 4th AIAA/CEAS Aeroacoustics Conference, Toulouse, France, 1998.
80 Corke, T. C., Thomas, F. O., "Dynamic Stall in Pitching Airfoils: Aerodynamic Damping and Compressibility Effects," Annual Review of Fluid Mechanics, Vol. 47, pp. 479 – 505, 2015.
81 Rojratsirikul, P., Wang, Z., Gursul, I., "Unsteady Fluid-Structure Interactions of Membrane Airfoils at Low Reynolds Numbers," Experiments in Fluids, Vol. 46, pp. 859-872, 2009.
82 Rojratsirikul, P., Genc, M. S., Wang, Z., Gursul, I., "Flow-Induced Vibrations of Low Aspect Ratio Rectangular Membrane Wings," Journal of Fluids and Structures, Vol. 27, pp. 1296-1309, 2011.
83 Wu, P., Ifju, P., Stanford, B., Sällström, E., Ukeiley, L., Love, R., Lind, R., "A Multidisciplinary Experimental Study of Flapping Wing Aeroelasticity in Thrust Production," 50th AIAA/ASME/ASCE/ASC Structures, Structural Dynamics and Materials Conference, AIAA Paper No. 2009-2413, Palm Springs, CA, 2009.
84 Stillwell, W. H., "X-15 Research Results with a Selected Bibliography," NASA SP-60, 1965.
85 Dowell, E. H., "Panel Flutter: A Review of the Aeroelastic Stability of Plates and Shells," AIAA Journal, Vol. 8, No. 3, pp. 385 – 399, 1970.
86 Freund, J. B., "Numerical Simulations of Flowing Blood Cells," Annual Review of Fluid Mechanics, Vol. 46, pp. 67 – 95, 2014.
87 da Silva, A. R., Scavone, G. P., van Walstijn, M., "Numerical Simulations of Fluid-Structure Interactions in Single-Reed Mouthpieces," Journal of the Acoustic Society of America, Vol. 122, pp. 1798 – 1809, 2007.
88 Davis, G. A., Bendiksen, O. O., "Transonic Panel Flutter,"34th AIAA/ASME/ASCE/AHS/ASC Structures, Structural Dynamics and Materials Conference, AIAA Paper No. 1993-1476, La Jolla, CA, 1993.
89 Bendiksen, O. O., Davis, G. A., "Nonlinear Traveling Wave Flutter of Panels in Transonic Flow," 36th AIAA/ASME/ASCE/AHS/ASC Structures, Structural Dynamics and Materials Conference, AIAA Paper No. 1995-1486, New Orleans, LA, 1995.
90 Crowell, A. R., Miller, B. A., McNamara, J. J., "Computational Modeling for Conjugate Heat Transfer of Shock-Surface Interactions on Compliant Skin Panels," 52nd AIAA/ASME/ASCE/AHS/ASC Structures, Structural Dynamics and Materials Conference, AIAA Paper No. 2011-2017, Denver, CO, 2011.
91 Gordnier, R. E., Visbal, M. R., "Computation of Three-Dimensional Nonlinear Panel Flutter," Journal of Aerospace Engineering, Vol. 16, No. 4, pp. 155 – 166, 2003.
92 Visbal, M. R., Gordnier, R. E., "Numerical Simulation of the Interaction of a Transitional Boundary Layer with a 2-D Flexible Panel in the Subsonic Regime," Journal of Fluids and Structures, Vol. 19, pp. 881 – 903, 2004.
93 Ostoich, C., Bodony, D. J., Geubelle, P. H., "Aeroelastic Response of a Panel Under High Speed Turbulent Boundary Layers Using Direct Numerical Simulation," 51st AIAA Aerospace Sciences Meeting, AIAA Paper No. 2013-0096, Grapevine, TX, 2013.
94 Ostoich, C., Bodony, D. J., Geubelle, P. H., "Interaction of a Mach 2.25 Turbulent Boundary Layer with a Fluttering Panel Using Direct Numerical Simulation," Physics of Fluids, Vol. 25, 2013.
95 Willems, S., Gülhan, A., Esser, B., "Shock Induced Fluid Structure Interaction on a Flexible Wall in Supersonic Turbulent Flow," *Progress in Flight Physics*, Vol. 5, pp. 285 – 308, 2013.
96 Beberniss, T., Spottswood, M., Eason, T., "High-Speed Digital Image Correlation Measurements of Random Nonlinear Dynamic Response," Proceeding of the SEM Annual Conference, Society of Experimental Mechanics, 2011.
97 Spottswood, S. M., Beberniss, T. J., Eason, T. G., "Full-field, Dynamic Pressure and Displacement Measurements of a Panel Excited by Shock Boundary-Layer Interaction," 19th AIAA/CEAS Aeroacoustics Conference, AIAA Paper No. 2013-2016, 2013.

98 Gogulapati, A., Deshmukh, R., Crowell, A. R., McNamara, J. J., Vyas, V., Wang, X. Q., Mignolet, M., Beberniss, T., Spottswood, S. M., Eason, T. G., "Response of a Panel to Shock Impingement: Modeling and Comparison with Experiments," 55th AIAA/ASME/ASCE/AHS/SC Structures, Structural Dynamics and Materials Conference, AIAA Paper No. 2014-0148, National Harbor, MD, 2014.
99 Gogulapati, A., Deshmukh, R., Crowell, A. R., McNamara, J. J., Vyas, V., Wang, X. Q., Mignolet, M., Beberniss, T., Spottswood, S. M., Eason, T. G., "Response of a Panel to Shock Impingement: Modeling and Comparison with Experiments – Part 2," 56th AIAA/ASME/ASCE/AHS/SC Structures, Structural Dynamics and Materials Conference, AIAA Paper No. 2015-0685, Kissimmee, FL, 2015.
100 Avitabile, P., Niezrecki, C., Helfrick, M., Warren, C., Pingle, P., "Noncontact Measurement Techniques for Modal Correlation," *Sound and Vibration*, Vol. 44, No. 1, pp. 8 – 13, 2010.
101 Siebert, T., Crompton, M. J., "Application of High Speed Digital Image Correlation for Vibration Mode Shape Analysis," Proceedings of the SEM Annual Conference, Society of Experimental Mechanics, Indianapolis, IN, 2010.
102 Timpe, A., Ukeiley, L., Zhang, Z., Hubner, J. P., Ifju, P., "Flow and Structure Measurements of a Passively Compliant Wing," 50th AIAA Aerospace Sciences Meeting, AIAA Paper No. 2012-1210, Nashville, TN, 2012.
103 Giovannetti, L. M., Banks, J., Boyd, S. W., Turnock, S. R., "Fluid Structure Interaction in High Performance Catamaran C-Foils Under Load," 5th High Performance Yacht Design Conference, Auckland, NZ, 2015.
104 Zhang, C., Miorini, R., Katz, J., "Integrating Mach-Zehnder Interferometry with TPIV to Measure the Time-Resolved Deformation of a Compliant Wall Along with the 3D Velocity Field in a Turbulent Channel Flow," *Experiments in Fluids*, 56: 203, 2015.
105 Fontaine, R.A., Bobbitt, B., Elliott, G.S., Austin, J.M., Freund, J.B., "Design and Demonstration of a New Small-Scale Jet Noise Experiment," 50th AIAA Aerospace Sciences Meeting, Nashville, TN, January 2012, AIAA Paper No. 2012-0682.
106 Willems, S., Gülhan, A., Burkard, E., "Shock Induced Fluid Structure Interaction on a Flexible Wall in Supersonic Turbulent Flow," 4th European Conference for Aerospace Sciences, 2011.
107 Willems, S., Gülhan, A., Burkard, E., "Shock Induced Fluid-Structure Interaction on a Flexible Wall in Supersonic Turbulent Flow," Progress in Flight Physics, Vol. 5, pp. 285-308, 2013.
108 Gaspers Jr., P. A., Muhlstein Jr., L., Detroff, D. N., "Further Experimental Results on the Influence of the Turbulent Boundary Layer on Panel Flutter," NASA TN D-5798, 1970.
109 Muhlstein Jr., L., and Gaspers Jr., P. A., "An Experimental Study of the Influence of the Turbulent Boundary Layer on Panel Flutter," NASA TN D-4486, 1968.
110 Sylvester, M. A., and Baker, J. E., "Some Experimental Studies of Panel Flutter at Mach Number 1.3," NACA TN 3914, 1957.
111 http://www.matweb.com/search/datasheet.aspx?matguid=025d4a04c2c640c9b0eaaef28318d761, accessed Sept. 28, 2016.
112 Brick, R. M., Pense, A. W., Gordon, R. B., *Structure and Properties of Engineering Materials*, 4th Ed., McGraw-Hill Inc., New York, NY, p. 17, 1977.
113 Askeland, D. R., Phule, P. P., *The Science and Engineering of Materials*, 4th Ed., Brooks/Cole-Thomson Learning, Pacific Grove, CA, 2003.
114 Soedel, W., *Vibrations of Shells and Plates*, 3rd Ed. Revised and Expanded, Marcel Dekker, Inc., New York, NY, p. 183, 2004.
115 Herges, T., "The Effects of Micro-Vortex Generators on Normal Shock Wave/Boundary Layer Interactions," Ph.D. Dissertation, Department of Aerospace Engineering, University of Illinois at Urbana-Champaign, Urbana, IL, December 2013.
116 Ostman, R., "Active Control of Supersonic Boundary Layers Using Electric Arc Plasma Actuators," Master's Thesis, Department of Aerospace Engineering, University of Illinois at Urbana-Champaign, Urbana, IL, December 2013.
117 Lazar, E., DeBlauw, B., Glumac, N., Dutton, C., Elliott, G., "A Practical Approach to PIV Uncertainty Analysis," *27th AIAA Aerodynamic Measurement Technology and Ground Testing Conference*, AIAA Paper 2010-4355, 2010.
118 Reedy, T., "Control of Supersonic Axisymmetric Base Flows Using Passive Splitter Plates and Pulsed Plasma Actuators," Ph.D. Dissertation, Mechanical Science and Engineering Department, University of Illinois at Urbana-Champaign, Urbana, IL, December 2013.

119 Benedict, L. H., Gould, R. D., "Towards Better Uncertainty Estimates for Turbulence Statistics," *Experiments in Fluids*, Vol. 22, pp. 129 – 136, 1996.
120 Elsinga, G. E., Scarano, F., Wieneke, B., Van Oudheusden, B. W., "Tomographic Particle Image Velocimetry," *Experiments in Fluids*, Vol. 41, No. 6, pp. 933 – 947, December 2006.
121 Scarano, F., "Tomographic PIV: Principles and Practice," Measurement Science and Technology, Vol. 24, 012001, 28 pp., 2013.
122 Haller, G., "An Objective Definition of a Vortex," Journal of Fluid Mechanics, Vol. 525, pp. 1 – 26, 2005.
123 Elsinga, G. E., Adrian, R. J., van Oudheusden, B. W., and Scarano, F., "Three-Dimensional Vortex Organization in a High-Reynolds-Number Supersonic Turbulent Boundary Layer," Journal of Fluid Mechanics, Vol. 644, pp. 35 – 60, 2010.
124 Callum, G., Wieneke, B., "Volume Self-Calibration for Stereo-PIV and Tomographic PIV," *9th International Symposium on Fluid Control Measurement and Visualization 2007*, Vol. 1, pp. 135 – 145, 2007.
125 Liu, T., Guille, M., Sullivan, J. P., "Accuracy of Pressure Sensitive Paint," *AIAA Journal*, Vol. 39, No. 1, 2001, pp. 103 – 112.
126 Correlated Solutions, Inc., "Digital Image Correlation: Overview of Principles and Software," SEM 2009 Workshop Presentation, University of South Carolina, obtained at: https://www.researchgate.net/file.PostFileLoader.html?id=54abf43ad039b1e37f8b45aa&assetKey=AS%3A273664212176896%401442258040146, March 2016.
127 Sutton, M. A., Orteu, J., Schreier, H. W., *Image Correlation for Shape, Motion and Deformation Measurements: Basic Concepts, Theory and Applications*, Springer Science+Business Media, LLC, New York, NY, 2009.
128 "Vic-3D 2010 Reference Manual," published by Correlated Solutions, Inc., obtained from www.correlatedsolutions.com.
129 "Vic-3D 2007 Testing Guide," published by Correlated Solutions, Inc., obtained from www.correlatedsolutions.com.
130 Zaman, K. M. B. Q., "Far-Field Noise of a Subsonic Jet Under Controlled Excitation," *Journal of Fluid Mechanics*, Vol. 152, pp. 83 – 111, 1985.
131 Tam, C. K., Seiner, J. M., Yu, J. C., "Proposed Relationship Between Broadband Shock Associated Noise and Screech Tones," *Journal of Sound and Vibration*, Vol. 110, No. 2, pp. 309 – 321, 1986.
132 Massey, K. C., Ahuja, K. K., "Screech Frequency Prediction in Light of Mode Detection and Convection Speed Measurements for Heated Jets," AIAA Paper No. 97-1625, 1997.
133 Babinsky, H., Harvey, J. K., *Shock Wave-Boundary Layer Interactions*, Cambridge University Press, New York, NY, 2011.
134 Clemens, N., Narayanaswamy, V., "Low-Frequency Unsteadiness of Shock Wave/Turbulent Boundary Layer Interactions," *Annu. Rev. Fluid Mech.*, 2014, 46:469-92.
135 White, F. M., *Viscous Fluid Flow*, 3rd Ed., McGraw-Hill, New York, NY, p. 434, 2006.
136 Dowell, E. H., *Aeroelasticity of Plates and Shells*, Noordhoff International Publishing, Leyden, The Netherlands, 1975.
137 Clift, R., Grace, J. R., Weber, M. E., "Bubbles, Drops, and Particles," Academic Press, Inc., New York , NY, 1978, pp. 111-112.
138 Gregory, J. W., Asai, K., Kameda, M., Liu, T., and Sullivan, J. P., "A Review of Pressure-Sensitive Paint for High-Speed and Unsteady Applications," *Proceedings of the Institution of Mechanical Engineers, Part G: Journal of Aerospace Engineering*, Vol. 222, No. 2, pp. 249 - 290, 2008.
139 Crafton, J., Forlines, A., Palluconi, S., Kuang-Yu, H., Carter, C., and Gruber, M., "Investigation of Transverse Jet Injections in a Supersonic Crossflow Using Fast Response Pressure-Sensitive Paint," 29th AIAA Applied Aerodynamics Conference, Honolulu, HI, AIAA Paper No. 2011-3522, 2011.

Appendix A: Compliant Surface Material Traceability Report

In order to ensure uniformity in product performance, Precision Brand Products, Inc., documents the material and chemical properties of their products by lot number. By request, a traceability report can be obtained for any item. In this study, the compliant-model surface was constructed using a 0.003”-thick sheet shim stock. The material was 1010 Cold-Rolled Full-Hard Steel, cut into 6” wide strips. The package obtained in this study contained 12” long segments. The lot number was #5502702-06. The traceability report is presented in Figure 116.

The material properties portion of the report contains the material hardness, tensile and yield stresses, and the percent elongation. The values are insufficient to estimate more valuable elastic properties, such as the Modulus of Elasticity (or Young’s Modulus), E, Poisson’s ratio, ν, or coefficient of thermal expansion, α, which may be necessary for the characterization of the material and for the estimation of the compliant-surface free vibration natural frequencies. Elastic material properties are commonly reported for 1010 steel, but specific values for the material in its quoted “cold-rolled full-hard” state are more difficult to come by. However, as discussed in Section 2.5.2, elastic material properties are primarily governed by interatomic bond strength. As the cold-rolling and hardening processes do not act on an atomic level, but instead affect the material microstructure, the elastic material properties are negligibly affected as a result of the processing events. Instead of influencing the slope of the stress-strain curve, processing steps acting at the material microstructure level instead influence the extent of the linear (elastic) region of the stress-strain curve. Therefore, the material property specifications for the unprocessed material like E and ν can be safely used to characterize the materials used in the current study, despite the fact that the quoted material did not undergo exactly the same processing steps.

PRECISION BRAND.
ISO 9001:2008 Certified Company

February 20, 2015

.003" x 6" 1010 Cold Rolled Full Hard Steel

Chemical Analysis

Carbon (C)	.050	Chromium (Cr)	.016	Nitrogen (N)	
Manganese (Mn)	.330	Molybdenum (Mo)		Tin (Sn)	
Phosphorus (P)	.014	Aluminum (Al)	.032	Titanium (Ti)	
Sulfur (S)	.008	Boron (B)		Vanadium (V)	
Silicon (Si)	.013	Columbium (Cb)			
Nickel (Ni)	.012	Copper (Cu)	.018		

Hardness	91 R15T
Tensile psi	94,600-95,800
Yield psi	94,500-95,000
Elongation %	1.00%
Specification(s)	ASTM A109 (Chemistry) AISI 1010
Other	RoHS /DFAR Compliant
Country of Origin	USA
Heat No.	460655
Coil No.	7695-14-15
PBP Lot No.	55027-xx_06

We hereby certify that the above information conforms to the mill certificates provided by our suppliers for the material with the lot number listed above.

Precision Brand Products, Inc.

K. Hahn

Representative
K. Hahn

www.precisionbrand.com
PRECISION BRAND PRODUCTS, INC. 2250 CURTISS STREET, DOWNERS GROVE IL 60515 USA
PHONE: (630)969-7200 FAX: (630) 969-7275

Figure 115. A copy of the traceability report for the material used in the compliant-surface model construction.

Appendix B: PIV Uncertainty Code

The UIUC Gas Dynamics Group has developed a PIV uncertainty measurement code that has been implemented in a MatLab environment. The code, originally published by Lazar et al.,[117] provides an estimate of measurement uncertainty in the mean due to contributions from equipment effects, particle lag, and the PIV-processing algorithm. The code has been passed between members within the Gas Dynamics research group and continually refined and improved upon.

A summary of the PIV uncertainty code as it currently exists is presented within this section. The methodology employed by the code is summarized, and a review of the updates that have been applied to the code since the original publication is provided. Although many of these code updates were carried out by the current author, others (especially Ryan Fontaine) also contributed to these updates. Whenever possible, those who contributed to certain sections have been acknowledged.

B.1 Overview of the Current Capabilities

Currently, the PIV measurement uncertainty code is capable of estimating both instantaneous and mean uncertainties in PIV-measured velocities due to four contributing sources. Uncertainties are calculated in two orthogonal (typically along the streamwise and streamwise-normal) directions. The four sources of error contribution are equipment, particle-lag, PIV-processing algorithms, and sampling. Equipment errors are due to timing, imaging, and optical effects. The particle-lag analysis judges how well the seed particles follow the flow. There are many potential sources for particle lag errors, including drag, buoyancy, thermophoresis, gravity, and pressure gradients (to name only a few). For most experiments conducted in our lab group, particle drag is the dominant source of particle lag errors. Consequently, the current PIV uncertainty code considers particle drag, but neglects the other terms. The PIV-processing error is estimated by comparing the results from instantaneous vector fields to those obtained using synthetic particle images. The synthetic particle images are generated from the instantaneous vector fields. Any changes in the results can be attributed to the PIV-processing algorithms. Lastly, sampling effects quantify how well the finite data set represents the actual conditions (or infinite population). This is accomplished by making use of the definition of standard deviation and its associated confidence levels. This calculation is simplified by the fact that they are often already carried out in the course of PIV post-processing while considering turbulence quantities.

The instantaneous velocity uncertainties are estimated by combining the contributions from equipment, particle-lag, and PIV-processing using the root-sum-square method. Each of these three source terms are estimated based on an instantaneous vector field. A subset (in this case 50) instantaneous vector fields are used to obtain 50 instantaneous velocity uncertainties. These 50 instantaneous velocity uncertainties form a subset that is assumed to be representative of the mean. The mean velocity uncertainties are then estimated using that subset, while also accounting for the sampling term (which accounts for the size and variation of the entire data set of, in this case, 1000 image pairs).

B.2 Equipment Effects

PIV equipment uncertainty (w_{equip}) stems from timing, imaging, and optics. Timing delay manifests itself through both jitter in the laser firing and in the pulse delay time. Imaging and optical uncertainties are due to image calibration (board lengths in both dimensional units and pixels), image scaling factor, and optical aberrations. The optical aberrations are lumped into a single lens distortion term, which was assumed to be some fixed proportion of the overall calibration board length. These parameters, identified and summarized in Table 13, were combined as shown in Equation 20, using the root-sum-square method. The table also includes the values that were used in the uncertainty calculations presented in Section 2.6.3.

$$w_{u,equip} = \tilde{u}\sqrt{\left(\frac{1}{L}w_l\right)^2 + \left(\frac{-l}{L^2}w_{L1}\right)^2 + \left(\frac{-l}{L^2}w_{L2}\right)^2 + \left(\frac{l}{\lambda L}w_\lambda\right)^2 + \left(\frac{-l}{\Delta t\, L}\right)^2 [w_{t1}^2 + w_{t2}^2]} \qquad (20)$$

Table 13. Sources of planar PIV equipment uncertainty.

Symbol	Definition	Value
$\tilde{u}$	PIV velocity, pixel reference frame	varies
l	calibration board length, dimensional	70.75 mm
w_l	uncertainty, dimensional calibration board length	1 μm
L	calibration board length, pixels	2560 pixels
w_{L1}	uncertainty, calibration board length, pixels	1 pixel
w_{L2}	image distortion due to aberrations, pixels	0.005*L pixels
λ	lens-to-illumination plane distance, dimensional	0.2413 m
w_λ	uncertainty in lens-to-illumination plane distance	1 mm
Δt	laser pulse delay	0.50 μs
w_{t1}	first pulse firing timing uncertainty	1 ns
w_{t2}	second pulse firing timing uncertainty	1.5 ns

B.3 Particle Lag

The ability of the seeding particles to accurately track the flowfield can be quantified by the particle lag (or slip) measurement uncertainty, w_{lag}. The particle lag error is quantified by the slip velocity, which is the difference between the flowfield ($\underline{u_f}$) and particle (u_p) velocities. This difference arises due to a variety of causes including the effects of particle drag, pressure and temperature gradients, buoyancy, gravity, and others. For this PIV uncertainty estimation, it was assumed that only particle drag appreciably influenced the particle slip error.

B.3.1 The Original Code Drag Model

With this simplification, the particle lag error term is entirely due to particle drag. Newton's Second Law can used to relate the local particle drag to its mass and acceleration. The drag force term can be estimated using the customary aerodynamic formulation using the drag coefficient (C_D), the dynamic pressure (based on the slip velocity), and the particle frontal area. Rearrangement and simplification of terms yields an estimate for the slip velocity as a function of six quantities, as shown in Equation 21. The particle density (ρ_p = 912 kg/m^3) and diameter (d_p = 1 μm) are known. Note that the experiments were conducted using seed particles of two different diameters, but there is no way to accurately estimate their distribution within the flowfield.

Therefore, all calculations were carried out using the larger particle diameter to yield a conservative uncertainty estimate.

$$w_{lag} = u_{slip} = \frac{4\rho_p d_p^2}{3\mu_f C_D Re_p} a_p \tag{21}$$

The remaining quantities are as of yet unknown: a_p (particle acceleration), μ_f (local fluid viscosity), C_D (particle drag coefficient), and Re_p (particle Reynolds number). The local particle acceleration is obtained from the PIV-velocity field using finite difference calculations. Before calculating the acceleration fields, holes in the vector fields were filled using a linear interpolation vector post-processing step so as not to negatively affect the local particle acceleration finite difference calculations. The local fluid viscosity is determined through the use of Sutherland's equation, while the local temperature is computed using the measured total temperature and PIV-measured flow speed via the adiabatic energy equation. See Lazar et al. for details concerning the calculation of a_p and μ_f.[117]

At this point, Stokes' assumption, which relates C_D and Re_p via a simple algebraic relationship ($C_D = 24/Re_p$), can be called upon to eliminate the final unknowns. The slip velocity can then be solved for directly, and the particle lag uncertainty (entirely due to particle drag) can be estimated.

The use of Stokes' drag law is convenient because of the mathematic simplifications it supplies, but it is based on the assumption that $Re_p \ll 1$. Outside of that range, the relationship breaks down and the slip velocities (and particle lag uncertainty estimations) are necessarily inaccurate. Stokes' assumption is often valid, but in areas of very strong accelerations, such as near shock waves, it may break down. This weakness has been recognized, indeed Lazar et al.[117] acknowledge it too, but the fact that its use makes the mathematics tractable has so far outweighed its inaccuracies for uncertainty estimation purposes.

B.3.2 Improvement to the Particle Lag Estimation

Whether or not the Stokes' assumption has been broken can be easily tested after the fact. Upon using it, the slip velocity can be calculated, which can then be used to check the Re_p estimation using its definition, shown in Equation 22.

$$Re_p = \frac{\rho_p d_p u_{slip}}{\mu_f} \tag{22}$$

Figure 117 displays a plot of Re_p as calculated by Equation 22 for a single instantaneous velocity field. Clearly, Stokes' assumption is violated often in this case. Figure 118 allows for the assessment of what proportion of velocity vectors fall under various values of Re_p for the same

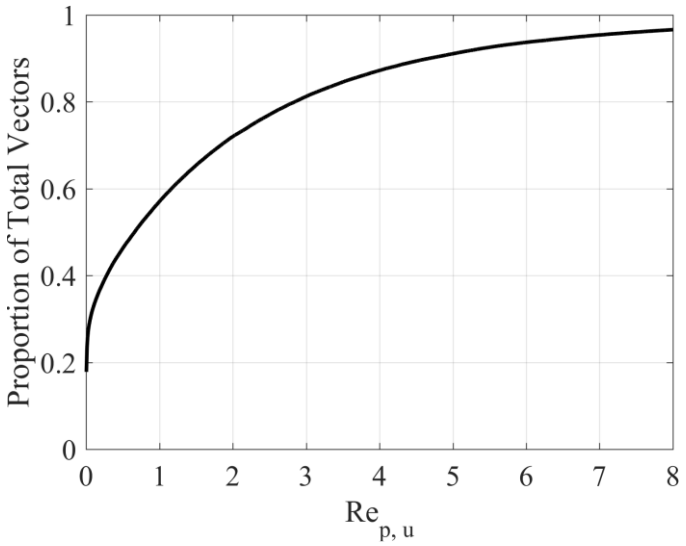

Figure 116. Only a small proportion of the total vectors satisfy the Stokes' assumption.

instantaneous velocity field. In this case, only 46% of the vectors fall under $Re_p \leq 0.5$; the remaining vectors do not satisfy the Stokes' assumption. For the instantaneous vector field considered here, the maximum Re_p is approximately 85. Consequently, the particle drag and particle-lag uncertainty estimations should not be trusted.

In order to overcome this problem, an iterative scheme was introduced that allows for an improved particle drag prediction. As in the original code, Stokes' assumption was initially

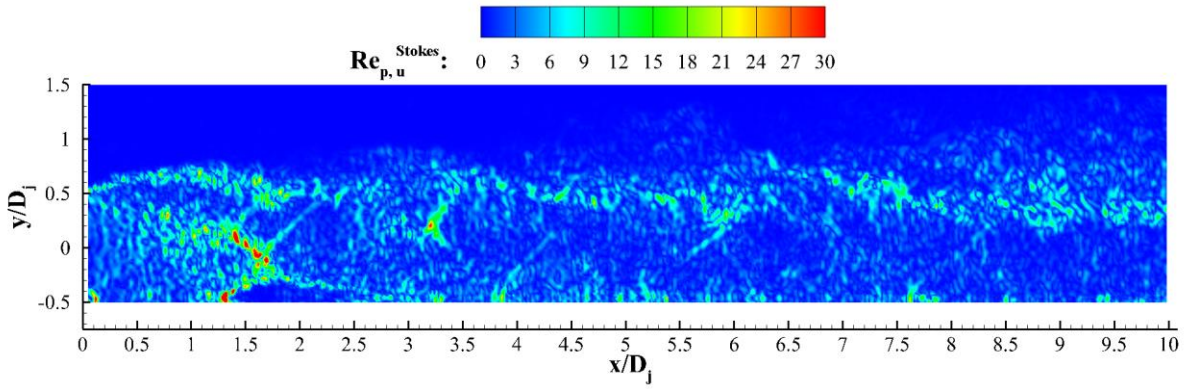

Figure 117. Particle Reynolds numbers (u-component) are well outside of the Stokes' regime ($Re_p \ll 1$).

applied, because it provides an initial guess for the local slip velocity. Once an initial guess was in hand, there was no longer a need to mathematically eliminate Re_p or C_D, and a more complicated C_D-to-Re_p relationship could be used instead. Once the new drag relationship had been applied, a new slip velocity could be calculated. In this manner, the slip velocity was iterated upon until the iteration process converged. It was found that ten iterations were sufficient to reliably bring all velocity vectors within an instantaneous snapshot to convergence (little to no change in u_{slip}, Re_p, and C_D).

The updated particle drag model, taken from Clift et al,[137] is given in Equation 23. It is valid for $Re_p < 800$, and falls with +5% to -4% of the true C_D within that range. A number of other drag prediction models are presented by Clift et al; this particular one was chosen for its relative simplicity and broad Re_p range, which makes it simple to implement into the code. Comparison of the new particle drag model with the Stokes' drag model shows that they agree very well for $Re_p \ll 1$. This further simplifies the code implementation as neither the drag model nor the convergence criteria need to be assessed on a vector-by-vector basis. Instead, the iterative procedure can be applied to all of the velocity vectors within a single instantaneous result at once. Vectors for which the Stokes' assumption was valid are essentially unchanged even after going through the iterative process. Meanwhile, results for vectors that did break Stokes' assumption are refined to have a better estimation for particle Reynolds number, slip velocity, particle drag coefficient, and, ultimately, particle lag uncertainty.

$$C_D = \frac{24}{Re_p}\left(1 + 0.15Re_p^{0.687}\right) \quad (23)$$

Figures 119 a) and b) display the particle lag uncertainty estimation using the original and modified versions of the code, respectively, for a single instantaneous *u*-velocity field. They are normalized by the maximum mean velocity, U_{max} = 576 m/s. Modifying the particle drag estimation algorithm resulted in a tremendous reduction in the particle-lag uncertainty estimation, particularly for the extreme velocity vectors (near maximum speed). Using the Stokes' model, the maximum uncertainties was 1.61U_{max}; after the addition of the expanded domain drag model, the maximum uncertainty was reduced to 0.61U_{max}. It should be noted that the maximum uncertainty can be misleading as only an extremely small percentage of the vectors have uncertainties of such a large magnitude. The median particle-lag uncertainty using the original method was 0.0205U_{max}, while for the modified method it was 0.0182U_{max}.

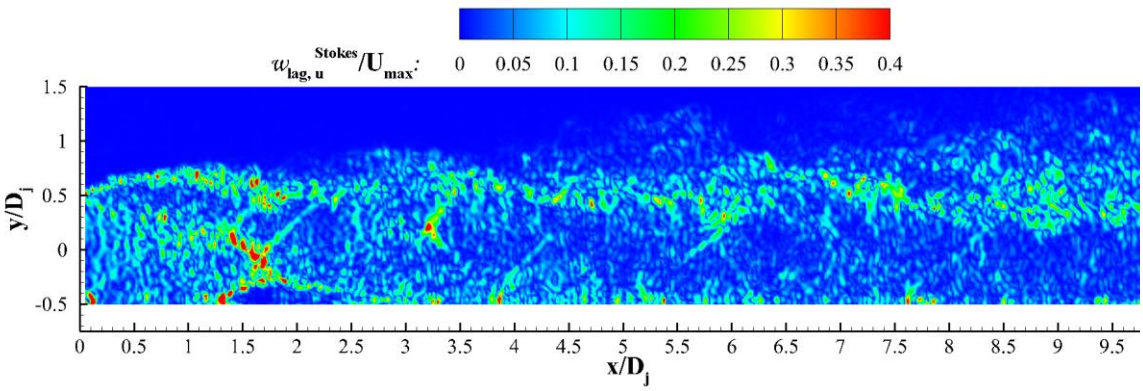

a)

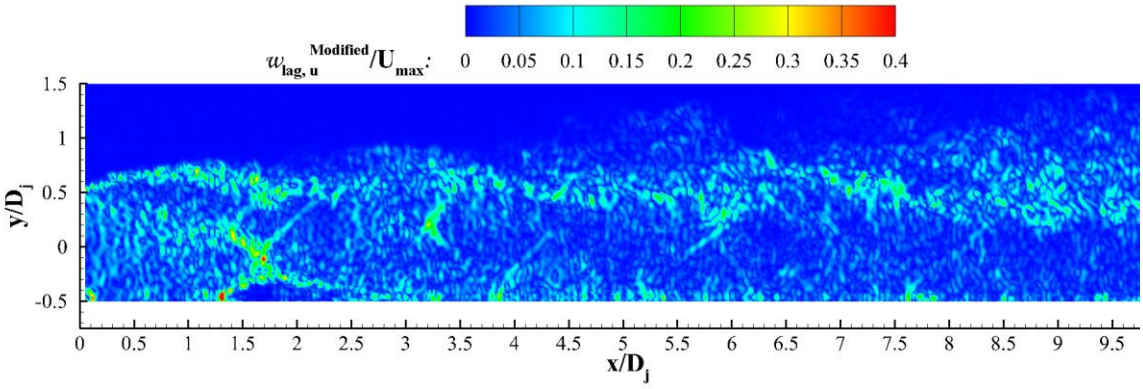

b)

Figure 118. Instantaneous particle-lag uncertainties calculated using a) the original Stokes' regime code, and b) the modified code with an expanded Re_p domain.

B.4 PIV-Processing Algorithm

The uncertainty due to PIV-processing is assessed through the use of synthetic particle images. For each instantaneous PIV velocity field, 36 synthetic particle image pairs were produced. The synthetic particle image generation MatLab code uses a parallel-processing for-loop, so the number of synthetic particle image pairs is typically set to some multiple of the number of processors available on the computer running the code.

The synthetic particle images were generated using the velocity vector fields. This was carried out by mapping the velocity vector field onto the camera field of view. Synthetic particles were randomly positioned within the image space. Then, a central differencing scheme was applied to shift the particle locations forward and backward by a half time-step each. In this manner, t and $t + dt$ particle images were created and the resulting vectors were automatically appropriately placed.

Care was taken to produce realistic synthetic particles images. The number of particles, variations in particle intensity and diameter, the loss/gain of particles due to through-sheet motion, and edge velocity-vector effects were all accounted for. See Lazar et al. for further details.[117] These particle image pairs were then processed in DaVis using the exact same processing steps used for the original experimental particle images. The difference between each mean synthetic vector field and its corresponding instantaneous velocity field was catalogued. This difference accounts for the uncertainty within the processing steps/algorithms in a single lumped term.

Before PIV processing can be conducted on the synthetic particle images, several specific steps must be followed. The synthetic particle images are generated from the instantaneous velocity vector fields. The velocity vectors exist on a uniformly spaced grid, that is, within a dewarped reference frame, so as to correct for distortion and perspective imaging effects. Consequently, the synthetic particle images also exist in a dewarped coordinate frame. PIV processing conducted on the dewarped synthetic particle images results in a misalignment between the true velocity vector fields and the synthetic vector fields. Attempts were made to overcome this problem by bypassing the application of the DaVis calibration and using a simple spatial scaling instead. This idea has merit since it would allow for PIV-processing of the dewarped synthetic images and yield synthetic velocity vectors within the exact same coordinate frame. Unfortunately, DaVis draws upon the calibration files twice for two-camera systems: once to dewarp the particle images, and then again during PIV-processing to apply a “calibration

correction". Since the DaVis calibration is used more than once, this is not a valid solution after all.

The problem can be rectified by inverting the DaVis calibration to warp the synthetic images from the 'world' frame to the 'raw' frame before conducting the PIV processing. The following steps are carried out. Once the synthetic particle images have been created, they are imported into a new DaVis project. The spatial calibration used for the raw images is also imported into the project. Next, an image distortion step is applied to all images using the "world frame to raw frame" processing step contained within the "image mapping" processing group. Once the images have been distorted, they are exported to a second DaVis project. The original calibration is loaded, and then the calibration is applied to all images to rescale them from a pixel-based frame to a dimensional frame (typically mm). At this point, PIV processing can be carried out on the synthetic images. The *exact same steps* are used in processing the synthetic images as were used for the original images.

Representative PIV-processing uncertainties are shown in Section 2.6.3 for a single instantaneous snapshot for both primary directions. In the streamwise direction, PIV-processing uncertainties are higher near the vertical edges of the each camera's field of view, and at a minimum in the center. In the wall-normal direction, PIV-processing uncertainties are found to be higher near the bottom of each camera's field of view and at a minimum near the center (which happens to fall near the top of the measurement domain). In both directions, the PIV-processing uncertainties have minimum values that are well less than 1% of U_{max}, and the maximum values are on the order of 3% of U_{max}.

These variations in the PIV-processing uncertainties point to a misalignment between the instantaneous and synthetic vectors near the edges of the camera fields of view. Since the uncertainty is at a minimum near the centers of each camera's field of view, and grows with increasing distance from the center, the observed effect is believed to be due to perspective and distortion effects induced by the imaging system. The instantaneous vectors are generated from experimentally-obtained particle images and therefore contain imaging effects, such as those generated by the camera lenses. The DaVis calibration takes these effects into account and corrects for them in the raw images. The synthetic particle images, however, do not contain the imaging-system distortions, as they were not obtained using a physical imaging system. Application of the

DaVis calibration to the synthetic particle images, therefore, leads to a slight mismatch of the instantaneous and synthetic vectors.

If the imaging system distortion effects could be separated from the DaVis calibration and quantified, the synthetic particle images could be corrected. Although these types of distortion effects can and have been quantified in the past, they require significant effort and extensive knowledge and expertise in lens/imaging optics. The overall image-system distortion effect was considered relatively small and therefore no additional corrective steps have been taken. It is noted that since the effect served to increase the error, the PIV-processing uncertainty estimations are considered to be conservative.

The severity of this effect is dependent on the imaging system (lenses and cameras) used, the type of calibration employed, and the degree of perspective in the images. Therefore, if these effects can be minimized, the distortion effect can be decreased too. Past experience has shown that the distortion effects are small in cases where the camera views the laser sheet in a perpendicular manner, and becomes important in applications where there are large perspective effects (such as when using scheimpflug adapters or there are otherwise large changes in index of refraction).

B.5 Sampling Effects

The sampling uncertainty is a term that is applicable when calculating the uncertainties in the mean. The mean uncertainty is estimated using the instantaneous uncertainties obtained from the $n = 50$ instantaneous velocity vector fields. For each instantaneous vector field, the contribution from equipment, particle-lag, and PIV-processing were calculated. These three contributions were combined to give 50 instantaneous experimental uncertainties, w_{exp}, according to Equation 24.

$$w_{exp} = \sqrt{\left(w_{equip}\right)^2 + \left(w_{lag}\right)^2 + \left(w_{proc}\right)^2} \tag{24}$$

The total experimental uncertainty in the mean, $w_{exp,total}$, was calculated by combining the instantaneous uncertainties from each of the 50 snapshots analyzed. This was conducted on a vector by vector basis according to Equation 25.

$$w_{exp,total} = \frac{1}{N}\sqrt{\left(w_{exp,1}\right)^2 + \left(w_{exp,2}\right)^2 + \cdots + \left(w_{exp,N}\right)^2} \tag{25}$$

Finally, the total uncertainty in the mean, w_{total}, is found by combining the total experimental uncertainty in the mean with a statistical term that accounts for the effect that

sampling size may have on the means obtained using the *N* (50) image subset of *n* (1000) total images. The statistical term employs the standard deviation from the total image set, $S_{\bar{x}}$, (which is easily obtained in PIV post-processing) and a t-test. The total uncertainty in the mean is calculated independently for the mean flow velocities in the streamwise and transverse directions. Equation 26 shows how the calculation is carried out:

$$w_{total} = \sqrt{\left(w_{exp,total}\right)^2 + \left(t_{n,P} S_{\bar{x}}\right)^2} \tag{26}$$

B.6 Turbulent Statistics: Uncertainties in the Mean

Uncertainties in the mean can also be calculated for turbulence quantities. Most commonly, these include the uncertainties in the turbulence intensities and Reynolds stresses. There are two turbulence intensity uncertainties (one in each primary direction), denoted by $w_{\overline{u'}}$ and $w_{\overline{w'}}$, respectively. Similarly, there are two Reynolds normal stress uncertainties, denoted by $w_{\overline{u'u'}}$ and $w_{\overline{w'w'}}$, and a Reynolds shear stress uncertainty, denoted by $w_{\overline{u'w'}}$. Using the assumption of a normal distribution, these uncertainties were determined as recommended by Benedict and Gould.[119] The uncertainties in these quantities are dominated by statistical convergence. Thus, the formulations given in Equations 27 – 31 contain the familiar 1.96 factor associated with a 95% confidence interval from the mean. Uncertainties for 99% confidence intervals can also be determined by substitution of 2.58 for 1.96 instead. Benedict and Gould state that a total of 1000 measurements is considered a "safe" number of instantaneous measurements to achieve near-normal distributions for turbulence uncertainty quantification.[119] In the current study, $n = 1000$.

$$w_{\overline{u'}} = 1.96\sqrt{\frac{(\overline{u'u'})}{2n}} \tag{27}$$

$$w_{\overline{w'}} = 1.96\sqrt{\frac{(\overline{w'w'})}{2n}} \tag{28}$$

$$w_{\overline{u'u'}} = 1.96\sqrt{\frac{2(\overline{u'u'})^2}{n}} \tag{29}$$

$$w_{\overline{w'w'}} = 1.96\sqrt{\frac{2(\overline{w'w'})^2}{n}} \tag{30}$$

$$w_{\overline{u'w'}} = 1.96\sqrt{\frac{(\overline{u'u'})(\overline{w'w'}) + (\overline{u'w'})^2}{n}} \tag{31}$$

B.7 Uncertainties in Fluctuating Quantities

The methodology employed in the following section was developed by Ryan Fontaine. It has been copied here with minor revisions for consistency in the use of symbols.

In addition to uncertainties in the mean, uncertainties in the fluctuating velocities are also calculated. The mean fluctuating quantity, $\overline{x'}$, is calculated using Equation 32.

$$\overline{x'} = \frac{1}{\nu}\sum_{i=1}\sqrt{(\bar{x} - x_i)^2} \tag{32}$$

Both $\bar{x}$ and x_i will have associated uncertainty values that have been calculated in a manner described previously. The uncertainty in each fluctuating value is then a root-sum-square of the uncertainty in the mean and the uncertainty in an instantaneous measurement as shown in Equation 33.

$$w_{inst.fluctuation} = \sqrt{(w_{\text{mean}})^2 + \left(w_{inst\,velocity}\right)^2} \tag{33}$$

The uncertainty in the mean instantaneous fluctuation (turbulence statistics) is then the root-sum-square of the uncertainties of each instantaneous fluctuation divided by the number of total samples. This operation is shown in Equation 34.

$$w_{inst.,total} = \frac{1}{N}\sqrt{\left(w_{\text{inst.}_1}\right)^2 + \left(w_{inst._2}\right)^2 + \cdots + \left(w_{inst._N}\right)^2} \tag{34}$$

Finally, this uncertainty propagation can be combined with uncertainty based on the number of samples taken to find a total uncertainty in the instantaneous fluctuation as shown in Equation 35. Here, the Student-t distribution value is based on N = 50 samples as the standard deviation of the fluctuation is not known for the entire n = 1000 set.

$$w_{total} = \sqrt{\left(w_{\text{inst.,total}}\right)^2 + \left(t_{N,P} S_{\overline{x'}}\right)^2} \tag{35}$$

B.8 Summary of Code Improvements

The following is an outline of the evolution of the UIUC Gas Dynamics PIV Uncertainty Code. When approximate dates are known, they have been included. It is believed that most of the code improvements/revisions have been included in the following list, but it is possible that there are missing steps (and contributors).

1. Lazar et al.[117] present the original paper at the 27th AIAA Aerodynamic Measurement Technology and Ground Testing Conference in Chicago, IL (July 2010).
2. Robyn MacDonald (summer undergraduate researcher) streamlines the code and begins to modify it so that it accepts inputs (instead of hard-coding everything). Robyn also participates in a seed particle sizing experiment, and determined that the ViCount smoke machines generate particles with diameters in the 0.2 – 0.3 μm range.
3. Todd Reedy, Tommy Herges, Brad DeBlauw, Nachiket Kale, Becca Ostman, Jason Hale, and others use the code for their dissertations/theses. It is unclear if they made significant updates, changes, or improvements.
4. Ryan Fontaine makes the first significant modifications late in 2014. Jon Retter may have assisted. The following major changes were made:
    a. The code was expanded to run multiple times on instantaneous snapshots instead of just once (for a mean velocity flow field). This update includes the introduction of the MatLab *parfor* loop (parallel processing for-loop).
    b. Incorporation of the independent calculation of the instantaneous uncertainties, and their propagation to the uncertainties in the mean. This step included combining contributing sources of uncertainty, the calculation of the sampling error in that framework, as well as the addition of the uncertainty in fluctuating values.
5. Ruben Hortensius begins to make updates in February 2016. They include:

a. Fixed a bug in the preallocation of some particle lag error estimation variables (only the last image results were saved).
b. Fixed a bug in the use of Sutherland's viscosity relationship. Also renamed some variables to avoid the use of duplicate variable names.
c. Various code improvements, reorganization, and code vectorization steps. Improved and added additional code commentary.
d. Added an alternative method to calculate the local fluid temperature (which is used in Sutherland's equation to estimate the local fluid viscosity, μ_f). The original code estimates total temperature using the freestream Mach number and static temperature and the makes use of the adiabatic energy equation to calculate local temperature. The alternative method uses the adiabatic energy equation directly (as total temperature is a known measured quantity).
e. The particle lag error estimation was significantly modified so that particle drag can be estimated over a wider range of Re_p. This overcomes the issue incurred by use of the Stokes' assumption ($Re_p \ll 1$). The modification is made using an iterative approach. First, the Stokes' assumption is used. Then, the particle slip velocity is calculated and used to calculate Re_p by its definition. Then, a more complicated (wider Re_p range) particle C_D model is used to calculate a new particle drag, which yields an updated slip velocity. This loop is run for ten iterations.

6. Rohit Gupta uses and modifies the code in March 2016. He makes the following changes:
   a. Added an out-of-plane velocity component term to the synthetic particle image generator.
   b. Removed superfluous lines within the synthetic particle image generator.
   c. Various other code reorganizations and commentary.
7. Ruben Hortensius makes additional modifications in April 2016. They include:
   a. Increased the speed of the synthetic particle image generator by rewriting the code to transform the velocity vector grid onto the image (pixel) space. The original code used a very generic function called *scatteredInterpolant* that was able to both interpolate and extrapolate, but was exceedingly slow. The process was separated into a very fast interpolation step in the interior (using *griddata*) followed by extrapolation at the edges (using *scatteredInterpolant*). This increased the speed of the code by a factor of 3-4.

b. Fixed another issue in the code to transform the velocity vector grid onto the image (pixel) space. The original code extrapolates the velocities at the edge of the vector field out onto an oversized image (pixel) space. However, PIV-processing sometimes results in zero vectors within the edge rows/columns, which lead to poor extrapolations. The code was modified so that zero values along the edges of the vector field were replaced with interpolated values first. Then, the extrapolation onto the image (pixel-space) was allowed to proceed.
c. Updated the entire code to use the newer version of readimx (v2.1), which is the LaVision-supplied MatLab add-on that allows for the reading and writing of DaVis *.im7* and *.imx* image and vector files.
d. Various additional code vectorization steps, especially within the synthetic particle image generator.
e. Modified the entire code to allow for both one and two camera arrangements (side-by-side cameras).

8. Ruben Hortensius discovers the image warping/dewarping issue encountered when carrying out PIV processing of the synthetic particle images while estimating the PIV-processing uncertainty. He develops the solution procedure outlined in Section B.3. The solution involves warping the synthetic particle images in DaVis by inverting the calibration, sending the warped images to a new project, applying the DaVis calibration to rescale the images, and then proceeding with PIV-processing from there. This problem is not usually encountered in applications where the imaging plane is viewed normally; it is primarily an issue when large perspective and/or distortion effects are present.

Appendix C: Unsteady Pressure-Sensitive Paint

Typical time responses for conventional pressure-sensitive paints are on the order of milliseconds. The time response is governed by the rate at which oxygen diffuses into the paint. In turn, the rate of oxygen diffusion is proportionally related to the square of paint thickness and inversely related to the diffusion coefficient. Accordingly, there are two primary avenues by which fast-response PSPs were developed: decreasing the paint thickness or increasing the diffusion coefficient.[138] Porous PSPs were developed in an effort to increase the paint's permeability to oxygen, and hence, the diffusion coefficient. Porous PSPs feature increased surface area and surface-bound luminophores (instead of within the paint). These characteristics of porous PSPs result in an increased diffusion coefficient, and increased response times.

Fast-response pressure-sensitive paint measurements were acquired for the rigid-surface case as part of this study. It was hoped that these measurements would provide insight into the unsteady nature of the flow as well as the unsteady pressure loading incurred by the surface. Data were obtained for h/D_j = 0.50 and 0.55, and for NPR = 5.0 and 4.0. Within this appendix, all of the presented data were obtained for the h/D_j = 0.50, NPR = 5.0 operating condition for the rigid-surface model at 7 kHz.

C.1 Experimental Setup

A porous fast-response PSP was generously supplied by ISSI, Inc. This particular PSP is a three component, single-luminophore high-speed PSP. It has been successfully used at rates in excess of 10 kHz.[139] It has quoted pressure and temperature sensitivities of 0.6% per kPa and 3.0% per °C, respectively. The photo-degradation rate is very high (1% per minute of excitation) and the shelf life of only three months makes the use of this particular PSP challenging. ISSI applied the base layer to the rigid-surface model and then supplied the overspray (luminophore-containing layer). The overspray was applied at the University of Illinois with an airbrush just prior to data collection in several thin, even, coats. The overspray, which can be reapplied, was applied several times over the course of the experiments.

The experimental setup is shown in Figure 120. The same water-cooled excitation lamp and reflector were used in this experiment as for the conventional PSP. The excitation lamp illuminated the model surface at a slight vertical angle so at to allow the high-speed camera to view the surface in a normal manner. A 16 GB Photron SA-5 high-speed camera, fitted with a 50

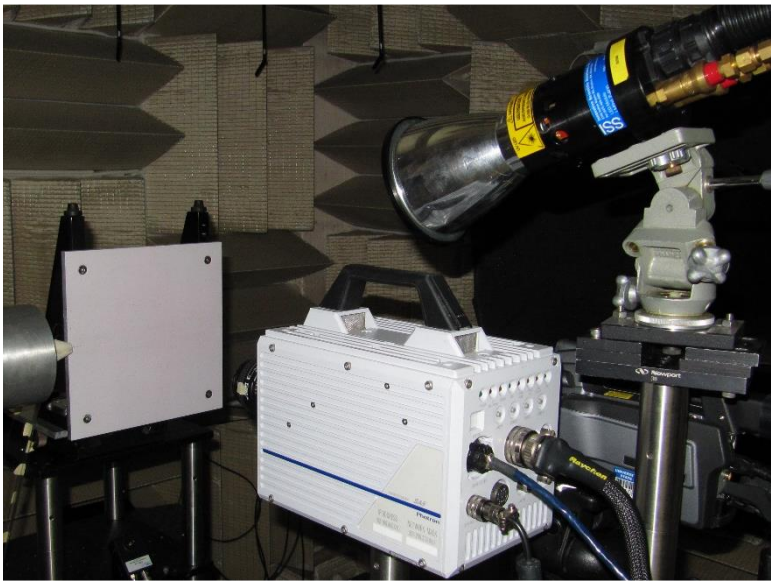

Figure 119. The unsteady PSP experimental setup includes an illumination source and a normal-viewing high-speed camera.

mm f1.4 lens was used to obtain images. 14,000 full-resolution (1024 x 1024 pixels) images were obtained at 7 kHz (142.6 μs exposure), and an additional 30,000 reduced-resolution (896 x 416 pixels) images were obtained at 20 kHz (49.76 μs exposure). The field of view extended approximately 120 mm, leading to a scaling factor of 0.124 mm/pix. At least 1000 background (lens cap covered) and wind-off images were acquired prior to each run. Optical bandpass filters were used to isolate the paint response from the excitation and background wavelengths. As with the conventional PSP, the radiometric method, which is described in Section 2.7.1, was used to analyze the data.

C.2 Initial Results

The fast-response PSP was calibrated using the conventional (UNIFIB) PSP results. This was accomplished by calculating the mean unsteady PSP intensity ratio, and then using the mean steady PSP pressure ratio to construct a calibration curve. This method is identical to that used to calibrate the steady PSP, except in this case, the pressure taps are virtual. The condition at each virtual pressure tap was determined by calculating the mean value from the pixels located at that tap's location. The virtual pressure tap diameters were set to a physically representative value (10 pixels, 1.2 mm). 19 virtual pressure taps were generated with a 50-pixel increment between tap locations along the jet centerline. The resulting calibration, presented in Figure 121, yielded large

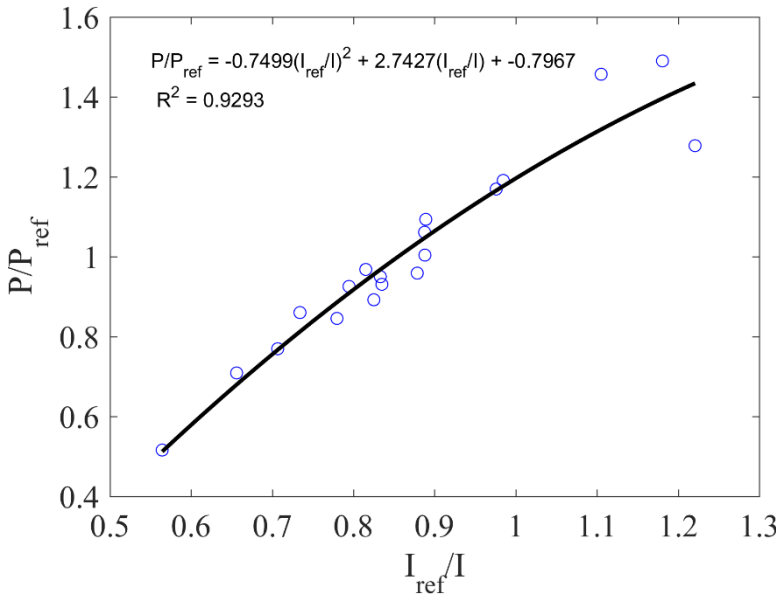

Figure 120. The unsteady PSP calibration curve generated using virtual pressure tap data obtained from the steady PSP results.

R-squared values (although not as large as those seen in the steady PSP calibrations). The calibration curve could then be applied to both the mean and instantaneous unsteady PSP data.

The unsteady PSP pressure calibration was applied to the mean unsteady PSP intensity ratio image, and the results were compared to those obtained using the steady PSP. Figures 122 and 123 present the steady (for reference) and unsteady PSP results, respectively. Within the jet core, both PSPs have similar qualitative trends. However, upon comparison of the actual values, it becomes apparent that the unsteady PSP results have lower amplitudes in regions of both high and low pressure. In addition, the overall extent of features (in the transverse direction) within the unsteady PSP data is narrower than for the steady PSP data. Far from the jet, the two results differ greatly. The steady PSP results are virtually constant everywhere, with a $P/P_{ref} = 1$ outside of the jet, as expected. The mean unsteady PSP results, however, show a clear banding effect that aligns with the flow pattern. For the unsteady PSP, P/P_{ref} is approximately unity only near the edge of the jet, and it is in excess of 1.3 near $y/D_j = \pm 4$.

It was hypothesized that temperature effects were responsible for the unexpectedly poor agreement between the steady and unsteady PSP results. Due to its effect on the oxygen-quenching process, temperature is one of the largest sources of error in PSP, and the high sensitivity of the unsteady PSP used in this study exacerbated the effect. The effect is much less pronounced in the

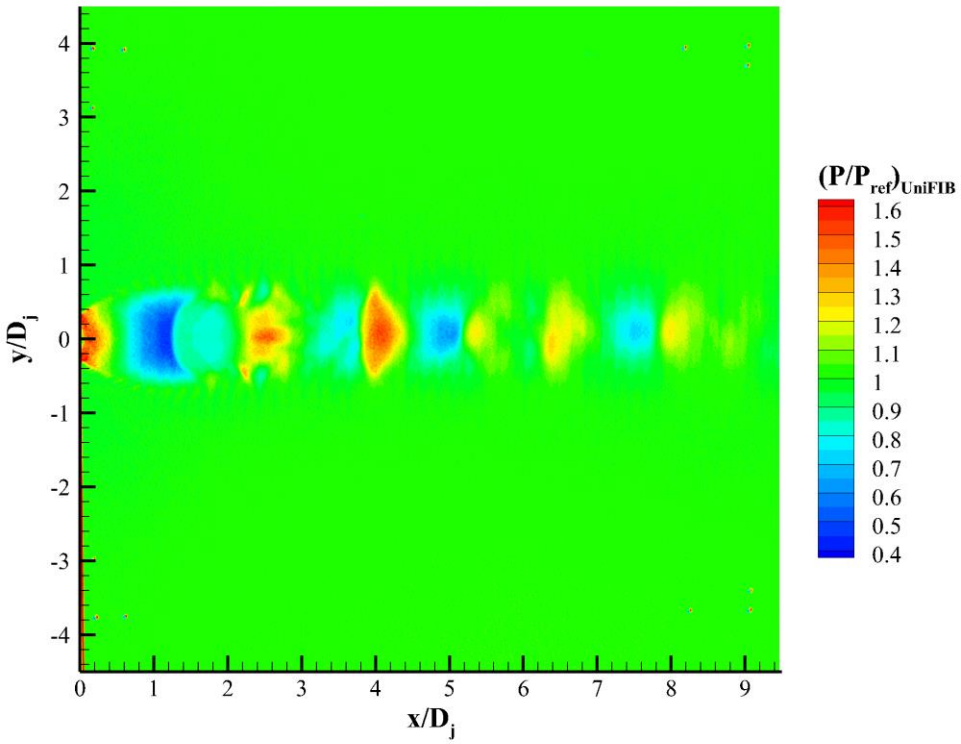

Figure 121. The steady PSP (UniFIB paint) results.

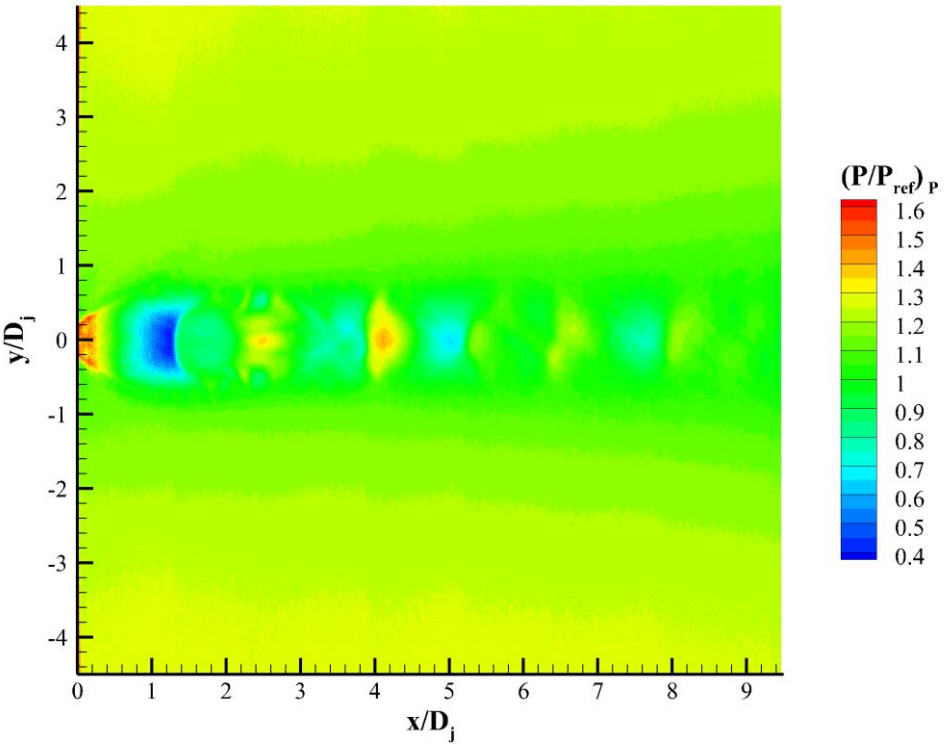

Figure 122. Results obtained for the unsteady PSP using the original calibration scheme do not agree well with those obtained for the steady PSP.

steady PSP results because that paint is relatively insensitive to temperature variations. This motivated an inspection of the model surface temperatures using an infrared camera.

C.3 Surface Temperature Measurements

Surface temperatures were measured using an infrared (IR) camera, as shown in Figure 124. The camera viewed the surface in a normal manner. No separate illumination source was required. The FLIR SC620 research-grade camera has an IR sensor with 480 by 640 pixels, a sensitivity of less than 40 mK, and an accuracy of ± 2% of the reading. The measurement range is from -40 °C to +500 °C. The camera has an integrated 3.2 megapixel visual camera and is capable of data collection in both still-image and video forms. Data were obtained and viewed using FLIR's ExaminIR software program and then exported to MatLab for further analysis. IR surface temperature data were obtained for the aluminum high-speed PSP rigid-surface model (paint applied), and for an acrylic rigid-surface model that had been treated with several thin coats of matte black high-temperature spray paint. Images were obtained over the course of several minutes. Temperature and unsteady PSP data could not be obtained simultaneously because the temperature-effect hypothesis was not formulated until after the shelf-life of the PSP had expired.

A representative temperature map, obtained after several minutes of run time and using the unsteady PSP rigid-surface model (aluminum, PSP base coat, and expired PSP overspray), is presented in Figure 125. The jet total temperature and ambient temperatures were both

Figure 123. The infrared camera experimental setup for rigid-surface model temperature measurements.

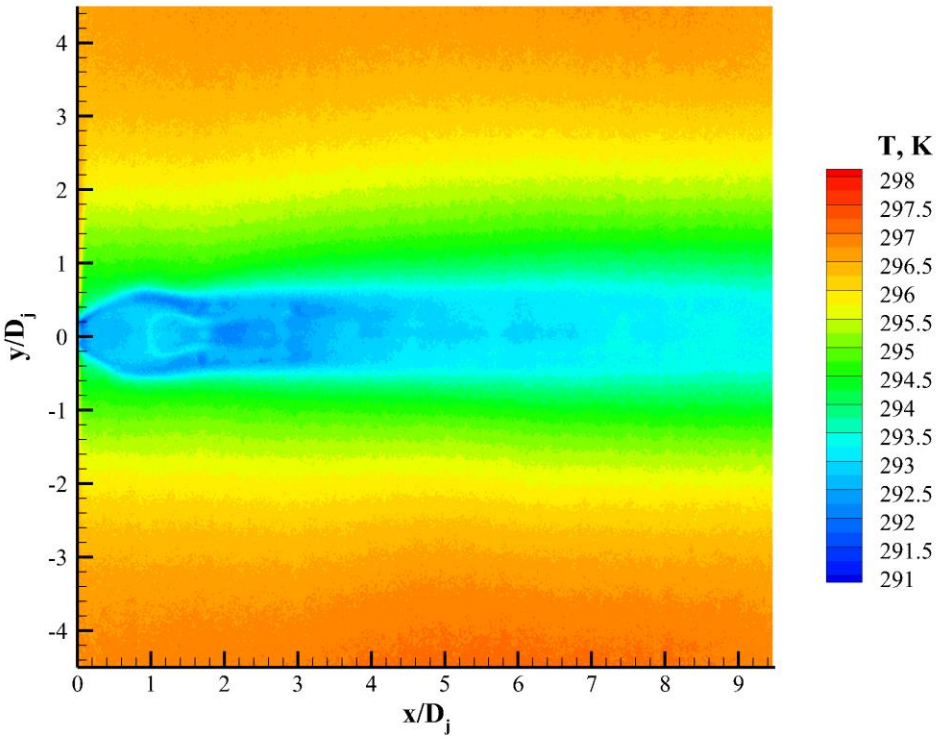

Figure 124. Surface temperature map at steady-state operation.

approximately 298 K for this case. The surface temperature is clearly seen to decrease in the vicinity of the jet, and the decrease is most pronounced in regions of extremely high shear and/or flow rates. Within the core of the jet, the minimum observed temperature was approximately 291.5 K, leading to a maximum temperature change of approximately 8 K. Far from the jet, temperatures remained relatively unchanged (at $y/D_j = \pm 4$, the surface temperature is approximately 298 K).

The temperature changes induced by the jet flow are believed to be significant enough that they would affect the unsteady PSP calibration. However, it was proposed that knowledge of the surface temperature could be used to correct the unsteady PSP calibration and thereby eliminate the temperature variation effect. Two temperature-correction schemes were developed and applied; both are based on the idea that an unsteady PSP calibration can be created by taking into account the local temperature. They are described in the following sections.

C.4 PSP Calibration Using Local Temperature Correction

Both temperature-effect correction schemes are founded on the idea that the local conditions can be used to create local calibrations. The local condition was defined by the known steady pressure and temperature (from the steady PSP and the IR-camera, respectively) at each point within the measurement field of view. As with the initial calibration attempt, the pressure

and temperature conditions were sampled at virtual pressure taps. Using these data, calibrations were created to generate pressure ratios as a function of local temperature and local intensity ratio (also sampled from virtual locations). More than 1200 virtual pressure taps were distributed throughout the field of view, with a slightly heavier density in the vicinity of the jet core.

The first temperature-correction scheme generates independent calibrations within distinct temperature bands. This method was used because the surface temperature map (see Figure 125), shows that temperature varies relatively smoothly and over relatively long spatial scales. The number of calibrations created is dependent on the number of temperature bands chosen. The validity of each calibration is influenced by the number of measurement locations contributing to the calibration as well as the spread of the data used. A calibration obtained using this method is shown in Figure 126 using seven equally spaced temperature bands (where each temperature band is shown in a different color). The high-temperature calibrations (dark blue, black, cyan, and magenta) each have narrow intensity ratio ranges, but align with each other nicely. For these temperatures, the separate calibrations transition smoothly from one to the next, implying that few, wider band, calibrations could be used instead. As the temperature continues to decrease, the data points within each calibration begin to show increased spread and the curve fits are accordingly less good (green). The low-temperature calibrations (blue and red) have two dominant features. First, there is a great deal of spread in the data points, making for poor curve fits. Second, despite

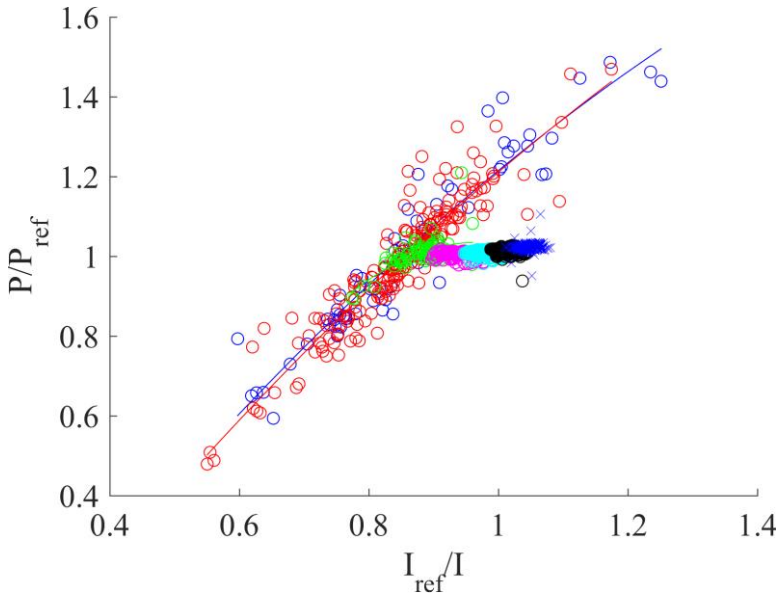

Figure 125. Temperature-corrected unsteady PSP calibration curves generated using the temperature-band method.

the large spread, there is a clear shift to a much wider intensity-ratio range and an increased calibration slope. This shift, from a shallower slope at high temperatures and a higher slope at low temperatures, occurs quickly. The goodness of the overall calibration is therefore reliant on how seamlessly the independent calibrations blend together, particularly near the transition region. This is in turn dependent on the number of temperature bands chosen, their respective limits, and the number of data points within each band. The number of points used in each calibration is roughly proportional to the amount of surface area encompassed within each temperature band.

The mean unsteady PSP results obtained using the temperature-banding method are presented in Figure 127. Overall, the agreement with the steady PSP results is much improved as compared to when using the original unsteady PSP calibration (see Figures 122 and 123). Within the jet core, both the amplitudes and the transverse extent of the features agree much better than before. Outside of the jet, the pressure ratio is very uniform, and near unity. This is both expected, and in agreement with the measurements obtained using the steady PSP.

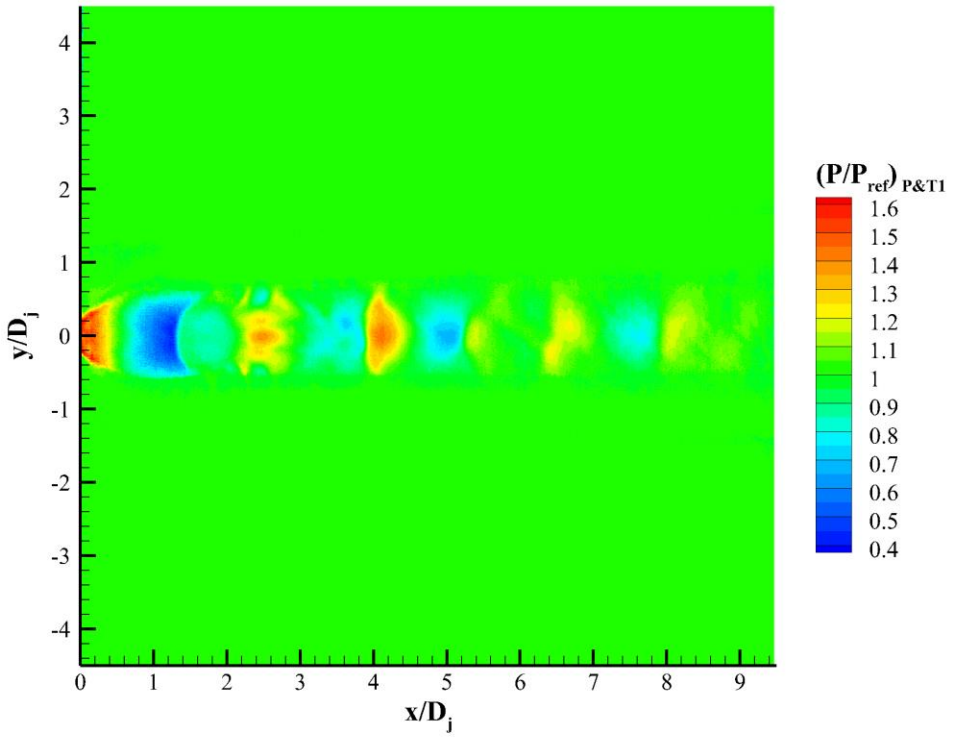

Figure 126. Temperature-corrected unsteady PSP results (temperature-band method) compare much more favorably to the steady PSP results.

A second temperature-correction scheme was also applied. In this case, local surface temperature, steady PSP pressure ratio, and unsteady PSP intensity ratio were all recorded as before using virtual taps. Then, MatLab was used to generate a surface calibration using the *fit* function. This yielded a single expression defining unsteady PSP pressure ratio as a function of local surface temperature and local intensity ratio. A variety of different fit-types were investigated including two-variable polynomials (up to 5th degree). The calibration selected for use, a polynomial of the 2nd degree in intensity ratio and 2nd degree in temperature, is shown in Figure 128. The selected calibration had an R-squared value of 0.851. R-squared values obtained for other polynomial functions were only marginally higher and did not yield surfaces that appeared realistic.

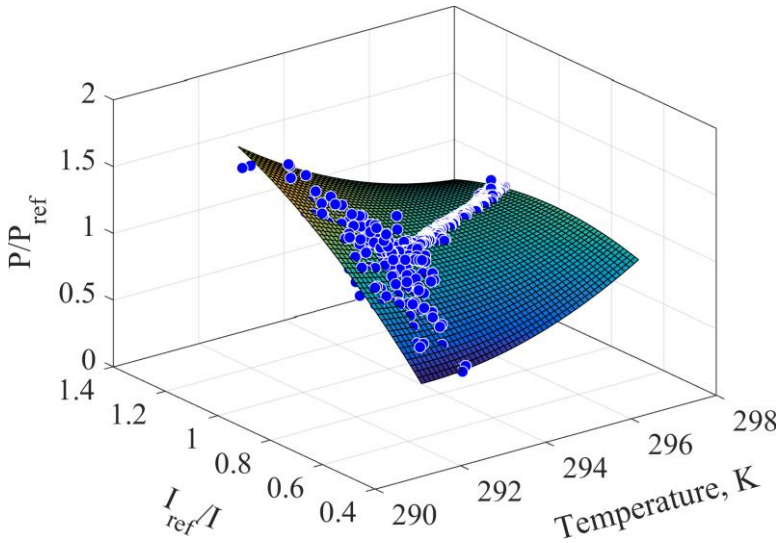

Figure 127. Temperature-corrected unsteady PSP calibration curves generated using the surface-fit method.

Two weaknesses with this temperature-correction scheme are apparent upon inspection of the calibration surface. First, at low temperatures, there is a large degree of spread in the points used for the calibration. This naturally makes curve or surface fitting challenging. Second, as the temperatures increase, the data points begin to cluster along a line. This means that there are large portions of the temperature, intensity-ratio domain that do not contain any data points. The calibration curve does not have points to fit to in these regions and therefore cannot be trusted. Still, it is unlikely that any data points would fall into these extrapolated regions of the calibration surface.

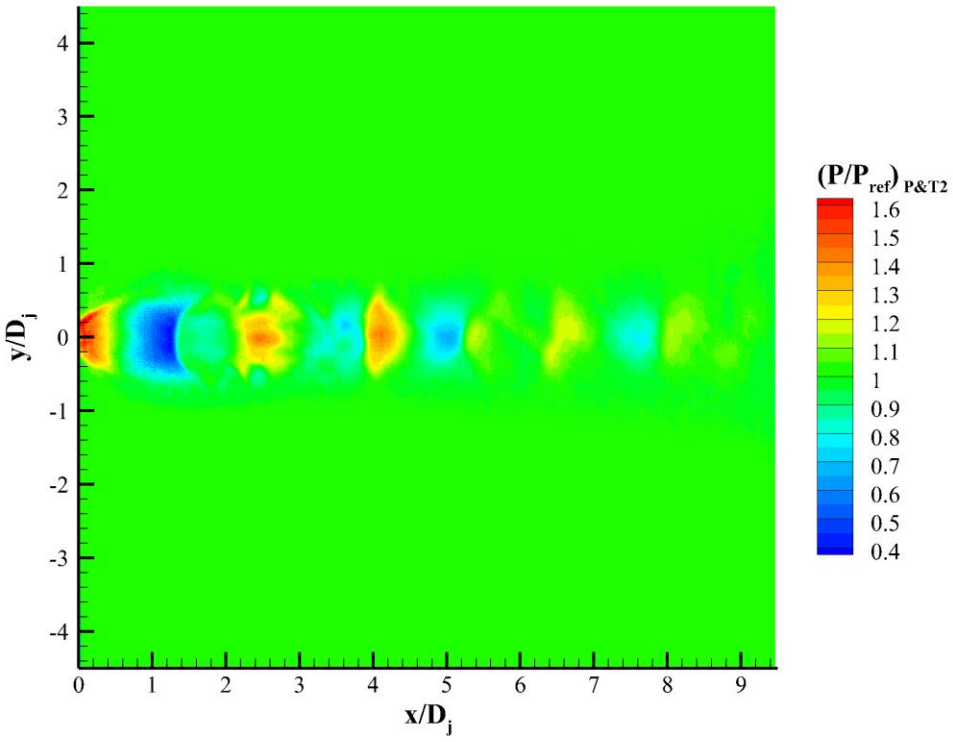

Figure 128. Temperature-corrected unsteady PSP results (surface-fit method) compare much more favorably to the steady PSP results.

The results obtained using the alternative temperature-correction scheme are presented in Figure 129. As with the other temperature-correction scheme, the new results are much improved compared to the original (Figure 123). Again, the jet core pressure fluctuation amplitudes are similar to those seen in the steady PSP results (Figure 122). In this case, the features are similarly sized. Far from the jet, the pressure ratio is near unity, and it is uniform throughout. Of the three unsteady PSP calibration methods tested, the single-surface temperature-correction method yielded results that were in best agreement with the steady PSP results.

The results obtained using the original unsteady PSP calibration were unequivocally suspect due to the high temperature sensitivity of the paint. Accordingly, the data obtained using the original calibration were not used for unsteady analysis. Two temperature-corrected unsteady PSP calibration schemes, which made use of the measured surface temperatures, were developed and implemented. The evidence suggests that both of the temperature-corrected unsteady PSP calibration schemes were effective, but neither had calibrations with sufficiently high curve fit scores (R-squared values) to instill complete confidence in those results either. Still, attempts were made to conduct time-history data analyses on the temperature-corrected unsteady PSP data.

C.5 Time-History Data Analyses

Time-history data analyses, similar to those conducted for the high-speed schlieren (see Section 3.2.3), were also carried out for the unsteady PSP data. The temperature-corrected (single-surface) unsteady PSP calibration was used for this analysis. First, the calibration was applied to each instantaneous image within the time-resolved data images. Then, a time-history of pressure at specific locations was generated using the virtual pressure tap method. The fluctuation about the mean was calculated for each virtual pressure tap. These pressure-fluctuation time-histories were then analyzed using Fast-Fourier Transform (FFT) methods, nearly identical to those conducted for the high-speed schlieren.

Time-series data were acquired at 13 virtual pressure taps, as shown in Figure 130. Most of the selected locations were positioned along the jet centerline. Some were specifically placed at local pressure maxima/minima, and others were placed in regions with intermediate pressures. Four additional locations within the jet core, but removed from the centerline, were also considered. Finally, one location far away from the jet, where the pressure ratio was expected to be near unity at all times, was also considered.

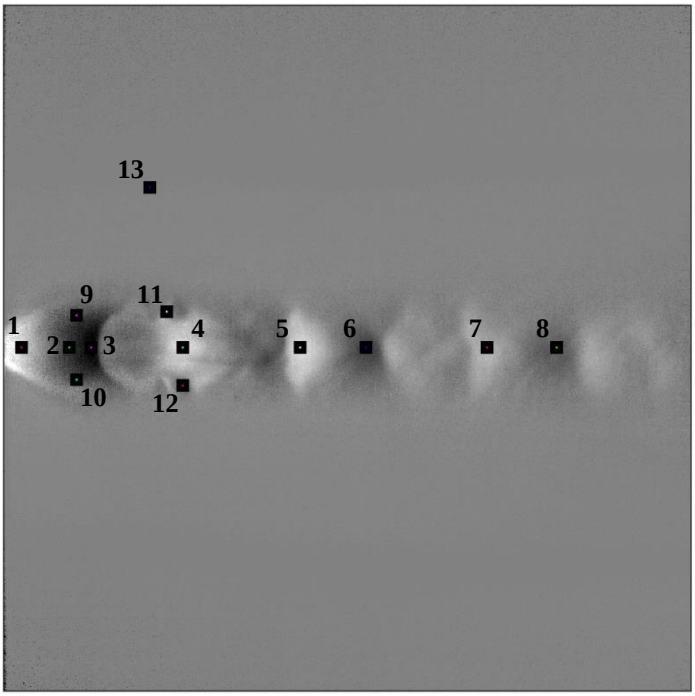

Figure 129. The black boxes denote the locations at which time-series data were catalogued.

The resulting power spectral density curves are presented in Figure 131. No distinct peaks were observed for any of the locations considered. These results point to broadband oscillation in the unsteady pressure. Similar results were observed for other locations, and for other operating conditions. However, since the unsteady PSP calibrations required the use of the correction schemes outlined previously, confidence in the resulting data is not very high. Therefore, the results of the time-series analysis should only be considered qualitatively correct.

Further validation of the temperature-corrected unsteady PSP calibration scheme developed here is required before these results can be quantitatively considered.

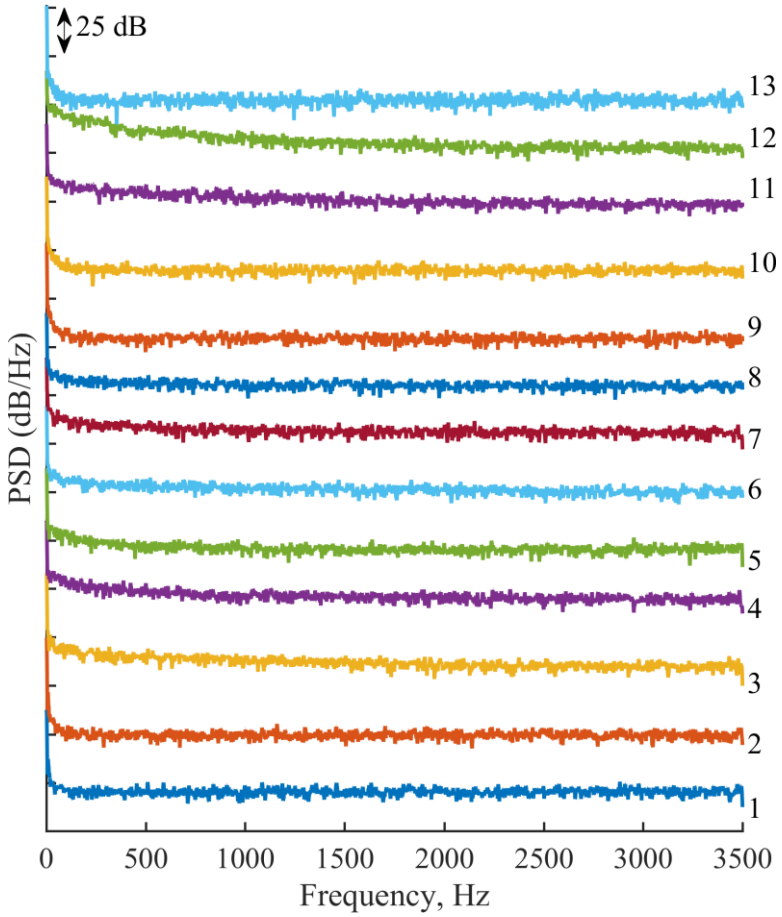

Figure 130. No dominant peaks were observed in the PSDs for any of the 13 locations considered.